Synthesis of Novel Porous Nanostructures *via* Template-Directed Methods and Applications in Photovoltaics

By

Ali Shahroozi

A thesis submitted in fulfilment of the requirements for the degree of

Doctor of Philosophy

School of Life Sciences

University of Sussex

September 2014

Declaration

I hereby declare that this work has not been submitted in any substance to another University for the award of any other degree or other academic or professional distinction.

Signed……..

Ali Shahroozi

Acknowledgments

First, I would like to express my sincere gratitude to my main supervisor Dr. Qiao Chen for his insightful guidance, support and encouragement which made this study possible.

I would like to thank my co-supervisor Dr. Mark Osborne for his helpful advice, especially in the field of “quantum dots”.

I gratefully acknowledge Thomas Samuels and Charles Creissen, two former Mchem students, who were able to assist me in some of my experimental work with immense enthusiasm and proficiency.

I am thankful to Dr. Julian Thorpe for his assistance in TEM imaging and permission to use the Gold Sputterer. Many thanks to Mr. Michael Henry and Ms. Frances Chick for providing me with chemicals and glassware every time I needed them.

I also wish to express my special thanks to Brnyia Alwhshe, Giacomo Canciani, Tom Draper, Wei Cheat Lee and Yuanxing Fang, my wonderful and understanding office colleagues. They have provided me with valuable scientific advice as well as being my true friends. My special thanks to Tom Draper for helping me with any technical difficulties I encountered using various computer software. I will miss them all!

Finally, and most importantly, I would like to thank my closest friends, parents, brother and sister for their love and support during this journey.

I am, and will always be, forever grateful to anyone who I have crossed paths with and helped me during my PhD studies.

Dedicated to my parents, for all they’ve done for me throughout my life!

"And still, after all this time, the Sun has never said to the Earth,

"You owe me."

Look what happens with love like that.

It lights up the sky."

Hafez

University of Sussex

Ali Shahroozi

PhD

Synthesis of Novel Porous Nanostructures *via* Template-Directed Methods and Applications in Photovoltaics

Summary

First, PMMA (poly(methyl methacrylate)) colloidal spheres were synthesised using surfactant free emulsion polymerisation (SFEP) process. The effects of temperature, monomer concentration and seeding in the SFEP process were investigated. PMMA colloidal crystals were fabricated using two different self-assembly techniques; the vertical deposition *via* evaporation and a modified floating (air-water interface) technique. The floating technique made it possible to fabricate 2D and 3D colloidal crystals with controlled thickness through multiple depositions.

Once self-assembled, the PMMA colloidal crystals were used as templates to synthesise different 2D and 3D metal oxide inverse opal structures. Different colloidal crystal templating techniques including vacuum assisted and horizontal templating *via* sol-gel infiltration were used to produce highly ordered inverse opal structures. A comprehensive temperature dependent study on the formation of 3D TiO_2 inverse opals was carried out. Successful synthesis of different metal oxide hollow spheres was made possible using a simple sol-gel templating approach. By using seeded polymerisation combined with template-directed synthesis, sphere-in-sphere hollow spheres were successfully

synthesised, with independent compositions for both the inner and outer spheres.

By using a modified templating technique, it was possible to synthesise bilayered inverse opals with different metal oxide layers. A successful production of such a bilayered/heterojunction system was realised. By using secondary templating combined with a chemical bath deposition (CBD) process, it was also possible to grow ZnO nanorods onto this bilayered inverse opal structure producing a hierarchical hybrid nanostructure. This novel structure was further sensitised by narrow band gap CdSe/ZnS core-shell quantum dots and used in PEC water splitting experiments. The results were very promising and showed stepwise increase in photoefficiency for every step in the synthesis of the novel hierarchical structure of quantum dot sensitised ZnO nanorods on bilayered TiO_2/ZnO inverse opal**.** Increasing surface area, enhancing charge separation, faster charge transport, better light scattering and visible light absorption all played their parts in such a sequential photoenhancing system. Bilayered TiO_2/ZnO inverse opal was also used as a photoanode material in dye sensitised solar cell (DSSC) devices and showed improved photoenhancement. The photonic crystal properties of ZnO inverse opal was investigated by coupling it to potassium titanate ($K_2Ti_4O_9$) nanobelts. Such configuration showed higher photoefficiency in DSSC devices compare to a single system of titanate.

In summary, these strategies offer a novel approach for the synthesis of hierarchical structures with each part playing a role in enhancing light harvesting for better energy conversion.

Table of Contents

List of Figures

List of Tables

Abbreviations

°C	Degree centigrade
2D	2 dimensional
3D	3 dimensional
3DOM	3 dimensionally ordered macroporous
AIBA	2’2-azobis(2-methylpropionamidine) dihydrochloride (source: Sigma-Aldrich, Pcode: 101108936, form: granular, assay: 97%)
AIBN	Azobisisobutyronitrile
ALD	Atomic layer deposition
AM	Air mass factor
atm	The standard atmosphere; an international reference pressure defined as 101325 Pa and used as a unit of pressure
CB	Conduction band
CBD	Chemical bath deposition
CdSe/ZnS QDs	Cadmium selenide / zinc sulfide core-shell quantum dots (source: Evident Technologies, core-shell Evidots in toluene, Cadskll Green, absorption (AB):531 nm, emission (EM):548 nm, Conc: 1.3 mg/ml, nmol/ml: 61.21)

CMC	Critical micelle concentration
$Cu(CO_2CH_3)_2.H_2O$	Cupper(II) acetate monohydrate (source: Sigma-Aldrich, Pcode: 101199201, puriss. p.a. ≥ 99.0% (RT))
CVD	Chemical vapour deposition
D	Diameter
D*	Excited state
D^+	Oxidised ground state
D^0	Reduced ground state
DDT	Dynamic diffraction theory
DFT	Density functional theory
DI	Deionised
DLS	Dynamic light scattering
DSSC	Dye sensitised solar cell
EDX	Energy dispersive X-ray
E_g	Band gap energy
eV	Electron volt
FCC	Face centred cubic
$Fe(NO_3)_3.9H_2O$	Iron(III) nitrate nonahydrate (source: Sigma-Aldrich, ACS reagent, assay: ≥ 98%)

Fe_2O_3	Iron(III) oxide (source: Sigma-Aldrich, nanopowder, 50-100 nm particle size (TEM), assay: 97% trace metal basis)
FF	Fill factor
FTO	Fluorine doped tin oxide
FWHM	Full width half maximum
h	Hour
HCl	Hydrochloric acid (source: Fisher Chemical, S.G. 1.16 (32%), Pcode: 11/1100/PB17)
HMT	Hexamethylenetetramine (source: ACROS ORGANICS, Pcode: 232890010, assay: 95.5%)
HOMO	Highest occupied molecular orbital
$H_2PtCl_6.6H_2O$	Chloroplatinic acid hexahydrate (source: Alfa Aesar, Pcode: 11051, assay: 99.9%)
I	Current
I_2	Iodine (source: Sigma-Aldrich, assay: ≥ 99.99% trace metals basis)
IEC	International Electrochemical Commission
IPA	Isopropanol (source: Fisher Scientific, Pcode: 10315720)

J_{SC}	Short circuit current
JCPDS	Joint Committee on Powder Diffraction Standards
K_2CO_3	Potassium carbonate (source: Fisher Scientific, Pcode: 10121440, assay: 99%)
KPS	Potassium persulphate
LED	Light emitting diode
LiI	Lithium iodide (source: Alfa Aesar, ultra-dry, 99% (metal basis))
LUMO	Lowest unoccupied molecular orbital
M	Molar
MMA	Methyl methacrylate (source: Sigma-Aldrich, Pcode: 101098307, assay: 99%)
N-719	Ditetrabutylammonium cis- bis(isothiocyanato)-bis(2,2'-bipyridyl-4,4'dicarboxylato) ruthenium(II) dye (source: Sigma-Aldrich, Pcode: 703214)
NaI	Sodium iodide (source: Sigma-Aldrich, assay: 99.999% trace metals basis)
NaOH	Sodium hydroxide (source: Fisher Chemical, Pcode: S/4920/60)

NH_4OH	Ammonium hydroxide (source: Fisher Scientific, Pcode: 10111660, ammonia (NH_3) solution 35%)
NHE	Normal hydrogen electrode
nm	Nanometer
P25	Titanium dioxide (source: Evonik Industries Co.)
PBG	Photonic band gap
PC	Photonic crystal
PEC	Photoelectrochemical
PMII	1-methyl-3-n-propylimidazolium iodide (source: Alfa Aesar, assay: 98%)
PMMA	Poly(methyl methacrylate)
PS	Polystyrene
PVA	Polyvinyl alcohol (87-89% hydrolysed, M_w 85000 ~ 124000)
QD	Quantum dot
RHE	Reversible hydrogen electrode
rpm	Revolutions per minute
RVS	Residual volume structure
SDS	Sodium dodecyl sulphate

SEM	Scanning electron microscope
SFEP	Surfactant free emulsion polymerisation
ShS	Shell structure
STH	Solar to hydrogen conversion efficiency
TBP	4-tert-butylpyridine (source: Sigma-Aldrich, Pcode: 142379, assay: 96%)
TEM	Transmission electron microscope
TEOS	Tetraethyl orthosilicate (source: Sigma-Aldrich, Pcode: 101063053, assay: ≥ 99.0% (GC))
TFI	Trifluoroacetic acid (source: Sigma-Aldrich, Pcode: 101089864, assay: 99%)
THF	Tetrahydrofuran
$TT^{i}P$	Titanium tetra-isopropoxide (source: Sigma-Aldrich, Pcode: 205273, Assay: 97%)
USAXS	Ultrasmall-angle synchrotron X-ray scattering
UV	Ultraviolet
V	Voltage
VB	Valence band
Vis	Visible

V_{OC}	Open circuit voltage
XRD	X-ray diffraction
$Zn(NO_3)_2.6H_2O$	Zinc nitrate hexahydrate (source: Alfa Aesar, Pcode: 12313, Assay: 99%)
$Zn(CH_3COO)_2.2H_2O$	Zinc acetate dihydrate (source: Sigma-Aldrich, ACS reagent, assay: ≥ 98%)
η	Photoconversion efficiency
μm	Micrometer

Chapter 1: Introduction

Nanoscience is the study of materials with dimensions ranging from several nanometres to several hundred nanometres[1]. A predominant feature of nanostructures is their possession of large surface to volume ratio which is significantly larger than that of bulk materials[2]. Optical and electronic enhancements can also be achieved using nanostructures including the formation of photonic band gaps[3] and increasing charge transfer[2, 4] properties.

Fabrication of porous nanostructures with different shapes and sizes has stimulated much interest in the last decade. Metal oxide inverse opals and hollow spheres have received particular attention due to their facile preparation and morphological advantages including high surface area, high degree of porosity and enhanced optical properties. They have broad applications in many areas including photonics, drug delivery, sensing, photocatalysis and photovoltaics[2, 5]. Colloidal spheres with nanometre diameters are often used as building blocks for the formation of inverse opals[6] and hollow spheres[7] with variable chemical composition. The self-assembled structure of such colloidal spheres are usually referred to as colloidal crystals[8]. The utilisation of inverse opals and hollow spheres as working electrodes in photovoltaic devices including PEC water splitting and dye sensitised solar cells are promising due to their high specific surface area, reduced transport length for both mass and charge transport[7], high interconnected porosity and unique photonic light scattering properties[9]. In the last decade, photonic crystals using porous ordered nanostructures has attracted much attraction with a focus on the transport and manipulation of light. The interaction of light with such materials

which possess periodic modulation in their structures has led to a range of interesting and unique effects with many promising applications such as the production of waveguides and optical sensors[10, 11]. The slow photon, mirror effect and the creation of resonant modes are some of the useful properties[12] of photonic crystals. These photonic properties and their potential applications will be discussed later in Section 1.3 in more detail. Apart from the photonic properties of these porous nanostructures, such materials have also gained interest in medicine, in particular in tissue engineering for the regeneration of tissues and organs damaged by injuries or diseases[13]. These structures, for example, can serve as scaffolds to serve as physical supports for cells to attach and migrate, as well as to create the necessary environments for the cells to respond. Inverse opals are of particular interest in this field, due to the interconnectivity of their pores which makes them suitable to support the migration of cells and transport of oxygen, nutrients, and wastes. In recent years, inverse opal scaffolds such as poly(D, L-lactide-co-glycolide)[13] and β-tricalcium phosphate[14] with micron sized pores have also been developed for the growth of blood vessels.

The concepts, properties and synthetic approaches behind colloidal spheres, colloidal crystals, photonic crystals, inverse opals and hollow spheres will be explained here in detail.

1.1 Colloidal Spheres

Colloids are small solid particles in a medium that's usually fluid. The typical size of colloidal particles ranges from nanometers to micrometers. Spherical

colloids may represent the simplest form that a colloidal particle can adopt during nucleation or growth process, as driven by minimisation of interfacial energy[15]. Spherical colloids can be synthesised from organic[16] or inorganic[17] materials. The most studied and best established examples of colloidal spheres as the building blocks for fabricating porous materials are inorganic silica (SiO_2) and polymer latexes[18, 19] such as poly(methyl methacrylate) (PMMA)[20] and polystyrene (PS)[15]. This is because they can be readily synthesised in the form of micro or nanosized spheres with well-established synthetic techniques. They can also be easily removed from the system once they have served their purpose as templates[15].

In 1968 Stober, Fink and Bohn[21] developed a method to synthesise monodisperse colloidal silica spheres. This method, also known as the SFB method (honouring all three authors), is still considered as the simplest and most effective route to create silica spheres[22, 23]. This method utilises a sol-gel route in a base catalysed reaction, using ammonia, ethanol, water and tetraethyl orthosilicate (TEOS). By controlling the amount of reactants, spherical SiO_2 particles with low polydispersity in various sizes[24] ranging from 50 nm to 1 μm can be obtained[25]. The reaction mechanism for the formation of SiO_2 colloidal spheres can be explained as following[25]:

(1) $Si(OC_2H_5)_4 + 4H_2O \rightarrow Si(OH)_4 + 4C_2H_5OH$

(2) $nSi(OH)_4 \rightarrow (SiO_2)_n + 2nH_2O$

The first step is hydrolysis, in which the ethoxy group ($Si(OC_2H_5)_4$) is replaced by OH group to form silicon hydroxide ($Si(OH)_4$). In the second step, silicon hydroxide undergoes polycondensation to form a SiO_2 network.

Traditional techniques to prepare organic colloidal spheres include emulsion[15] and surfactant-free emulsion polymerisation (SFEP) [26, 27]. These have been the methods of choice because of the monodisperse spheres that they yield. The monomers used in the synthesis of PMMA and PS are methyl methacrylate (MMA) and styrene. Figure 1.1 illustrates the polymerisation of MMA to form PMMA.

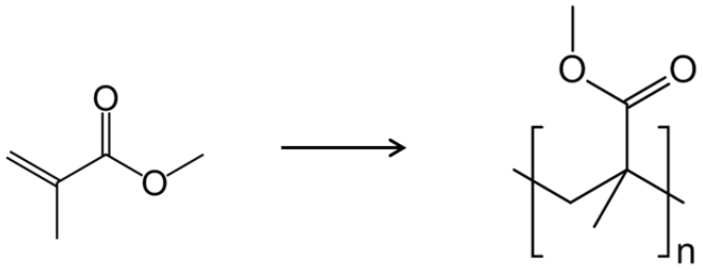

Figure. 1.1 A scheme showing the polymerisation of methyl methacrylate to form poly(methyl methacrylate).

The main components of a classical emulsion polymerisation include a monomer, a dispersion medium (usually water), an emulsifier (surfactant), and an initiator (usually water-soluble)[15].The monomer is dispersed as an aqueous emulsion (droplets of monomer in water with average diameter of 1-100 μm) with the help of the surfactant. In this process, the surfactant is added to stabilise the droplets of monomer in water. The excess surfactant creates micelles (~10 nm in diameter) in the water. A small amount of monomer diffuses through the water to the micelles. The polymerisation begins with the decomposition of the water-soluble radical initiator during which a burst of primary free radicals are generated. The individual radicals enter the micelles to polymerise the monomer. Propagation and termination take place within the micelles. First, the monomer in each individual micelle quickly polymerises and

then the growing chain (oligomer) terminates. At this point the majority of the micelles which are swollen by the monomer turn into small polymer particles. More monomer encapsulated in emulsion droplets diffuses to the growing particles, where more initiators will eventually react. The growth of polymer particles will stop when all the monomer in the emulsion droplets has been depleted and all remaining monomer is located in the particles. The final product is a dispersion of polymer particles (colloids or latexes) in water[15]. The surfactant can have an effect on the final colloidal particles diameter, increasing the amount of surfactant allows smaller particles to be stabilised and decreases coagulation of smaller particles[28].

The surfactant free emulsion polymerisation (SFEP) is a unique variation of emulsion polymerisation. This method involves the polymerization of monomers without the presence of a surfactant and hence differs from the "classical emulsion polymerisation"[29]. In the SFEP process only three components are required; monomer, initiator and solvent[26] (water in the case of PMMA and PS). Several mechanisms have been proposed for particle nucleation and growth during polymerisation using SFEP. It is generally understood that the polymerisation process in SFEP depends on the water solubility of the monomer[30]. In a typical SFEP process, first free radicals are formed by thermal decomposition of a water-soluble initiator such as potassium persulphate (KSP) in the aqueous phase. For poorly water-soluble monomers such as styrene, the free radicals begin to polymerise some of the monomers dissolved in equilibrium in water forming charged oligomers (growing chains). The resulting charged oligomers are only charged at one end, which are surface active and act as surfactants and form micelles[30]. For more water-soluble

monomers such as MMA however, particles are formed by the precipitation of growing chains upon achievement of a critical chain length (60-80 for MMA monomer) as a consequence of becoming increasingly insoluble in water[30]. In both cases, the subsequent polymerisation is analogous to the “classical emulsion polymerisation” with further polymerisation of free monomers taking place exclusively in monomer swollen particles[26].

An alternative growth mechanism was proposed by a study carried out by Telford et al.[31] for the formation of polystyrene colloidal spheres using SFEP in the presence of large amounts of initiator. They have suggested that after the formation of water-insoluble polymer chains, they collapse and form precursor particles. These precursor particles are too unstable to remain isolated due to too few charged initiator radicals to stabilise them. They will tend to form small aggregates by rapid coagulation, until they achieve enough surface charge to be individually stable and form mature particles (nucleation step). The mature particles can then swell with monomer and the continuously forming precursor particles and their aggregates. The growth of the particles terminates when all the monomer and initiator species are used up.

Although, the growth mechanism of polymer colloidal spheres using SFEP process is possibly less well understood than that of surfactant mediated emulsion polymerisation, it is still considered a powerful technique for the formation of monodisperse colloidal spheres. This is because the time for the formation of monomer swollen particles (in the case of the first two proposed mechanisms) or mature particles (in the case of the third proposed mechanism) is short, but the time during which the particles grow is very long[26, 31].

With respect to initiators, the best ionic initiators for the variation of emulsion polymerization processes are the azobisamidines, because they are water-soluble compounds with higher decomposition constant and efficiency factors than other common radical initiators such as azobisisobutyronitrile (AIBN)[32]. The other commonly used water-soluble initiator is potassium persulphate (KPS)[30, 33] which was mentioned previously. Due to the lack of surfactants in SFEP processes, these ionic initiators serve a dual purpose of both initiating the polymerisation and also providing stability to the colloidal particles through their charged end groups[34]. For instance, the initiator potassium persulphate introduces a small negative surface charge and the initiator 2'2-azobis(2-methylpropionamidine) dihydrochloride (AIBA) introduces a small positive charge surface to the colloidal particles[5]. In this work, AIBA was chosen. Figure 1.2 shows the structure (a) and the decomposition process (b) of AIBA initiator in water forming two free radicals respectively[32].

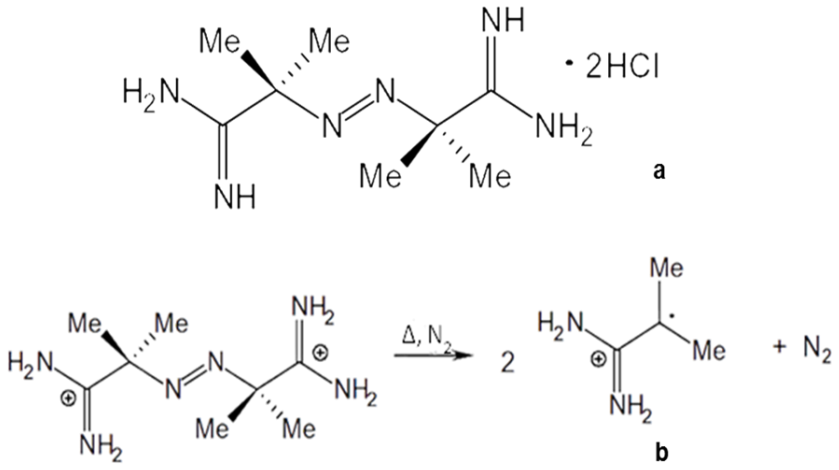

Figure. 1.2 (a) The structure of 2'2-azobis(2-methylpropionamidine) dihydrochloride (AIBA) and (b) decomposition of AIBA in water to form two radicals and a molecule of nitrogen.

Upon thermal decomposition of the AIBA initiator, two radicals are formed per initiator due to the thermal homolytic cleavage (chemical bond dissociation) of a C-N bond (~290 $kJmol^{-1}$)[35], which subsequently add to the double bond of the MMA monomer (initiation stage). In the propagation stage, the MMA monomers are added successively to the free radical end of the polymer chain which causes the chain (oligomer) to grow. In each step, the consumption of a free radical is accompanied by the formation of a new, larger free radical (charged oligomer). Finally, the polymerisation stops by consumption rather than formation of new free radicals, such as the combination of free radicals. As mentioned previously, in the SFEP process, the charged oligomers of MMA precipitate to form particles after reaching their critical chain length as a consequence of becoming increasingly insoluble in water[30]. The aggregation of the oligomers into particles is in such a way that, the charged initiator part of each oligomer faces outward interacting with water and the increasingly insoluble hydrophobic polymerised part of the oligomer faces inward. Polymerisation continues in the monomer swollen particles or by aggregation of mature particles until all the monomer and initiator species are used up as discussed previously[36]. In such systems, the spheres produced will be slightly charged with their polar initiator end facing outward which will therefore prevent them to form aggregates in water after polymerisation ends due to the repulsive electrostatic forces. The factors which explain the colloidal stability of PMMA spheres in suspension will be discussed in the next section (Section 1.2).

In the field of inverse opal and hollow sphere nanostructures, the polymerised organic and inorganic colloidal spheres which serve as templates

can be removed chemically or thermally once the appropriate material has been templated against them[16]. In the case of inorganic silica spheres, a dilute HF or NaOH solution is sufficient to completely remove the spheres without altering the morphology of the inverted structure [5, 37]. Calcination is the method used for the removal of latex polymers including PS and PMMA due to their low melting points and low temperature thermal decompositions[15, 38, 39]. Chemical etching via toluene[37] or tetrahydrofuran (THF)[27] is another approach for the removal of latex polymer spheres in templating methods. In templating processes, PMMA colloidal spheres are preferred to PS, as they tend to have better wettability with polar solvents (such as water and alcohol), shorter polymerisation time (1-2 hours compare to 48 h for PS), milder removal conditions and do not need the addition of citrate ions[40].

1.2 Colloidal Crystals

Colloidal crystals can be referred to as opals. Opal comes from the Greek word *opalus* meaning “to see a change of colour”[28]. It describes a gemstone in nature due to its iridescent colour[10]. Opals show rainbow colours despite being composed of colourless silica (SiO_2) spheres[41]. The origin of iridescence in opals comes from the ordered array structure of closely packed monodisperse colloidal silica spheres, which causes light to diffract from the planes of the spheres. In other words the colour phenomenon arises from the dispersion of incident light due to random orientation of the domains (this is also a property of photonic crystals which will be discussed later). Butterflies, other insects, marine creatures and even flora exhibit such phenomenon. Artificial opals can also be prepared that act on or operate using the same principle [10, 27, 41, 42].

There are two main strategies to create artificial opals or colloidal crystals; microfabrication (the so-called top-down approach) and colloidal crystal self-assembly (the so-called “bottom-up” approach)[11, 43].

The main methods used in microfabrication of colloidal crystals are nanolithography[43] and nanoimprinting[5]. Nanolithography is a process for fabricating functional nanostructures from bulk materials by introducing patterns with at least one lateral dimension between the size of an individual atom and approximately 100 nm[44]. In conventional nanolithography, periodic structures are produced by first exposing a monomer or a polymer-coated surface to localised photoirradiation (usually through a mask) to polymerise or induce cross-linking or decomposition reactions in the selected areas. Then by removing the selected areas of the film (covered with monomer) through dissolution in an appropriate solvent, the ordered nanopatterned colloidal crystals are obtained. Nanoimprinting is a variation of nanolithography approach, in which patterns are created by pressing a mould against a softened thermoplastic or a liquid polymer precursor. This creates patterns by mechanical deformation of imprint resist. By subsequent cooling or photocuring the polymer (using UV light) of the moulded material, the surface relief pattern is trapped giving rise to the patterned structures[11]. Such top-down approaches can be expensive, slow and may not be able to cover large structural areas and depth[43].

The self-assembly of colloidal spheres into colloidal crystals on the other hand is one of the most convenient routes to create artificial opals. This approach is simpler and less expensive than the top-down approach and can yield 3D colloidal crystals with controlled thickness[15, 43, 45]. It is the natural

tendency of monodisperse spherical particles to self-assemble into a close-packed ordered arrangement[45]. Another advantage of using this approach is the fact that such colloidal crystals can serve as templates for further processing including patterning, introducing controlled defects and infiltration to produce porous materials including inverse opals[46-53].

The interaction of two monodisperse colloidal particles suspended in a solvent which are electrostatically stabilised are generally explained as the combination of van der Waals attraction and electrostatic repulsion as described by Derjaguin-Landau-Vervey-Overbeak (DLVO) theory[15, 54, 55]. Figure 1.3 shows the schematic of DLVO potential; the attractive van der Waals potential and the repulsive electrostatic potential, and the combination of the two opposite potentials as a function of distance from the surface of a spherical particle.

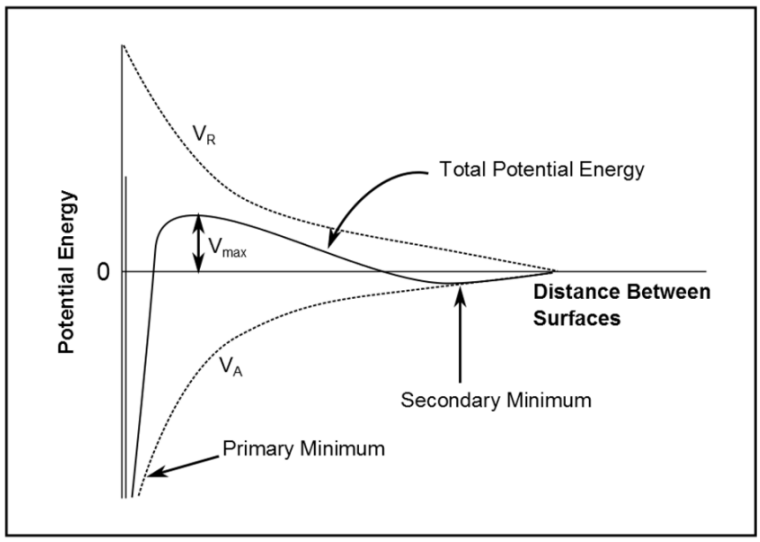

Figure. 1.3 Schematic of DLVO potential: V_A = attractive van der Waals potential, V_R = repulsive electrostatic potential[54].

When the distance is far from the colloidal particle surface, both attractive van der Waals and repulsive electrostatic potential reduce to zero. Near the surface of the particle, there is a deep minimum (primary minimum) in the potential energy produced by the van der Waals attraction. At this region, when the separation between the particles is so small and dominated by van der Waals forces, an irreversible aggregation of distinct particles into large particles can occur which is called coagulation. At a distance just a little farther away from the surface, there exists a maximum, as the repulsive electrostatic potential dominates the attractive van der Waals potential. This maximum in potential energy is also known as repulsive barrier. If the repulsive barrier is greater than ~ 10 kT, where k is Boltzmann constant, there will be stability between the two spherical particles and agglomeration will not occur. This is because the collisions of two particles produced by Brownian motion will not overcome the repulsive barrier[54].

The existence of an electric charge on the surfaces of colloidal particles is a major source of kinetic nonlability where ions of opposite charge tend to cluster nearby, and an ionic atmosphere is formed giving rise to two regions of charge[55]. The first region is a radius of a fairly immobile spherical layer of charges that adhere tightly to the surface of the colloidal particle which may include water molecules (if that is the solvent) and is the major factor in determining the mobility of the particles. The electrokinetic potential difference at the radius of sphere relative to its value in the distant, bulk medium is called the Zeta potential[55]. In the second region of charge, the charge unit attracts an oppositely charged ionic atmosphere (counter ions). The inner shell of charge and the outer ionic atmosphere is called the electrical double layer. The

secondary minimum in the DLVO potential curve as seen in Figure 1.3 originates at large particle surface separations when the concentration of counter ions is high enough (*i.e.* high ionic strength of colloidal suspension). If secondary minimum is established, particles are likely to aggregate with each other. This aggregation at the secondary minimum is called flocculation[54]. The flocculated particles can usually be redispersed again through agitation. In colloidal science, the ionic strength of the suspension is increased by addition of highly charged ions, acting as flocculating agents for particle aggregation. The coalesce of the colliding particles by breaking through the electric double layer only occurs if the collision is sufficiently energetic to disrupt the layers of ions and solvating molecules. This breaking through the electric double layer may therefore occur at high temperatures and may explain why sols precipitate when they are heated. The protective role of the electric double layer is therefore very important and explains why colloidal suspensions may coagulate at their isoelectric point (*i.e.* at the pH at which the particles carry no net electrical charge)[55].

Apart from the electrostatic stabilisation mechanism explained by DLVO theory above, Steric stabilisation, also called polymeric stabilisation, is another method widely used for the stabilisation of colloidal particle suspensions in order to produce narrow size distributions and to prevent agglomeration[54]. In contrast to electrostatic stabilisation which is a kinetic stabilisation method, steric stabilisation is a thermodynamic stabilisation method (therefore has an advantage in that, the particles are always redispersible). This method is usually used in nanoparticle growth by adsorbing a polymeric layer on the surface of nanoparticles serving as a diffusion barrier to the growth species, resulting in a

diffusion-limited growth in the subsequent growth of nuclei. Such behaviour will result in the reduction of the size distribution of the initial particle, leading to monosized nanoparticles[54].

Monodisperesed colloidal spheres can be self-assembled into ordered 2D and 3D arrays on solid substrates or on the surface of liquids using a number of strategies. Many self-assembly techniques with different ordering mechanisms have been introduced over the years for the production of colloidal crystals including;

Gravity sedimentation[43, 56, 57], centrifugation[43, 58], vacuum infiltration[59], horizontal deposition[20, 60-62], vertical deposition *via* dip drawing[50, 63-69], vertical deposition *via* evaporation[47-49, 70-73], spin coating[74, 75], physical confinement[15, 76, 77],air/water interface (floating)[78, 79] and exterior fields including electric and magnetic-field directed[71] self-assemblies.

The gravity sedimentation technique is one of the earliest colloidal crystal self-assembly techniques which involves the natural sedimentation of colloidal spheres in a solution due to the natural gravitational field. This technique was first used for silica spheres[21]. This technique can be very time consuming and may take weeks to months to perform. Other variations of this technique were later developed to increase the rate of self-assembly including vacuum infiltration[59] and centrifugation[80]. However it was still challenging to prepare high quality colloidal crystals by these techniques. Numerous defects such as cracks and grain boundaries could be detected and the thickness of the resulting colloidal crystals could not be well controlled[81].

Park and Xia[82] were the pioneers of physical confinement self-assembly technique. In this technique, colloidal crystals are formed in a physically confined cell in which a colloidal suspension is squeezed between two planar substrates spaced by a porous sidewall with small patterned channels. By continuous sonification, the spheres settle in their thermodynamically favoured positions. This method can reduce colloidal crystal preparation time. However, it requires special equipment and may not work for colloidal spheres with large diameters, as the holes in the channels are usually very small.

Assembling latex colloidal spheres under the effect of external fields (exterior fields)[81], such as electric and magnetic fields has become a popular technique for the construction of colloidal crystals. In electric field directed self-assembly, highly charged monodisperse latex spheres are assembled into ordered colloidal aggregates by applying an electric field between two electrodes[83]. The self-assembly can be controlled by varying the electric field strength and the viscosity of the solution. Magnetic fields have also been used widely for the fabrication of colloidal crystals. For example ordered colloidal crystals of γ-Fe_2O_3[84] and Fe_3O_4[85] nanoparticles dispersed in water have been prepared in the presence of a external magnetic field, forcing the nanoparticles to align and order in the direction of the field.

Spin coating is another technique to fabricate ordered colloidal crystals. By the use of shear-induced ordering mechanism, large areas of well-ordered colloidal crystals with uniform thickness can be obtained[75]. The thickness of the prepared colloidal crystals can be controlled simply by changing the spinning time and speed. The drawback of this technique however, is the need to use

highly viscous colloidal sphere suspensions which makes the required dispersion process tedious[81].

The most common self-assembly techniques are horizontal deposition and variations on vertical deposition[37, 81]. Both approaches are straightforward experimentally and control can be exerted over the colloidal crystals produced. The technique of horizontal deposition[20, 60-62] sees drops of the colloidal sphere solution placed horizontally onto a substrate. The solvent is then allowed to evaporate, leaving behind a film of colloidal crystal. Two variations for vertical deposition process exist. The first variety, “vertical deposition *via* dip drawing”, has a substrate suspended vertically in a colloidal sphere solution, which is then slowly pulled out of the solution. The rate of substrate removal can be varied to change the thickness of the colloidal crystal[53-59]. The other method of vertical deposition is “vertical deposition *via* evaporation”; this involves suspending the substrate in a colloidal sphere solution and allowing the solvent to evaporate. This can be carried out in vacuo or under atmospheric conditions in an oven[36-38].

It was discovered that the main driving forces in both horizontal and vertical deposition techniques are capillary interactions and convective transport at the meniscus drying front. This was originally investigated by Denkov et al[86]. A two stage mechanism for the formation of a 2D array of colloidal crystal on a flat substrate was proposed. This is illustrated in Figure 1.4.

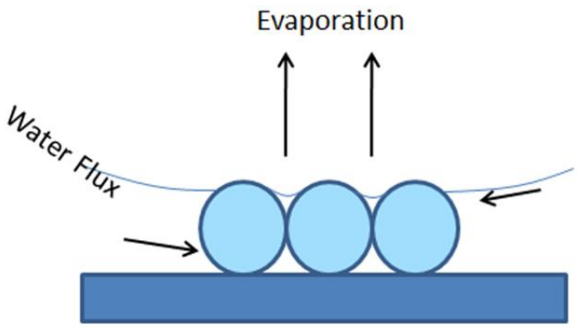

Figure. 1.4 Schematic of the formation of a 2D array of colloidal crystals on a horizontal substrate.

In the first phase, through evaporation of the solvent, there exists an instance when the thickness of the solvent layer containing the spheres becomes less than the colloidal sphere diameter. Deformation of the meniscus (the liquid-air interface) gives rise to capillary interactions between particles. The closely orientated spheres form a 2D cluster (nucleus) of ordered spheres because of these interactions. Once the nucleus is formed, the second stage of crystal growth occurs by convective transport of spheres toward the ordered nucleus. This convective transport is induced by solvent evaporation from concave-shaped menisci. The increase in the local curvature increases the local capillary pressure, which draws in the liquid to the nucleus from the thicker parts of the meniscus where the pressure is higher. The spheres inside this convective influx are pressed to the nucleus by the hydrodynamic pressure of the liquid and attached to the other spheres in this region by the capillary attraction. Eventually a close-packed array of 2D colloidal crystals is formed on the substrate. A similar mechanism that explains 2D colloidal crystals can be applied for 3D systems. This is because controlling the capillary forces and the convective particle flux during solvent evaporation can determine the 2D or 3D nature of the colloidal crystals[87]. In the case of 3D colloidal crystal formation,

the convective particle flux dominates, causing additional spheres to be drawn towards the crystal front driven by the evaporation of the solvent from within the drying colloidal crystal layer[5]. In this process, the crystal thickness could be controlled by the concentration of the latex suspension or particle diameter[71, 88]. Figure 1.5 shows a schematic representation for the formation of a 3D colloidal crystal using the vertical deposition technique.

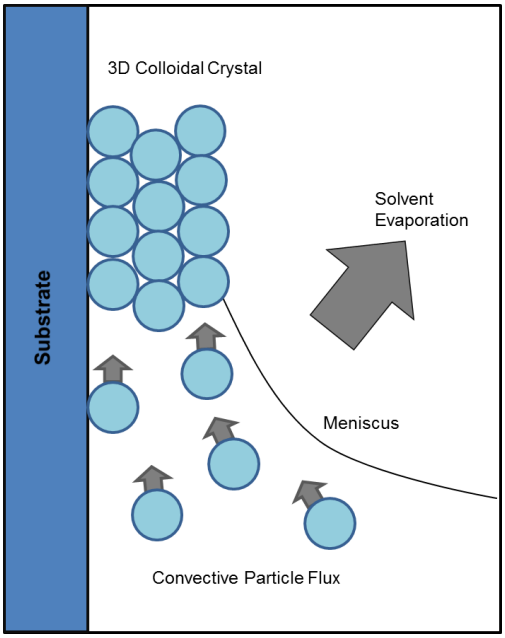

Figure. 1.5 Schematic of the formation of a 3D colloidal crystal using the vertical deposition technique.

Another technique for producing colloidal crystals is self-assembly at an air-water interface, the “floating technique”. The self-assembly processes take place on the surface of the liquid. A benefit of this method of interfacial assembly is that it is fast and can produce monolayer colloidal crystals exclusively[89, 90]. The ordering mechanism in the floating technique relies on surface forces in the liquid as well as forces between the colloidal spheres. It is energetically favourable for spherically-shaped particles to come together on

the surface of a liquid. This is due to interface deformations, as particles adsorbed at the surface of a liquid they can deform it[91]. The fluid interface may be distorted by the particle in several ways such as: particle buoyant weight, particle confinement in a liquid film, electric field and roughness effects. These interface deformations can attract and repel each other leading to interface mediated interactions. The so-called “capillary interactions” originate from the overlap of interfacial deformations created around the particles[91]. Once they are in contact, the spheres adhere to each other via Van der Waals attractions. In addition, as most latex colloidal spheres including PMMA and PS spheres are weakly charged, the electrostatic interaction can result in interparticle repulsion as well increasing the mobility of spheres in close proximity to one another. Such forces can therefore increase the orderliness in the formation of colloidal crystals [89, 90]. The quality of monolayer colloidal crystals created by using this self-assembly technique can be affected by a variety of factors including colloidal particle concentration, zeta potential of the colloidal particles in the suspension, surface tension of the water phase, hardness of the colloidal particles, the addition of spreading solvents and salts in the suspension[92].

3D colloidal crystals fabricated by self-assembly techniques tend to form a close-packed face centred cubic (FCC) crystal structure with (ABCABC…) stacking or a hexagonal close-packed (HCP) with (ABABAB…) stacking, in which their (111) planes are parallel to the underlying substrate. It is usually difficult to distinguish between these two crystal configurations in colloidal crystal fabrication. The FCC structure is energetically favoured over HCP[33, 43, 65, 78, 93], although the energy difference is small. The FCC ordering has also been confirmed by ultrasmall-angle synchrotron X-ray diffraction (USAXS) and the

tilting of TEM images in a previous study[43]. In this periodic structure, each sphere is in contact with 12 other spheres (i.e. 6 in the same layer, 3 in the layer above, and 3 in the layer below) with 24% of the volume being air and 76% colloidal spheres[15, 20, 43, 52, 68, 94].

1.3 Photonic Crystals

Since Yablonovich[95] and John[96] in 1987 independently proposed the concept of the photonic band gap and the realisation of its vast potential applications, scientists have been focused on the development of colloidal crystals (opals) and their inverted structures (inverse opals) as photonic crystals.

Photonic band gap (PBG) materials or photonic crystals (PCs) are highly ordered spatially periodic structures constructed from alternating regions of dielectric materials with different refractive indices, with periods on the scale of visible light wavelengths (380-750 nm)[43, 46, 97, 98]. In principle, the band structure of a PBG crystal can be obtained by solving the Maxwell equations that contain a spatially periodic function for the dielectric constant[15]. Such materials diffract photons from a lattice of dielectric planes in a manner analogous to the behaviour of electrons with respect to an atomic crystal lattice. In other words, it appears that allowed bands and forbidden gaps for photons exist. Periodicity affects the propagation of electromagnetic waves in the material due to Bragg diffractions on lattice planes. The result is a photonic band gap (PBG or stop band), a band of frequencies where light propagation in the photonic crystal is forbidden. This is the optical analogue of electronic band gaps seen in semiconductors[10, 27, 37, 99, 100]. Photonic crystals are also called the

“semiconductors for photons” with the advantage that photons have no mass or electrical charge unlike electrons in semiconductors [56, 101]. At the photonic band edges, the group velocity of light is reduced and the photon density of states is enhanced. For photons, the degree of attenuation in group velocity in real crystals depends on the dielectric contrast between the high and low refractive index materials, the thickness and the structural quality of the photonic crystal. The photons propagating with reduced velocity at the band edges are also called slow photons. Ozin and his group[12] were the pioneers to demonstrate the effect of slow photon phenomenon in photochemical reactions. They used TiO_2 inverse opal as a photonic crystal material and investigated the photocatalytic degradation of adsorbed methylene blue dyes. They found that when such photochemical reaction was activated by light at a wavelength corresponding to the photonic stop band edges of the inverse opal, light absorption and photodegradation efficiency of the dyes were enhanced by 22%. Aside from the slow photon effect in photonic crystals, these structures can also be used as photonic crystal mirrors to create localised states when coupled to a non-structured surface. Molouk and his colleagues[102, 103] were the pioneers in using this phenomenon in dye sensitised solar cells. They cast a TiO_2 inverse opal on a TiO_2 thin film photoanode based DSSC and illuminated from the photonic side. The bilayer structure showed 26% increase in overall efficiency. Interestingly they found out that, a single TiO_2 inverse opal layer structure did not contribute to photoefficiency enhancement, as the stop band reflectivity outweighed the slow photon phenomenon leading to decreased light harvesting. Therefore, in applications where enhancement over a broad spectral range is desired, bilayered architecture may be more advantages by using the photonic

crystal mirror effect. In another study, O'Brien et al[104] coupled TiO_2 inverse opal to a Si solar cell and achieved 138% photoperformance by improving the light absorption of Si. They attributed this behaviour to the creation of partially localised resonant modes within the Si by the inverse opal. The highly amplified absorption over a range of frequencies in this opal-Si configuration, compared to a film backed by a perfect mirror can have far reaching implications in other scientific and technological areas, such as organic and inorganic light emitting diodes and lasers[12].

The colour in photonic crystals arises form diffraction of light which can be altered by changing the angle of incident light, the refractive index contrasts, lattice constants and filling factors in colloidal crystals and inverse opals (Chapter 4). Because the photonic band gap wavelength is directly proportional to these variables, the colour of such materials can be shifted to higher or lower wavelength colours simply by increasing or decreasing the size of the colloidal spheres used as the building blocks or by filling the voids with solvents with different refractive indices[27, 41, 42]. These striking colours and colour changes in photonic crystal materials and the compositional flexibility of using colloidal crystals (Section 1.2) and inverse opals (Section 1.4) as photonic crystals, make them suitable candidates in chemical sensors, optical filters, or photonic pigments[15, 27].

The range of applications for these materials is vast. Wavelengths of light can be blocked irrespective of their direction and polarisation, photons can be localised at specific frequencies and stimulated emission can also be modulated or controlled[15, 67]. They can also act as waveguides to propagate specific wavelengths in certain directions. When defects that locally break the spatial

periodicity of a photonic crystal are introduced in a controlled manner, the wave guiding phenomenon occurs. Defects introduce states that lie in the photonic band gap, which allows light to propagate but only in those regions defined by the defect structure. When light propagates in this fashion, optical losses can be very low, because beam propagation is not based on total internal reflection[100]. These properties can be utilised in telecommunication systems, LEDs, semiconductor diode lasers and enhancing the performance of optoelectronics[15, 27].

1.4 Inverse Opals

Once the colloidal spheres are self-assembled into colloidal crystals, they can be used as templates to produce Inverse opal materials. Inverse opals can also be called photonic crystals[42] due to their unique optoelectronic properties caused by their distinctive and highly ordered periodic structures[27]. Template-directed synthesis (or colloidal crystal templating) [25, 30-33, 38, 65, 77] is known as one of the most convenient, versatile and cost effective methods for generating 2D and 3D inverse opal structures. This method has been successfully applied to prepare inverse opal materials with diverse compositions including metals, metal oxides, semiconductors, organic polymers and carbons [15, 27, 38, 39].

In this method the colloidal crystal (opal) template serves as a scaffold with voids (pores) infiltrated with the materials of interest. Two different infiltration techniques have been employed to grow materials within the pores of the colloidal crystal templates[105]. When the material is grown (synthesised) inside the structure, it is identified as *chemical* infiltration and when it is only

infiltrated having been prepared previously is called *physical* infiltration[45]. By then removing the template *via* wet chemical etching or calcination, a macroporous “inverse opal” material with a close-packed arrangement of inverted air spheres is created which is the replica of the original template[15, 27, 38, 39].

In *physical* infiltration, the materials of interest are first synthesised with particles smaller than the pores of the colloidal crystal (usually in the form of nanoparticles in solutions). They can then infiltrate the pores of the colloidal crystals. The usual method involves dipping the colloidal crystal into a solution containing the material. Organic dyes infiltrating the pores of a colloidal crystals is an example of physical infiltration[105]. The other method of infiltration, is electrophoretic deposition[5]. Here, the colloidal crystal acts as a working electrode in an electrochemical cell, and is placed with a counter electrode in a suspension of preformed nanoparticles. By introducing an electric field between the two electrodes, the nanoparticles fill the interstitial pores of the colloidal crystal, if their surface charge is opposite to the charge of the colloidal crystal working electrode (this can be done using zeta-potential measurements). The drawback of this method is that, the nanoparticles can block entry to lower-lying colloidal crystal layers, which leads to poor filling throughout the structure. The other drawback is that, the choice of substrate is only limited to conductive substrates.

Chemical infiltration include sol-gel[53, 61, 106] and electrodepostion[45, 49, 62] methods. In the sol-gel approach, the precursor of the interested material is capable of solidification *via* a sol-gel approach (hydrolysation and subsequent condensation) within the pores of the colloidal crystal without swelling or

dissolving the template[15, 27]. Electrodeposition has been widely used to infiltrate a large variety of metals including gold, silver, nickel into colloidal crystals creating 2D and 3D inverse opals[105]. This technique is also useful for the synthesis of conductive polymers such as polyaniline (PANI)[5]. In this approach, the colloidal crystal is first grown on a working electrode surface of an electrochemical cell in a two electrode system, similar to the electrophoretic deposition stated previously. A suitable electroplating solution is then used as the precursor solution. The desired material is formed between the interstitial pores of the colloidal crystal by electrodepostion, using either cyclic voltammetry or galvanostic deposition. The deposition builds up starting from the conductive substrate of the colloidal crystal working electrode, growing outward through the colloidal crystal. This method, therefore, avoids pore blockage during infiltration and fills the interstitial pores completely due to this outward infiltration. The deposition electrical current can be used to control both the deposition rate and the thickness of the deposited layer. The template can be removed by solvent extraction[5]. The drawback for electrodeposition is that, it can only be performed if the colloidal crystal template is grown onto a conductive substrate (similar to the electrophoretic process)[107].

Recently, gas based infiltration approaches such as chemical vapour deposition (CVD)[38, 45] or atomic layer deposition (ALD)[45] have shown promise in the synthesis of inverse opal structures. In a typical CVD process[54], a volatile compound of the interested material reacts with other gases chemically to produce a non-volatile solid that deposits atomistically within the pores of the colloidal crystal. In CVD methods, two types of reactions can take place; gas phase (homogeneous) and surface (heterogeneous) reactions, in which gas

phase reactions dominate with controlled temperature and partial pressure of the reactants, leading to a homogeneous nucleation. There are a variety of chemical reactions which can take place in CVD including pyrolysis, reduction, oxidation, compound formation, disproportionation and reversible transfer, depending on the precursors used and the deposition conditions applied. Electrochemical vapour deposition (EVD)[54] is a modified form of CVD which has been developed to deposit solid phase from gaseous precursors on highly porous substrates or inside porous media. In a typical EVD process, a porous substrate separates metal precursor(s) and oxygen source which will subsequently inter-diffuse and react with each other when they concur to deposit the corresponding solid metal oxides. Oxygen precursors diffuse much faster than metal precursors and as result, the deposition occurs at the entrance of pores on the side facing the metal precursors, and plug the pores. In this process, the oxygen source (which can be a water vapour, oxygen, or air or a mixture of them) is reduced at the oxygen/film interface to produce oxygen ions which are transferred in the film. As the oxygen vacancies diffuse in the opposite direction, they react with the metal precursors at the film/metal precursor interface. This process will then continuously form metal oxide in or between the pores. EVD has been explored for fabricating gas-tight dense solid electrolyte films on porous substrates. The most studied EVD synthesised system has been the yttria-stabilised zirconia films on porous alumina substrates with applications mainly in solid oxide fuel cells and dense membranes.

Atomic layer deposition (ALD) which is also known as atomic layer epitaxy (ALE), atomic layer growth (ALG), atomic layer CVD (ALCVD), and a

molecular layer epitaxy (MLE)[54], can be considered as a special modification of the CVD method, or a combination of vapour-phase self-assembly and surface reaction. In this technique, metallic and nonmetallic precursors are deposited between the pores of the colloidal crystal in alternating reaction steps, to build up the desired structure, one layer at a time. Therefore, in a typical ALD approach, monolayer colloidal crystals are filled and stack up to produce the 3D structure. In this technique, first the surface of a monolayer is activated on the colloidal crystal surface by a chemical reaction. Then, the precursors are introduced into the deposition chamber which will react with the active surface species and form chemical bonds with them. Since the precursors deposited between the pores of the colloidal crystal cannot chemically react with themselves, therefore the surface has to be activated again for the next deposition. In each deposition step, either the same or different precursors can be subsequently introduced to the deposition chamber and react with the activated monolayer on the colloidal crystal deposited previously. By repeating the steps, more layers stack up leading to the 3D structure. In both CVD and ALD techniques, the desired inverse opal is obtained after removing the colloidal crystal template[5]. The drawback in those approaches comes from the relatively high temperatures needed for infiltration which can limit the usable organic colloidal crystal templates, such as PS and PMMA [105].

In general, the sol-gel infiltration approach can be considered as the method of choice[37] for the synthesis of metal oxide inverse opals. This method is advantageous in several respects including excellent homogeneity, easy control of film thickness, ability to coat large and complex shapes, and low-temperature and low-cost processing[53]. Figure 1.6 illustrates the schematic

diagram of colloidal crystal templating by sol-gel infiltration for the synthesis of metal oxide inverse opals.

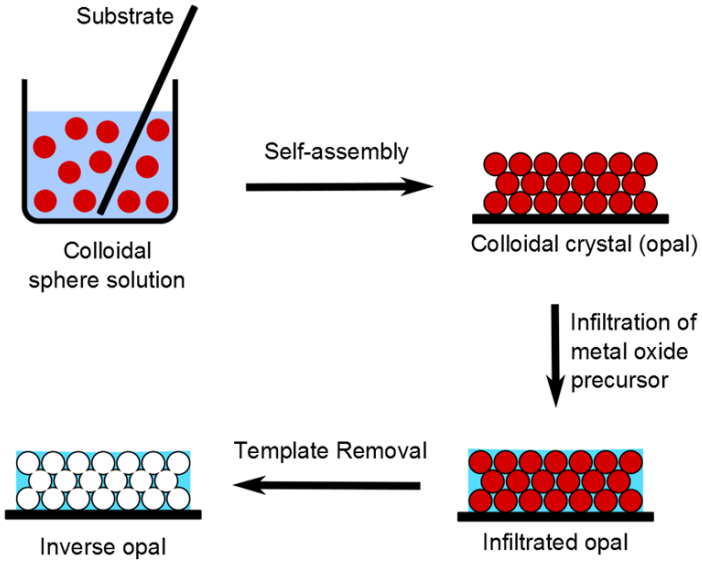

Figure. 1.6 A schematic showing the synthesis of an inverse opal using colloidal crystal templating via sol-gel infiltration[37].

As it can be seen from Figure 1.6, the colloidal spheres are first self-assembled to fabricate a close-packed colloidal crystal (*via* vertical deposition technique in this scheme). Then, the interstitial gaps in the colloidal crystal structure is infiltrated with an appropriate metal oxide precursor. The precursor usually consists of a metal salt[27, 43, 61, 107] (alkoxide, acetate or nitrate) solution. Such a precursor then goes through a sol-gel process forming a network of hydrolysed gel. The gel is further solidified and condensed[27] *via* ageing in air. In the next stage, the polymer colloidal crystal is removed by either chemical etching or careful calcination[16, 43]. This results in three dimensional ordered macroporous (3DOM)[5] or inverse opal structures with interconnected tetrahedral and octahedral sites, which were previously air gaps. Calcination has an advantage over chemical etching in the template removal stage. This is

because the inverted metal oxide structure can be reinforced and transformed from its amorphous phase to the more desired crystalline phase at elevated temperatures[5]. The inverse opal pore size is determined by the diameters of the original colloidal spheres[15] as can be seen in Figure 1.6.

Three kinds of inverse opal structures have been reported with different morphologies[108];

1) Shell structures (ShS), which can be produced by incomplete filling of the opal by the metal oxide precursor and the final product consists of spherical shells around the air spheres.

2) Skeleton structures, which can be produced again by incomplete filling of the opal with the metal oxide precursor (similar to ShS). But this time, the final product consists of cylinders connecting the tetrahedral and octahedral voids among the close-packed air spheres.

3) Residual volume structures (RVS), which can be produced if the whole space between the spheres is filled with the metal oxide precursor (complete filling).

The conventional sequential steps of self-assembly, infiltration and template removal shown in Figure 1.6 can produce defects and cracks in the final inverse opal product[109]. The cracking may occur upon solvent evaporation both at the colloidal self-assembly[110] and at the precursor infiltration[111] stages due to a combination of dehydration, contraction[19] and associated local capillary forces. Hatton et al.[109] demonstrated a unique process of colloidal co-assembly by combining the self-assembly and infiltration processes into one step. In his paper, Hatton reported that the colloidal spheres were allowed to assemble directly from a precursor containing a sol-gel solution for the fabrication of SiO_2

inverse opals. Robust and crack-free inverse opal films were fabricated after template removal due to the “gluing” action of the sol-gel matrix.

1.5 Hollow Spheres

Metal oxide hollow spheres can be prepared by different approaches including template-based or template-free approaches[7]. Template free approaches using hydrothermal or solvothermal reactions[112] have been proved to be simple and efficient. Hydrothermal and solvothermal reactions are very similar, where the synthesis is conducted in a stainless steel autoclave in a hot environment under high pressure (T>100°C, P>1 atm)[113]. The only difference is that in hydrothermal method, water is used as the main solvent, but solvothermal route is usually not aqueous[114]. In one study, Yang et al[115] synthesised tin oxide (SnO_2) hollow spheres by directly adding tin chloride ($SnCl_4$) to the aqueous solution of sucrose and then hydrothermally treating it at 190°C for 24 h. A composite of SnO_2 and carbon was yielded through condensation polymerisation and carbonisation of sucrose. The $SnCl_4$ was hydrolysed and the resulting SnO_2 hollow spheres were obtained by removing the carbon core *via* calcination. In another study, Hoa et al[114] synthesised Tungsten oxide (WO_3) hollow spheres using solvothermal method. Tungsten hexachloride (WCl_6) and urea were dissolved in ethanol in a Teflon-lined autoclave and treated at 180°C for 8 h followed by calcination at 400°C in air for 2 h to produce the hollow spheres. In both of these studies, the surface of the hollow spheres produced were not smooth as a result of formation of too many aggregates of nanocrystals. It is also difficult to control the size and morphology of hollow

spheres with these approaches. Therefore, template-based methods are still promising for the synthesis of high quality hollow spheres with uniform morphologies[7]. In template-directed synthesis, colloidal spheres are used directly as templates to produce hollow spheres of different materials including metal oxides[116]. Fabrication of these materials does not require the prior self-assembly of the colloidal spheres into colloidal crystals as is the case for the fabrication of inverse opal structures[27]. In this method, the desired metal oxide precursor gradually covers and stabilises onto the colloidal sphere core template by sol-gel processes (*via* hydrolysation and condensation reactions)[7]. Then by removing the template by wet chemical etching or calcination, the hollow sphere material is produced. The pore size of the hollow sphere is determined by the diameter of the original colloidal spheres. Figure 1.7 illustrates the schematic diagram of template-directed synthesis for the production of metal oxide hollow spheres using PMMA colloidal spheres as the serving template.

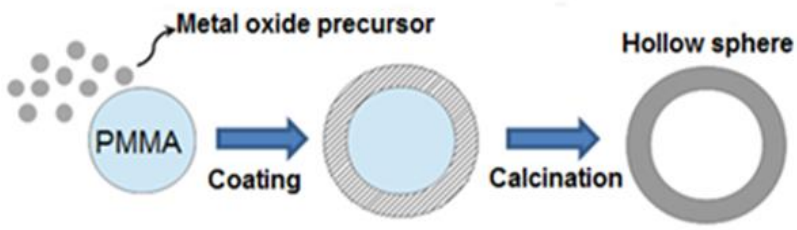

Figure. 1.7 Schematic diagram of template-directed synthesis for the production of metal oxide hollow spheres.

As it can be seen in Figure 1.7, first the polymer colloidal sphere is exposed to a precursor containing one of various metal salts such as alkoxides, acetate or nitrate in the presence of water. The precursor gradually covers the

sphere *via* controlled surface precipitation of inorganic metal oxide precursors or by direct surface reactions utilising specific functional groups on the polymer sphere cores to create core-shell composites[112, 117]. The precursor's tendency to cover the sphere can be due to the slightly charged nature of the PMMA sphere forming a weak electrostatic interaction with the metal salt. Then by the sol-gel process, the precursor is geleated and stabilised onto the PMMA sphere. After further ageing and condensation of the sol-gel system, the sphere template is removed forming the metal oxide hollow sphere[118, 119].

In template-directed approaches *via* sol-gel reactions for both metal oxide hollow spheres and inverse opals, the core templates (here PMMA spheres) are removed with appropriate solvents in the final step in order to yield the porous nanostructures. The core organic spheres are dissolved into macromolecule chains with the solvent and diffuse through defects in the metal oxide (mesopores)[120] of the metal oxide shells and frameworks[117]. The organic polymer spheres can also be thermally removed through a calcination process, in which the polymer spheres are decomposed and oxidised into CO_2 and water. It is important to increase the calcination temperature gradually during the template removal stage. This can prevent the precipitation of unwanted carbon deposits in the mesopores of metal oxide shells which may block these very small pores and result in an unsuccessful template removal (with some traces of template residues being left behind)[120]. The gradual calcination process can also help to keep the integrity of the porosity of the final structures[121] (*i.e.* the macropores of hollow spheres and inverse opals) and prevent their collapse (Chapter 5).

Titanium dioxide coatings have been explored frequently due to the excellent photocatalytic properties of TiO_2[119, 122-125]. In template-directed synthesis *via* sol-gel coating, the polymer spheres are coated usually by titanium tetra-isopropoxide (TT^iP) as the main sol-gel precursor, however alternatives such as $Ti(SO_4)_2$ have also been used[124]. Similar methods have been applied to the coating of polymer spheres with SiO_2[118] and SnO_2[119]. The production of solid TiO_2 spheres (core spheres) have also been reported in the literature. Wang et al[126] synthesised the TiO_2 spheres by a rapid microwave treatment (at 150°C for 10 minutes) of spherical titanium glycolate precursors, obtained by mixing tetraethyl titanate with ethylene glycol followed by adding the precursor into a solution containing acetone and water. Due to the nature of TiO_2, their hollow sphere nanostructures can be promising in photovoltaic and photocatalytic applications, the oxide layer is porous and therefore has a high surface area due to the presence of inner and outer surface areas of the hollow sphere[7].

1.6 Thesis Objectives

The principles of PEC water splitting and dye sensitised solar cells (DSSC), the two applications used to test the photocatalytic properties of the novel nanomaterials in this work, will be explained. Additionally, characterisation techniques including electron microscopy (SEM and TEM), energy dispersive X-rays (EDX), dynamic light scattering (DLS), powder XRD and UV/Vis spectroscopy will be explained. The characterisation techniques used to study the optical and crystal properties of colloidal crystals and inverse opals will also be discussed.

The production of high quality monodisperse PMMA colloidal spheres using the surfactant free emulsion polymerisation (SFEP) process, and using them to fabricate highly ordered PMMA colloidal crystals, are the first two experimental objectives in this thesis.

Once self-assembled, the PMMA colloidal crystals have been used as templates for the production of different 2D and 3D metal oxide inverse opal nanostructures including TiO_2, ZnO and Fe_2O_3 inverse opal systems.

PMMA colloidal spheres were also be used prior to self-assembly to produce various metal oxide hollow sphere nanostructures including TiO_2, SiO_2, ZnO and CuO hollow spheres. A new method of combining seeded polymerisation with the templating approach has been developed in this work for the production of novel sphere-in-sphere hollow spheres of a SiO_2/TiO_2 system with increased surface area.

The final objective of this thesis is to produce novel inverse opal nanostructures and utilise them as photoelectrodes in both PEC water splitting and dye sensitised solar cell (DSSC) devices. Bilayered TiO_2/ZnO inverse opal nanostructures have been synthesised for the first time using a modified templating approach. The successful synthesis of hybrid hierarchical nanostructures of bilayered TiO_2/ZnO with further growth of ZnO nanorods coupled with quantum dots has been the ultimate goal of this thesis. Such a hierarchical system can increase the photoefficiency of photovoltaic devices significantly due to opto-electronic enhancement abilities, contributed from each individual layer and component of this novel nanostructure.

Chapter 2: Applications and Characterisation Methods

2.1 Abstract

In this chapter, the principles of PEC water splitting and dye sensitised solar cells (DSSCs) are explored. The PEC testing of the synthesised nanostructures gives direct insight into the properties and performance of these materials. Additionally, the general principles of electron microscopy (SEM and TEM), energy dispersive X-rays (EDX), dynamic light scattering (DLS) and powder XRD, and their use as characterisation techniques, are explained. The principles of band gap determination of semiconductors using UV/Vis spectroscopy will also be discussed. Some characterisation techniques which can be used to study the optical and crystal properties of colloidal crystals and inverse opals due to their periodic natures are also explored.

2.2 Photoelectrochemical (PEC) Water Splitting

Using the sun's energy to split water in order to create hydrogen is a promising development to replace fossil fuels[127]. Unlike steam-reforming of hydrocarbons, photocatalytic water splitting is an inexpensive, renewable and an environmentally safe process with minimum greenhouse gas emission[128] . Metal oxide semiconductors have been widely used in PEC water splitting devices due to their relative low cost, their inertness and scalability for production purposes[129]. Their performances in harvesting solar energy as a renewable energy source are critical in determining the efficiency of hydrogen generation. The process of splitting water generally consists of three steps:

1) When the energy of incident photons from sunlight matches or exceeds the band gap of a photocatalyst, the photogenerated electrons are transferred from the valence band (VB) to the conduction band (CB). An equivalent number of holes is then left in the valence band producing electron – hole pairs.
2) The excited electron – hole pairs migrate to the surface of the photocatalyst.
3) The electron-hole pairs cause redox reactions with the chemical species (electron donors or acceptors) adsorbed on the photocatalyst surface.

In the case of an n-type semiconductor photocatalyst, the holes at the surface of the electrode react with the water molecules of an aqueous electrolyte, oxidising them to dioxygen (O_2). Subsequently, electrons travel through the underlying substrate and are transported to the counter electrode (cathode) where they reduce water molecules to dihydrogen (H_2). At a high current density, hydrogen and oxygen generation can be visualised through the evolution of gas on the cathode (usually platinum) and the photoanode (the photocatalyst) respectively. For a p-type semiconductor electrode, the opposite occurs resulting in O_2 and H_2 formation at the counter electrode and semiconductor electrode respectively (i.e. cathodic photocurrent behaviour as opposed to anodic photocurrent from n-type semiconductors).

Figure 2.1 shows the schematic diagram of a PEC cell configured for an n-type photoanode water splitting system. It is common practice for PEC water splitting experiments to use a reference electrode (usually *Ag/AgCl*). This is used to measure half-reactions in the PEC cell and by doing this Fermi energy levels can be measured with respect to the reference electrode energy level.

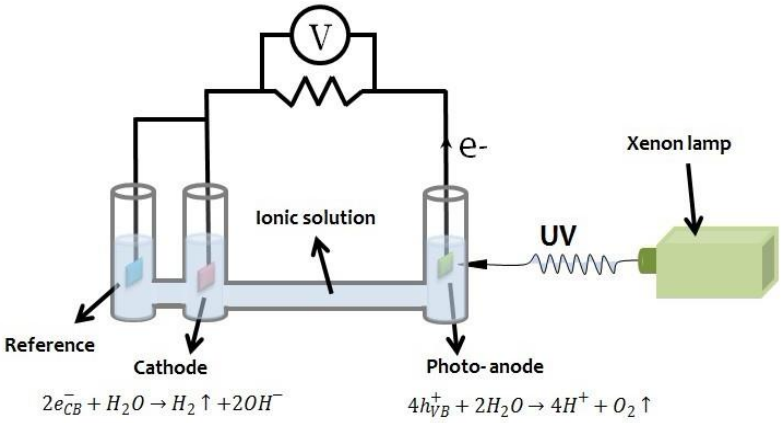

Figure. 2.1 A schematic showing the principle of a photo-electrochemical cell for n-type photocatalytic water splitting.

When the photoanode is immersed in a redox electrolyte, the charge carriers are transferred at the semiconductor/electrolyte interface until an equilibrium is reached (i.e the same Fermi energy level at both sides of the interface is reached). This charge transfer process results in bending of the energy bands either upwards (n-type semiconductor) or downwards (p-type semiconductor) due to the generation of an electric field close to the surface of the semiconductor. This phenomenon is called Schotky contact[130], where the recombination of the electrons and holes are prevented and the electrons are trapped at the interface surface states.

Upon light illumination, a photovoltage is generated in the photoelectrode due to the separation of the photogenerated electron(e^-) – hole (h^+) pairs in the Schotky contact region. The charge separation persists until the bands are flattened. Then the charge separation and photovoltage can no longer be increased upon light illumination anymore. The presence of light leads to lowering of the H^+/H_2 potential. By applying an external bias the Fermi level of

the cathode (Pt counter electrode) increases to above the H^+/H_2 energy level, leading to electron transfer to H^+ ions of the electrolyte for hydrogen generation[131].

For a spontaneous water splitting to occur, the semiconductor should have a valance band edge lower and a conduction band edge higher than that of oxidation and reduction potential of water respectively. Another requirement to satisfy this spontaneous process is that the semiconductor photoelectrode should have a minimum band gap of 1.9 eV. Based on the Gibbs free energy change for splitting water which is 237 KJ mol^{-1}, the minimum band gap requirement should be 1.23 eV (at room temperature), but due to thermodynamic losses and overpotentials (about 0.7 eV)[130], a higher voltage is needed to ensure fast kinetics at different stages. Figure 2.2 illustrates the relationship between the band edge energies of a selection of semiconductors with respect to water splitting redox potentials.

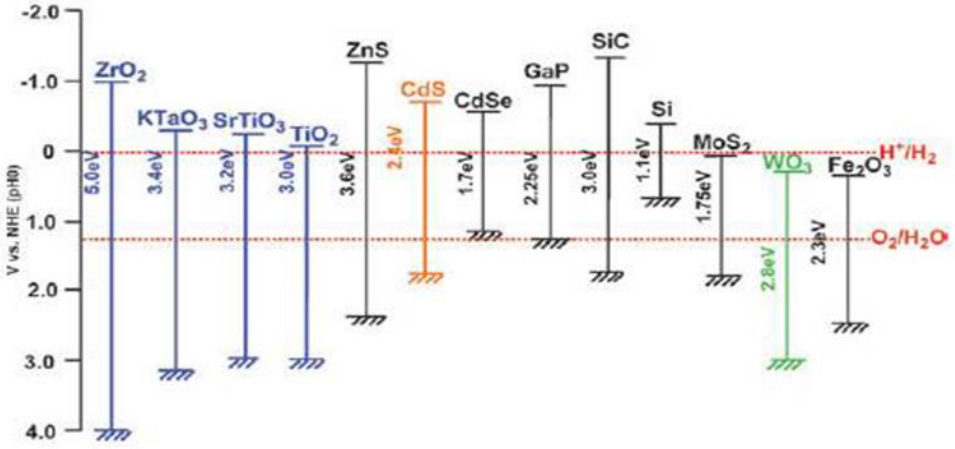

Figure. 2.2 Schematic representation of relationship between the band position of some semiconductors with respect to water redox potential (figure was reproduced from Li et al[132]).

Reading from Figure 2.2, cadmium sulphide (CdS), for example, is a suitable candidate for spontaneous water splitting (without applying a bias potential), as the valence band and the conduction band edge position straddles the water redox potential. Moreover, the band gap of 2.3 eV allows for light harvesting in the visible light region utilising a significant portion of the solar spectrum. On the other hand, iron oxide (Fe_2O_3) cannot split water unassisted due to its conduction band edge being less than that of reduction potential of water. For metal oxides, the valence band edge mainly consists of p-band formed by the p orbital of oxygen anion and the conduction band edge consists by the d and/or s-bands formed by the d and/or s orbitals of the transition metal cation in the oxide. However, the valence band can also be formed by the d orbital, when the transition metal cation has filled or partly filled d orbitals[133]. The positon of band gaps for metal oxides can be determined mainly by the Madelung energy (*i.e.* the electrostatic energy of each ion in the crystal lattice), the electron affinity of oxygen, the ionisation potential of the transition metal in the case of the metal containing no other metal cations, the polarisation effect between the atomic orbitals and the mutual interactions between the valence band and the conduction band[133]. The fluctuation of the valance band edge is due to the symmetry of the crystal, and the electronic structure of the neighbouring cations. In the case of ZnO, for example, the filled 2p levels of O^{2-} and empty 4s levels of Zn^{2+} are separated when the ions are brought together to form a solid[134].

Water splitting experiments are usually set up in a three electrode system at ambient conditions with *Ag/AgCl* acting as the reference electrode. The performance of any PEC cell can be best described by measuring its

efficiency. Assuming that all the current that follows through the outer circuit corresponds to water splitting reaction without any competing side reactions, the photon-to-hydrogen efficiency can be calculated from the following equation[135, 136] :

$$\eta = J(E^{\circ}_{rev} - |E_{app}|) / I_{light} \qquad \text{(Equation 2.1)}$$

where η is the photoconversion efficiency, J is the photocurrent density (mA / cm^2), I_{light} is the incident light intensity (mW / cm^2), E°_{rev} is the standard reversible potential (1.23 eV) and E_{app} is the applied (bias) voltage that is added to the system to assist the water splitting reaction. $E_{app} = E_{meas} - E_{aoc}$, where E_{meas} is the electrode potential (*vs Ag/AgCl*) of the working potential and E_{aoc} is the electrode potential of the same working electrode under open circuit condition under illumination. The measured potential versus the *Ag/AgCl* of the photoelectrode can be converted to the potential with respect to the reversible hydrogen electrode (*RHE*) according to Nernst equation[137]:

$$E_{RHE} = E_{Ag/AgCl} + 0.059\ pH + E^{\circ}_{Ag/AgCl} \qquad \text{(Equation 2.2)}$$

(where $E^{\circ}_{Ag/AgCl}$ = 0.1976 V at 25°C and pH = 13.6 for a PEC cell in a conventional 1 M KOH electrolyte solution[135]).

Since Fujishima's experiment (the pioneer of first PEC water splitting experiment in 1972)[138], one of the major challenges for scientists has been to optimise the photocatalytic properties of the semiconductor photoelectrode to enhance light harvesting. In this context, various attempts have been made to enhance the design, synthesis routes and modifications of semiconductor materials. Utilising nanostructured semiconductors such as metal oxide inverse

opals and hollow spheres with high surface areas and enhanced opto-electronic properties can be considered beneficial as photoanode materials in PEC water splitting devices.

It has been reported that the efficiency of water splitting reaction is greatly influenced by the electron transfer process, band gap energy and band structure of the semiconductor photoelectrodes. Thus, enhancement of visible light harvesting can significantly improve the efficiency of the PEC water splitting devices. In this regard, the semiconductor nanostructures can be modified by various strategies such as: doping, metal ion loading, composites of metal oxides, dye-sensitisation and bilayered systems[131].

In this work, bilayered metal oxide inverse opal (TiO_2/ZnO) nanostructures are the photoanodes of choice to increase light harvesting properties through the formation of heterojunctions at the interface which may enhance charge separation and suppress the rate of recombination of the photogenerated electron-hole pairs. Moreover, the photonic properties of each individual inverse opal may assist to enhance the efficiency of the system[102, 103, 139, 140]. Such bilayered inverse opals have been successfully combined with another nanostructure, namely ZnO nanorods in order to further improve the light harvesting of the system. One of the fundamental properties of nanorods is their high electron diffusion length due to the direct electron pathway they offer, as they are one-dimensional with minimal cracks or grain boundaries[2, 4]. Therefore the growth of nanorods on the bilayered inverse opals may reduce charge traps and recombination centres. Additionally, their high surface area may be beneficial in PEC light harvesting. Furthermore, the hybrid photoanode nanostructures, have been sensitised with narrow band gap CdSe/ZnS core

shell quantum dots to increase light harvesting in the visible region of the spectrum in this work. The synergistic effect originating from the contribution of each individual layer and component of these hierarchical nanostructure photoanodes for the enhancement of the overall PEC water splitting efficiency, will be discussed in Chapter 6 comprehensively.

2.3 Dye Sensitised Solar Cell (DSSC)

The amount of energy coming from the sun to earth is gigantic; it is estimated to be 3×10^{24} J/year. This number is about 10^4 times more than that of current consumption by mankind. In other words covering only 0.1% of the earth surface with conversion efficiency of 10% would suffice to satisfy the energy needs for all the earth's human population[2].

The conversion of solar energy to electricity by photovoltaic solar cell devices has undergone three generations of evolution from the initial single silicon solar cells to the second semiconductor thin film based solar cells and now, the third generation solar cells represented by dye sensitised solar cells (DSSCs)[2, 141]. Although DSSCs efficiency performances are not yet compatible to the first and second generation solar cells (10-11% compare to 20-30% reported for the first and second generation)[2], in terms of cost and substrate flexibility they are superior, which keep researchers enthusiastic to investigate them. The first DSSC was developed by O'Regan and Gratzel in 1991[142]. Their cell was based on a film of TiO_2 nanostructure which was sensitised with a ruthenium complex in an organic electrolyte. They achieved conversion efficiencies between 7.1-7.9% under simulated solar light illumination. Their

success was mainly due to two important factors; first the use of a TiO_2 nanostructure was responsible for achieving high surface area and thus allowing better absorption of dye molecules onto it. Secondly, due to the strong chemisorption between the dye molecules and the TiO_2 film through the carboxylic groups of the ruthenium complex. Since then researchers have been working on DSSCs to increase both the conversion efficiency and the stability of the cells. Recently, more sophisticated tandem cells[143] which are the combination of two types of DSSCs have been developed and show great promise.

Figure 2.3 shows the schematic principle of a DSSC. In this system, two electrodes exist; an anode and cathode which are made up of usually transparent FTO glasses. On the anode, the semiconducting nanomaterial, such as TiO_2, is first deposited followed by coating by a sensitising dye (usually Ru complexes). This electrode is the working electrode (or photoanode) of the cell. On the cathode a thin film of platinum (Pt) is coated and is called the counter electrode. The two electrodes are placed parallel to each other with face to face configuration with a space of about 30-40 microns. This space is then filled with an electrolyte solution (usually iodide (I^-) / triiodide (I^-_3) couple) acting as a conducting media. Under illumination of light, the dye molecules interact with photons and electrons are excited to the LUMO (D^*) that is energetically above the conduction band edge of the semiconductor. This photo-excitation leads to the generation of electron – hole pairs. The photo-generated electrons are injected into the conduction band of the semiconductor, while holes are left behind in the oxidised ground state (D^+) of the dye and are rapidly regenerated (reduced to D^0) by electron donation from iodide in the

electrolyte. This dye regeneration prevents the back transfer of electrons from the semiconductor to the dye (or so called “suppressing recombination”). The electrons in the semiconductor conduction band travel through an external circuit to the Pt counter electrode where they regenerate the electrolyte by reducing the triiodide to iodide and thus completing the circuit.

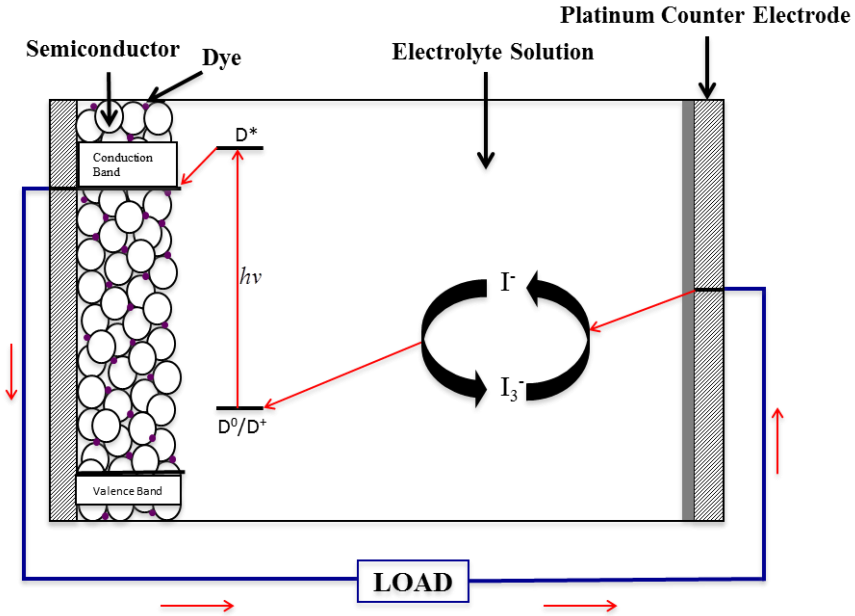

Figure. 2.3 Schematic principle of operation in DSSC (red arrows represent the movement of electrons).

The voltage generated under illumination corresponds to the difference between the Fermi level of electron in the semiconductor (E_f) and the redox potential of the electrolyte (E_{red})[144] which is also called the open-circuit voltage (V_{oc}). Figure 2.4 shows a diagram illustrating the origin of V_{oc} in a DSSC. The variation of V_{oc} can be explained by a shift of the conduction band edge potential of the semiconductor (E_{cb}) and/or a change of electron lifetime (τ). In terms of electron lifetime, as electron lifetime decreases, back recombination increases, resulting in a decrease in V_{oc}. A shift in conduction band edge

potential of the semiconductor to a lower level can also decrease the value of V_{oc} by reducing the difference between E_{red} and E_f. For example, heating[145] the semiconductor based photoelectrode during a DSSC experiment can shift the conduction band edge to a lower level and result in a decrease in V_{oc}.

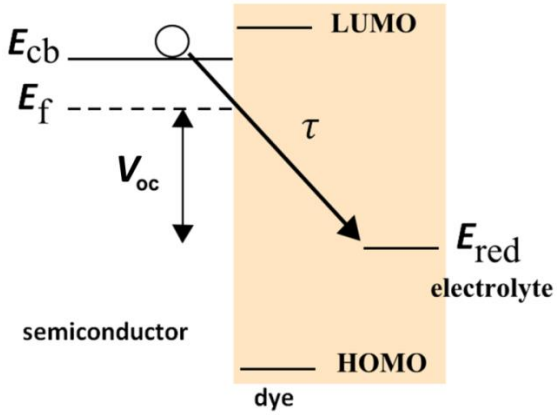

Figure. 2.4 A schematic showing the origin of V_{oc}. E_f : Fermi level, E_{red} : electrolyte redox level, E_{cb} : conduction band edge level of semiconductor and τ : electron lifetime[145].

The role of the dye in DSSCs is important. It acts as an “antenna” for photon capturing in the visible region of solar spectrum and also in assisting electron injection into the photoanode semiconductor surface[146]. Organic dyes have been intensively studied in recent years for both increasing the optical properties and better adsorption onto the semiconductor surface. The N-719 (ditetrabutylammonium-cis-bis(isothiocyanato)bis(2,2’-bipyridyl-4,4’-dicarboxylato) ruthenium(II)) is one of the various organic dyes that is also commercially available. It possesses a narrow band gap of 2.29 eV with absorption band in the visible region at about 535 nm[147]. It also has a high

LUMO relative to the semiconductor conduction band which makes the electron injection energetically favourable.

Optimising the electrolyte is another important factor in enhancing the conversion efficiency in DSSCs, as it has a direct role in improving the open circuit voltage (V_{oc}). It is therefore important to find electrolytes with redox couples which are closely matched to the oxidised dye energy level (HOMO) to increase the V_{oc}. Ionic electrolytes are promising in this regard. The third important factor for enhancing the efficiency is to optimise the photoanode material used in DSSCs. A good photoanode material can significantly reduce the energy loss caused by for example charge recombination, electron trapping (from defects), optical reflections etc. Nanostructure materials are promising candidates in this regard, as their properties such as porosity, high internal surface area, enhanced charge transfer and electron transport can contribute to increased electron diffusion length, decrease back recombination and also enhance physical effects such as photon localisation. All these enhancement factors can contribute to reduce energy loss in DSSCs[2].

The performance of DSSC can be determined by measuring the power conversion efficiency (η). It is defined as the percentage of the solar power that is converted from absorbed light to electrical energy and can be estimated from the following equation[141]:

$$\eta = \frac{P_m}{P_{in}} = \frac{J_{sc}V_{oc}FF}{P_{in}} \qquad \text{(Equation 2.3)}$$

where P_{in} is the input power, P_m is maximum power output, J_{sc} is the short circuit photocurrent density (i.e. when voltage is equal zero), V_{oc} is the open

circuit voltage (when current is equal zero) and FF is the fill factor. The fill factor can be calculated using the following equation:

$$FF = \frac{I_m V_m}{J_{sc} V_{oc}} = \frac{P_m}{J_{sc} V_{oc}} \qquad \text{(Equation 2.4)}$$

where I_m and V_m are the photocurrent and voltage at maximum power respectively. The maximum photocurrent and voltage from a DSSC are defined by J_{sc} and V_{oc}. However, under both these conditions, the power of the solar cell is zero. The fill factor (FF), represents the electrochemical efficiency of the DSSC (Equation 2.4). It is defined as the ratio of the maximum power from the DSSC to the product of V_{oc} and J_{sc} and can be obtained from the current-voltage (*I-V)* curve as shown in Figure 2.5. The fill factor is measured form the area of the largest rectangle which can fit into the *I-V* curve and corresponds to the maximum power output.

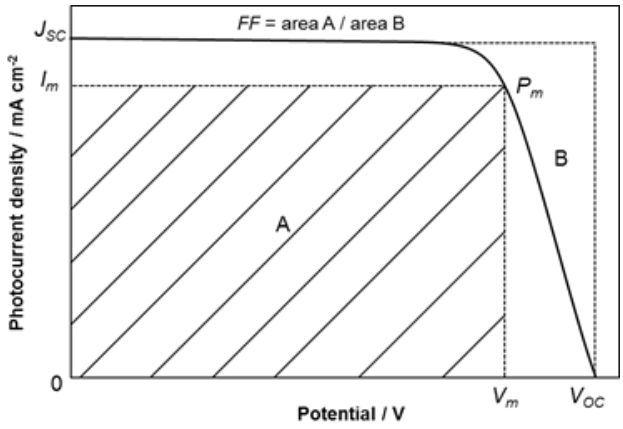

Figure. 2.5 A typical I-V curve representing fill factor ($\boldsymbol{FF}$). Short circuit current ($\boldsymbol{J_{sc}}$), open circuit voltage ($\boldsymbol{V_{oc}}$), maximum power output ($\boldsymbol{P_m}$), photocurrent at maximum power ($\boldsymbol{I_m}$) and voltage at maximum power ($\boldsymbol{V_m}$).

A large fill factor is desirable, as it corresponds to an *I-V* sweep that is more square-like[141]. Its value is always less than one. The closer the FF to 1, the greater the electrochemical efficiency. From Equation (2.3), it is clear that in order to enhance the photoefficiency of the cell, efforts should be made to increase J_{sc}, V_{oc} and FF.

It is known that the short circuit current (J_{sc}) can be calculated by the following expression[148]:

$$J_{sc} = q\ \eta_{lh}\ \eta_{inj}\ \eta_{cc}\ I_0 \qquad \text{(Equation 2.5)}$$

where q is the elementary charge, η_{lh} is the light harvesting efficiency of the cell, η_{inj} is the charge-injection efficiency, η_{cc} is the charge-collection efficiency and I_0 is the light flux. η_{lh} is commonly obtained by the amount of adsorbed dye and light scattering of the photoanode material and η_{cc} is determined by the competition between the charge collection and recombination in the cell. Therefore by optimising these two parameters, J_{sc} can be increased which subsequently leads to higher efficiencies.

As it was previously stated, V_{oc} can be considered as the voltage generated corresponding to the difference between the Fermi level of the electron in the semiconductor and the reduction energy level of redox electrolyte under illumination. V_{oc} is also related to the relative electron injection and recombination current densities and is proportional to the following expression[149], ln $(J_{inj} / n_{cb}\ k_{et}\ [I_3^-])$, where J_{inj} is the charge flux resulting from the dye-sensitised electron injection, n_{cb} is the concentration of electrons at the surface of the photoanode material, $[I_3^-]$ is the concentration of the triiodide ions

in the electrolyte and k_{et} is the rate constant for triiodide reduction to iodide (or electron recombination). Therefore, by moving the conduction band edge level of the photoanode semiconductor to a more negative (i.e. higher) electrochemical potential or by suppressing the rate of electron recombination under the same amount of charge flux (J_{inj}), V_{OC} is increased and subsequently leads to higher efficiencies.

Metal oxide inverse opals[140] and hollow spheres[7, 150] can be considered as promising photoanode nanomaterials in DSSC devices. Their high internal surface areas and porosity can result in effective dye sensitisation, electrolyte infiltration and charge collection[151] leading to efficiency enhancements. Their photonic and light scattering properties[140] can also give positive contributions in this regard.

2.3.1 Light Source for Photoexcitation in Photovoltaics

The standard light intensity setting is important for reliable testing of photovoltaic (PEC water splitting and DSSC) devices, which is related to an average power generated by the sun. The power density at the sun's surface is 62 MW m^{-2} and it reduces to 1353 W m^{-2} at the point just outside the earth's atmosphere. As solar light passes through the atmosphere, the spectrum is attenuated by scattering and absorption due to atmospheric conditions[152]. If parameter l_0 is the thickness of the atmosphere normal to the earth's surface, then the optical path length of solar radiation across the atmosphere (l) at an incident angle (α) is given by[153]:

$$l = \frac{l_0}{cos\alpha} \qquad \text{(Equation 2.6)}$$

The ratio l/l_0 is called the air mass factor (AM), since the absorption increases with the mass of air through which the radiation passes. Outside the earth atmosphere, the spectrum is denoted as AM 0 and on the surface of the earth for perpendicular incidence is denoted as AM 1. For moderate weather, the standard spectrum used is AM 1.5[153], which corresponds to an incident angle of 48.2° relative to the surface normal and gives a mean irradiance of 100 mW cm^{-2}, defined as 1 sun.

In this work, the light source used was a focused 300 W xenon arc lamp to simulate solar radiation with a focused illumination spot area of 1 cm^2. For the DSSC experiments (Chapter 7), the light source was calibrated to comply with the standard 1 sun power radiation set by the International Electrochemical Commission (IEC) (standard #60904-1, 2006). This gives power of 100 mW cm^{-2} with an Air Mass 1.5 Global (AM 1.5G) filter at a constant temperature of 25°C. For the PEC water splitting experiments (Chapter 6), the light source was calibrated and set at 300 mW cm^{-2}. The final photoefficiency results were then numerically recalibrated to the 1 sun radiation. As the experiments were designed to compare the light harvesting properties of different nanomaterials, it was important to use the same light power settings throughout the work, so there were no discrepancies between results.

The AM 1.5G filter used in this work was to ensure that the solar spectrum was correct for standard testing conditions. In order to exemplify how the filter affects the wavelength of incident light in photovoltaic experiments, two

radiation spectra were obtained, one representing the xenon light source spectrum with AM 1.5G filter and one without the filter (Figure 2.6).

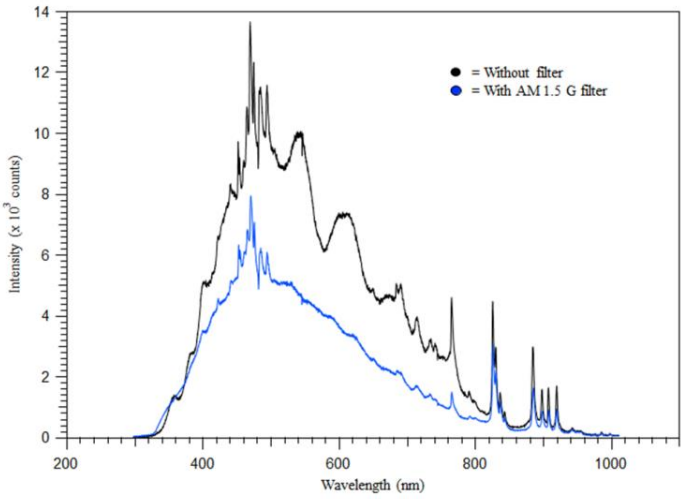

Figure. 2.6 Output spectrum of xenon light source with (blue) and without (black) the AM 1.5G filter.

From Figure 2.6, it can be seen that the intensity of the light with the filter present (blue) is decreased and the spectrum looks flatter. This may suggest that the spectrum has been corrected for atmospheric conditions where solar light intensity is reduced by absorption or scattering. A large portion of both spectra lie in the visible region (390 to 700 nm) with some extending into the infrared and UV regions. This suggests that the xenon light source used in this work for photoexcitation purposes was very close to that of sunlight.

2.4 Scanning Electron Microscopy (SEM)

The scanning electron microscope (SEM)[154] is a commonly used tool in materials science to observe the nano and microstructure of samples[155]. The

fundamental mechanism behind the electron microscope is the observation of electron interaction with a material rather than photon (optical) interaction, as seen in optical microscopy. SEM uses a high-energy beam of electrons to interact with the atoms that make up the sample, producing signals, which contain information about the sample's surface composition and topography. The electron beam displays wave-like properties. For an electron microscope, the typical electron energy ranges from 5 to 30 keV, which corresponds to a sub-nanometre de Broglie wavelength range of 0.017 to 0.007 nm respectively. Different signals can be generated when an electron beam comes into contact with the sample. First, an electron source accelerates a stream of high energy electrons toward a sample. The high energy electrons are then decelerated upon contacting the surface of the sample where a number of scattering events takes place. High energy backscattered electrons and lower energy secondary electrons can both be released, after bombardment, from the atoms close to surface of the sample to construct an SEM micrograph. X-rays can also be emitted by relaxation of electrons to lower orbitals in atoms close to the surface of the sample which can give compositional information.

The backscattered electrons and secondary electrons can be distinguished, due to differences in their energies, by the detector. Backscattered electrons have energy near to that of the incident electron beam, whereas secondary electrons typically have energies of <50 keV. Backscattered electrons are ones which undergo elastic interactions with the sample surface, whereas secondary electrons originate due to inelastic scattering of the incident beam of electrons. Such secondary electrons are ejected from the K-shells of atoms at the surface or within a few nanometres of the surface of the sample. In

SEM, in contrast to TEM, it is inelastic scattering which provides information on the sample. Inelastic scattering is dominant when the energy of the electron beam is in the range of 5-30 keV.

In the SEM, a beam of electrons is focused and raster scanned across the sample. The electrons produced from the sample are detected as a function of the position of the incident beam. Figure 2.7 shows a schematic view of a scanning electron microscope (SEM) instrument. The electron gun produces a high intensity beam of electrons which can be focused by the lenses. In this work, the electron source is a tungsten hair-pin filament. Electrons are ejected from a metal filament through thermionic emission[156]. A current is applied across the filament at the top of the column of the microspore. In this thermionic electron source, the current heats the filament *via* resistive heating, where the work function of the material is overcome via heating at a high positive voltage bias of +5-20 KV which releases electrons with high kinetic energy; accelerating electrons through the column.

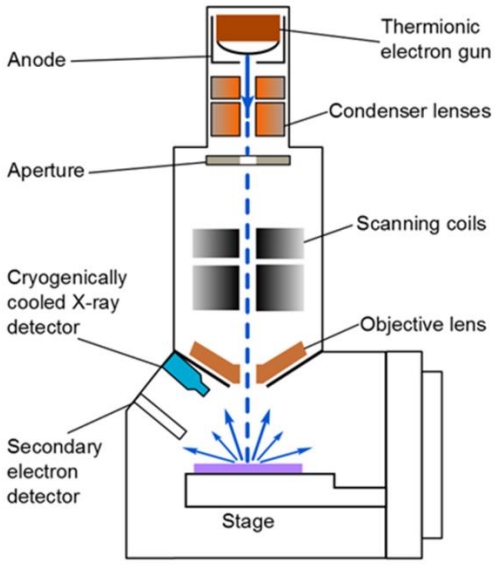

Figure. 2.7 A schematic showing scanning electron microscope (SEM)

The role of the condenser lenses is to focus the electron beam into a small electron probe (reducing the beam size) and adjust the shape. The aperture removes any unwanted stray electrons. The two pairs of scanning coils deflect the electron beam to achieve raster scanning and are controlled to image the sample surface in a scanning mode. The beam is deflected along a straight line, at the end of this line it is deflected to the beginning of the next line and so forth. At the same time the signal at each point being scanned is displayed on the monitor to be observed by the operator. The final sets of lenses are the objective lenses, converging the electron beam into a fine and focused beam. A stigmator can be found inside the objective lenses. The stigmator is a set of coils that have two dimensional control (x-y) of the beam and corrects any astigmatism of the beam. They can form a round sharp electron beam which focuses on the sample surface.

A vacuum environment is also needed by the SEM. It prevents the electron source from oxidising due to the presence of oxygen in the chamber which can reduce the lifetime of the tungsten filament source and thus lead to a change in the energy of the emitted electrons. The vacuum also increases the mean free path of the electrons in the sample chamber. Furthermore, it prevents electron beam scattering inside the column. The vacuum is maintained by a diffusion pump backed by a roughing rotary pump. All the SEM images in this work have been taken using a JEOL JSM-820 SEM with a EDX detector.

2.5 Energy Dispersive X-ray Spectroscopy (EDX)

In addition to backscattered and secondary electron detection, an SEM equipped with an X-ray detector can be used to analyse the composition of the

sample based on X-ray fluorescence. The energy dispersive X-ray (EDX) detector measures the energy of the X-ray created *via* the bombardment of electrons striking the surface of the sample. If an inner-shell electron in an atom is excited above the Fermi level by the incident electron beam in the SEM and ejected, then another electron in a higher energy level can lose energy in the form of an X-ray to fill the empty state[155]. The transition is allowed as long as the dipole selection rule is obeyed (*i.e.* electrons from p-orbitals may fill empty states in s-orbitals, but s-orbitals in higher shells cannot). The energy of the X-ray corresponds to the binding energy difference between the core level and upper level. Moreover, each element has its own distinctive X-ray emission. There are also primary signals present due to electron relaxation *via* the K_α transitions, where an electron in the L shell replaces a missing electron in the K shell. The distinctive elemental X-ray emissions are independent of the kinetic energy of the primary electron. X-ray fluorescence can also be generated by other transitions but at a lower energy. Together with the K_α emission, it is possible to identify both the elements and their relative concentrations in the sample.

The X-ray detector is cryogenically cooled by liquid nitrogen. The detector is a semiconductor diode, a few millimetre thick. The electron-hole pairs are generated by the X-rays which are separated by the electric field in the diode. The current produced across the device can then be analysed.

2.6 Transmission Electron Microscopy (TEM)

In TEM, electrons are emitted from a sharp tip of an electron gun which are accelerated through a vacuumed column with the presence of electrostatic and

magnetic fields using various lenses to form a sharp electron beam in the direction of the sample. The electron beam is transmitted through the sample, interacting with the sample as it passes through. TEM gives a high spatial resolution due to the small de Broglie wavelength of electrons when they are accelerated to high speeds[155]. The resolution can be limited by imperfections in the optics and also by vibrations of atoms in the sample. An image is formed from the interaction of the electrons transmitted through the sample; the image is magnified and focused and can be displayed on a fluorescent screen or detected by a camera. The sample has to be very thin (around 100 nm) so that most of the electrons can pass through it without significant inelastic scattering. The ultra-thin sample is usually mounted on a copper mesh supporting a transparent thin film to hold such sample. All the TEM images in this work have been taken using a Hitachi-7100 TEM with an axially mounted Gatan Ultra-Scan 1000 CCD camera.

2.7 Dynamic Light Scattering (DLS)

Dynamic light scattering (DLS)[55, 157, 158], also known as photon correlation spectroscopy[159], is a technique for determining the size distribution profile of macromolecules, proteins, nanoparticles or spherical colloidal polymers, by measuring the random changes in the intensity of light scattered from a suspension or a solution.

Light can be scattered by a molecule or a particle with a diameter much smaller than the wavelength of the light if the molecule has a polarizability different from its surroundings. This is called Rayleigh Scattering. The intensity

of the scattered light is related to the direction of polarisation of the incident light, scattering angle, and the properties of the solution itself. Assuming the incident light is linearly polarised with defining angles, then the scattered light will also be linearly polarised. The direction of polarisation lies in the plane determined by the direction of the incident light beam and the scattering direction[157]. If the scattered light is projected as an image onto a screen it will generate a “speckle” pattern of dark and bright spots[160], in which the dark spots correspond to the regions where the diffracted light from the particles arrives out of phase interfering destructively and the bright spots correspond to the regions where the diffracted light arrives in phase interfering constructively. When this behaviour is extended to a very large number of particles in solution, it results in fluctuations in light intensity[55], as a result of their Brownian motion (the random motion of the suspended particles, colliding with the solvent molecules). In such a system, the distance between the particles is constantly changing which results in a Doppler Shift between the frequency of incoming light and the frequency of the scattered light, which results in the broadening of the scattered wavelength. The fluctuation of light intensity depends on the diffusion coefficient, D, which is a measure of the rate of particle motion (diffusion velocity) and is given by Stokes-Einstein relation[55, 157]:

$$D = \frac{kT}{6\pi\eta\mathrm{a}} \qquad \text{(Equation 2.7)}$$

in this equation, k is the Boltzmann constant, T is the temperature, η is the viscosity of the solution and a is the hydrodynamic radius of the particle. An important feature in Equation 2.7 is that, it is independent from the charge of the diffusing species. Therefore, this equation can be applied to neutral molecules

and particles in the solution. As it can be seen form the equation, the diffusion coefficient, D is inversely proportional to the radius of the particle, *a*, and therefore, the small particles diffuse faster than larger ones in a system undergoing Brownian motion. The rate of the fluctuations in the intensity of light depends on how fast the particles are moving[158]. This is the key concept in DLS measurement on the size of the particles in a suspension.

In a typical DLS experiment, a monochromatic light source, usually a laser, is sent through the molecule or particle solution, and the scattered light intensity is detected as a function of scattering angle and time. The detector is typically a photomultiplier which is positioned at 90° to the light source and collect the scattered light from the sample. collimating lenses are also used to focus the light source to the centre of the sample holder. The lenses also prevent saturation of the photomultiplier tube[157]. The detected spectrum of scattered light which are Doppler shifted frequencies as a result of particle movement are processed by a device called a digital correlator. This device can convert the frequency data into intensity autocorrelation function mathematically and plot it as a function of delay time (the function of the correlator is essentially to compare the intensity of two scattering signals over a short period of time and calculate the extent of similarity between the two using the correlation function). The decay of the autocorrelation function is then used to extract particle size. Faster decays correspond to smaller particles and slower decays to larger particles. For monodisperesed

population of particles in a solution, the correlation function $G(\tau)$ is treated as a single exponential decay[157, 159]:

$$G(\tau) = e^{(-2\Gamma\tau)} \quad \text{(Equation 2.8)}$$

where τ is the decay time and Γ is the decay constant is proportional to the diffusion coefficient (D) and is obtained from the relation:

$$\Gamma = -Dq^2 \quad \text{(Equation 2.9)}$$

where q is the scattering wave vector and is given by:

$$q = \frac{4\pi n}{\lambda}\sin(\frac{\theta}{2}) \quad \text{(Equation 2.10)}$$

where n is the refractive index of the sample (particle solution), λ is the wavelength of the laser light source and θ is the scattering angle (the angle at which the detector is located with respect to the sample). After calculating D form Equation 2.9, and inserting it into Stokes-Einstein equation (Equation 2.7), the size of the particle, a, can be determined. DLS can then be extended to real samples that contain a distribution of particle sizes by calculating the intensity weighted mean size, known as the z-average size by writing the exponential decay of autocorrelation function (Equation 2.8) as a power series. The linear decay constant will be then proportional to the average diffusion coefficient and will be used to extract average particle size. From the DLS data, it is also possible to extract size distribution data by converting the measured autocorrelation function into what is known as an electric field autocorrelation function[159]. Of course, all these complicated mathematical relations will be

solved by using an appropriate DLS software package[161]. At the time of carrying out the experiments in this work, DLS was unavailable.

2.8 X-ray Diffraction (XRD)

Crystal structures of nanomaterials can be identified by use of an X-ray diffractometer. Diffraction techniques depend on the interface between waves reflected from the periodic arrangement of atoms within the crystal[162]. In X-ray diffraction (XRD), the X-rays strike the surface of a crystal structure and are partially diffracted by the atoms in the lattice. The part of the X-ray that is not diffracted passes through to the next plane of atoms, where again part of the X-ray is diffracted and the rest passes through to the next plane. This causes an overall diffraction pattern. If the X-rays diffracted by consecutive planes are in phase, constructive interference occurs and the diffraction pattern shows a peak, however if they are out of phase, destructive interference occurs and there is no peak. The angle at which constructive interference occurs defined by the spacing between the planes of the lattice and the wavelength of the X-ray; following Bragg's Law[163] (Equation 2.11). Diffraction peaks only occur if:

$$sin\theta = \frac{n\lambda}{2d} \qquad \text{(Equation 2.11)}$$

where θ is the angle of incidence of the X-ray, n is an integer, λ is the wavelength of the incident X-ray, d is the spacing between the planes in the atomic lattice. Figure 2.8 shows the schematic of Bragg's law.

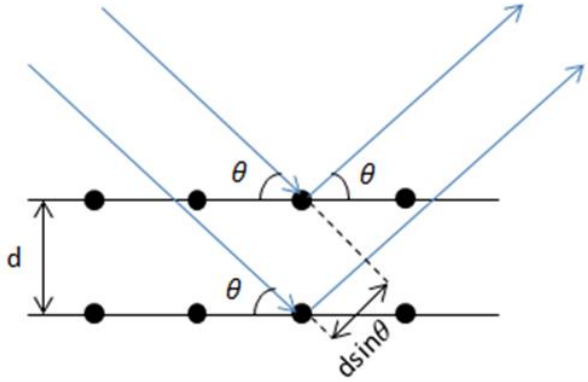

Figure. 2.8 A schematic of Bragg's law

Figure 2.8 shows that the X-ray traverses an extra length of $2dsin\theta$ between consecutive planes of the lattice. Constructive interference occurs when this length is equal to an integer multiple of the wavelength of the X-ray. This is only possible because X-ray wavelengths are comparable to lattice spacing. The sample under study will have many of these consecutive planes. The cumulative effect of constructive interference from successive planes produces narrow fringes or Bragg peaks at the angles corresponding to the separation of particular sets of planes.

An XRD instrument consists of an X-ray source (usually an X-ray tube), a sample stage, a detector and a way to vary angle θ. The sample is first placed onto the sample stage. The X-ray is then focused on the sample at some angle θ. The detector arm rotates by 2θ as the sample rotates by θ. By doing this, the X-ray source is kept stationary, and the detector is always in the line of sight of the diffracted X-ray beam. The detector reads the intensity of the X-ray it receives at angle 2θ away from the X-ray source path.

The spectrum produced by XRD, consists of a series of diffraction peaks. The positions of the peaks are determined by the lattice spacing of the sample under study. The phase of the crystal structure can be identified by these characteristic peaks. The peak height is an approximation of the peak intensity, and the peak area is the real measure of the peak intensity. The peak height corresponds to the number of crystallites diffracting X-rays, and can be used to determine the composition of the sample. If the sample has a preferred orientation, the peak height will be intense at the Bragg angle corresponding to the preferred orientation. The crystal grain (crystallite) size can be calculated from the Debye-Scherrer equation[43], which can be written as:

$$D_{avg} = \frac{K\lambda}{\beta cos\theta} \qquad \text{(Equation 2.12)}$$

where D_{avg} is the mean crystallite dimension of a particular plane, K is the shape factor (0.89 in this work), λ is the wavelength of the x-ray source which has a value of 1.540598 Å in this work, θ is the Bragg angle of the diffraction peak (degrees) and β is the line-width of the diffraction peak (i.e. FWHM; full width half maximum) corrected for instrument broadening (radians 2θ). The increased periodicity in larger crystallites increases the strength of the diffraction of the x-ray for different planes making them narrower and more intense. With smaller crystallites which have lower periodicity the peak broadens. The shape factor, *K*, in Equation (2.12) also known as the Scherrer constant may vary from 0.62 to 2.08, depending on the shape of the crystal domain, but can be taken at 0.89-0.9 for spherical crystals with cubic symmetry with mean crystallite size less than 30 nm[164]. In this work, it was assumed that

the crystallites of the diffracting samples obeyed these criteria which would correspond to the 0.89 value for the shape factor.

There are also other factors that determine the width β of a diffraction peak. These include: the presence of defects to the perfect lattice, differences in strain in different crystal grains and the size of the crystallites. Strains are due to imperfections within the crystalline lattice, including vacancies, dislocations, stacking faults and others. The lattice strain (ε_{str}) of a particular plane can be calculated from the Stokes and Wilson formula[165], which can be written as:

$$\varepsilon_{str} = \beta/(4\ \tan\theta) \qquad \text{(Equation 2.13)}$$

All XRD patterns were recorded and analysed using a Siemens D500 X-ray diffractometer with a copper anode emitting at 1.5418 Å and analysed by the X'Pert HighScore Plus software.

2.9 UV / Vis Characterisation

Measurement of diffusive reflectance with a UV/Vis spectrophotometer, is a standard method in the study of absorption properties of materials[166]. In the case of semiconducting nanomaterials in photovoltaic applications, band gap determination and reflectance/absorption studies are of major interest. In PEC water splitting experiments, for example, the charge carriers (photogenerated electron-hole pairs) produced by the absorption of photons at wavelengths below the semiconductor band gap wavelength are diffused to the electrolyte medium (*i.e* the photogenerated holes for oxygen evolution) and the conducting substrate (*i.e* the photogenerated electrons for hydrogen evolution) which drive

the water splitting reactions. These charge carriers have small diffusion lengths (~200 nm or less in TiO_2), therefore it is important that the semiconductor has a large absorption coefficient for sub-band-gap wavelengths. Such absorption coefficients can be determined by diffusive reflectance measurements. Furthermore, band gap determination of nanomaterials using this spectroscopic technique may allow one to test and optimise their band gaps with the aim of harvesting as large a portion as possible of the solar spectrum when used as photoelectrodes in photovoltaic devices.

When a semiconductor absorbs photons with energy higher than that of its band gap, an electron is transferred from the valence band to the conduction band resulting in an abrupt increase in the absorbency of the semiconductor to the wavelength corresponding to the band gap energy. In order to determine the precise values for the optical band gaps when using reflectance spectroscopy, the measured reflectance values are first converted to absorbance by using the Kubelka–Munk transformation function[167]. This function is generally used for the analysis of diffuse reflectance spectra obtained from the weakly absorbing samples[168]. It can be expressed as following:

$$k = \frac{(1-R)^2}{2R} = \frac{\propto}{S} \qquad \text{(Equation 2.14)}$$

where k is the Kubelka-Munk function which corresponds to the absorbance, R is the reflectance, $\propto$ is the absorption coefficient and S is the scattering coefficient. $\propto$ is related to the incidental photon energy and can be expressed using Tauc's relation[169]:

$$\propto h\upsilon = A\left(h\upsilon - E_g\right)^m \qquad \text{(Equation 2.15)}$$

where A is a constant and depends on the properties of the material, $h\upsilon$ is the photon energy in eV ($h\upsilon = \frac{hC}{\lambda(nm)} = \frac{1236}{\lambda(nm)}$), $E_g$is the band gap and m is a constant and takes different values depending on the type of electronic transition. For a direct allowed band gap material such as ZnO, $= \frac{1}{2}$.

Therefore:

$$khv = h\upsilon \frac{\propto}{S} = \frac{A\left(h\upsilon - E_g\right)^{1/2}}{S} \qquad \text{(Equation 2.16)}$$

which can be re-written as:

$$(khv)^2 = \left(\frac{A}{S}\right)^2 \left(h\upsilon - E_g\right) \qquad \text{(Equation 2.17)}$$

By plotting $(khv)^2$ vs $h\upsilon$, the value of band gap (E_g) can be determined by extrapolating the linear part of the graph to the horizontal (x) axis.

An ISP-REF integrating sphere coupled with a fibre optic cable to an ASEQ LR1 broad-range spectrometer was used to obtain reflectance spectra of the nanostructure samples in this work.

2.10 Characterisation of Colloidal Crystals and Inverse Opals

Studying the internal structure of colloidal crystals and their inverted structures inverse opals (Chapter 1) is inherently difficult. Using electron microscopy (SEM and TEM) or light scattering (DLS) techniques cannot give a detailed characterisation of these 3D structures. The information obtained by these methods can only give insight about the surface structure of such crystals[5, 170].

Due to the periodic structure of these materials, with their periodicity on a similar length scale as the wavelength of the UV and visible lights, diffraction may use such light sources as a probe of the symmetry and unit cell parameters. The diffraction of light by these periodic structures along specific directions that cause the opalescent colour (Chapter 4), will give rise to photonic stop-bands. The positions of these stop-bands are characteristic for some of the lattice planes of the crystal structure. The intensity and spots profile of the light diffraction is related to ordering, defects and grain boundaries over large area of the sample. In this technique, the laser wavelength should be smaller than the lattice spacing of the colloidal crystal or inverse opal. The diffraction follows the Bragg's formula[5]:

$$sin\theta = \frac{\lambda}{d\sqrt{3/2}} \qquad \text{(Equation 2.18)}$$

where λ is the laser wavelength and d is the centre-to-centre distance between the pores of the colloidal crystal or inverse opal. The diameter of the spheres can also be evaluated from the value of *d*, if the spheres are close-packed. A modified version of the Bragg's formula[6] was used in Chapter 4 for this purpose.

X-ray techniques such as ultrasmall-angle synchrotron X-ray scattering (USAXS, also called microradian X-ray diffraction)[5, 170], also have the required penetration depth to study the interior of these crystals. In this characterisation technique, a monochromatic X-ray parallel beam with a wavelength of the order of one Angstrom (Å) is focused at a detector using a set of Beryllium compound refractive lenses positioned next to the sample. The diffraction patterns are then recorded at various sample rotation angles allowing to obtain information about ordering in different crystallographic directions. The analysis can distinguish

between stacking sequences inside the structure. Calculations of peak intensity ratios can then provide information about the relative ratios of the different stacking sequences in the periodic sample. For example, using USAXS, it was revealed that TiO_2 and SiO_2 inverse opals were composed of twinned FCC structures (*i.e.* ABC…-ABC… stacking), with a small fraction of HCP fragments (*i.e.* ABABAB… stacking) and random hexagonally close-packed structures. This study also revealed that single domains (*i.e.* patches with no grain boundaries) of the same crystallographic structure could be detected in the inverse opals[170].

Chapter 3: Preparation and Study of PMMA Colloidal Spheres *via* Surfactant Free Emulsion Polymerisation (SFEP)

3.1 Abstract

PMMA (poly(methyl methacrylate)) colloidal spheres were synthesised using a surfactant free emulsion polymerisation (SFEP) process. The diameter of the spheres was determined using Stokes' law *via* the centrifugal sedimentation method. The effects of temperature, monomer concentration, seeding and metal oxide inclusion in SFEP process were investigated. The spheres became larger with increasing concentration of MMA monomer and smaller with increasing reaction temperature. The seeding technique made it possible to synthesise bimodal sphere populations and also produce monodisperse single sized population of large spheres with diameters above 500nm. The effect of metal oxide inclusion during the SFEP process was also investigated.

3.2 Introduction

The surfactant free emulsion polymerisation process is the most popular method for preparing monodisperse organic colloidal spheres for the self-assembly of colloid crystals[26]. This method has some advantages compared to the classical surfactant mediated approach. It has the advantage of being simpler, by not having the surfactant component during polymerisation. It is also assumed that due to the lack of surfactant species, disposing of the waste

solvent is more environmentally friendly[30, 34]. Because of the chain growth mechanism, all charged end groups are covalently linked to the polymer chain which terminates by radical combination to form a chain with two charged end groups so all monomer should be linked to two end groups. As a result the colloidal spheres produced by SFEP are ionically stabilised, but have a rather low charge density, which is advantageous for the self-assembly of the spheres into colloid crystals. In the surfactant mediated emulsion polymerisation, the colloidal spheres can aggregate (glue) together due to the migration of free surfactants between them, preventing the formation of high quality colloidal crystals[26]. Particle size distributions can also be rather broad as a result of secondary nucleation in systems containing surfactants[34] making them less useful in colloidal crystal applications. Because of these reasons, the polymerisation of choice in this work has been SFEP.

Seeded polymerisation is another polymerisation method which can be used for generating colloidal spheres. This seeding strategy is popular for use in dispersion polymerisation systems. In one study, polystyrene (PS) particles were used in a seeded dispersion polymerisation of methyl methacrylate[171] producing large particles of PMMA. Some PMMA particles showed PS seeds encapsulated inside them, while others did not. The use of PMMA as seeds in surfactant free emulsion polymerisation of methyl methacrylate may give rise to similar incorporation behaviour and produce larger spheres or even bimodal populations of spheres. Such behaviours can be important in the world of templating, as the changes in the diameter of the spheres can directly influence the pore sizes produced in the inverted structures of inverse opals and hollow spheres, leading to different opto-electronic properties.

The seeding polymerisation *via* SFEP may also be expanded and not be limited to organic polymers. In particular the inclusion of metal oxide materials directly into the polymerisation process can be of interest and may produce core-shell like structures of polymer-metal oxide and then convert to spherical metal oxide nanostructures by removing the organic polymers. If such structures are produced, they can be utilised directly as photoanodes in photovoltaic applications due to their enhanced surface area. Previous studies have shown co-polymerization of organic and inorganic metal oxide systems[172-174] at the same time with the use of an anionic surfactant such as sodium dodecyl sulphate (SDS) in the polymerisation process. The role of SDS[161, 172, 173] as a suitable anionic surfactant is to act as the counter to the cationic nature of metal oxides for more effective encapsulation or incorporation to occur. The advantages of using these kind of surfactants can be due to; firstly, the metal oxide particles are better re-dispersed in the aqueous phase due to the stabilising effect of SDS molecules which are adsorbed on the particle surface. Secondly, the adsorbed surface of the particles become more hydrophobic, thus creating a micelle like structure with the inorganic particle in the centre. The concentration of SDS used will be just above its critical micelle concentration (CMC) level where micelles can be formed. Additionally the isoelectric point is shifted to lower pH values. The isoelectric point, is the pH at which a particular particle carries no net electrical charge. The net charge on the particles is affected by the pH of the surrounding environment. For instance, in acidic environments protons (H^+) attach to basic groups and the net charge is positive. In basic media the net charge is negative as a result of proton loss. Therefore due to the presence of anionic SDS surfactants in the aqueous phase, the

surface charge density of the metal oxide particles will become more positively charged leading to perhaps better electrostatic interaction with the negatively charged SDS surfactants attached to the organic polymers. For the more negative metal oxide particles on the other hand, such as silica, the electrostatic interaction between the monomer chains and silica, supress the repulsive force between the negatively charged SDS and silica particles[172]. The organic polymer chains are then physically bound by entanglement or chemically bound by covalent bonding to the inorganic metal oxide particles.

In this work, first the SFEP process for the synthesis of monodisperse PMMA colloidal spheres was performed and the effects of different synthetic parameters including monomer concentration and temperature on the size of the spheres has been discussed. The two-step seeded SFEP was performed to produce ideally larger monodisperse PMMA colloidal spheres. The inclusion of metal oxides including P25 and iron oxide in SFEP processes without the use of surfactants have also been investigated.

3.3 Experimental Procedures

3.3.1 Synthesis of PMMA Colloidal Spheres *via* SFEP

The SFEP procedure was adapted from earlier work of Schroden et al[27]. Synthesis was carried out in a 3-necked round-bottomed flask. A 20×10 mm oval shaped magnetic stir bar was added to the flask. Poor stirring during synthesis would result in undesired polydispersed spheres and agglomerates.

The oval shaped magnetic bar was important for the round bottom flask in this experiment for maximum homogeneous stirring.

The flask was placed in a large beaker water-bath, which was then placed on a magnetic stirrer-hotplate. The hotplate had a thermocouple probe attached to it. The probe was inserted inside the water bath for temperature control. The 3-necked flask was fitted with a water-cooled condenser and nitrogen pipe and sealed with glass stoppers. Teflon tape was used to wrap around the end of the condenser before inserting it to the flask. This was done for better sealing and also for preventing the resulting polymerised PMMA solution from sticking the two glasswares together.

Using a graduated cylinder, 32 ml of deionized water was added to the flask. The nitrogen gas was turned on and set with a slow flow rate of approximately 2 ml per second. The flow of nitrogen was kept throughout the reaction to eliminate the inhibition effect of oxygen. The water was turned on with a slow flow for the condenser. The stirrer was turned on and set to a speed of 350 rpm and the temperature of 70˚C. After the temperature reached 70˚C (around 15 minutes), 1.48M (6.0 ml) of methyl methacrylate was measured and added to the flask while maintaining the 70˚C.

When conditions were stable (the mixture was allowed to mix for approximately 1 hour), 0.035 g of 2’2-azobis(2-methylpropionamidine) dihydrochloride (AIBA) initiator was weighed and added to the reaction flask. This compound decomposed with heat and produced free radicals for the polymerization reaction. Within a few minutes a milky white suspension was observed. The reaction was allowed to run for another 90 minutes at these

conditions. During this time the temperature of the reaction mixture rose by about 5-10˚C before returning to 70˚C (which was normal for an exothermic reaction). After 90 minutes, the heating was discontinued and the reaction mixture was allowed to cool to room temperature. In a successful polymerization there should be no noticeable smell of MMA at the end of the experiment. After cooling, the solution was transferred to a centrifugal vial.

The solution was purified from any unreacted monomers or agglomerates, firstly by submitting it to ultra-sonication for 2 hours. Then the sphere solution was centrifuged 3 times for 30 minutes in each instance at 6000 rpm. In each centrifugation cycle, the water that collected at the top of the mixture was decanted from the bottom sedimented PMMA spheres. The vial containing the white spheres was then redispersed with deionised (DI) water for the next cycle of centrifugation.

Two series of experiments were carried out to see the effects of different parameters on sphere diameter. The first series of experiments examined the effect of MMA monomer concentration. The polymerisation temperature was kept constant at 70^0C and the monomer volume was varied (3, 4, 5, 6, 7 and 10 ml corresponding to concentrations of 0.8, 1.04, 1.27, 1.48, 1.68 and 2.24 M respectively) while maintaining the water volume to 32 ml. The second series of experiments examined the effect of polymerisation temperature. The MMA concentration was held constant at 6 ml (1.48 M) while the polymerisation temperature was varied (60, 70, 75, 80 and 85^0C).

3.3.2 Centrifugal Sedimentation Method for Sphere Diameter Measurement Using Stokes' Law

PMMA colloidal spheres using 1.27 M (5 ml) MMA monomer in otherwise similar SFEP process as before (Section 3.3.1) were synthesised and transferred to a 50 ml centrifuging vial and placed vertically inside a centrifuge. The centrifuge speed was set to 4000 rpm. By centrifuging, the heavy colloidal spheres would sediment. The height of the sedimented solid PMMA spheres (settling height) in the vial was measured as a function of centrifuging time duration. The sphere diameters were then determined from settling velocities according to Stokes' law.

3.3.3 Seeded SFEP Process

PMMA colloidal spheres with sphere diameter ~414 nm were used as seeds in the seeded polymerisation experiment (seed sphere size). PMMA sphere seeds of varying amounts of 0.3, 0.5, 0.75, 1, 1.5 and 2 g were added to water to create seed suspensions with corresponding concentrations of 7.9, 13.2, 19.7, 26.3, 39.5 and 52.6 mg/ml respectively. The experimental set up and procedure was carried out similar to the original SFEP process described earlier (Section 3.3.1). 15 ml of PMMA colloidal sphere seed solution was added to the flask first and then 17 ml of deionised water was added to make up the 32 ml solvent (as it was the case in the original SFEP experiment). Once the starting solution reached 70^0C, the desired amount of MMA monomer was added. The reaction was left for 90 minutes before transferring to a vial for purification as previously.

3.3.4 Synthesis of Metal Oxide/PMMA Sphere Composite *via* SFEP Process

The procedure was carried out in a typical surfactant free emulsion polymerization with the exception that the metal oxide powders were added to the system prior to polymerization. For the synthesis of PMMA spheres containing TiO_2, 1.6 g of P25 was mixed with 32 ml of water and heated to reach 70˚C under a flow of nitrogen. Once the temperature stabilized, 6 ml of MMA monomer was added to the mixture. After about 30 minutes, 0.035 g of initiator was added to the mixture and the polymerization was carried out for 90 minutes. The final product was ultra-sonicated for 2 hours and then washed two times by centrifuging for 20 minutes at 6000 rpm. To remove the PMMA, a portion of the sample was calcined for 2 hours at 450°C with a ramping rate of 5˚C/min and then cooled down naturally inside the oven to reach ambient temperature. For the synthesis of PMMA spheres containing iron oxide, 1 g of nano-sized iron oxide powder was used in the otherwise similar synthesis procedure described before.

3.4 Results and Discussion

3.4.1 PMMA Sphere Size Measurement Using Stokes' Law

Stokes' law describes the force required to move small spherical particles in a viscous fluid medium at specific velocity.

Stokes's law can be written as:

$$F_d = 6\pi\mu V d \tag{3.1}$$

where $F_d$is the drag force of the fluid on the sphere, μ is the fluid viscosity, d is the sphere diameter and V is the sphere's settling (or terminal) velocity.

By assuming a vertical direction, there are three forces acting on a sphere in a quiescent fluid. Buoyancy force (F_b- tendency to float the sphere), drag force (F_d- viscous drag of the fluid on the sphere) and gravitational force. The first two forces act upwards on the sphere and the latter acts downwards:

$$F_b + F_d = mg \tag{3.2}$$

The buoyancy force is simply the weight of displaced fluid. As the volume of sphere is:

$$V_{sphere} = \frac{4}{3}\pi r^3 \tag{3.3}$$

where (r = sphere radius) and mass of displaced fluid:

$$(m_{fluid\ displaced}) = V_{sphere} \times \rho_{fluid} \tag{3.4}$$

where ρ_{fluid} is the density of the fluid. Then by combining Equations (3.3) and (3.4), the buoyancy can be written as:

$$F_b = m_{fluid\ displaced} \times g = \frac{4}{3}\pi r^3 \rho_{fluid} g \tag{3.5}$$

where g is gravitational acceleration.

By substituting Equations (3.1) and (3.5) into equation (3.2), the following expression can be obtained:

$$\frac{4}{3}\pi r^3 \rho_{fluid} g + 6\pi\mu V d = mg \tag{3.6}$$

(m = sphere mass). By re-arranging and substituting the mass of sphere, Equation (3.6) can be re-written as [175]:

$$V = \frac{2r^2(\rho_{sphere} - \rho_{fluid})g}{9\mu} \tag{3.7}$$

By further rearranging Equation (3.7) and replacing r with $\frac{D}{2}$ where D is the diameter of the sphere, the following equation for sphere size measurement is obtained:

$$D = \sqrt{\frac{18\mu V}{g(\rho_{sphere} - \rho_{fluid})}} \tag{3.8}$$

To determine the PMMA sphere diameter using Equation (3.8), the two unknown variables, sphere settling velocity (V) and the gravitational acceleration (g) (which is the centrifugal acceleration in this work) should be first calculated. Centrifugal acceleration can be calculated using the following equation:

$$g = r\omega^2 \tag{3.9}$$

where r is the radius of rotation (i.e. the measured distance from the centre of the centrifuge to the vial containing the sphere solution) and ω is the angular velocity of the centrifuge. The angular frequency of the centrifuge has a unit of rad/s and can be written as:

$$\omega = 2\pi f \tag{3.10}$$

where f is the frequency of rotations per second. By combining Equation (3.9) and (3.10), g can be re-written as:

$$g = 4\pi^2 f^2 r \tag{3.11}$$

To measure the settling velocity (V), the height of the sedimented PMMA spheres in the vial (settling height) are plotted as a function of centrifugal time. The gradient of the best fit straight line corresponds to the sphere settling velocity. Figure 3.1 shows an example of the plot.

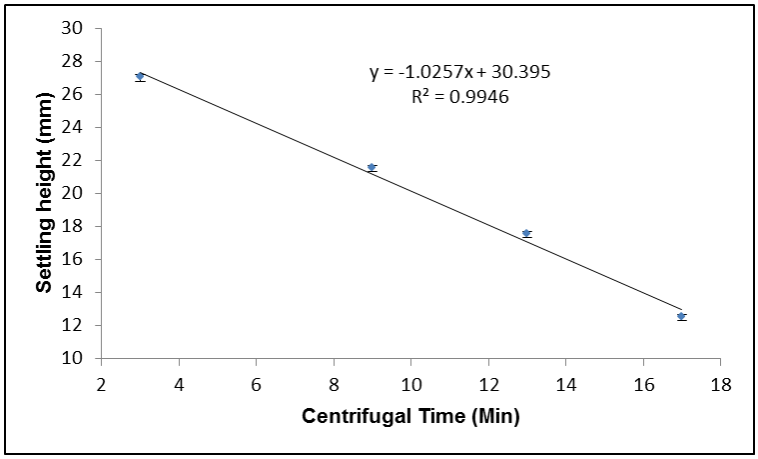

Figure. 3.1 The plot of settling height as a function of centrifugal time for PMMA spheres polymerised by SFEP process using 1.27 M MMA monomer.

The settling velocity of PMMA spheres polymerised by SFEP process using 1.27 M MMA monomer can be determined from the gradient of the straight line which is 1.0257 mm/min.

The centrifugation was fixed at 4000 rpm in this experiment and the radius of rotation was measured to be 9.5 cm (0.095 m). By inserting those values in Equation (3.11), the centrifugal acceleration can be calculated:

$$g = 4 \times \pi^2 \times (\frac{4000}{60}\ s^{-1})^2 \times 0.095m = 16651.77ms^{-2}$$

As all the parameters in Equation (3.8) are known, the diameter of PMMA spheres can be calculated as following:

μ (water viscosity) = 1.002 g/msec (cp)

ρ_{PMMA} = 1.18 g/cm^3 = 1.18×10^6 g/m^3

ρ_{water} = 1 g/cm^3 = 1×10^6 g/m^3

g = 16651.77 m/s^2

V = 1.0257 mm/min = 1.7095×10^{-5} m/s

$$D = \sqrt{\frac{18\times1.002 g/msec\times1.7095\times10^{-5} m/s}{16651.77 m/s^2\times(1.18\times10^6\ g/m^3 - 1\times10^6\ g/m^3)}}$$

$= 3.21\times10^{-7}$m = 321 nm

The average diameter of the spheres using SEM is about 383 nm. Therefore there is a 16% discrepancy between the measured sphere diameter and the diameter calculated by Stokes' law. This difference between the two values can be attributed to the existence of impurities including external particles or unreacted monomers[60] left inside the PMMA sphere solution. Furthermore the theoretical values of the parameters used in Equation (3.8) including viscosity of the solution and the density of PMMA spheres may be different from the experimental values, giving rise to deviations from the actual diameter of the PMMA spheres. The true value of the suspension viscosity will be higher than that of pure water, affected by small PMMA particles, fragmented initiators and unreacted monomers. The real density of the synthesised PMMA sphere is expected to be smaller than the value measured from bulk dry PMMA material, since it may contain trapped monomer and solvent (water). Both give smaller measured value of the sphere diameter through the Stokes' law. The

experimental error may be reduced by further purification of PMMA sphere suspension and good calibration of the PMMA sphere density. To the best of the author's knowledge, PMMA sphere size measurement using Stokes' law has not been carried out previously. This method can become valuable when used in parallel with SEM measurements to evaluate the monodispersity and purity of the entire batch of sphere solution produced after polymerisation.

Waterhouse et al[43] used dynamic light scattering (DLS) to measure the diameter of PMMA spheres and then compared them with their SEM results. Although DLS gave them the possibility to measure the polydispersity index (PDI) of the PMMA spheres (very monodisperese PMMA spheres were produced using the similar adapted SFEP approach from Schroden et al[27] which was used here as well), but their size measurements showed SEM results were 20% smaller than those determined by DLS. They attributed this discrepancy to shrinkage of the PMMA spheres upon drying for SEM measurements. Similar findings were reported by Armini et al[176]. They showed that, the diameters of the PMMA spheres measured by DLS were larger by 57% than those determined by SEM as a consequence of DLS measuring the diameter of solvent-swollen spheres, whereas the SEM measured the spheres in the dry state. During polymerisation, they took out PMMA sphere samples at different time intervals and found that, the average standard deviation for the size measured by DLS was 12%, while for the size measured by SEM, was 3% for the first 50 minutes of polymerisation. After approximately 75 minutes, the reaction had ended and the growth of PMMA spheres stopped which led to the samples become more monodisperse, however the variation in size distribution

(polydispersity) was still more preannounced in DLS measurements, which was attributed to the swelling effect.

Zheng et al[177] used Stokes' law to study the sedimentation and precipitation of Cu and Al_2O_3 nanoparticles suspended in carboxymethyl cellulose (CMC) aqueous solution. They demonstrated that by increasing the viscosity of the CMC fluid, the deposition rate of the nanoparticles was reduced (Equation 3.7) and the concentration distribution in the container was more uniform which led to less agglomeration of particles.

3.4.2 Effect of SEM Electron Beam on PMMA Spheres

When analysing PMMA spheres *via* SEM, it is important to know that the heat produced by the SEM electron beam can alter the size and behaviour of the spheres Figure 3.2 shows the SEM images of a cluster of 4 spheres sputtered with a layer of gold scanned at different time intervals under constant exposure of electron beam at (a) 0, (b) 4, (c) 8 and (d) 12 minutes. As can be seen from the SEM images, a gap between the layer of gold coating and the PMMA sphere becomes more visible on the spheres with increasing SEM electron beam exposure time (~ 90 nm in thickness of gold coating in image 3.2(d)). This is due to the release of water content inside the PMMA spheres by electron beam heating, and thus results in shrinkage of spheres. This phenomenon can be important in colloidal crystal templating techniques where inverse opals are made (Chapter 5). It indicates that one of the reasons for structural shrinkage

during calcination in inverse opal synthesis can be due to the water loss experienced by PMMA spheres acting as templates.

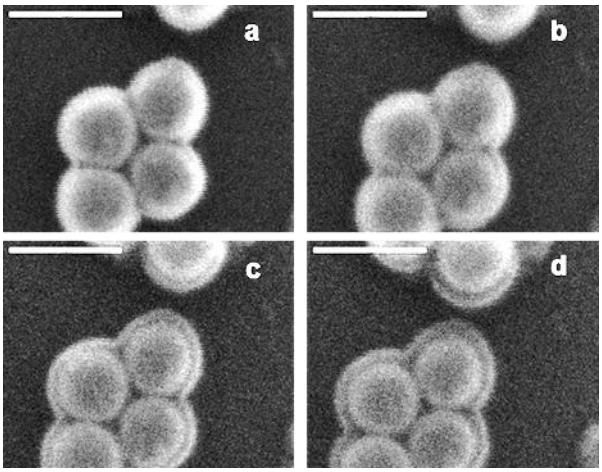

Figure. 3.2 Effect of SEM electron beam on PMMA spheres as a function of time; (a) 0, (b) 4, (c) 8 and (d) 12 minutes. Scale bars: 1μm.

3.4.3 Concentration Dependent SFEP

Figure 3.3 shows the SEM images for PMMA spheres synthesised at different MMA monomer concentrations. The overall standard deviation (polydispersity) in size distribution is about 8 nm which further confirms the good quality of the spheres.

The interesting phenomenon that can be observed in all the images in Figure 3.3 (apart from image 3.3(f) corresponding to 2.24 M sample) is that the spheres are self-assembled into colloidal crystals. The colloidal crystal formation phenomenon is comprehensively discussed in the next chapter, but it can be mentioned here that a deposition of a few drops of sphere solution onto a piece of aluminium foil can give rise to ordered colloidal crystals without any

complicated procedures. Although aluminium foil as a substrate for colloidal crystal fabrication has limitations when used in photovoltaic applications (mainly due to lack of chemical & mechanical stability and transparency), it can be a simple and fast method for colloidal crystal fabrication.

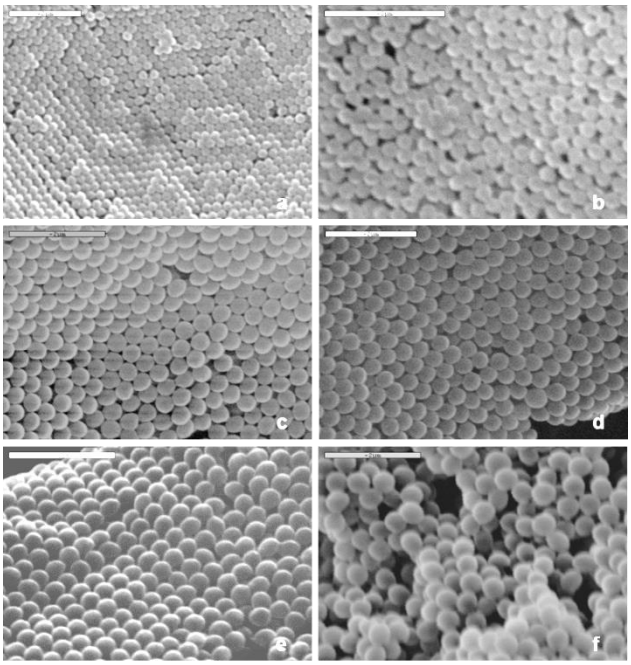

Figure. 3.3 SEM images showing sphere formation using (a) 0.8, (b) 1.04, (c) 1.27, (d) 1.48, (e) 1.68 and (f) 2.24 M monomer concentrations with corresponding mean sphere diameters of (a) 286, (b) 307, (c) 383, (d) 414, (e) 424 and (f) 501 nm respectively. Scale bars: 2μm.

For the 2.24 M monomer sample, self-assembly does not occur. This could be due to the nature of the spheres that are deviating from spherical into more ellipsoidal morphologies with irregular shapes. Therefore self-assembly becomes more difficult to achieve a minimum surface energy. The deviation from the spherical shape in the SFEP process using 2.24 M of monomer can be due to low stability of MMA micelles in water at such high volumes of MMA.

Figure 3.4 illustrates how the diameters of the PMMA spheres are affected with increasing monomer concentration in SFEP process. From the plot, it can be seen that there is a linear increase in PMMA sphere diameter as the concentration of MMA increases. When the concentration of MMA is 0.8 M, the synthesised spheres are approximately 286 nm and this increase with concentration to a value of 501 nm, indicating that SFEP is a versatile process which can produce spheres over a range of hundreds of nanometres.

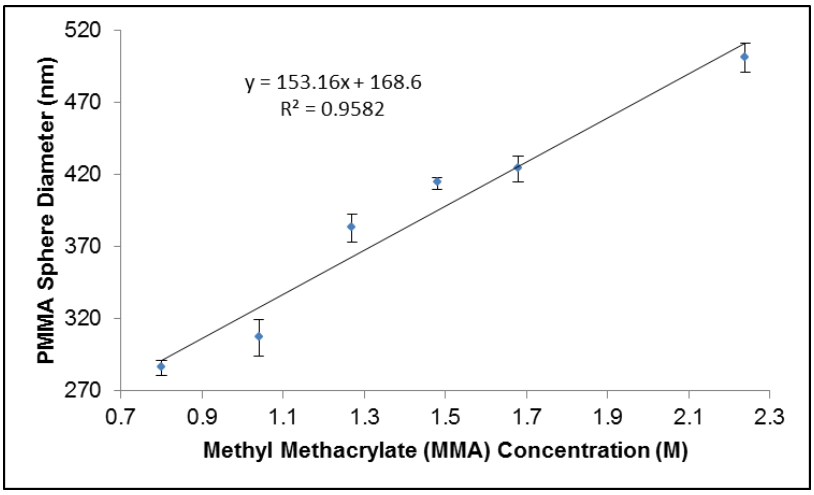

Figure. 3.4 The plot of PMMA sphere diameter as a function of MMA monomer concentration.

These results are consistent with previous studies[26, 30, 176, 178] and show increase in PMMA sphere diameter is attributed to increase in the amount of MMA monomer. Increasing the monomer : initiator ratio may increase the diameter of the polymer spheres produced. By increasing the amount of monomer relative to the amount of initiator, more monomer is shared around the same number of initiator molecules which leads to the formation of larger particles. Moreover, increasing the concentration of MMA means there are more

monomer in the monomer droplets to be diffused to the growing monomer swollen particles.

However, an alternative growth mechanism for the relationship between sphere diameter and monomer concentration during SFEP has been suggested by Egen et al[26] by using various methacrylate monomers. They reported that very early during polymerisation, small polymer particles are formed (which is consistent with the models outlined in Chapter 1 for SFEP processes) and their concentration depends on such properties as solubility of the monomer in the water phase, solubility of the growing charged oligomers and their critical coagulation concentration. After the nucleation step, the particles grow till all monomer is consumed. Therefore the volume of the colloids increase linearly with the ratio monomer to water, while the selection of the monomer determines the number of colloids per volume of water (more hydrophobic monomers give rise to larger colloids).

3.4.4 Temperature Dependent SFEP

Figure 3.5 shows the SEM images for PMMA spheres prepared at different synthetic temperatures. The samples in all the images apart from the sample in Figure 3.5(a) (corresponding to 60°C synthetic temperature) show monodispersity, spherical and self-assembled colloidal crystal qualities. The sample produced at 60°C shows deviation from spherical toward ellipsoidal morphology, indicating that at low temperatures the spherical micelles cannot be stabilised.

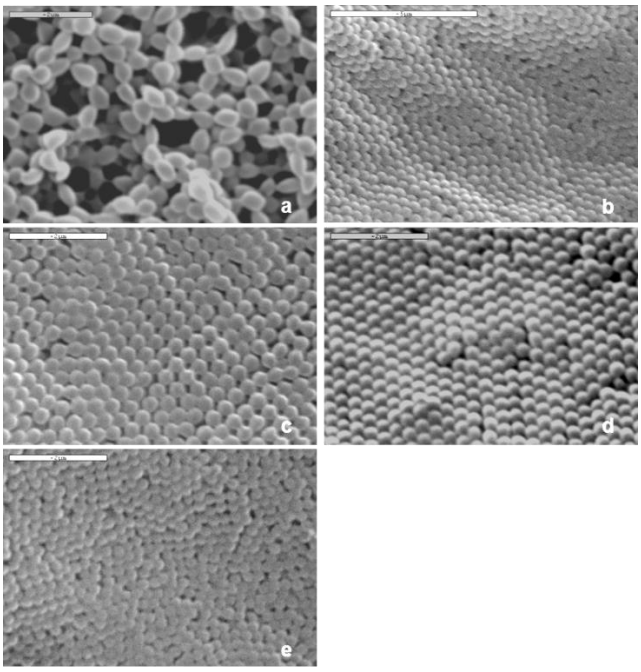

Figure. 3.5 SEM images showing sphere formation using synthesis temperatures of (a) 60, (b) 70, (c) 75, (d) 80 and (e) 85°C with corresponding mean sphere diameters of (a) 544, (b) 414, (c) 363, (d) 308 and (e) 234 nm. Scale bars: (a),(c),(d),(e) 2μm and (b) 5μm.

The SEM image in Figure 3.5(e) corresponding to the 85°C sample shows a degree of adhesion and fusing of the spheres with more defects in the colloidal crystal. This may be attributed to the high synthetic temperature, forcing the water used as the solvent during polymerisation to evaporate faster, in addition to being closer to the PMMA sphere melting point (160°C). To investigate this point further, a SFEP process was carried out at 95°C. The result showed that the spheres were completely fused together with no defined morphology. Moreover, carrying out the experiment at that high temperature resulted in the water used in the polymerisation process rapidly evaporating, producing a very small yield of polymerised PMMA spheres.

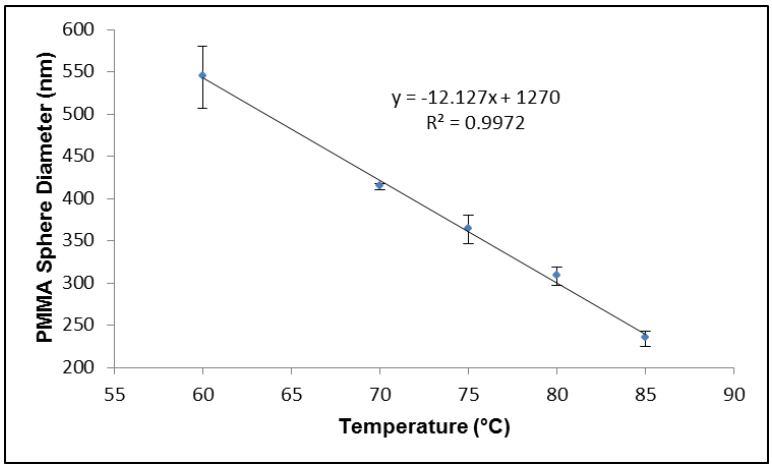

Figure. 3.6 The plot of PMMA sphere diameter as a function of temperature.

The plot in Figure 3.6 shows a linear decrease in PMMA sphere diameter as the temperature increases. The lower limit of spheres produced in this series of experiments is 308 nm at 80°C and the diameter of the particles produced at 60^0C is 544 nm. These results are consistent with previous studies[30, 43, 178]. This inverse dependence between the sphere size and the polymerisation temperature is due to the fact that raising the temperature of polymerisation increases the rate of thermal decomposition of the initiator. The increase in temperature also has the effect of increasing the solubility of the MMA monomer in water. Therefore, the concentration of growing chains at any one time increases making the monomer more available for termination by the free radicals resulting in stabilisation of smaller spheres[30].

Good quality spheres with diameters above 500 nm are difficult to achieve in a single step SFEP process by controlling in both concentration and temperature. They tend to form non-spherical particles with fused morphology. Previous study has shown that larger colloids have a lower surface charge than the smaller colloids due to the distribution of initiator charges around the

micelles.[26] Charges may also exist inside the polymer spheres rather than just on the surface with larger colloids, due to significant diameter increase during polymerisation, which makes it more difficult to expose the hydrophilic charged chain ends to the surface. The stability of the dispersion of larger colloids is further reduced as the monomer concentration in the polymerisation process becomes too high which may lead to very highly concentrated colloidal dispersions resulting to very high monomer : initiator ratio. This may result to for the unreacted monomers to destabilise the polymerisation process. These factors limit the stability of dispersions of larger colloidal spheres and result in a size limit to PMMA spheres produced by the single step SFEP process[26]. The lack of spherical morphology also limits the formation of ordered, defects free colloidal crystals. For the synthesis of larger spheres, the effective seeded SFEP process was developed in this work, which is demonstrated in the next section.

3.4.5 Seeded SFEP

Representative SEM images of the six samples produced by varying the concentration of PMMA seed added to the fixed amount of monomer concentration (1.48 M) in an otherwise typical SFEP process, are presented in Figure 3.7. The diameter of the seed sphere is ~ 414 nm.

From the SEM images in Figure 3.7, it can be seen that at low seed concentrations of 7.9, 13.2 and 19.7 mg/ml, corresponding to images a, b and c, bimodal distributions of spheres are observed. However at higher seed

concentrations of 26.3, 39.5 and 52.6 mg/ml corresponding to images d, e and f, single distributions of large spheres are observed with the presence of some loose extra-large spheres.

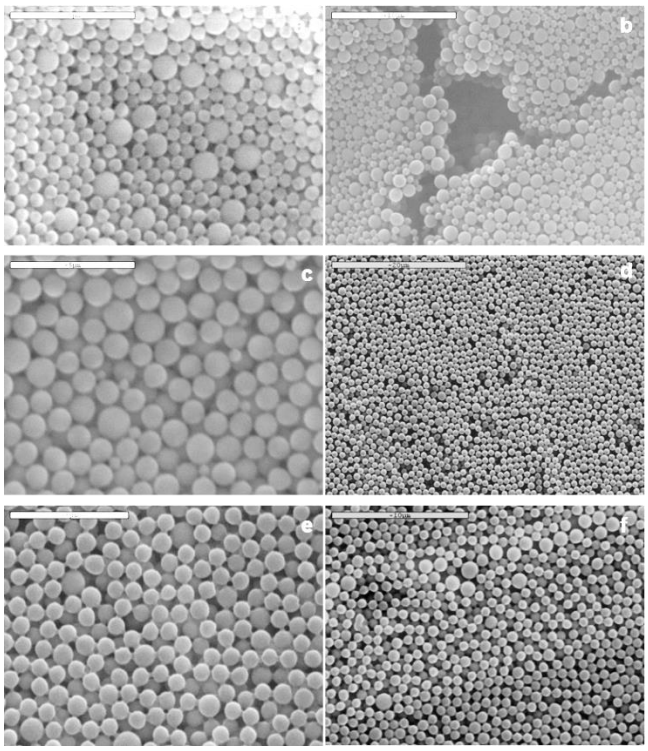

Figure. 3.7 SEM images of spheres produced by the seeded SFEP process. (a) 7.9 mg/ml seed, (b) 13.2 mg/ml seed, (c) 19.7 mg/ml seed, (d) 26.3 mg/ml seed, (e) 39.5 mg/ml seed, (f) 52.6 mg/ml seed. Scale bars: (a) 5μm (b) 10μm (c) 5μm (d) 20μm (e) 5μm (f) 10μm.

Figure 3.8 shows the sphere size distribution produced using different seed concentrations. The graphs are normalised by using the same number of measurements (500 measurements of sphere diameter were taken for each sample from SEM images).

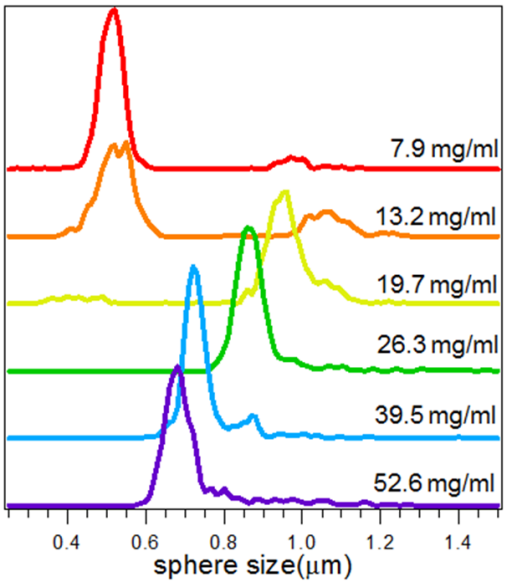

Figure. 3.8 Sphere size distributions of spheres produced using different seed concentrations. 500 measurements of sphere diameter were taken for each sample using SEM and then normalised to produce each graph. The average diameter of the seed sphere is about 414 nm.

From the graph in Figure 3.8, it can be seen that at low seeding concentrations (from 7.9 to 19.7 mg/ml), the amount of small spheres is decreased and the amount of large sphere population is increased by increasing the seed concentration. Another trend that can be detected from the graph is that at high seeding concentration (from 19.7 to 52.6 mg/ml), the diameter of the large sphere population decreases by increasing the seed concentration. The presence of bimodal sphere diameter distribution suggests that both seeded and unseeded growth may occur during the seeded SFEP process. The sphere populations become more singular above the 19.7 mg/ml seed concentration with the presence of some loose large spheres. These random large spheres are possibly formed because of aggregating of the seeds. The decrease in the diameter of the large spheres may be explained by

the fact that as the number of seed spheres increase there is less amount of monomer present to coat them (the monomer concentration remains the same in all the experiments).

The effect of monomer concentration on the size and behaviour of the spheres produced in seeded SFEP process at a constant seed concentration of 26.3 mg/ml was also studied in this work. Figure 3.9 shows the normalised sphere size distribution at different concentrations of MMA.

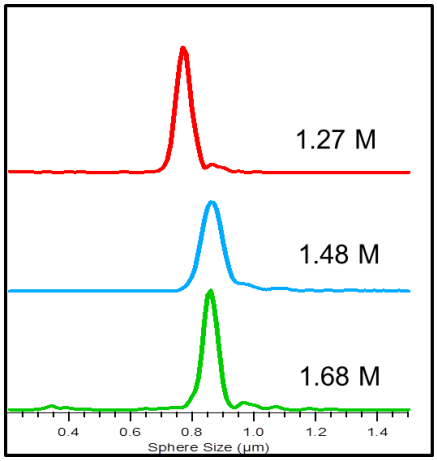

Figure. 3.9 Sphere size distributions of spheres produced using different MMA monomer concentrations.

From Figure 3.9, it is clear that as the monomer concentration is increased from 1.27 M to 1.48 M, the average diameter of the spheres also increases from approximately 750 nm to 950 nm. This may be due to the fact that more monomer is available around the same number of seeds as the monomer concentration is increased. When the concentration of monomer reaches 1.68 M, a low population of small spheres (~ 350 nm) is detected. This may be due to formation of new unseeded growth at this high monomer concentration. In other words, this can be the saturation point where no more

polymerisation around the seeds can take place and a new population of spheres start to grow.

By combining the results of the two sets of experiments based on varying the seed or monomer concentration while keeping the other constant, an optimised single population of large spheres can be realised. The optimised parameters for seed polymerisation are 1.27 M MMA monomer and 26.3 mg/ml PMMA sphere seed.

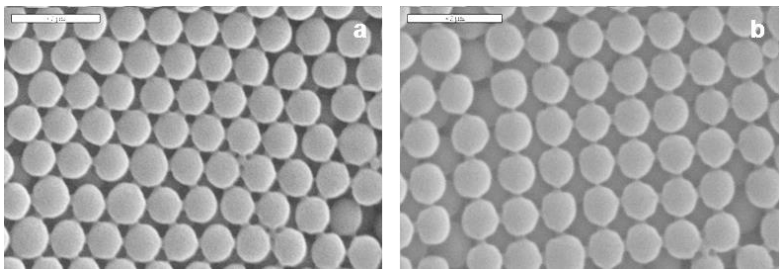

Figure. 3.10 SEM images showing (a) 111, (b) 100 domains of PMMA colloidal crystal of spheres produced by seeded SFEP using 1.27 M MMA and 26.3 mg/ml sphere seed. Scale bars: 2μm.

Figure 3.10 shows the SEM images of the optimised PMMA spheres synthesised *via* seed polymerisation. The spheres are self-assembled into ordered and close packed colloidal crystal exposing different domains at different areas. The exposed (111) domain in Figure 3.10(a) may belong to one of the thermodynamically favoured FCC or HCP crystal configurations, as it is difficult to identify the true 3D crystal packing from the top view of the SEM image. However, the exposed (100) domain in Figure 3.10(b) most likely belongs to the HCP crystal configuration due to systematic absence of this domain in FCC structure. The singularity in size and monodispersity of the

spheres makes it possible for the fabrication of such high quality colloidal crystals. The average diameter of the PMMA spheres produced is 780±7 nm. Therefore, this strategy allows the formation of monodisperse PMMA spheres with diameters above 500 nm when unseeded single step SFEP process is unsuccessful.

3.4.6 TiO_2 (P25) Powder / PMMA Sphere Composite

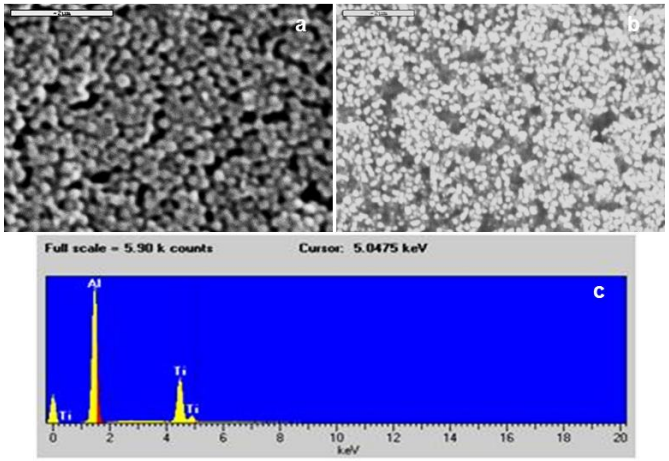

Figure. 3.11 SEM images of P25/PMMA sphere (a) before calcination, (b) after calcination and (c) the EDX spectrum of the product after calcination at 450°C. Scale bars: (a),(b): 2μm

Figure 3.11 shows the SEM images of P25/PMMA sphere composite produced by the SFEP process before calcination (a), after calcination (b) at 450°C for the removal of PMMA and the EDX spectrum of the product after calcination (c). The SEM images show some spherical morphology when the P25/PMMA sphere is produced *via* SFEP process (Figure 3.11(a)) and the loss of spherical morphology after calcination (Figure 3.11(b)). The EDX spectrum (Figure

3.11(c)) shows the presence of Ti in the sample after calcination. The large peak at the start of the EDX spectrum corresponds to aluminium which comes from the underlying aluminium foil substrate. The size of the spheres before calcination are 175±10 nm. A SFEP process under the same experimental condition without the inclusion of TiO_2 (P25) nanoparticles produces spheres with average diameter of 414 nm. There is a 58% reduction in size of the spheres when P25 is included in the polymerisation process. This suggests that in the propagation stage of SFEP when the metal oxide is included, the monomer chains may be shortened and also when the PMMA micelles are formed less monomers may be allowed inside for particle growth and hence much smaller spheres are formed. These two effects may arise due to the disturbance caused by inorganic TiO_2 nanoparticles acting as blocking agents in the polymerisation solution. After calcination, the spherical morphology of the sample is significantly reduced leaving randomly sized distribution of TiO_2 nanoparticle aggregates with sizes ranging from 110 to 175 nm. Such wide size distribution may be the result of low loading and uneven distribution of encapsulated TiO_2 nanoparticles during SFEP process.

For further investigation and the possibility of improving the quality of the TiO_2 spheres, a layer of titanium isopropoxide (TT^iP) precursor was coated on the sample. After the sol-gel process and solidification, the sample was calcined as before. The TT^iP coating is converted to TiO_2 during the calcination step, with the objective of stabilising the sphere morphology. Figure 3.12 shows the SEM image and the corresponding EDX pattern for the final product. The Au and Al peaks represent a layer of gold coating (for SEM analysis) and the

aluminium foil substrate respectively. A strong peak for the Ti element is clearly detectable.

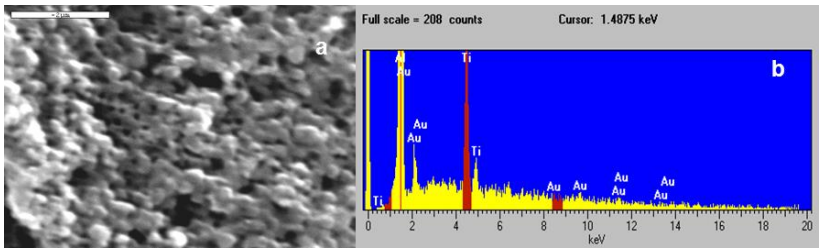

Figure. 3.12 SEM image (a) and EDX spectrum (b) of TT^{i}P coated P25 after PMMA removal at 450°C. Scale bar: 2μm.

The coated particles are of crystalline phase of anatase TiO2, as the XRD pattern in Figure 3.13 suggests. A strong peak corresponding to the (101) plane which is the characteristic peak of anatase phase according to the Joint Committee on Powder Diffraction Standards (JCPDS) database with reference number 841286. This confirms the successful completion of sol-gel and crystallisation process during coating.

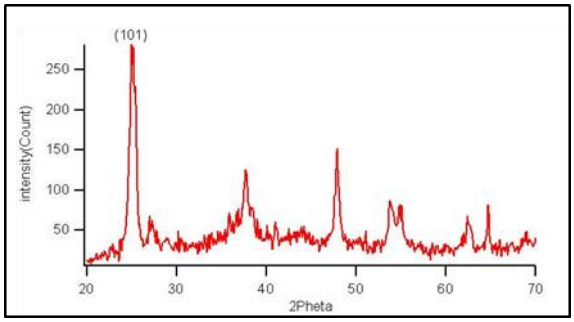

Figure. 3.13 XRD pattern for crystalline TiO_2 produced form TT^{i}P/P25 after PMMA removal at 450°C. Anatase peaks are present at 25.266°(101), 37.703°(004), 47.867°(200), 53.912°(105), 55.001°(211) and 62.745°(118).

As can be seen form the SEM image in Figure 3.12(a), some of the particles are spherical while majority of them are in aggregates with rough surfaces surrounding the TiO_2 shell interconnected during the sol-gel process. A conclusion that can be drown here is that, morphological quality of the P25/PMMA composite system *via* SFEP/calcination process is not yet optimised. Perhaps as literature has suggested[161, 172, 173] for other core/shell polymerisation systems, the inclusion of an anionic surfactant is needed for better partnership between the two phases (i.e. the organic polymer and the inorganic metal oxide) by increasing the surface charges between them.

3.4.7 Iron Oxide Powder / PMMA Composite

Figure 3.14 shows the SEM images of PMMA with iron oxide powder included in the SFEP process before calcination at different magnifications. The SEM images show that each colloidal particle has a hexagonal shape with average diameter of 330±10 nm. The diameter is shrunk by about 20% compared to the original PMMA sphere (~414 nm) polymerised without the presence of the iron oxide particles in the SFEP process. Similar to the P25/PMMA experiment discussed earlier, the addition of the metal oxide disturbs the polymerisation which makes the final colloids smaller. The morphology in this case is also deviated from the energetically favoured spherical shape. This may be due to the nature of the iron oxide particles that disturb the PMMA chains in micelle formation to form such hexagonal colloidal particles. The surface of the iron oxide can be charged and disturb the charged free radicals produced during initiation stage of polymerisation. This may lead to hydrophobic and hydrophilic

parts of the forming oligomers (long chain free radicals) to deviate from their natural energetically favoured formation of spherical micelles into more elongated shapes.

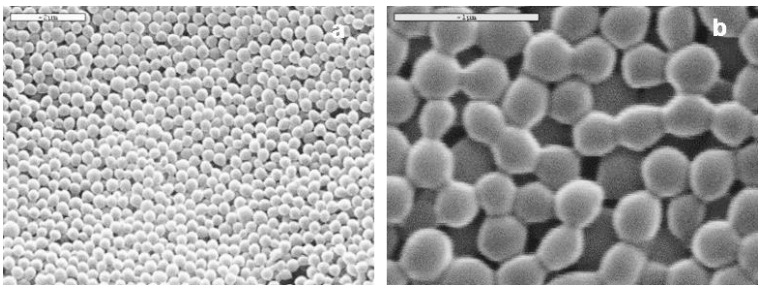

Figure. 3.14 SEM images of iron oxide/PMMA sphere composite *via* the SFEP process before calcination. Scale bars: (a) 2μm and (b) 1μm.

After calcination, the spherical morphology of the sample is reduced significantly leaving randomly sized distribution of iron oxide nanoparticle aggregates with sizes ranging from 195 to 545 nm. Figure 3.15(a) shows the SEM image of iron oxide/PMMA in the SFEP process after calcination at 450°C for PMMA removal. The corresponding EDX spectrum is shown in Figure 3.15(b). Such wide size distribution may be due to the low loading of iron oxide powder during SFEP process (smaller particles) and the formation of nanoparticle aggregates after calcination (larger particles). The EDX spectrum (Figure 3.15(b)) shows the presence of Fe in the sample after calcination. The large peak at the start of the EDX spectrum corresponds to aluminium which comes from the underlying aluminium foil substrate. As it was mentioned earlier, by adding a correct anionic surfactant such as sodium dodecyl sulphate (SDS) and treating the surface of the metal oxide particles prior to use, the stability of the system may be enhanced.

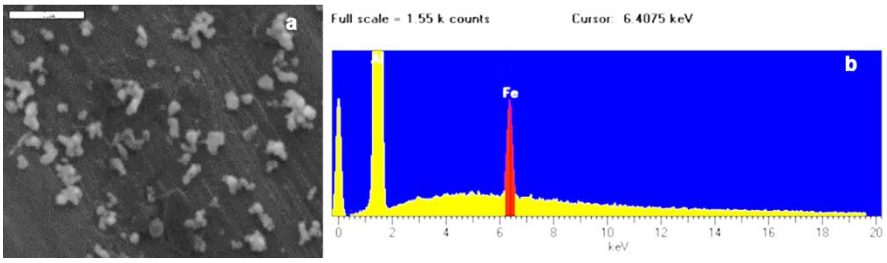

Figure. 3.15 (a) SEM image of iron oxide/PMMA in the SFEP process after calcination at 450°C and (b) the EDX spectrum of the product. Scale bar: 2μm.

Although, both sets of experiments outlined here are considered unsuccessful in regards to the true formation of core/shell systems of PMMA/metal oxide, it has been demonstrated that by addition of metal oxide into the SFEP process without any pre-treatment, the PMMA colloidal spheres get smaller and in the case of iron oxide, morphological alteration can also occur producing hexagonal PMMA colloidal particles. These phenomena can be considered useful when PMMA spheres with smaller sizes or non-spherical shapes are of importance.

3.5 Conclusion

SFEP is a facile polymerisation technique with the use of only three components (water, monomer and initiator). It is at the same time a powerful technique for PMMA sphere synthesis with controllable synthetic conditions including monomer concentration and temperature to produce desirable spheres with different sizes and morphologies. The use of seeding in the SFEP process makes it possible to produce spheres larger than 500 nm where it is not possible to create them *via* an unseeded single step SFEP process. Adding

metal oxide powder into the SFEP process may cause reduction in the size of the PMMA spheres. Due to the low loading of metal oxides and the aggregates of the nanoparticles, the calcination process will destroy the spherical morphology of the residual of metal oxides. By adding a suitable surfactant, it may be possible to synthesise optimised PMMA/metal oxide core/shell systems using this facile seeded SFEP process.

The production of monodisperse PMMA spheres with controllable sizes makes it possible to use them directly as building blocks for the synthesis of homogeneous metal oxide hollow sphere nanostructures. They can also be first self-assembled into highly ordered PMMA colloidal crystals and then be used as templates for the synthesis of different metal oxide inverse opal nanostructures with high degree of porosity and interconnectivity. Such systems with their large surface areas can be used in photovoltaic devices with enhanced light harvesting properties.

Chapter 4: Production and Study of PMMA Colloidal Crystals *via* Colloidal Crystal Self-Assembly

4.1 Abstract

PMMA colloidal crystals were successfully fabricated using two different self-assembly techniques; vertical deposition by evaporation and a modified floating (air-water interface) approach. A temperature dependent study using the vertical deposition approach was carried out. Monolayer PMMA colloidal crystals were produced using the floating technique. By multiple depositions, 3D double-layer and triple-layer colloidal crystals were successfully fabricated. The photonic crystal properties of PMMA colloidal crystal were also investigated. The crystal was opalescent under illumination and had a typical photonic stop band in the visible region of the spectrum.

4.2 Introduction

Once PMMA colloidal spheres are formed *via* the SFEP process, they can be self-assembled into colloidal crystals. Such highly ordered close-packed structures can serve as templates for the synthesis of inverse opals and photonic crystals with the potential for use in a variety of applications including photovoltaics.

Although controlling the thickness of colloidal crystals using different techniques is achievable, with so many variables in the experimental conditions, such as concentration of the colloidal spheres, rate of solvent evaporation and

type of the substrate used[3], it is often a challenging task to achieve good control of the colloidal crystal thickness. Considering that the floating technique can produce monolayer colloidal crystals, it is theorised that multilayers may be created using this technique by repeating the technique on the same deposited substrate until the desired layers are achieved. If such an approach is successful, it will be a powerful, facile technique to produce 3D colloidal crystals with controlled thickness. This hypothesis forms the investigations described in this chapter.

Colloidal crystals can be considered as photonic crystals due to their periodic structures constructed from alternating regions of refractive indices (PMMA sphere and air in the case of PMMA colloidal crystal), thus the successful fabrication of colloidal crystals can result in a photonic stop band in the visible region as discussed previously in Chapter 1. Through precise material design, the colours in colloidal crystals acting as photonic crystals can be tuned reversibly by applying external physical or chemical stimuli[6]. The alteration of the photonic stop band characteristics can be achieved by varying the refractive index contrast, the lattice constant and/or the filling factor of the colloidal crystal. From the photonic stop band it is also possible to calculate the diameter of the original PMMA colloidal sphere using a modified form of the Bragg equation of diffraction[43]. In this work, the photonic properties of PMMA colloidal crystals fabricated by the floating technique have been investigated.

4.3 Experimental Procedures

4.3.1 PMMA Colloidal Crystal Fabrication *via* Vertical Deposition

A PMMA sphere solution was previously synthesised using the SFEP process using 6 ml of MMA monomer (average sphere diameter of 414 nm). This was used for colloidal crystal fabrication experiments. The synthesis and purification processes were discussed in the last chapter. After the last centrifugation, the top water was discarded and the white spheres were left to dry in an oven at 40°C for 6 hours.

Figure. 4.1 An image illustrating the vertical deposition setup for PMMA colloidal crystal fabrication.

Once dried, a PMMA sphere suspension in water (1.5 wt%) was prepared. The PMMA suspension (25 ml) was added to a 50 ml glass beaker. A microscope glass slide was then etched for 1 hour in sodium hydroxide solution (30 wt%) to increase its hydrophilicity[179] in order for better PMMA sphere attachment. The glass slide was then washed thoroughly with DI water several times. It was then suspended in the beaker. This was achieved by gently attaching a cotton bud to the top of the glass slide using aluminium tape and then resting the cotton bud on the lip of the beaker. The beaker with the slide

suspended in it was placed in an oven at fixed temperature for 48 hours. After this time the water in the beaker had evaporated leaving a white film of the closed-packed PMMA colloidal crystal on the glass slide. Five different oven temperatures of 52°C, 63°C, 73°C, 85°C and 94°C were used to evaluate the temperature effect on the colloidal crystal quality. Figure 4.1 shows a typical vertical deposition set-up prior to placing it in the oven.

4.3.2 PMMA Colloidal Crystal Fabrication *via* Floating Approach

PMMA spheres solution (3 ml) previously produced *via* SFEP process with an average sphere diameter of 383 nm was mixed with ethanol (3 ml) in a small vial (producing a 1:1 ratio by volume). A microscope glass slide was cut with a diamond pen to produce a 2 cm^2 piece. It was then cleaned twice by ultra-sonication, for 10 minutes in acetone and DI water respectively. The glass was then placed in the center of a Petri dish. DI water was poured into the Petri dish, covering the sides of the glass specimen without covering its surface. A drop of the PMMA/ethanol solution was pipetted onto the centre of the glass. More DI water was then carefully added to the petri dish (from one side only). The water level raised until it covered the surface of the glass and just touched the PMMA solution contact line. This step was performed delicately as excess water would leave the PMMA solution submerged and the experiment would not be successful. Once the PMMA solution and water made contact, the PMMA solution rose on top of the water surface. This was driven by the differences in surface energy between the ethanol suspension and the water in the Petri dish[92, 180]. After a few seconds, all of the suspension had risen from the glass, forming an iridescent monolayer island of PMMA colloidal crystal on the water

surface. During this step the glass was completely immersed under the water. More water was then carefully added to the Petri dish to raise the water level to facilitate the next step, in which the colloidal crystal was picked up onto a substrate[89, 90].

A microscope glass substrate was cleaned with the same procedure described earlier (Section 4.3.1). The cleaning process for an FTO glass sample was as follows;- it was soaked ultra-sonically for 10 minutes in isopropanol followed by 5 minutes in DI water. The titanium plates were cleaned by first immersing in dilute HCl solution (3M) for 15 minutes followed by washing with DI water. The plate was then polished with sand paper.

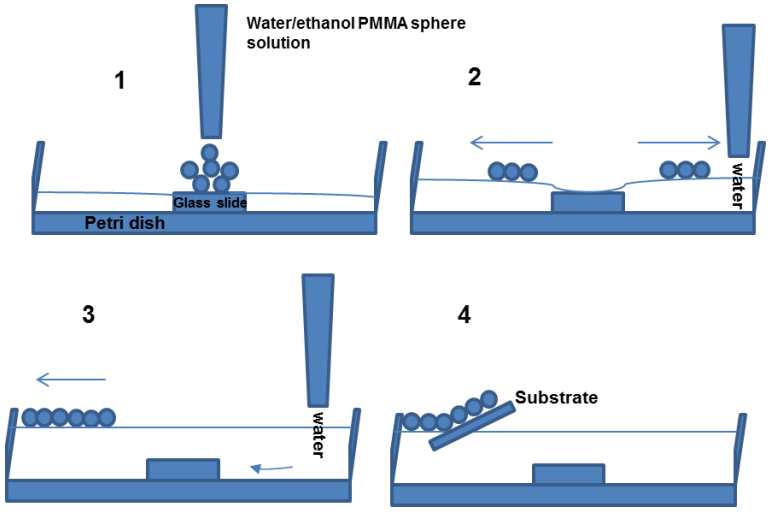

Figure. 4.2 Schematic of PMMA colloidal crystal fabrication by the floating approach.

The substrate was immersed carefully into the water and was slowly lifted up from below the colloidal crystal at a shallow angle (10-20°). The substrate was then left to dry in air for 15 minutes. For fabricating a double layer colloidal crystal, once the deposited monolayer colloidal crystal was fully dry, the above procedure was repeated on the same substrate. To produce a

multilayered PMMA colloidal crystal, the procedure was repeated until the desired number of layers was obtained. Figure 4.2 shows a schematic diagram of the different steps taken in making a fabrication a monolayer PMMA colloidal crystal using the floating approach.

4.4 Results and Discussion

4.4.1 Temperature Dependent Vertical Deposition Approach

All five samples produced at the different temperatures (52°C, 63°C, 73°C, 85°C and 94°C) by the vertical deposition approach for 3D multilayered colloidal crystal fabrication show self-assembled PMMA spheres with good colloidal crystal quality. There is also no obvious systematic difference in thickness within the experimental temperature range. Figure 4.3 shows the SEM images for the PMMA colloidal crystal produced at (a) 52°C, (b) 73°C and (c) 85°C.

As it can be observed in Figure 4.3, all of the SEM images show high levels of ordering with close-packed structures. The PMMA structures tend to be FCC with their (111) planes parallel to the underlying substrate. This configuration is most favoured thermodynamically [43], however Norris et al[181] suggested that the common assumption that the preferred FCC crystal structure in self-assembly processes is solely driven by thermodynamic equilibrium (static assembly) is not correct. Rather, they suggest it is an example of dynamic self-assembly in which viscous drag caused by the fluid flow between the sphere pores form such a structure. The effective confinement space between the air

cavities (pores) of touching spheres in 3D PMMA colloidal crystals created by the ABCABC stacking of the FCC structure can be calculated mathematically[182]. If *r* is assumed to be the radius of PMMA spheres, then the confinement space inside the tetrahedral and octahedral cavities can be estimated by spheres of radius 0.225*r* and 0.414*r* respectively. The largest particle (assuming spherical shape) that can pass through freely from cavity to cavity has a radius of 0.156*r*.

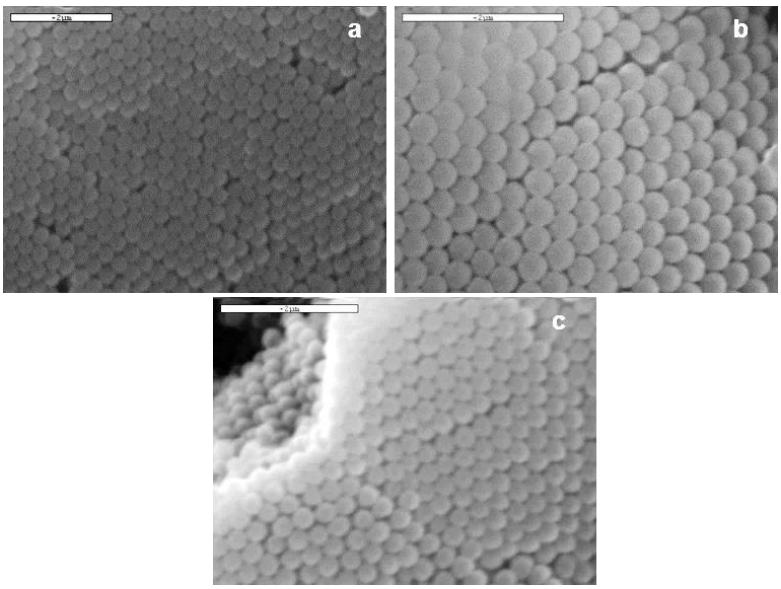

Figure. 4.3 SEM images showing the top views of 3D multilayered PMMA colloidal crystals fabricated *via* vertical deposition method at (a) 52°C, (b) 73°C and (c) 85°C. Scale bars: 2μm.

The samples show a 2-3% reduction in diameter during colloidal crystal formation. This decrease may be due to condensation and loss of water (locked in after polymerisation) in each sphere during drying or the deposition process at raised temperature. The sphere diameter shrinkage however, is approximately the same for all of the samples. This suggests that at these medium-range temperatures, sphere size does not depend on temperature.

An important phenomenon that can be observed with increasing temperature is the formation of necking (connection between the spheres), which becomes more pronounced as temperature increases. The SEM image in Figure 4.4 shows the necking between the PMMA spheres for the sample self-assembled at 94°C.

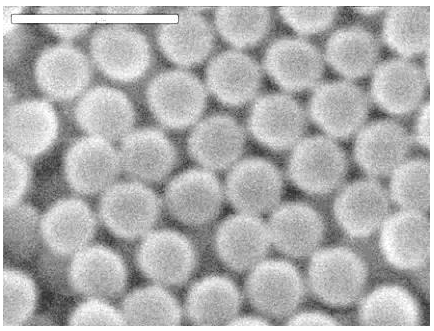

Figure. 4.4 SEM image showing the necking between PMMA spheres in a colloidal crystal assembled at 94°C. Scale bar: 1μm.

Necking occurs when capillary forces bring the spheres together in the self-assembly process; it can increase the distance between the spheres.[43] Necking can be important to increase the mechanical strength of colloidal crystals especially when they are going to be employed as templates for processes such as inverse opal fabrication.

Another phenomenon observed in the samples is the change in quality of the colloidal crystals in different areas of the film. Figure 4.5 shows an SEM image taken from just below the original meniscus contact line (i.e. air/water/substrate contact line) of the sample self-assembled vertically at 94°C. The schematic diagram showing this region is also presented in Figure 4.5.

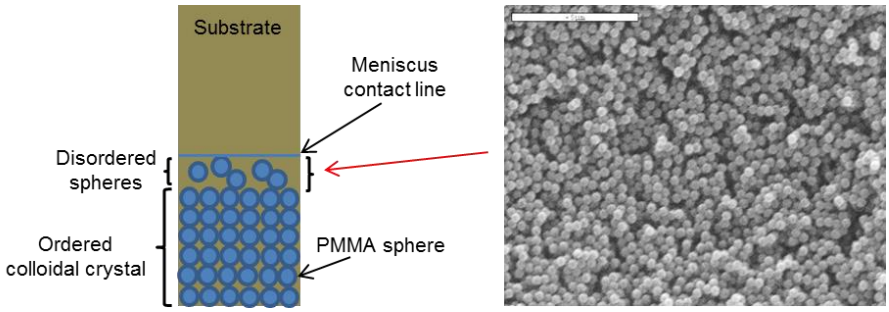

Figure. 4.5 SEM image and schematic representation showing PMMA self-assembly just below the original meniscus contact line. Scale bar: 5μm.

As can be seen from the SEM image and its schematic diagram in Figure 4.5, the spheres are not completely self-assembled into an ordered colloidal crystal at this region. There is a portion of spheres loosely floating around. This can be attributed to the low concentration of the spheres at the region just below the meniscus contact line. The self-assembly quality is enhanced further down the film as shown in Figure 4.3. This suggests that a concentration gradient in the vertical deposition self-assembly technique exists. The concentration gradient is due to the gradual evaporation of water inside the beaker which increases the concentration of the spheres in the solution. Therefore more spheres are available at the bottom of the beaker leading to better self-assembly on the bottom region of the glass substrate which is positioned vertically in the beaker. However due to this concentration gradient, the film at the bottom of the glass substrate can be thicker than the top. If the film is too thick, it will eventually shear, crack and peel off the glass substrate. This leaves some bear areas at the bottom of the substrate. The shearing occurs in a vertical direction, which can first be seen as macroscopic cracks on the film prior to detachment.

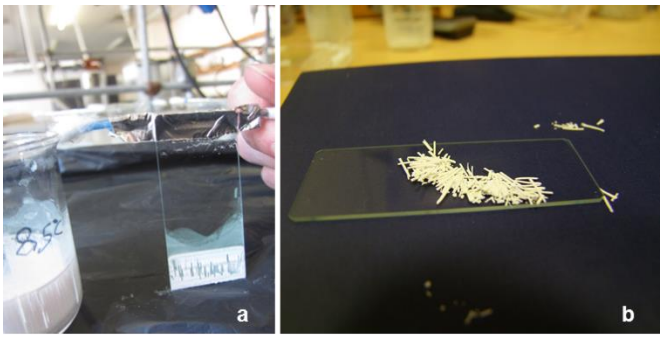

Figure. 4.6 (a) No Colloidal crystal coverage and (b) the detached strips of colloidal crystals due to peeling off at the bottom of the substrate for the 85°C sample.

Figure 4.6(a) shows an image of a substrate with its colloidal crystal film peeled off at the bottom (85°C sample). Figure 4.6(b) shows the image of the PMMA colloidal crystal strips that have fallen off the glass substrate off the same sample. The strips were gathered from the bottom of the beaker and placed on a microscope glass slide for better clarity.

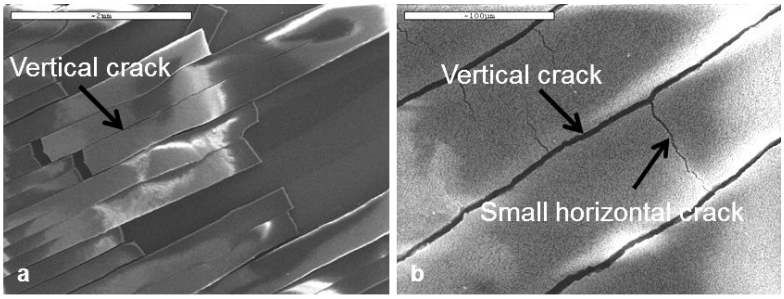

Figure. 4.7 SEM images showing (a) low magnification and (b) high magnification of vertical macroscopic cracks formed due to PMMA sphere concentration gradient on the vertically deposited substrate for the 85°C sample. Scale bars: (a) 2mm and (b) 100μm.

Figure 4.7 shows the SEM images of the vertical macroscopic cracks produced by the effect of the concentration gradient, which are eventually peeled off from the substrate.

As it can be seen from the low magnification of SEM image (Figure 4.7(a)), only vertically formed cracks can be observed. Such cracks are also observable by eye, however, when looking at the SEM image at a higher magnification (Figure 4.7(b)) horizontally formed small cracks can also be observed. Both forms of cracks are present for all samples produced at different temperatures. Apart from the concentration gradient effect, other phenomena may also be responsible for the formation of these well-aligned macroscopic cracks. For instance, the gravitational forces can lead to the water inside the sphere solution traveling downwards, forcing it to form alley-like pathways among the spheres as cracks. Densification caused by volume shrinkage of the colloidal crystals during self-assembly stage upon drying may also cause fissures, apparent as vertical lines[183]. As mentioned previously in this section, the PMMA sphere size shrinkage of about 2-3% are observed for all the samples after self-assembly compared to the original PMMA spheres, confirming the overall volume shrinkage for the colloidal crystal samples. The water evaporation during the self-assembly process may also cause strong capillary forces contributing to such crack formation in the final colloidal crystal films[5].

In evaporation induced colloidal crystal formation techniques driven by capillary forces at the meniscus, such as the vertical deposition approach, there are many parameters that should be optimised in order to yield high quality colloidal crystals[101]. The parameters include the type of the substrate used,

solvent, air pressure, humidity, moving speed of the meniscus contact line, the use of surfactants, temperature and concentration of the colloidal spheres. The vertical deposition technique for colloidal crystal fabrication appears to be a convenient route, but it does not guarantee the formation of large areas of high quality colloidal crystals on the substrate.

4.4.2 Floating Deposition Approach

The SEM images of the monolayer colloidal crystal film removed from the water surface by a glass substrate are shown in Figure 4.8.

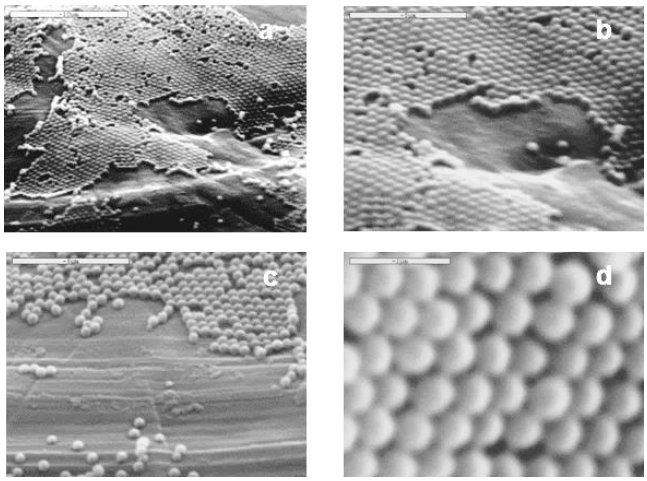

Figure. 4.8 SEM images of monolayer PMMA colloidal crystal fabricated using the floating approach. Scale bars: (a) 10μm, (b),(c) 5μm and (d) 1μm.

The images clearly show the monolayer 2D PMMA colloidal crystal structure created using this modified floating technique. The size of the PMMA spheres after self-assembly remains constant as the spheres prior self-assembly (c. 383 nm). As seen from the SEM images in Figure 4.8, large areas of monolayer 2D colloidal crystals are formed without any cracks. A low level of defects and imperfections in the form of separate spheres on top of the

monolayer can be detected. Such imperfections may originate from the spheres that are mixed with the water in the Petri dish instead of staying afloat.

An important step in the floating approach is the deposition of the colloidal spheres onto the surface of the liquid, as they can easily sink and disperse into the bulk liquid. When the liquid used is water, ethanol is added to the colloidal sphere solution in equal volumes before depositing onto the water surface. The role of ethanol is to act as a spreading agent[180]. The mixture of water:ethanol has lower density than pure water (0.911 compare to 1 g/cm^3 at ambient temperature[184]), which enhances the floating of the PMMA spheres. Also, the addition of ethanol improves the hydrophobic nature of the solvent, which improves the dispersion of the PMMA spheres. The water-ethanol mixture has also a higher vapour pressure and evaporation rate than pure water. When the ethanol containing sphere solution is correctly placed onto the water surface, it immediately spreads over it and when the ethanol evaporates, the colloidal spheres stay floating on the water surface leading to effective self-assembly of monolayer colloidal crystal through attractive interactions among the spheres.

The SEM images in Figure 4.9 show the formation of 3D PMMA colloidal crystal structures when the floating deposition is repeated twice to produce double-layers (in Figure 4.9(a) and (b)) and thrice to produce triple-layers (Figure 4.10(c)). As is observed in these images, uniform 3D multilayer PMMA colloidal crystal films with large coverage areas can be fabricated using this approach. An important advantage this method has over other mainstream methods, such as vertical deposition, is its versatility. Colloidal crystals can stack on top of each other with different sizes, morphologies and composition

due to the layer-by-layer nature of the floating depositions on the substrate. Therefore, synthesising layer-by-layer heterostructured inverse opals of different metal oxides may become possible using this stepwise self-assembly approach when combined with templating *via* sol-gel infiltration (Chapter 6).

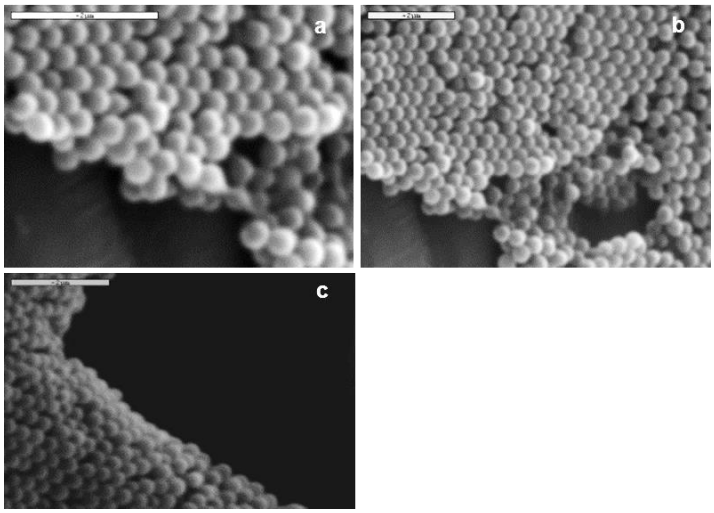

Figure. 4.9 SEM images showing 3D PMMA colloidal crystals formation when the floating deposition is repeated twice to produce double-layers (a) and (b) thrice to produce triple-layers (c). Scale bars: 2μm.

Again, as per the monolayer films produced by this method, some imperfections and defects can appear on the surface of multilayer films. They are possibly caused by the spheres mixed in the water during substrate being removed. Furthermore there are also some small cracks detectable on the surface when more layers are added to the colloidal crystal film. The small cracks can be observed clearly in the SEM image of Figure 4.9(d). These could be attributed to the electrostatic attractions[185] between the substrate and the colloidal spheres once the spheres are lifted up from the water surface. These forces can prevent the spheres from free moving on the glass substrate. By changing the glass substrate to a charge neutral titanium plate this problem

may be limited. The electrostatic phenomenon between the spheres and the glass substrate is present when using any self-assembly techniques and is not exclusive to the floating approach.

The monolayer colloidal crystals produced here were used in templating procedures in Chapters (6 and 7) for their applications in PEC water splitting and solar cell experiments. Therefore, conductive substrates such as titanium metal and FTO glass are of interest for PMMA colloidal crystal deposition. Figure 4.10 shows an image of a monolayer PMMA colloidal crystal film deposited on a titanium plate using the floating technique. The experimental procedure and the conditions are identical as before when using a microscope glass slide, as the substrate as described in Section 4.3.2.

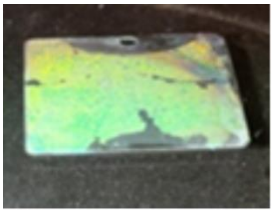

Figure. 4.10 Monolayer PMMA colloidal crystal deposited on a titanium plate using the floating technique.

The opalescent properties of the film can be clearly observed in the photo in Figure 4.10. The colours are produced when the camera light flash is used when taking the image. The opal like behaviour of the film confirms the photonic properties of the PMMA colloidal crystals which will be discussed in the next section. The colloidal crystal film covers almost the entire surface of the titanium plate, which makes it a good candidate for templating and photovoltaic processes.

The modified floating self-assembly approach is considered as a convenient technique, as the whole process occurs in a few minutes at room temperature without optimising any conditions or needing any special facilities. Large areas of high quality, monolayer PMMA colloidal crystals are produced using this method, which can later be converted to 3D multilayers with a well-controlled thickness.

4.4.3 Photonic Crystal Properties of PMMA Colloidal Crystals

Figure 4.11 illustrates the photos of a monolayer PMMA colloidal crystal film deposited on a microscope glass slide substrate using the modified floating technique (a) without illumination and (b) under the illumination of visible light.

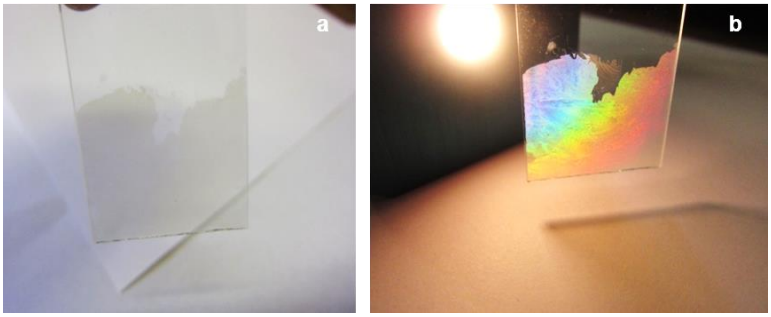

Figure. 4.11 Images showing a monolayer PMMA colloidal crystal film (a) without and (b) under visible light illumination.

The range of colours detected in Figure 4.10(b) during visible light irradiation are caused[6, 27, 41, 42] by the diffraction of visible light from the colloidal crystal, which possesses a periodic array of low and high refractive index areas of air and PMMA spheres. The difference in colour at different regions is caused by the changes in the angle of incident light. This colour phenomenon is

independent of electronic processes seen in most other colourful materials which derive their colour by the absorption of visible light, which causes electronic transitions that absorb or emit specific bands of light. A peculiar property of the PMMA colloidal crystal acting as a photonic crystal is its ability to "filter" light. As previously described in Chapter 1, when white light, which contains all visible colours of light, is shined on such structure, some wavelengths are forbidden from passing through the colloidal crystal and are reflected instead (photonic band gap phenomenon). The remaining wavelengths are unaffected by the colloidal crystal, and they simply pass through.

The optical properties of the colloidal crystal (opal) can be described by a modified Bragg's Law of diffraction due to its ordered periodic structure. A combination of Bragg's law of diffraction ($m\lambda = 2dsin\theta$) and Snell's law of refraction ($n_0 sin\theta_0 = n_1 sin\theta_1$) can be written as[6]:

$$m\lambda = 2d\sqrt{n^2 - n_0^2 sin^2\theta} \qquad \text{(Equation 4.1)}$$

In which m is the order of diffraction, n_0 and n are the incident refractive index and lattice refractive index respectively, d is the spacing between the planes in the lattice, λ is the light wavelength and θ is the angle between the incident light and the surface normal of the lattice.

For close-packed colloidal crystals with FCC structures, the refractive index n can be taken as an average of refractive indices of the spheres and the interstitial spaces. Equation (4.2) shows this relation:

$$n_{avg} = \emptyset n_{sphere} + (1 - \emptyset) n_{voids} \qquad \text{(Equation 4.2)}$$

where $\emptyset$ is the solid volume fraction of the structure. Parameter d as the interplanar spacing between hkl indices of Miller planes can be written as:

$$d_{hkl} = \frac{D\sqrt{2}}{\sqrt{h^2+k^2+l^2}} \quad \text{(Equation 4.3)}$$

As the (111) plane is the predominant plane for the PMMA colloidal crystal,

$$d_{hkl} = D\sqrt{\frac{2}{3}} \quad \text{(Equation4.4)}$$

where D is the average centre-to-centre distance between spheres in a close packed lattice that is geometrically identical to the sphere diameter.

For the first order diffraction ($m = 1$) from FCC (111) planes of the PMMA colloidal crystals, Equation (4.1) can be written as follows, assuming that $n_0 \approx 1$:

$$\lambda = 1.633D\sqrt{n_{avg}^2 - sin^2\theta} \quad \text{(Equation 4.5)}$$

where λ is the reflectance peak maximum of UV/Vis spectrum measured in nm. For such a structure, this maximum peak corresponds to the position of the photonic band gap (PBG), or stop band where the propagation of light is forbidden. Using the normal incidence of light ($\theta = 0^{\circ}$) and combining Equation (4.2) with (4.5), λ_{max} can be written as:

$$\lambda_{max} = 1.633D[\emptyset n_{sphere} + (1-\emptyset)n_{voids}] \quad \text{(Equation 4.6)}$$

For PMMA colloidal crystals at room temperature, the refractive indices for PMMA and air are $n_{PMMA} = 1.492$ and $n_{air} = 1.000$ respectively. The volume fraction of PMMA spheres in the FCC structure is $\emptyset = 0.74$ (and thus 0.26 for

air). By inserting these values in Equation (4.6), the following equation is obtained:

$$\lambda_{max} = 1.633 \times 1.364 \times D \qquad \text{(Equation 4.7)}$$

The normal incidence reflectance spectrum of the monolayer PMMA colloidal is obtained using a UV-Vis reflectance spectrometer and λ_{max} extracted (Figure 4.12).

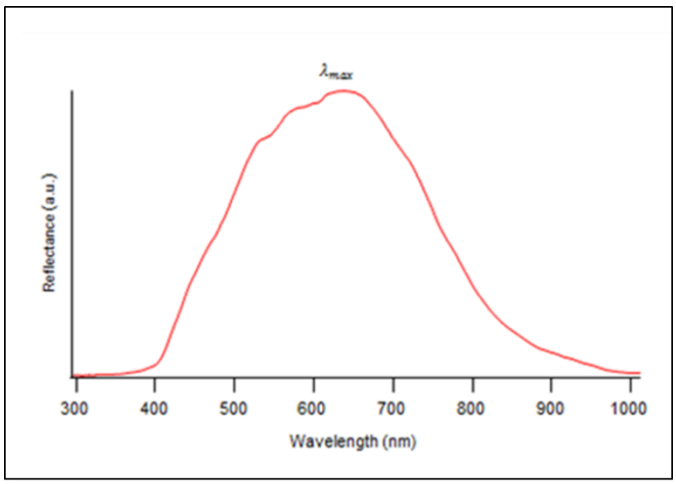

Figure. 4.12 UV-Vis reflectance spectrum collected from monolayer PMMA colloidal crystal.

From the spectrum in Figure 4.12, the reflectance maxima (λ_{max}) is positioned at 627 nm. The PMMA Sphere diameter (D) can now be calculated using equation (4.7): $D = 281\ nm$.

This value is 27% less than the original average sphere diameter determined by the SEM, which is 383 nm. The discrepancy in value may be due to the over simplification of assumptions when using the modified Bragg formula. For instance, the true volume fractions of air and the PMMA sphere

can differ from the ideal values of 0.74 and 0.26, due to crystal defects and size distribution of the PMMA spheres. Such defects and dislocations of the spheres may also interfere the diffraction of light and change the lattice constant parameter in the equation. As literature suggests, the modified Bragg equation is not exact because it does not include attenuation of the incident beam and assumes identical contributions from each lattice plane[19]. The position of the reflection peak maxima (λ_{max}) does not consider all the scattering effects and should be altered by a more rigorous treatment of dynamical diffraction theory (DDT)[42] by using X-ray scattering techniques[19, 186, 187]. Although the sphere diameter is not in good accordance with the SEM measurements, the existence of the reflectance maxima (λ_{max}) confirms the photonic crystal properties of the PMMA colloidal crystal. This technique has been used widely in the literatures[20, 43]. The Bragg reflection seen in the spectrum is attributed to the periodic arrangements of the PMMA colloidal spheres and confirms the high quality of the colloidal crystal produced using the floating technique.

4.5 Conclusion

The PMMA colloidal crystals produced in this work with both the vertical and the modified floating techniques showed high quality ordered arrays of self-assembled PMMA spheres. The PMMA spheres used to fabricate such structures were monodisperese which further confirms their successful polymerisation prior to self-assembly.

The modified floating approach can be considered as a powerful technique for colloidal crystal fabrication. Its simplicity combined with its

production of large areas of opalescent monolayer or multilayer photonic colloidal crystals in a short timeframe makes it an attractive proposition. Furthermore, its multiple deposition abilities can ease the difficulties in controlling the thickness of the colloidal crystals; a major challenge associated with many other colloidal crystal self-assembly techniques.

Photonic crystal properties of the PMMA colloidal crystals make them good candidates to be utilised not only in templating techniques for production of inverse opals and also as opalescent materials for multiple applications, such as displays, sensors, information storage, decoration, camouflage, art and mimicking biological systems[27, 41, 42].

Chapter 5: Preparation and Study of Multiple Metal Oxide Inverse Opals & Hollow Spheres Using Template-Directed Synthesis

5.1 Abstract

Various 2D and 3D metal oxide inverse opal nanostructures including TiO_2, Fe_2O_3 and ZnO were successfully synthesised using colloidal crystal templating *via* sol-gel infiltration. A comprehensive temperature-dependent study on the formation of 3D TiO_2 inverse opal was carried out, which revealed a reduction in the size of the air spheres after template removal. By using the template-directed synthesis *via* sol-gel coating, several metal oxide hollow sphere nanostructures, including TiO_2, SiO_2, ZnO, and CuO were synthesised. The synthesis of SiO_2/TiO_2 sphere-in-sphere hollow spheres was achieved for the first time using a combination of seeded polymerisation and templating processes.

5.2 Introduction

Inverse opal and hollow sphere nanostructures of several materials including metal oxides, can be synthesised by templating against PMMA colloidal crystals and colloidal spheres *via* sol-gel infiltration or coating. As discussed previously in Chapter 1, metal oxide inverse opals can be readily synthesised from colloidal crystal (opal) templates, by first filling the voids of the opal with a metal oxide precursor, followed by hydrolysis and condensation reactions (sol-gel

chemistry) of the infiltrated precursor, and finally by removing the original opal template by calcination or wet chemical etching. The synthesis of metal oxide hollow spheres follows a similar mechanism, with the exception of using each individual PMMA colloidal sphere as a template for sol-gel coating, instead of infiltrating the PMMA colloidal crystals (opals).

The synergistic effects arising from the semiconducting properties of the metal oxide in combination with morphological enhancements of the inverse opals and hollow spheres, make them ideal candidates for use as photoelectrodes in photovoltaic devices[106, 150]. In particular, inverse opal and hollow sphere structures have been demonstrated to enhance electron transport and light trapping properties of such devices[106, 126, 188-190]. This is due both to an increase in the optical path length and also an enhancement in the multiscattering properties. These in turn are induced by highly accessible surfaces and relatively large pore sizes of these nanostructures[7, 191]. In addition, inverse opals provide an additional photonic band gap effect, which enhances the light-matter interactions by controlling the propagation of light[140, 191]. The ordered arrangement of the porous structure with a uniform repetition of low and high refractive index areas leads to diffraction of light in a manner similar to the diffraction observed with colloidal crystals[43] (Chapter 4).

For the synthesis of inverse opals *via* colloidal crystal templating using sol-gel infiltration, the choice of infiltration technique can play a critical role in the quality of the final structure. A common method of infiltration is dip coating[40, 192], where the colloidal crystal substrate is vertically immersed in the precursor solution and then withdrawn slowly. Using this method may cause overlayer at the surface as a result of excess precursor. The presence of an overlayer can

significantly reduce the opto-electronic properties of the inverse opal by diminishing the porosity of the structure. Sandwich capillary infiltration[9] is another technique which may reduce the amount of the overlayer on the inverse opal sample. In this infiltration technique, first the colloidal crystal substrate is covered by placing a glass cover slide on top of it and then clamping the two together. subsequently, the interstitial gaps of the colloidal crystal are filled with the sol-gel precursor as a result of the pressure difference and capillary forces. This infiltration technique can reduce overlayer on the surface of the inverse opal, however very clean substrates are needed and the choice of substrate may be limited. Vacuum assisted[5, 27] and horizontal[61, 193] sol-gel infiltration are two other methods to produce high quality inverse opals with minimum overlayers. These two methods will be used in this chapter to synthesise various 2D and 3D metal oxide inverse opals. They are facile and can yield high quality inverse opals. For the synthesis of 3D inverse opals, colloidal crystal templating using vacuum assisted sol-gel infiltration is a method of choice, as the application of suction through the 3D colloidal crystal template will assist the process by enhancing uniform infiltration throughout the 3D multilayered template. For the synthesis of 2D monolayer inverse opals, horizontal infiltration may be beneficial. In this method, the precursor is placed dropwise carefully on the edges of a thin colloidal crystal film. In this work, by modifying the precursor solution, synthesis of 2D monolayer inverse opals have been made possible *via* horizontal infiltration approach. The successful synthesis of the 2D metal oxide inverse opals are particularly important here, as they will be used as the building blocks for the preparation of hierarchical photoanode samples for water splitting and dye sensitised solar cell experiments in Chapters 6 and 7.

The chemical composition of the sol-gel precursor is another important factor in determining the quality of the final inverse opal product. For example, titanium tetra-isopropoxide ($TT^{i}P$) which is commonly used as the main precursor in the production of TiO_2 inverse opals should be handled with care. As this precursor is air/moisture sensitive (hydrolysing very fast), and hence makes it difficult to control the degree of infiltration. This is because premature condensation and cross-linking of the precursor clogs the voids of the colloidal crystal template at the surface[193]. Diluting the titanium alkoxide with ethanol can decrease its reactivity and also increase its penetration through the colloidal crystal template by improving the wetting properties of the sol-gel precursor. Ethanol can also be used to lower the viscosity of the sol-gel precursor[193], as extensive polymerisation of $TT^{i}P$ precursor prior to infiltration can increase viscosity and result in incomplete filling of the template[5]. Furthermore, addition of HCl[27] and/or trifluoroacetic acid[9] to this alkoxide precursor can decrease the rate of condensation in the sol-gel process, preventing premature TiO_2 precipitation upon exposure to air. The use of trifluoroacetic acid can also increase the precursor hydrophobicity, which can facilitate the infiltration process[9] by allowing more uniform wetting of the PMMA colloidal crystal template and giving greater control over the degree of infiltration throughout the entire structure[193]. In this work, for the synthesis of 3D TiO_2 inverse opals, the more conventional route of adding ethanol and HCl solvents to the $TT^{i}P$ precursor (with or without addition of water) has been used for improving infiltration and the quality of the final inverse opal structure. However, for the synthesis of 2D monolayer TiO_2 inverse opals, a modified precursor with the addition of trifluoroacetic acid to the $TT^{i}P$/ethanol/HCl has been employed. The

very thin layer of 2D monolayer PMMA colloidal crystal (~410 nm) is very delicate to perform the infiltration procedure on, without forming any unwanted overlayers. By adding this inorganic acid, the amount of precursor which is necessary to wet and infiltrate the interstitial gaps of the colloidal crystal could be reduced considerably. In this work, by only adding 4 drops of the modified precursor to the edges of the template using horizontal infiltration, with subsequent drying and calcination, homogenous, robust monolayer TiO_2 inverse opals have been produced.

For the synthesis of other metal oxide inverse opal systems including ZnO and iron oxide, similar sol gel infiltration routes has been carried out by using zinc acetate and iron nitrate as the main metal salt precursors in the sol-gel infiltration process. Additionally, hollow spheres of various metal oxides including TiO_2, SiO_2, ZnO and CuO has been successfully synthesised in this work using sol-gel coating. For TiO_2 and SiO_2 sphere coating, their metal alkoxides namely TT^iP and TEOS have been used in the sol-gel process respectively. For the other two metal oxide systems, ZnO and CuO, their metal acetates namely zinc acetate and copper acetate have been used as the main sol-gel precursors for coating respectively. For the latter two systems, by using only water and their metal acetate salts in the coating procedure, it has been possible to produce high quality hollow spheres after template removal through calcination. This novel sol-gel route is promising, as it is easy and fast and thus, may be applied for the synthesis of other metal oxide hollow sphere nanostructures.

The formation of sphere-in-sphere hollow spheres as another specifically designed nanoarchitecture gives superior properties compared with those of

simple hollow spheres, with respect to surface area enhancement and light scattering properties[194]. Previously the formation of such structures *via* a solution-based chemical technique, which uses carbonaceous microspheres as sacrificial templates has been reported[195, 196]. These techniques are limited by the resulting sphere-in-sphere structures consisting of only one species of metal oxide. Although this sphere-in-sphere synthesis technique was a breakthrough in the production of nanostructures with very high internal and external surface areas, it lacks versatility in the formation of heterostructured architectures. In this work, a novel synthesis technique combining seeded polymerisation processes with a templating approach has been used to synthesise hybrid sphere-in-sphere hollow spheres of different metal oxides. Figure 5.1 shows the schematic stages of sphere-in-sphere hollow sphere formation using the templating approach proposed in this work.

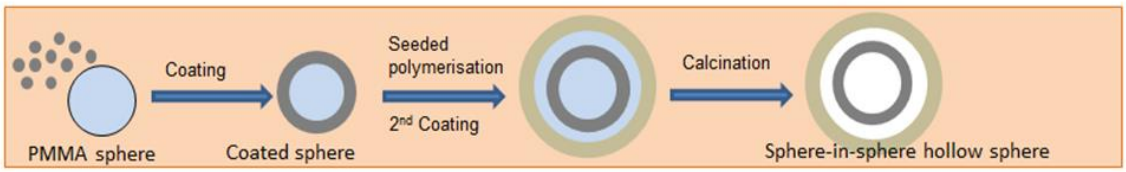

Figure. 5.1 Schematic showing the stages in the formation of sphere-in-sphere hollow sphere using template-directed synthesis.

As shown in Figure 5.1, the sphere-in-sphere procedure consists of three steps. PMMA spheres are initially coated by a metal oxide precursor through a sol-gel process. The coated spheres are then used as a seed in a SFEP process. The seeded polymerisation step is similar to that presented in Chapter 3 for the formation of large PMMA spheres, with the difference being that the seed is a coated PMMA sphere. After polymerisation, a PMMA shell covers the

outside of the coated sphere. This core-shell structure is further coated with another metal oxide precursor *via* a sol-gel process. After hydrolysation and condensation of the second sol-gel coating, the two PMMA layers are removed by chemical etching or calcination to form a sphere-in-sphere hollow sphere with two different metal oxide layers. This technique may be further extended to form multiple layers of metal oxide hetero-nanostructures leading to further opto-electronic enhancements.

5.3 Experimental Procedures

5.3.1 Synthesis of 3D Multilayer Titania (TiO_2) Inverse Opal *via* Colloidal Crystal Templating Using Vacuum Assisted Sol-Gel Infiltration

The procedure was adopted from an earlier work by Schroden et al[27]. In a 20 ml glass bottle, a mixture with the following composition was made by sequential addition of the following: ethanol (5.0 mL), HCl (1.0 ml), $TT^{i}P$ (5.0 ml) and water (2.0 ml). The mixture was stirred at ambient temperature for 2 hours. Following this, dried PMMA colloidal crystal (0.61 g, 414 nm spheres) previously prepared using a vertical deposition technique on a glass substrate were gently removed from the substrate using a metal spatula. In order to get the correct weight, some of the PMMA colloidal crystal strips that had fallen off the glass substrate into the bottom of the beaker during self-assembly were also collected (Chapter 4, Figure 4.6). The collected strips of colloidal crystal were placed onto a towel paper, and by using the back of a metal spatula were gently crushed into a

powder. Whilst applying vacuum through a Büchner funnel, a piece of filter paper was placed in the Büchner funnel. A few drops of absolute ethanol were added to the filter paper, in order to allow for better adhesion to the pores of the funnel. The powdered colloidal crystal was deposited as a 1 millimetre thick layer on the filter paper in the Büchner funnel using a metal spatula. This was done by spreading and lightly packing the powder, so it evenly covers the entire filter paper. Then an equal amount by mass of the TiO_2 precursor solution (0.61 g) was applied dropwise until the entire PMMA colloidal crystal template had been covered by capillary forces. The matching amount of precursor solution to that of the PMMA colloidal crystal template was to minimise the formation of overlayers on the pores once the inverse opal has been formed[5]. The suction was ceased after 30 minutes. The composite sample was allowed to dry (aged) at ambient conditions for 24 hours for complete hydrolysation and condensation of the sol-gel. Finally, the sample was transferred from the filter paper (by gently scraping the powder using a spatula) into a porcelain dish and calcined at 450˚C for 2 hours at ramping rate of 3˚C/min to remove the PMMA template. The sample was allowed to cool further to ambient temperature at a rate of 10˚C/min. The gradual and slow ramping rate was important to minimise the collapsing of the inverse opal pores during calcination and prevent incomplete removal of the template[121]. As sudden burning off of the PMMA template at lower temperatures (~160°C) and sudden crystal phase transition in the walls of the inverse opal at higher temperatures (~400°C) could result in structural collapse and also leave carboneous residues in the mesopores[120] of the inverse opal walls. For the temperature-dependent experiment, the inverse opal produced was divided equally into six samples. Five of the six samples

underwent further calcination (550, 650, 750, 850 and 950°C). Figure 5.2 shows the schematic of the preparation of inverse opal *via* vacuum assisted colloidal crystal templating.

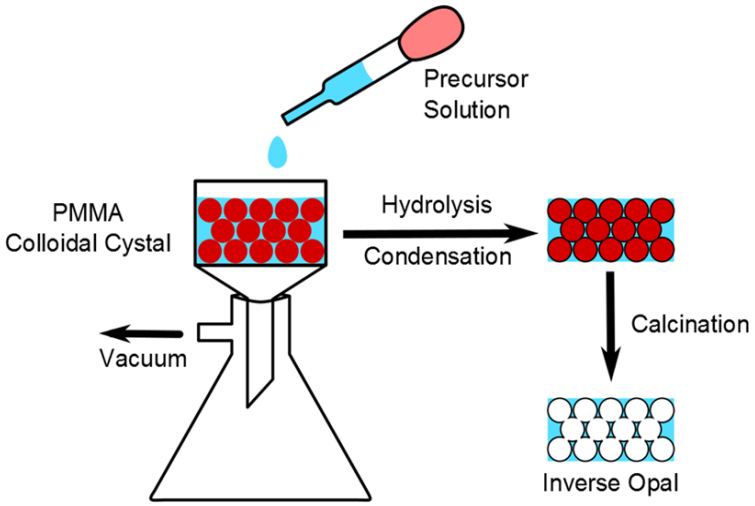

Figure. 5.2 A schematic showing the inverse opal synthesis *via* vacuum assisted colloidal crystal templating.

5.3.2 Synthesis of 3D Multilayer (Titania and Iron Oxide) & 2D Monolayer (Titania and Zinc Oxide) Inverse Opals *via* Colloidal Crystal Templating Using Horizontal Sol-Gel Infiltration

For the synthesis of 3D multilayer titania inverse opal, previously produced 3D PMMA colloidal crystal films (deposited on a glass substrate *via* the vertical deposition technique using 414 nm spheres) were used as the initial template. A TiO_2 precursor was prepared by mixing TT^iP (5.0 ml) and ethanol (5.0 ml) while stirring for 2 hours. The mixture was then diluted 10-fold with absolute ethanol to achieve a final concentration of 5 vol%. The PMMA colloidal crystal template was sintered at 85°C for 1 hour, in order to increase the film mechanical

strength and enhance capillary interactions. This occurs due to the temperature difference between the colloidal crystal and the precursor solution, which enhances capillary uptake of the precursor solution. The substrate was then placed horizontally. Using a pipette, a few drops of the diluted precursor were added dropwise at the edges of the colloidal crystal template. The precursor covered the template's interstitial gaps by capillary forces. After precursor infiltration, the sample was left to dry and age for 24 hour at ambient conditions. The substrate was calcined at 450˚C for 2 hour, at a ramping rate of 3˚C/min, in order to remove the template. Following calcination the sample was allowed to cool to ambient temperature at a rate of 10˚C/min. For the synthesis of 3D multilayer iron oxide inverse opals, the same procedure was carried out with a modified precursor. The precursor was changed to a mixture of iron nitrate (1 g), water (3 ml) and ethanol (3 ml).

For the synthesis of 2D monolayer zinc oxide inverse opal, previously produced 2D monolayer PMMA colloidal crystal deposited on a titanium (Ti) substrate *via* the floating technique (using 414 nm spheres) was used as the template. The ZnO precursor was prepared by adding zinc acetate (0.066 g) to a mixture of water (3 ml) and ethanol (3 ml) while being stirred for 2 hours to form a 0.05 M zinc acetate solution. Using a pipette, four drops of the precursor were added to the edges of the colloidal crystal template. The precursor was allowed to infiltrate the template interstitial gaps by capillary forces. The sample was then left to dry and age for 24 hours under ambient conditions before calcining at 450°C, with a ramping rate of 2°C/min, for 2 hours. The sample was then cooled to ambient temperature at a rate of 10°C/min.

In order to prepare the 2D monolayer titania inverse opal, the same procedure was carried out on a glass substrate with a modified precursor. The TiO_2 precursor was prepared according to an optimised version of a literature method[9] to suit this experiment. TT^iP (0.1ml) was added to a mixture of trifluoroacetic acid (0.08 ml) and HCl (0.02 ml) during vigorous stirring. After 30 minutes, ethanol (6.8 ml) was added to the mixture, forming a 0.05M TT^iP solution. The solution was then stirred for another 2 hours before deposition.

5.3.3 Production of Various Metal Oxide Hollow Spheres *via* Template-Directed Synthesis Using Sol-Gel Coating

5.3.3.1 Synthesis of Titania (TiO_2) Hollow Spheres

The procedure to make the TiO_2 sol-gel precursor was adapted from that of Kalele et al.[197], who used a sol-gel coating procedure to create silica-titania core-shell structures. Dried PMMA spheres (0.1 g) made previously using the SFEP process (sphere diameter 414 nm) were dispersed in ethanol (15 ml) using ultrasonic treatment for 6 hours. TT^iP and water at a volume ratio 0.04 : 0.1 ml TT^iP : water were added to the PMMA sphere suspension. The mixture was then stirred by a magnetic stirrer bar for 4 hours. After this period it was assumed that all TT^iP had been hydrolysed and condensed on the surface of the PMMA spheres. The solution was then centrifuged at 5000 rpm for 30 minutes. The top solvent layer was decanted off. The remaining white solid was dried in an oven at 40°C for 1 hour. The sample was then thoroughly washed with ethanol by centrifugation three times. This washing procedure was to ensure that all of the excess precursor material and other impurities were

removed. The sample was then calcined at 450°C for 2 hours with a ramping rate of 3°C/min in order to remove the PMMA sphere templates before being allowed to cool at a rate of 10°C/min.

In order to carry out TEM imaging, a small portion of the sample was removed from the substrate following calcination. The powder sample obtained was then suspended in ethanol (20 ml). A 5 µl drop of this suspension was deposited on a carbon film supported by a 3 mm copper grid and dried before use.

5.3.3.2 Synthesis of Silica (SiO_2) Hollow Spheres

The procedure to make the SiO_2 sol-gel precursor was a modified version of the Stober technique[21]. Dried PMMA spheres (0.1 g) made previously by the SFEP process (sphere diameter 286 nm) were dispersed in ethanol (15ml) using ultrasonic agitation for 6 hours. Following this, ammonia (0.75 ml) and water (3 ml) were added to the mixture and stirred using a magnetic stirrer bar for 30 minutes. TEOS (1.2 ml) was then added. The solution was mixed for another 4 hours before drying and ageing in an oven at 40°C for 12 hours. This allowed the TEOS to hydrolyse and condense. The sample was then washed thoroughly with ethanol through centrifugation three times in order to remove impurities. Following this, the solid was calcined at 450°C for 2 hours with a ramping rate of 3°C/min to remove the PMMA sphere templates. It was then allowed to cool at a rate of 10°C/min.

5.3.3.3 Synthesis of Zinc Oxide and Copper Oxide Hollow Spheres

In order to produce the zinc oxide sol-gel precursor, zinc acetate (0.01 g) was dissolved in deionised (DI) water (14 ml) to yield a zinc acetate (3 mM) solution. Similarly, for the copper oxide precursor, 3 mM solution of its metal salt in the form of copper acetate, was produced by dissolving in DI water (14 ml).

1 ml of PMMA sphere solution (corresponding to 0.095 g/ml of PMMA spheres) produced by the SFEP process (sphere diameter 414 nm) was added to each of the metal oxide precursor solutions. Each solution was then dispersed ultrasonically for 1 hour. The solutions were gravitationally filtered and washed thoroughly with ethanol and water. The purified solid samples were then dispersed in DI water. Five drops of each sample solution were placed on two separate clean glass slide substrates. The deposited substrates were left to dry in an oven at 40˚C for 1 hour. The samples were then calcined at 450˚C for 2 hour at ramping rate of 3˚C/min to remove the PMMA sphere templates. Following calcination, the samples were cooled to ambient temperature at a rate of 10˚C/min.

5.3.4 Synthesis of SiO_2/TiO_2 Sphere-in-Sphere Hollow Spheres *via* Seeded Polymerisation and Template-Directed Synthesis

For the synthesis of SiO_2/TiO_2 sphere-in-sphere hollow spheres, previously made SiO_2 coated spheres (0.05 g) prior calcination were used as the seed in a typical SFEP process using MMA monomer solution (6ml, 1.48 M) and initiator (0.035 g) as described in Chapter 3. The seeded polymer solution was centrifuged at 5000 rpm for 30 minutes. After centrifugation, the top layer of

solvent was decanted to yield a white solid. The semi-dried product (0.1 g) was dispersed in ethanol (15 ml) and mixed ultrasonically for 3 hours. $TT^{i}P$ (0.04 ml) and water (0.1 ml) were added to the mixture. The solution was then stirred using a magnetic stirrer bar for 4 hours before five drops of the solution were placed horizontally onto a clean glass slide. The deposited substrate was then dried in an oven at 40˚C for 1 hour. To remove the layers of PMMA formed between the two metal oxide coatings, the sample was calcined at 450°C for 2 hours at a ramping rate of 3˚C/min. Following calcination the sample was allowed to cool to ambient temperature at a rate of 10°C/min.

5.4 Results and Discussion

5.4.1 Temperature Dependent Study of 3D TiO_2 Inverse Opals Synthesised by Colloidal Crystal Templating Using Vacuum Assisted Sol-Gel Infiltration

The SEM image of a 3D TiO_2 inverse opal synthesised by colloidal crystal templating using vacuum assisted sol-gel infiltration using a PMMA template removal temperature of 650°C is shown in Figure 5.3. An ordered 3D inverse opal structure comprising of possibly FCC arrays of air sphere in TiO_2 can be observed in this image. The air spheres with an average diameter of 204 nm are the outline of the original PMMA colloidal spheres and the walls with an average thickness of 51 nm are the replica of the interstitial gaps in the original PMMA colloidal crystal, which are now infiltrated by TiO_2. The small holes (windows[5]) indicate the position of the air spheres in the underlying layer of the inverse opal connecting each air sphere to its nearest neighbours.

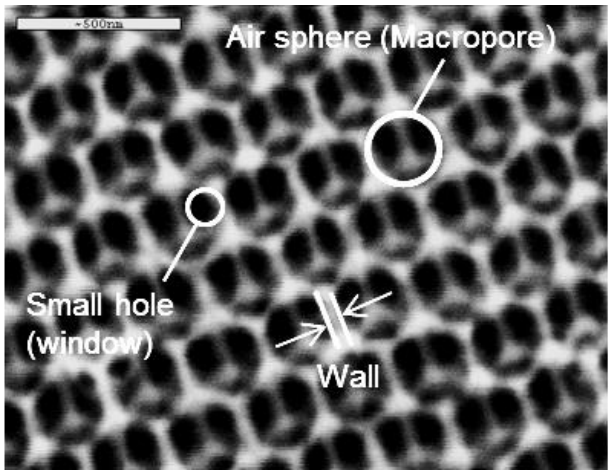

Figure. 5.3 SEM image of 3D TiO_2 inverse opal synthesised by vacuum assisted sol-gel infiltration templating at calcination temperature of 650°C. Average air sphere diameter and wall thickness are 204 nm and 51 nm respectively. The underlying substrate is a glass slide. Scale bar: 500nm.

The formation of a TiO_2 solid structure between the interstitial gaps of the PMMA colloidal crystal involves the process of sol-gel chemistry. The main precursor in the synthesis of TiO_2 inverse opals in this work is TT^iP ($Ti(OC_3H_7)_4$), which is an alkoxide of titanium (*IV*).

In a sol-gel process, network solids of TiO_2 are formed by the reactions of hydrolysis and condensation. In the hydrolysis step, TT^iP reacts with water (including air moisture), resulting in the replacement of an alkoxy group by a hydroxyl group and then the condensation of the hydrolysed $Ti(OH)_4$ occurs which leads to the growth of the polymeric TiO_2 network. As the growth process continues, a sol of small chains or branched structures forms. These chains continue to grow until they eventually gel to form a continuous solid network, at which point the network changes from liquid to solid. The reactions leading to the formation of the TiO_2 polymeric network solid are as follows[16]:

$Ti(OC_3H_7)_4 + 4H_2O \rightarrow Ti(OH)_4 + 4C_3H_7OH$ (hydrolysis)

$Ti(OH)_4 + Ti(OH)_4 \rightarrow 2TiO_2 + 4H_2O$ (condensation of water)

$Ti(OH)_4 + Ti(OC_3H_7)_4 \rightarrow 2TiO_2 + 4C_3H_7OH$ (condensation of i-propanol)

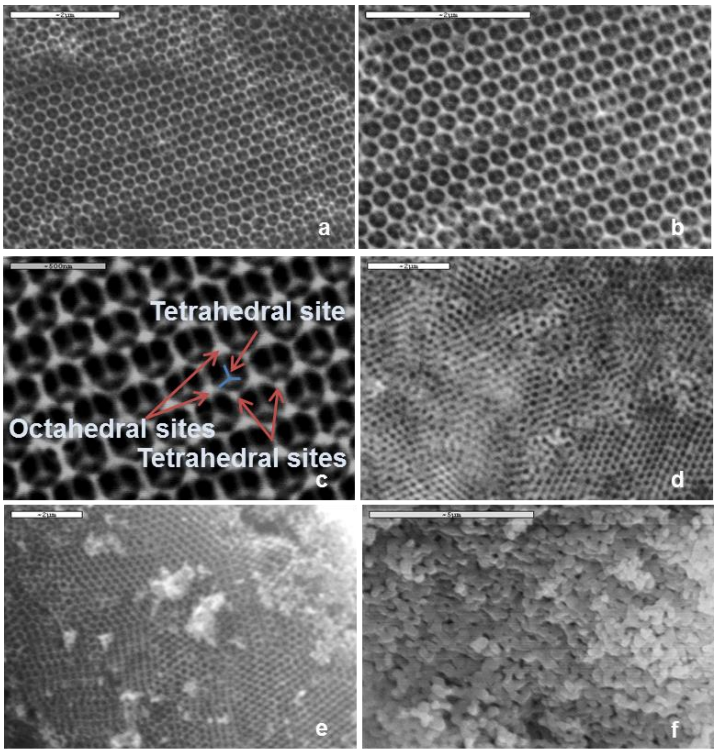

Figure. 5.4 SEM images of 3D TiO_2 inverse opals produced by vacuum assisted sol-gel infiltration templating at different calcination temperatures; (a) 450, (b) 550 (c) 650, (d) 750, (e) 850 and (f) 950°C. The interconnected tetrahedral and octahedral sites are shown in image (c) corresponding to the 650°C sample. Glass slide is used as substrate for all the samples. Scale bars: (a),(b),(d),(e): 2µm, (c) 500nm and (f) 5µm.

The sol-gel process is complete upon removal of the water molecules, the hydroxyl and alkoxy groups still attached to the TiO_2 by calcination, leaving pure TiO_2 metal oxide material. Therefore, the calcination process in the synthesis of TiO_2 inverse opals is not only performed to remove the PMMA

colloidal crystal temples, but it is also necessary to complete the reaction of the alkoxides to solid TiO_2. As one study reported, the Raman spectra of the infiltrated but not yet calcined colloidal crystals revealed complicated spectra that were very different from any known polymorph of TiO_2. It was considered that in this stage, the solid was a complex conglomerate that contained many hydroxyl and alkoxy groups[183].

Figure 5.4 shows the SEM images of 3D TiO_2 inverse opals produced by colloidal crystal templating using vacuum assisted sol-gel infiltration approach at different calcination temperatures between 450°C and 950°C.

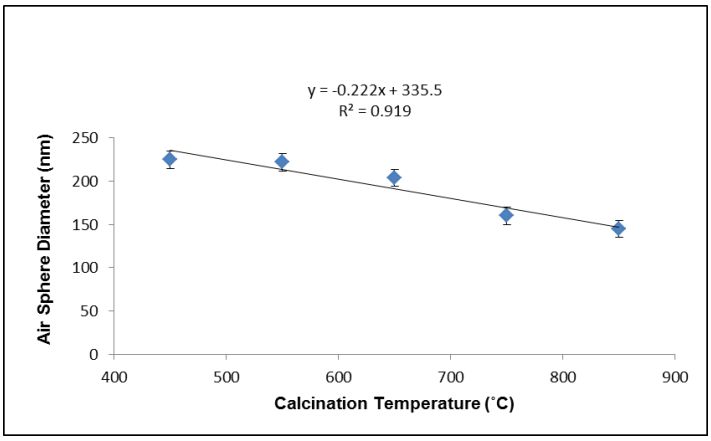

Figure. 5.5 3D TiO_2 inverse opal air sphere diameter as a function of calcination temperature.

The plot of the average diameter of the air spheres (macropores) inside each 3D TiO_2 inverse opal sample as a function of increasing calcination temperature is shown in Figure 5.5. The average diameter of the original PMMA spheres is 383 nm. The average diameter of the air sphere in the 3D TiO_2 inverse opal produced at 450°C is 225 nm. Therefore a large reduction in the diameter can be detected, which reduces linearly by increasing the calcination

temperature to an average value of 145 nm at 850°C. When the calcination temperature reaches 950°C, a complete loss of porosity in the inverse opal morphology occurs, as can be seen in the SEM image of Figure 5.4(f). On the other hand, the TiO_2 wall thickness increases linearly by increasing the calcination temperature as shown in Figure 5.6.

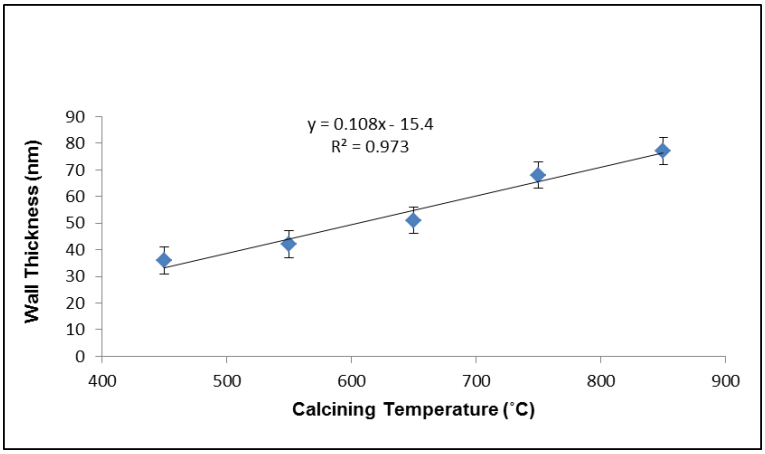

Figure. 5.6 3D TiO_2 wall thickness as a function of calcination temperature

From the plot, it can be seen that at the calcination temperature of 450°C, the inverse opal wall has an average thickness of 36 nm which increases linearly to an average value of 77 nm at 850°C. This behaviour indicates that the interconnected TiO_2 wall network in the inverse opal swells with increasing calcination temperature and may be the reason for the reduction of porosity (air sphere diameter) as a function of calcination temperature. The swelling phenomenon can be explained in terms of TiO_2 crystal growth in the walls of the inverse opal. Prior to calcination, the walls of the TiO_2 inverse opal are amorphous and convert to a crystalline phase at 450°C. The XRD patterns for the TiO_2 inverse opal at different calcination temperatures from 450 to 950°C are presented in Figure 5.7. At lower temperatures, no XRD patterns are obtained confirming that the inverse opal is in its amorphous phase.

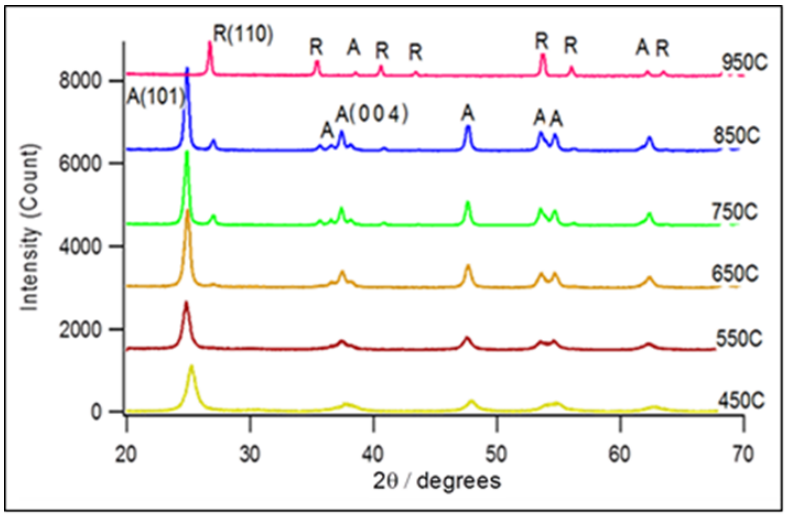

Figure. 5.7 XRD spectra of 3D TiO_2 inverse opals calcined at different temperatures ranging from 450 to 950°C (A=anatase and R=rutile). The indicated anatase (A) peaks are positioned at 24.98°(101), 36.61°(103), 37.39°(004), 38.25°(112), 47.67°(200), 53.53°(105), 54.78°(211) and 62.42°(118). The indicated rutile (R) peaks are positioned at 26.94°(110), 35.61°(101), 40.74°(111), 43.60°(210), 53.84°(211), 56.16°(220) and 63.56°(310).

In Figure 5.7, the XRD diffraction peaks indicated by the 'A' can be indexed to anatase TiO_2 (JCPDS card no. 841286) with peaks of (101), (103), (004), (112), (200), (105), (211) and (118) planes at the corresponding 2θ values of 24.98°, 36.61°, 37.39°, 38.25°, 47.67°, 53.53°, 54.78° and 62.42°. Those marked by 'R' are assigned to the rutile phase of TiO_2 (JCPDS card no. 881175) with peaks of (110), (101), (111), (210), (211), (220) and (310) planes at the corresponding 2θ values of 26.94°, 35.61°, 40.74°, 43.60°, 53.84°, 56.16° and 63.56°. From XRD measurements, a gradual conversion in crystallinity phase of the TiO_2 network from anatase to rutile can be observed as the calcination temperature increases from 450 to 950°C. Up to 650°C all the

diffraction peaks correspond to anatase (marked ‘A’ in Figure 5.7). Above this temperature diffraction peaks from the rutile phase gradually appear (marked ‘R’ in Figure 5.7), indicating phase transformation. The characteristic peak of anatase with the highest intensity is the 101 plane. For rutile, this is the 110 plane. As the calcination temperature increases from 450 to 850°C, those peaks associated with anatase phase TiO_2 become sharper, indicating that the higher calcination temperature promotes high crystallinity of anatase. Similarly, sharper and more intense rutile peaks can be detected as the calcination temperature increases from 650 to 950°C, indicating high rutile crystallinity. At the calcination temperature of 950°C, most of the anatase peaks transform to rutile, showing that at high temperatures, rutile is the stable crystal phase of TiO_2. Usually, phase transformation is accompanied with crystal growth[198]. The XRD patterns in Figure 5.7 show that by increasing the calcination temperature, the diffraction peaks corresponding to both the anatase and rutile phase become narrower, which indicates the increase of TiO_2 crystallite size in the walls of the TiO_2 inverse opal. The average crystallite sizes can be calculated using the Debye-Scherrer formula (Chapter 2). Figure 5.8 is a plot of TiO_2 crystallite size as a function of calcination temperature for the 004 (anatase) and 110 (rutile) diffraction planes. The size of the TiO_2 crystallites perpendicular to both the (004) and (110) diffraction planes in the TiO_2 inverse opal increase with increasing the calcination temperature. An increase from 16.4 to 26.6 nm for the (004) anatase and 20.7 to 52 nm for the (110) rutile diffraction planes is observed when the temperature is increased from 450 to 950°C.

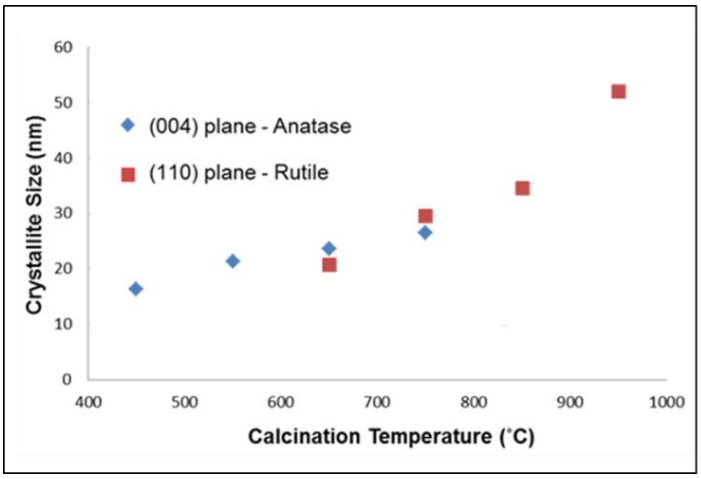

Figure. 5.8 TiO_2 Debye-Scherrer crystallite size as a function of calcination temperature for the anatase (004) and rutile (110) diffraction planes.

From this XRD study, it is possible to conclude that the increase in TiO_2 wall thickness as a function of calcination temperature is due to the growth of TiO_2 crystallites in the inverse opal walls, which leads to the reduction of size of the air spheres in the inverse opal. The XRD results obtained here with regards to the effect of calcination temperature on the crystallinity and phase transformation of TiO_2 inverse opals are consistent with previous studies carried out elsewhere namely on TiO_2 hollow spheres[7] and TiO_2 powders (P25)[198]. By looking at the SEM images in Figure 5.4, the skeletal structure of the inverse opal is well preserved at calcination temperatures of 450 to 650°C (Figure 5.4(a) to (c)). At temperatures above 650°C (Figure 5.4(d) to (f)), the porosity is gradually lost due to the rapid growth of the fused crystalline grains. When the temperature reaches 950°C, a complete loss of inverse opal morphology occurs. The growth of crystalline grains is possibly due to the increase in size of the TiO_2 crystallites nucleating to form the TiO_2 grains in walls of the inverse opal.

In terms of the morphological quality of the TiO_2 inverse opals produced at different calcination temperatures, the skeletal structure of the inverse opal is well preserved at calcination temperatures of 450 to 650°C as shown in the SEM images in Figure 5.4. This results in three dimensional ordered macroporous structures with interconnected tetrahedral and octahedral sites, which were previously air gaps in the original PMMA colloidal crystal template (Figure 5.4(c)). As the calcination temperature increases, a more significant volume loss may occur due to the loss of solvent content in the precursor as reported in other studies[151, 152]. As a result, the skeleton of the inverse opal may become less curved and may be considered as a skeleton of nodes connected by rod-like TiO_2 walls in the octahedral and tetrahedral holes[199, 200] of the original PMMA colloidal crystal template. From the SEM images in Figure 5.4, it is clear that the best optimisation of the skeleton occurs at 650°C.

5.4.2 3D Inverse Opals Syntheised *via* Colloidal Crystal Templating Using Horizontal Sol-Gel Infiltration

Figure 5.9 shows SEM images and EDX spectra of (a) 3D iron oxide and (b) 3D TiO_2 inverse opals produced by colloidal crystal templating using horizontal sol-gel infiltration approach on glass substrates at a calcination temperature of 450°C. The original 3D PMMA colloidal crystal templates were produced by a vertical deposition technique on the glass substrate. The quality of these 3D inverse opals is similar to the inverse opals synthesised by the vacuum assisted templating approach, described before in Section 5.4.1. Some reduction in the size of the air spheres (macropores) can also be observed. In both types of

inverse opals, an average air sphere diameter of 280 nm and an average wall thickness of 70 nm are observed. The average air sphere is less than the average diameter of the original PMMA sphere template (383 nm). The result of successful 3D inverse opal manufacturing is observed in both samples. The skeletal structures of the inverse opals are well preserved, which results in 3D porous structures with interconnected tetrahedral and octahedral sites (previously air gaps in the PMMA colloidal crystals).

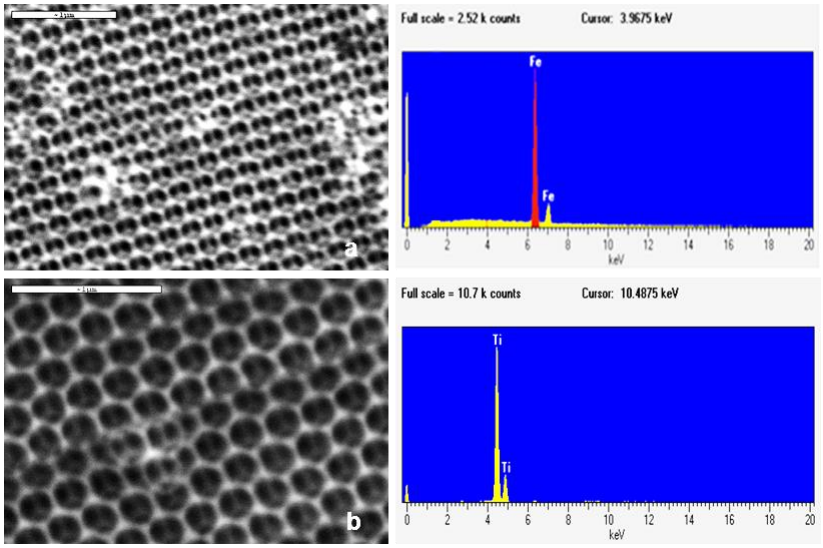

Figure. 5.9 (a) 3D iron oxide and (b) 3D TiO_2 inverse opals synthesised by colloidal crystal templating using horizontal sol-gel infiltration on glass substrates at calcination temperature of 450°C: SEM images (scale bars: 1µm) and EDX spectra.

The EDX spectra in Figure 5.9 shows that the 3D TiO_2 and iron oxide inverse opal networks consist of the Fe and Ti elements respectively. The inverse opal structure in both samples covers a relatively large area of the substrate, with few cracks and grain boundaries. The horizontal templating approach is easier and less time consuming than the more established vacuum

assisted approach in the synthesis of 3D metal oxide inverse opals and may be considered the method of choice for such systems. Although, more studies should be carried out to systematically analyse the quality of the samples made by this approach, in particular to see whether the precursor is penetrated evenly through the original 3D colloidal crystal template in the infiltration stage.

5.4.3 2D Metal Oxide Inverse Opals Syntheised *via* Colloidal Crystal Templating Using Horizontal Sol-Gel Infiltration

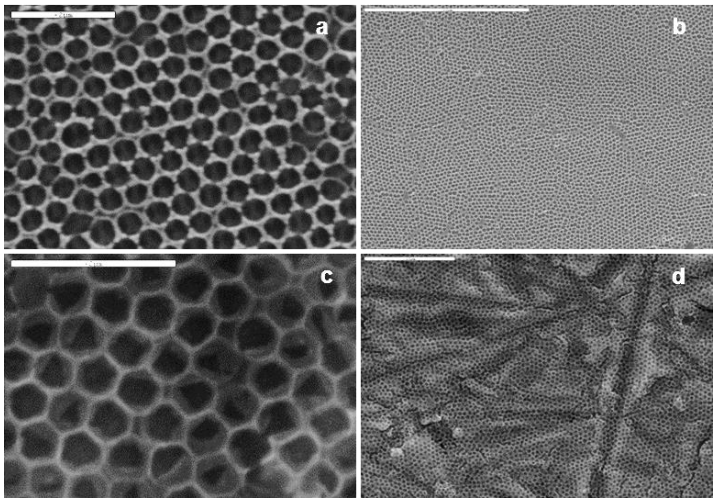

Figure. 5.10 SEM images of 2D monolayer ZnO (a, b) and TiO_2 (c, d) inverse opals produced *via* colloidal crystal templating using horizontal sol-gel infiltration at a calcination temperature of 450°C. The substrate for ZnO inverse opal is Ti and for TiO_2 inverse opal is a glass slide. Scale bars: (a),(c): 2μm and (b),(d): 20μm.

Figure 5.10 shows the SEM images for 2D monolayer inverse opals of ZnO (Figure 5.10(a and b)) and TiO_2 (Figure 5.10(c and d)). Firstly, a modified floating technique was used to produce monolayer PMMA colloidal crystals on

two different substrates; Ti (for ZnO sample) and glass (for TiO_2 sample). Horizontal sol-gel infiltration was subsequently employed to produce the 2D monolayer inverse opals. The monolayer PMMA colloidal crystals were removed by calcination at 450°C. The choice of substrate has no effect on the quality of the monolayer inverse opal samples produced.

The SEM images in Figure 5.10 portray the 2D nature of the structures. There is no underlying layer, connected by small holes, which was present in the 3D inverse opals. These holes indicate the position of the air spheres in the underlying layer and therefore are only present in the 3D inverse opals. In the 2D inverse opals, the average diameter of air spheres (macropores) is 410±6 nm and does not show a large variation in size from the original PMMA sphere (about 414 nm). The wall thickness is 85±10 nm and 70±10 nm for ZnO and TiO_2 respectively. The template removal and metal oxide wall crystallite growth stages (during calcination at 450°C) do not contribute to air sphere size reduction as observed in the 3D systems (Sections 5.4.1 and 5.4.2). This occurrence can be assigned to the more flexible structure of 3D inverse opals, which is in turn due to their 3D interconnectivity. In contrast, the 2D inverse opal is more rigid due its 2D monolayer framework, which is in contact to the substrate. The contractions caused by template removal and increase in wall thickness due to crystallite growth can lead to a contraction in the flexible inverted framework of the 3D inverse opal (a sponge-like behaviour). The more rigid 2D inverse opal remains structurally intact. The SEM images show that these macroporous structures are periodically ordered. Each macropore is surrounded by six equal macropores. The ordered macropores are connected to each other by ZnO (Figure 5.10(a, b)) and TiO_2 (Figure 5.10(c, d)) walls.

The low magnification SEM images in Figure 5.10(b and d) show that both inverse opals cover large areas with some defects and grain boundaries. 2D inverse opals seem to show better coverage than the 3D inverse opals. This may be due to their more rigid framework, which may reduce cracks and grain boundaries. The presence of large areas of ordered porous film is promising. The production of hierarchical heterostructures using different metal oxide inverse opal layers using this technique may lead to structures with enhanced photovoltaic properties. The synthesis of bilayered inverse opals and their applications in photovoltaics will be discussed in the next two chapters (Chapters 6 and 7).

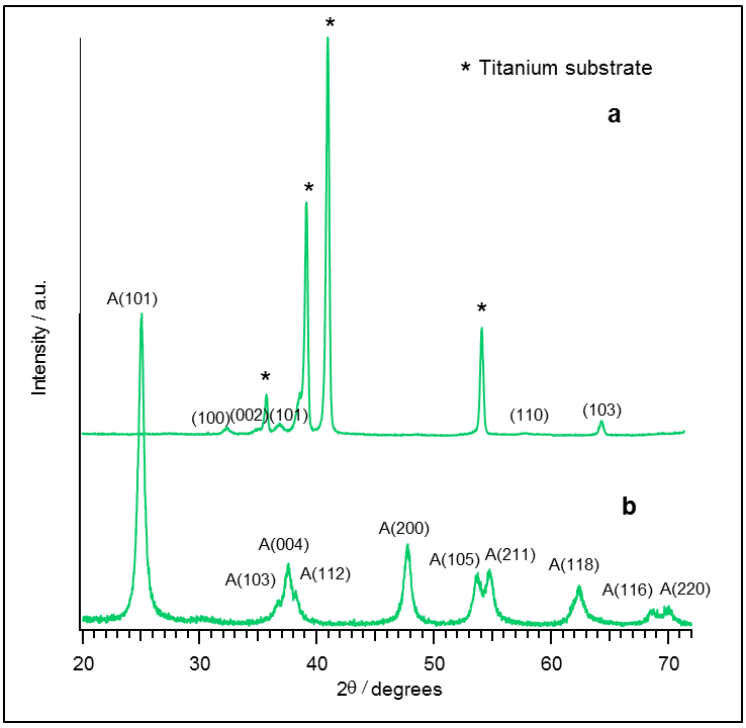

Figure. 5.11 XRD spectra for 2D monolayer inverse opals of (a) ZnO on Ti and (b) TiO_2 on glass. The peaks labelled with (*) correspond to the underlying Ti substrate (5.11(a)).

The XRD spectra of both 2D monolayer ZnO and TiO_2 inverse opals are shown in Figure 5.11. The peaks in the XRD pattern corresponding to the monolayer ZnO inverse opal deposited on Ti substrate (5.11(a)) can be readily indexed to the hexagonal wurtzite phase of ZnO according to the JCPDS card number 01-075-1526. The XRD peaks corresponding to the monolayer TiO_2 inverse opal deposited on a glass substrate (5.11(b)) are assigned to anatase TiO_2 according to the JCPDS card number 841286 with a tetragonal crystal system. The XRD spectra confirm that the interconnected walls of the monolayer inverse opals consist of either pure crystalline ZnO (Figure 5.11(a)) or TiO_2 (Figure 5.11 (b)), produced at a calcination temperature of 450°C. The peaks that are labelled with stars (*) correspond to the underlying Ti substrate (Figure 5.11(a)).

As mentioned previously, the wall thickness of the 2D ZnO and TiO_2 inverse opals measured from the SEM images in Figure 5.10 are 85±10 nm and 70±10 nm respectively. As the synthetic conditions used in the preparation of both samples were similar (using 0.05 M of precursor solutions and 414 nm PMMA spheres for the colloidal crystal templates), therefore the reason behind this difference in the wall thickness of these two monolayer inverse opal structures may lie in their crystal structures and defects densities. Figure 5.12 shows the stick-and-ball representation of the unit cell crystal structures of (a) anatase, (b) rutile phases of crystalline TiO_2 and (c) hexagonal wurtzite phase of ZnO.

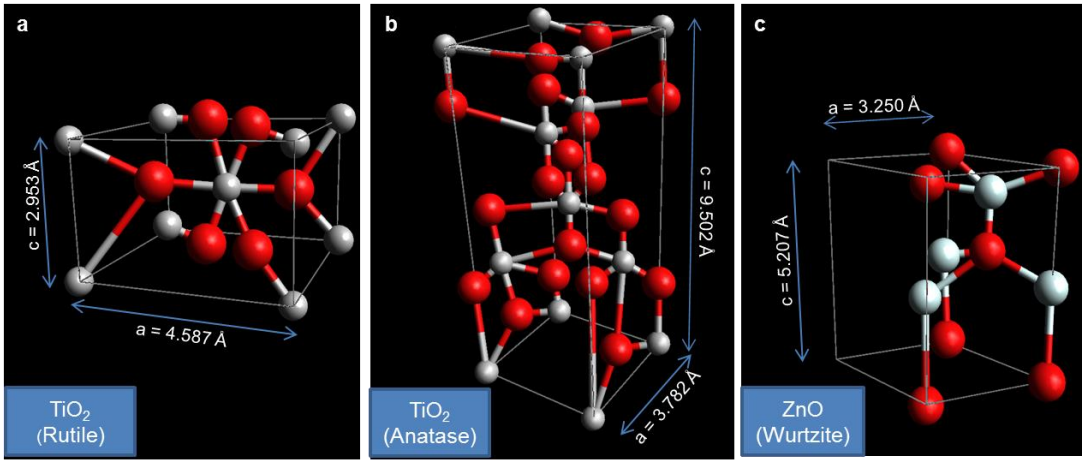

Figure. 5.12 Crystal structures of (a) rutile[201], (b) anatase[201] and (c) wurtzite[202]. The red balls correspond to oxygen atoms in all three structures. The grey balls in (a) and (b) correspond to Ti atoms and the white balls in (c) to Zn (Avogadro software was used to draw the crystal structures).

The XRD spectra in Figure 5.11 confirmed that the crystal structures of 2D TiO_2 and ZnO belonged to pure anatase (no rutile peak detected) and wurtzite phases respectively. From Figure 5.12, it is clear that the lattice parameter dimensions in anatase TiO_2 is larger than that of wurtzite ZnO; the lattice parameters of a = b = 3.782 Å and c = 9.502 Å for anatase[201] compare to a = b = 3.250 Å and c = 5.207 Å for wurtzite[202] can confirm this mismatch. Anatase has a tetragonal structure with the two lattice parameters in the ratio of c/a = 2.51 and coordinates 6 atoms per unit cell as can be seen in Figure 5.12(b). The TiO_6 octahedron is slightly distorted (rutile has also a tetragonal structure with the lattice parameters in the ratio of c/a = 0.644, but with a slightly smaller distortion of the TiO_6 octahedron than anatase) with a space group of D_{4h}^{19} in the Schoenflies notation and *$I4_1/amd$* in the Hermann-Mauguin notation (the space group of rutile in Schoenflies and Herman-Mauguin notations are D_{4h}^{14}

and $P4_2/mnm$ respectively)[203]. The weight density of the anatase crystal structure is 3.79 gcm^{-3} (the density of rutile is higher at 4.13 gcm^{-3})[201].

The wurtzite crystal structure on the other hand, has a hexagonal unit cell with the two lattice parameters in the ratio of $c/a = (8/3)^{1/2} = 1.633$ (in an ideal wurtzite structure). The wurtzite structure is composed of two interpenetrating hexagonal close packed (HCP) sublattices, each of which consists of one type of atom, either Zn or O displaced with respect to each other along the threefold c-axis by the amount of u = 3/8 = 0.375 (in an ideal wurtzite structure). The atoms in wurtzite ZnO structure are tetrahedrally coordinated in the unit cell, with every atom of Zn tetrahedrally coordinated with four atoms of O and vice versa (Figure 5.12(c)). Because of this tetrahedral coordination of wurtzite ZnO structure, the 4 nearest neighbours and 12-next nearest neighbours have the same bond distance in the crystal structure. Wurtzite structure belongs to the space group C_{6v}^4 in the Schoenflies notation and $P6_3mc$ in the Hermann-Mauguin notation and has a weight density of 5.606 gcm^{-3}.[202]

The larger unit cell and smaller density of anatase would suggest that, the walls of 2D anatase TiO_2 inverse opal should be thicker than that of 2D wurtzite ZnO inverse opal, if the same molar of metal ions were used for the inverse opal. However this is contradictory to our experimental observations (70 and 85 nm wall thicknesses for anatase and ZnO respectively).

Alternatively, the wall thickness could also be determined by the crystallinity and defect. With increase in the annealing temperature, the crystallites in both anatase and wurtzite grow in size as a consequence of reduction in the volume fractions of their grain boundaries[204]. Our XRD

diffraction in Figure 5.11 shows that the anatase diffraction peaks are in general broader than the peaks from ZnO. Using the Debye-Scherrer equation, the average crystallite sizes were calculated for anatase (23.0 nm) and ZnO wurtzite (32.4 nm). The smaller crystal size in anatase suggests the wall of the inverse opal would have smaller voids between crystal domains which will result in a thinner wall. On the other hand, the ZnO inverse opal has large crystal size and could leave large gaps between the crystal domain boundaries, which will lead to a thicker wall.

For preparing both inverse opals, the calcination conditions are identical (at 450°C for 2 hours). Thus the difference in the crystal size is related to the crystallisation kinetic behaviour, determined by the rate of hydrolysation and condensation of the sol-gel precursor solutions. $TT^{i}P$ is more water sensitive (hydrolyses faster) than zinc acetate. Therefore titanium hydroxide nanoparticles were formed in the sol-gel solution before applying to the colloidal crystal template. Such nanoparticles will limit the mass transportation during the calcination process in order to form large crystal domains. As a result, a more compact wall is formed in the inverse opal after calcination.

5.4.4 2D Monolayer Shell-Like Inverse Opals Produced by Colloidal Crystal Templating Using Horizontal Sol-Gel Infiltration

An interesting morphology is observed when the original 2D monolayer PMMA colloidal crystal template is not self-assembled entirely successfully. The PMMA spheres are not close-packed and form aggregates on the substrate. This behaviour occurs when the substrate is not hydrophilic enough (e.g. in the case

of glass substrates, when they are not cleaned thoroughly (Chapter 4) or at the regions of the substrate where PMMA sphere concentration is too low (concentration gradient behaviour). By infiltrating such a template with a metal oxide precursor and subsequently removing the template by calcination, a unique shell-like inverted metal oxide structure is produced, which is very similar in shape and morphology to its parent PMMA template (Figure 5.13).

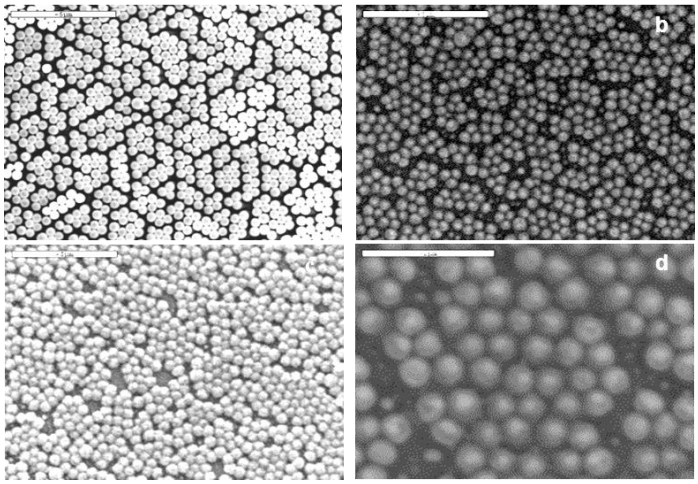

Figure. 5.13 SEM images of monolayer (a) non close-packed PMMA colloidal crystal template and (b, c, d) inverted shell-like ZnO nanostructure (shell-like inverse opal) on a glass substrate at calcination temperature of 450°C. Scale bars: (a),(b) and (c) 5μm and (d) 2μm.

The SEM image in Figure 5.13(a) illustrates a non close-packed PMMA colloidal crystal template. The SEM images in Figure 5.13(b, c and d) show a ZnO inverted structure with shell-like morphology, which resembles the original template, on a glass substrate (SEM images taken at different areas of the same sample). The monolayer shell-like ZnO inverse opal is produced after the template is infiltrated by the ZnO sol-gel precursor using horizontal infiltration. The procedure and the precursor composition used is identical to that used to

make monolayer ZnO inverse opals. After complete hydrolysation and condensation of the sol-gel, and subsequent calcination at 450°C to remove the PMMA template, the shell-like structure is formed on the glass substrate.

The formation of the shell-like structure is due to the large gap between the original PMMA spheres and the infiltrated ZnO precursor solution which is not sufficient to fill the gaps, meanwhile, the capillary forces between the PMMA spheres and the substrate attract the solution towards the spheres and form a shell on the outside of the PMMA spheres. After calcination, the PMMA core is removed and a hollow shell of ZnO is left on the substrate. The hollowed morphology can be identified in Fig. 5.13(d). This is due to the presence of empty cores observed from the broken spheres.

This experiment can be extended further to produce double shell structures with different metal oxide layers.

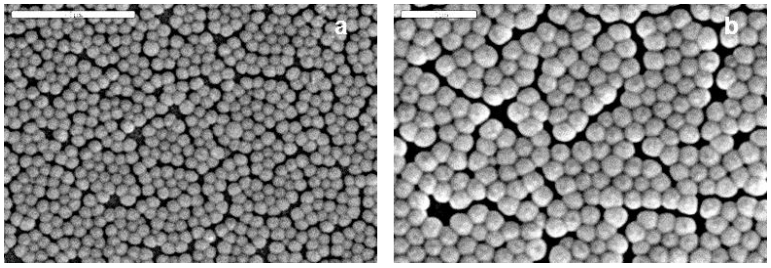

Figure. 5.14 SEM images of (a) low magnification and (b) high magnification of monolayer ZnO/TiO_2 double shell structure (shell-like inverse opal) on a glass substrate at calcination temperature of 450°C. Scale bars: (a) 5μm and (b) 2μm.

Figure 5.14 shows the formation of such a structure with a ZnO inner layer and a TiO_2 outer layer. This can be achieved by making the first mould by horizontal sol-gel infiltration of the ZnO precursor into the PMMA template. Then

after ageing it in air, the second mould can be made by infiltrating the TiO_2 precursor in the same fashion as before. The subsequent removal of the inner PMMA template gives rise to the ZnO/TiO_2 double shell nanostructure, a homogenous monolayer self-assembled on the glass substrate. The original PMMA sphere has an average diameter of 414 nm. The diameter of the inverted ZnO shell structure is 448 nm. The double shell ZnO/TiO_2 inverse opal structure has a further increased diameter of 482 nm. These incremental increases in diameter support the notion of successful coating, when forming the structure. The EDX spectrum in Figure 5.15 confirms the presence of Zn and Ti species, corresponding to the ZnO and TiO_2 layers. As prior, Au peaks are present as a result of the gold coating. Si and Ca peaks correspond to the underlying glass substrate with impurities. The elemental content of the Zn and Ti species is 84.8% and 15.2%, respectively, determined by EDX.

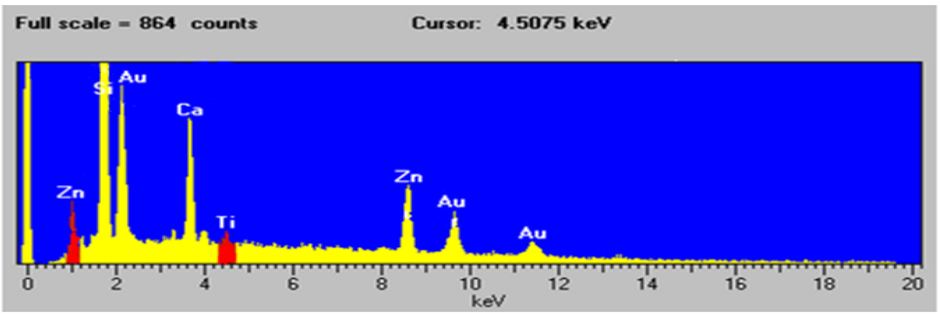

Figure. 5.15 The EDX spectrum of monolayer ZnO/TiO_2 double shell structure. Elemental contents: Zn (84.8%) and Ti (15.2%).

Using non close-packed PMMA sphere aggregates as a template is a powerful technique to produce 2D self-assembled metal oxide hollow shells. This facile technique can also be compared with those methods used to produce hollow spheres of metal oxides, including the templating approaches

discussed later in this chapter. This method can be used to form layers of monodisperse, homogenous and self-assembled hollow nanostructures and thus, can be directly deposited onto the desired substrate for further applications.

5.4.5 TiO_2 Hollow Spheres Created *via* Template-Directed Synthesis

In the case of the creation of TiO_2 hollow spheres from PMMA spheres using sol-gel coating, TT^iP is the main precursor and the hydrolysing agent is deionised water. Ethanol is the solvent in which reaction happens. The sol-gel process is similar to that of TiO_2 inverse opals described earlier in Section 5.4.1. The only difference here is that, the hydrolysis and condensation reactions to form the TiO_2 solid network occurs on the individual PMMA spheres by coating, instead of the sol-gel taking place in the interstitial gaps of the PMMA colloidal crystals as was the case in the synthesis of TiO_2 inverse opals. For the synthesis of TiO_2 hollow sphere, the TT^iP precursor gradually coats the outside of the suspended PMMA spheres in the solution by rapid stirring. The precursor's tendency to cover the sphere can be due to the slightly charged nature of the PMMA sphere forming a weak electrostatic interaction with TT^iP. After the completion of sol-gel reactions, by removing the PMMA sphere templates *via* calcination, the TiO_2 hollow spheres are created. Figure 5.16 shows the SEM image (5.16(a)) and an EDX spectrum (5.16(b)) of the TiO_2 hollow spheres, which were produced by the template-directed synthesis approach (using 414 nm PMMA colloidal spheres as template). A shrinkage of 10% can be seen in the air sphere during template removal (370 nm) from the

original PMMA sphere. The average wall thickness of the TiO_2 coating is approximately 40 nm.

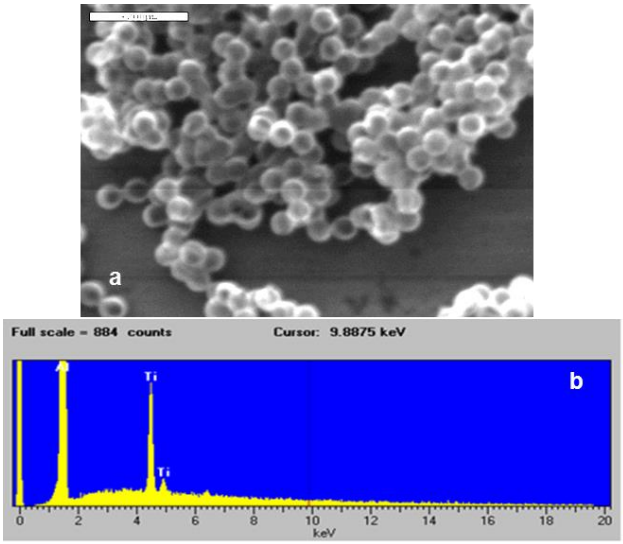

Figure. 5.16 (a) SEM image and (b) EDX spectrum for TiO_2 hollow spheres produced by template-directed synthesis. Scale bar: 2μm.

The dark feature in the centre of the sphere together with the white feature on the edge of the sphere from the SEM image in Figure 5.16(a) suggests that the spheres are hollowed. From the EDX spectrum in Figure 5.16(b), it is noticeable that the most intense titanium peak is due to K_α emission at 4.5 eV. Such emission involves titanium 2p electrons relaxing in energy to occupy the 1s orbital, following removal of a 1s orbital by the SEM electron beam. The peak at 4.9eV is due to K_β emission, which a 3p-1s orbital transition[205]. An extra peak corresponding to aluminium can also be detected in the EDX spectrum. This peak is due to the underlying aluminium foil substrate.

The hollow structure of the TiO_2 spheres is confirmed by the SEM image (Figure 5.17). This image shows some broken spheres after they have been damaged mechanically, by applying pressure to the sample using a spatula .

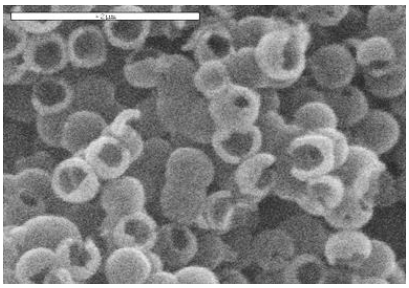

Figure. 5.17 SEM image showing the cut through version of TiO_2 hollow spheres damaged by mechanical force. Scale bar: 2μm.

The transmission electron microscopy (TEM) images also confirm the hollow nature of the TiO_2 coated spheres. The TEM image in Figure 5.18 shows the density contrast between the edge and the centre of the hollow spheres. This image also shows several spheres aggregated together by the coating process. The contrast in the TEM image can be used to judge the density of the material. A non-uniform density can be observed in spheres aggregated together, which indicates an anisotropic TiO_2 coating.

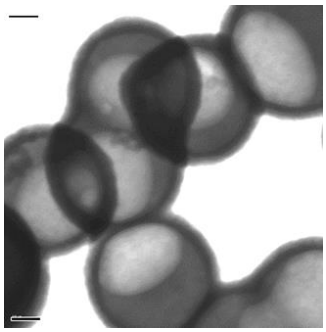

Figure. 5.18 TEM image showing aggregated TiO_2 hollow spheres. Scale bar: 100nm.

The XRD diffraction pattern of the TiO_2 hollow spheres formed after template removal at a calcination temperature of 450^0C can be seen in Figure 5.19.

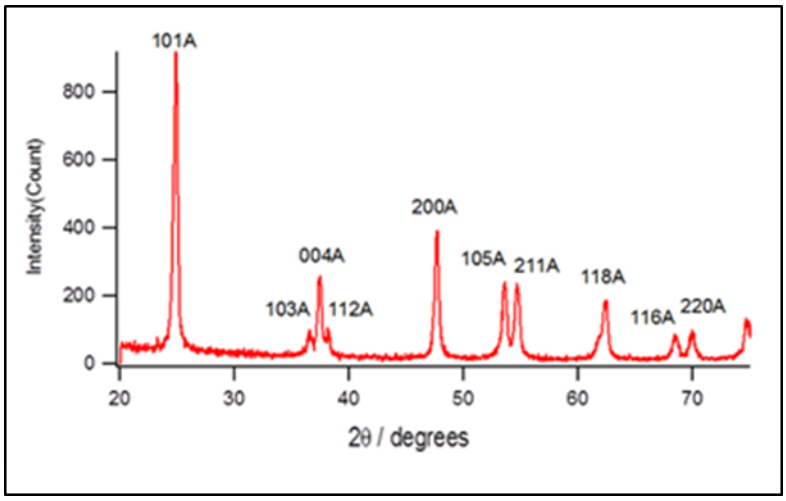

Figure. 5.19 XRD spectrum of TiO_2 hollow spheres calcined at 450°C (A=anatase).

The spectrum confirms that the TiO_2 layer coating formed at this temperature is in the anatase phase. The XRD pattern is indexed to anatase TiO_2 according to the JCPDS card number 841286 with a tetragonal crystal system (Figure 5.18). By employing the Debye-Scherrer formula, the average TiO_2 crystallite size perpendicular to the dominant anatase (101) plane has been calculated to be 18 nm.

5.4.6 SiO_2 Hollow Spheres Created *via* Template-Directed Synthesis

In the case of the creation of SiO_2 hollow spheres from PMMA spheres in the sol-gel coating process, TEOS is the main precursor and the hydrolysing agent is deionised water. Ammonia (NH_3) is used to catalyse the reaction and to obtain a basic medium and ethanol is the solvent in which the reaction happens. In this sol-gel process, network solids of SiO_2 are formed around the PMMA colloidal spheres by hydrolysis and condensation reactions. In the hydrolysis step, the silicon alkoxide salt (TEOS) reacts with water, resulting in the

replacement of an alkoxy group by hydroxyl group to form $Si(OH)_4$ and the liberation of ethanol. Condensation reactions occur between an hydroxyl group and an alkoxy group (alcoxolation), or two hydroxyl groups (oxolation), liberating ethanol and water in the process and forming siloxane groups ($\equiv Si-O-Si\equiv$)[22]. The three bars connected to the Si atoms represent bonds to three hydroxyl or alkoxy groups. After sometime, this growth process continues to form small chains or branched structures, until eventually they gel to form a continuous network solid of siloxane groups surrounding each individual PMMA colloidal sphere. As it was mentioned previously, the precursors tendency to cover each individual sphere can be due to the slightly charged nature of the PMMA sphere forming a weak electrostatic interaction with the sol-gel precursor. The sol-gel process is complete through calcination by removing the solvent and the organic products generated from the so-gel reaction. During calcination, the PMMA sphere cores acting as templates are also removed, leaving SiO_2 hollow sphere structures.

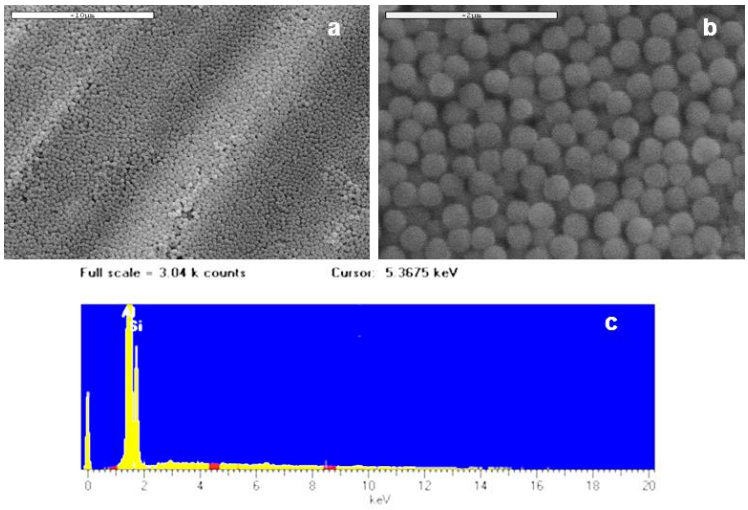

Figure. 5.20 SEM images of (a) low, (b) high magnification and (c) EDX spectrum of SiO_2 hollow spheres SEM. Scale bars: (a) 10μm and (b) 2μm.

Figure 5.20 shows the SEM image (a and b) and the EDX spectrum (c) of SiO_2 hollow spheres synthesised by the template-directed synthesis approach (using 286 nm PMMA spheres as template). The average diameter of the coated SiO_2 hollow spheres after calcination is 316 nm. This increase in size confirms the successful coating procedure. The SEM images show that the coated spheres of SiO_2 do not possess a similar transparent nature to that of the TiO_2 hollow spheres. This may be due to the dense coating of silica, which prevents optical penetration. A high concentration of TEOS (1.2 ml added to 15 ml sphere suspension) was used for SiO_2 formation. This is compared to a much lower concentration of TT^iP (0.04 ml added to 15 ml sphere suspension) when making the TiO_2. This is likely to result in the difference in appearance between the two structures, as SiO_2 hollow spheres are coated more thickly.

In a study carried out by Song et al[206], hollow SiO_2 spheres were synthesised using PMMA hollow particles as template with a hydrothermal method. The hollow nature of the spheres were confirmed by TEM and SEM, after template removal by calcination. Yuan et al[207], synthesised the hollow SiO_2 spheres on PS (polystyrene) sphere template. The hollow structures were confirmed by TEM imaging after template removal by chemical etching. The concentration of TEOS, as well as the order of precursor addition, played a big role on the coating thickness. The method in this work, can also be used for controlled morphology and thickness of the coating in a similar fashion by varying the concentrations of precursors. By lowering the TEOS concentration, the hollow nature of the SiO_2 coated spheres will probably be formed.

The EDX spectrum in Figure 5.20(c) shows an Si peak that arises from the SiO_2 hollow sphere. The Al peak is a result of the underlying aluminium foil

substrate. The nanoparticles that form the SiO_2 hollow sphere are amorphous and thus do not produce a useful XRD spectrum. This is because SiO_2 is crystallised at high calcination temperatures (~1200°C)[208]; at a calcination temperature of 450°C, SiO_2 remains in its more stable amorphous phase.

5.4.7 ZnO and CuO Hollow Spheres Created *via* Template-Directed Synthesis

The synthesis of TiO_2 and SiO_2 hollow spheres using the templating approach are usually performed by coating the sphere with an alkoxide-based precursor of $TT^{i}P$ or TEOS. For the preparation of other metal oxide systems, their acetate or nitrate salt may be used as the main precursor in the sol-gel reaction[209]. This idea is used in this work to prepare precursors for the synthesis of zinc oxide (ZnO) and copper oxide (CuO) hollow spheres. The SEM images in Figure 5.21 illustrates the hollow sphere structures of these two metal oxides with corresponding XRD spectra.

The average diameter of the PMMA sphere template is 414 nm for both samples in Figure 5.21. Some shrinkage in the air spheres can be detected (about 15%). The average coating thickness of the hollow spheres in Figure 5.21(a) corresponding to the ZnO hollow spheres is 84±8 nm and that of the CuO hollow spheres (Figure 5.21(b)) is 57±9 nm.

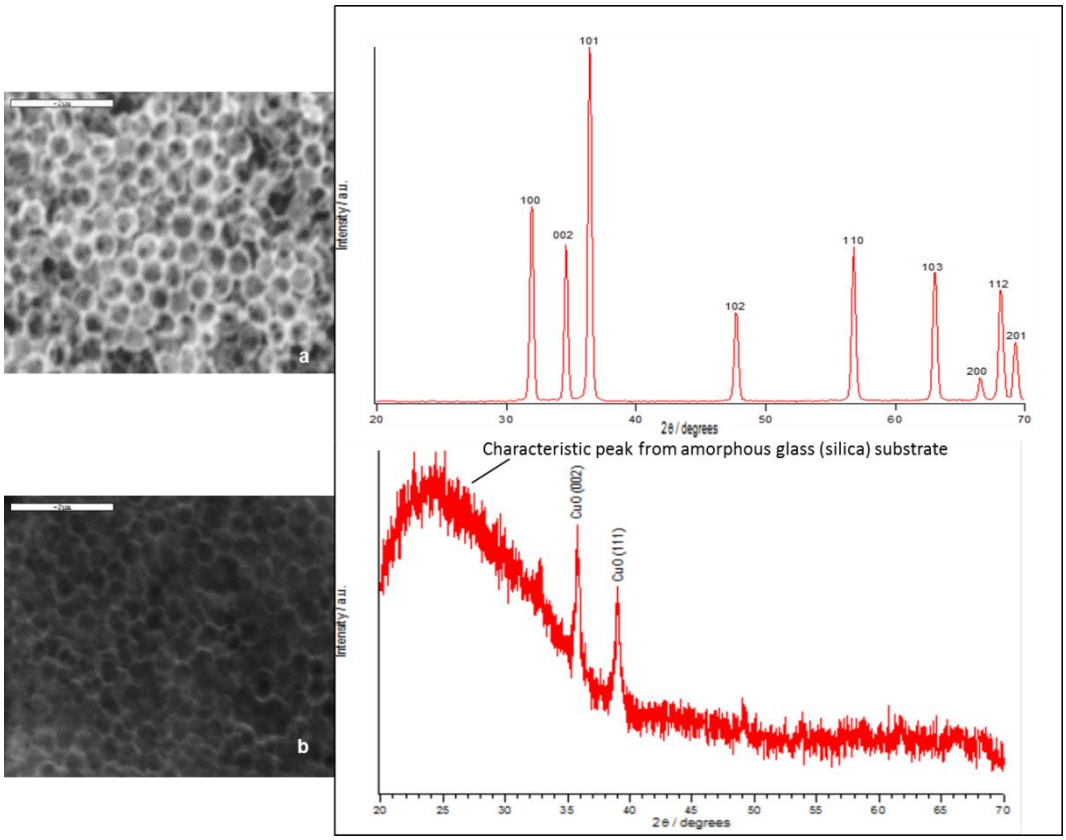

Figure. 5.21 SEM images and XRD spectra of (a) zinc oxide, (b) copper oxide hollow spheres produced *via* template-directed synthesis. Scale bars: 2μm.

The XRD peaks in Figure 5.21(a) are readily indexed to the hexagonal wurtzite phase of ZnO (JCPDS reference no. 01-075-1526). The two diffraction peaks in Figure 5.21(b) at around 2θ of 35.8 and 38.9 correspond to (002) and (111) planes of crystalline phase of CuO according to the JCPDS reference no. 01-080-1916. The broad peak at the beginning of the XRD spectrum corresponding to CuO (Figure 5.21(b)) is from the underlying amorphous glass (silica) substrate. Such peak is not detected in the first XRD spectrum (Figure 5.21(a)). This is because the deposited CuO hollow spheres on the glass substrate were less concentrated than those of ZnO sample during XRD

scanning. The XRD analysis confirms the successful synthesis of ZnO and CuO hollow spheres using the template directed synthesis *via* sol-gel coating.

The SEM images of ZnO and CuO hollow spheres look more interconnected than the TiO_2 (Figure 5.16) and SiO_2 (Figure 5.20) hollow spheres produced. The reason for the interconnectivity between the hollow spheres for these two samples may lie in a slight modification in their synthetic routes. The PMMA spheres used as templates for the synthesis of ZnO and CuO hollow spheres were in the suspended form in water when added to the metal oxide precursors for coating, as opposed to the dried PMMA spheres used in the other two samples (*i.e.* TiO_2 and SiO_2). As the PMMA spheres were suspended in an aqueous media, some precursors will be free as solute until the solution is dried. This residual precursor will be eventually forming the connections between the hollow spheres, which forms inverse-opal like structures.

This facile approach of creating hollow spheres can be used for making other metal oxide systems. In general, by dissolving a small amount of the desired metal acetate or nitrate (c. 0.01 g) in water with appropriate pH, the sol-gel precursor can be used to coat the spheres. Subsequent calcination after a period of ageing results in the formation of high quality hollow spheres. The metal oxide hollow spheres created by the template-directed synthesis approach can be used in applications including photovoltaics, due to their high surface area and their ability to enhance light scattering properties because of their hollow nature.

5.4.8 Sphere-in-Sphere Hollow Spheres Produced *via* Seeded Polymerisation and Template-Directed Synthesis

Following the coating of the metal oxide precursor, the spheres can be further used as seeds for secondary polymerisation as it was presented in Chapter 3. Then a new layer of metal oxide precursor can be deposited subsequently. After calcination, a unique sphere-in-sphere structure can be formed. The chemical components of the double spheres can be independently adjusted, which offers the freedom of adjusting the electronic, optical and chemical properties of the nanostructure. In this work, SiO_2/TiO_2 sphere-in-sphere hollow spheres were synthesised using this novel approach. Figure 5.22 shows the SEM image of this nanostructure. The outer white spheres correspond to TiO_2 and the inner dark spheres to SiO_2 as a consequence of sol-gel coating being performed in that order. The sol-gel precursor concentrations are identical to the single step coating procedure used before to produce SiO_2 and TiO_2 hollow spheres. Therefore, by looking at the SEM images of SiO_2 hollow spheres and TiO_2 hollow spheres shown previously in Figures 5.20 and 5.16 respectively, the colour contrasts are consistent with the SEM image here. The inner SiO_2 hollow sphere is not transparent due to the high concentration of TEOS solution (1.2 ml added to 15 ml sphere suspension) in the sol-gel process. The TiO_2 outer layer on the other hand, shows a white feature surrounding the inner SiO_2 hollow spheres due to its low TT^iP precursor solution concentration (0.04 ml added to 15 ml coated sphere seed suspension).

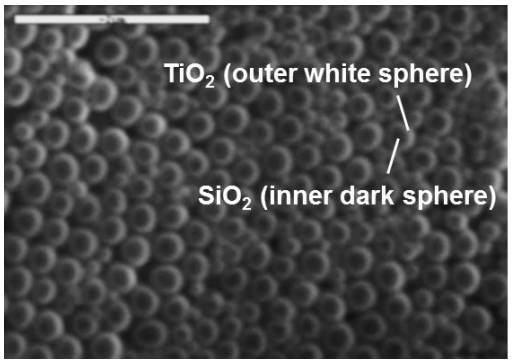

Figure. 5.22 SEM image of SiO_2/TiO_2 sphere-in-sphere hollow spheres produced by seeded polymerisation and template directed synthesis deposited on a glass substrate. Scale bar: 2μm.

For the synthesis of sphere-in-sphere hollow spheres, the average diameter of the unseeded original PMMA spheres is about 286 nm. The final SiO_2/TiO_2 hollow structures have an average diameter of 348 nm. The dark inner SiO_2 hollow spheres have an average diameter of 270 nm and the white outer TiO_2 hollow spheres have an average coating thickness of 78 nm. The average diameter of the SiO_2 hollow spheres and the coating thickness of the transparent TiO_2 hollow spheres are different from the single step coating procedures explained previously; 316 nm and 40 nm respectively. This could be due to the fact that, in the seeded polymerisation for second coating with PMMA, some of the hydrolysed TEOS precursor coated onto the PMMA sphere seeds might be removed by rapid stirring in water, resulting in smaller SiO_2 hollow spheres in the final product. In the case of TiO_2 coating, in the single step procedure, the diameter of the original PMMA spheres were 414 nm compared to possibly still smaller seeded plus coated 286 nm spheres used here for second coating, resulting in the availability of more TT^iP to coat the smaller spheres and therefore giving rise to thicker TiO_2 hollow spheres. In

addition, it should also be mentioned that, due the nature of the final double coated product, it is difficult to precisely measure the white and dark regions from the SEM image in Figure 5.22.

From the schematic diagram in Section 5.2, different stages in the formation of sphere-in-sphere hollow sphere were shown clearly. One of the main purposes of introducing the second synthesis of PMMA using SFEP process was to introduce a layer between the two metal oxide shells which would then be removed to create sphere-in-spheres. The other purpose of using this PMMA template layer between the two metal oxide coating layers was to serve as an organic media for better organic/inorganic interaction leading to a better coating process. However, the use of both SEM and TEM (the latter not shown here) could not clearly show the gap between outer and inner metal oxide shells. Therefore, the assumption of such hollow nature between the two coatings has to be investigated further using high resolution scanning electron microscopy, HRSEM[210].

The inorganic/organic nature of PMMA/metal oxide precursor may give rise to a better electrostatic interactions between them than those of metal oxide/metal oxide precursor interactions. There is also possible for a direct surface reaction between PMMA/metal oxide due to the presence of functional groups on the PMMA organic surface, which may result in the creation of a core-shell composite (Chapter 1, Section 1.5). A similar experiment was carried out in this work to coat the TiO_2 shell on the SiO_2 hollow sphere without the use of the second PMMA synthesis, but with no success due to the aggregation and phase separation of the suspension.

From the SEM image in figure 5.22, the presence of another population of spheres with smaller sizes can be detected. This may be due to the following two reasons. 1) Production of polydispersed PMMA sphere populations during the first single-step and also the second seeded SFEP polymerisation processes may give rise to different populations in the final metal oxide hollow structures. 2) The fast hydrolysation of TEOS in the SiO_2 sphere coating step may give rise to small independent populations of SiO_2 particles (spheres). The subsequent TT^iP coating in the second coating procedure may then coat the small SiO_2 particles as well as the large SiO_2 coated spheres, giving rise to different populations.

Another interesting phenomenon that can be observed in the SEM image of Figure 5.22 is that, the SiO_2/TiO_2 sphere-in-sphere hollow spheres are self-assembled after the dropwise horizontal deposition onto the glass substrate. The self-assembly of these spheres may be assisted by different surface charges originating from both the SiO_2 and TiO_2 species. Another reason may be due to the gluing action, which is induced by the dense metal oxide spheres with binary size population, in which the smaller populations fill the gaps between the larger spheres for better contact and adhesion. Of course, the capillary forces and the convective flux at the meniscus region should not be denied, as these are usually the main driving forces in horizontal self-assembly approaches (Chapters 1 and 4).

5.5 Conclusion

The various templating routes introduced in this work for the creation of inverse opals, hollow spheres and sphere-in-sphere hollow spheres are powerful techniques to manufacture porous nanostructures. They offer a facile, cost effective and reliable route to manufacture porous nanostructures for many different metal oxides. Such structures are potential candidates for use in various applications such as photovoltaics[140, 188, 211] (including PEC water splitting and dye sensitised solar cells), lithium ion batteries[212], gas sensing[213] and chromatography[214].

The temperature study of 3D TiO_2 inverse opal shows that, the calcination temperature has an effect on the size of the air spheres due to the swelling of the TiO_2 walls. This behaviour may be used to prepare inverse opals with controllable air sphere diameters without changing the PMMA colloidal crystal template prior to each experiment.

The 2D monolayer inverse opal structures produced cover a large area of a substrate with some defects or grain boundaries and a good degree of uniformity. In addition, the synthesis process of these structures can be extended to form layer-by-layer 3D structures with controlled chemical composition by repeating the procedure onto the initial monolayer. The synthesis of such hierarchical porous heterostructures may be realised with the possibility of optimising the opto-electrical properties.

A universal approach for the synthesis of various metal oxide hollow spheres *via* templating was also presented in this work. The use of a simple precursor, an alkoxide, acetate or nitrate form of a metal salt in water and ethanol (the latter only when using alkoxides), produces high quality hollow

spheres in a facile manner. This approach may be extended for other metal oxide systems, making it a powerful technique for creating various metal oxide hollow spheres. This technique offers a simpler route compared to those previously reported in the literatures[172, 215-217].

The successful synthesis of sphere-in-sphere hollow spheres may increase the surface area, as well as the light scattering effects due to the formation of two layers. The net result may be enhanced opto-electrical properties compared to single layer hollow spheres. The technique of using seeded polymerisation with template-directed synthesis *via* sol-gel coating used in this work may be performed on other metal oxide systems.

Chapter 6: Synthesis of Novel Hierarchical Inverse Opal Based Nanostructures and their Applications in PEC Water Splitting

6.1 Abstract

By using a modified colloidal crystal templating technique, monolayer and bilayered inverse opal structures of ZnO and TiO_2/ZnO were successfully synthesised. ZnO nanorods were then grown on top of the inverse opals *via* chemical bath deposition (CBD) method. The nanorods-inverse opal hierarchical structures were further sensitised by narrow band gap CdSe/ZnS core-shell quantum dots. In a three electrode PEC water splitting set-up under illumination of a 300 W xenon arc lamp (AM 1.5G filter) with light intensity adjusted to 300 mW/cm^2 in a 1 M KOH electrolyte solution, the highest water splitting photoefficiency was recorded for the hierarchical QD sensitised ZnO nanorods on bilayered TiO_2/ZnO inverse opal structure at 2.35%, increased from 0.99% (QD sensitised ZnO nanorods on monolayer ZnO inverse opal), 0.78% (ZnO nanorods on bilayered TiO_2/ZnO inverse opal), 0.69% (bilayered TiO_2/ZnO inverse opal), 0.49% (bilayered ZnO/ZnO inverse opal), 0.32% (monolayer ZnO inverse opal) and 0.18% (ZnO nanorod aggregates).

6.2 Introduction

Titania (TiO_2) and Zinc oxide (ZnO) are two preferred n-type semiconductor metal oxides for PEC water splitting because of their band-edge positions, strong optical absorption, excellent chemical stability, photocorrosion resistance

and low cost. However, because of their wide band gaps (3.2-3.3 eV), only UV light is absorbed. Additionally they have fast electron-hole pair recombination due to a high density of trap states[218], these combined effects cause their efficiencies to be substantially limited when solar energy is directly used. In order to improve visible light absorption many approaches have been reported, including sensitisation, coupling with small band gap semiconductors, and elemental doping with other metal/non-metal ions[189, 219]. It is equally important to improve the morphology and electronic structure of TiO_2 and ZnO photoelectrodes to effectively suppress the rate of electron-hole recombination and allow better transportation of the photo-excited charge carriers[218, 220]. For instance, 1D nanostructures, such as metal oxide nanorods[221, 222], nanowires[223] and nanotubes[224, 225], have shown several advantages with respect to improved morphology and electronic properties, such as direct electron transport pathways, reduced carrier diffusion length and diminished charge recombination compared to conventional nanoparticle electrodes[4]. However, due to the insufficient surface area of 1D nanostructures, the overall energy conversion efficiency is low in comparison to the nanoparticle electrodes, therefore, a purpose-designed nanoarchitecture of the photoelectrode is central to compensate for the shortcomings of the 1D nanostructures to the further development of efficient energy conversion[2].

Periodically ordered inverse opal nanostructures have attracted increasing attention as effective photoelectrode materials by offering high specific surface area and porosity[9, 149]. Additionally, the inverse opals possess photonic crystal properties which enhance the light-matter interactions by controlling the propagation of light via back reflections, slow photons and

surface resonant modes[4, 140, 188]. As such, the inverse opal structure is expected to be an ideal photoelectrode candidate for energy conversion applications[188].

For these reasons, it is highly desirable to implement a hierarchical organisation[226] of 1D nanostructures coupled with inverse opals to benefit the combined opto-electronic enhancement effects arising from each individual component. Recently, Karuturi et al. presented a method to fabricate ZnO nanowire arrays coupled with 3D TiO_2 inverse opals and used as PEC photoanodes[4]. The realisation of a semiconductor nanowire/photonic crystal architecture was achieved by direct growth of nanowires on top of the inverse opal which showed intimate physical contact and thereby realised the dual benefits of light trapping and surface area enhancement. The efficiency improvement for their unique hierarchical structure could still be improved by introducing another layer of inverse opal of different metal oxide to create a heterojunction with an interface acting as a charge barrier to further reduce back recombination and increase charge transport in the PEC device.

In this chapter, a novel templating approach combining sol-gel infiltration with chemical bath deposition (CBD) will be described. It has been introduced initially for the first time to create, ZnO nanorods grown directly on a monolayer ZnO inverse opal, which was further sensitised using CdSe/ZnS core-shell quantum dots to enhance the visible-light absorption. Furthermore, for the first time, a hierarchical QD sensitised bilayered TiO_2/ZnO inverse opal nanostructure coupled with ZnO nanorods has been created to be used as a photoanode in PEC water splitting experiments. These results may lead to the construction of various nanorod- bilayered heterojunctioned inverse opal hybrid structures for diverse applications. Various sol-gel metal oxide precursor

chemicals such as Fe_2O_3, Cu_2O and SnO_2 [39, 192, 199] are available to produce desirable inverse opals.

6.3 Experimental Procedures

The substrates used in all the experiments in this chapter were titanium plates. These were cleaned thoroughly by soaking in a dilute HCl solution (1 M) for 15 minutes, followed by washing with DI water after carefully polishing with clean sandpaper. For better adhesion of the materials onto the substrates, two droplets of TT^iP solution (0.01 M) in ethanol was dropped onto the Ti plates and allowed to dry for 30 minutes. For PEC measurements, the thickness of the samples above the Ti plate surface was kept constant for each set of experiments by using the same number of colloidal crystal layers (each monolayer was 414 nm thick, corresponding to the average diameter of the PMMA spheres forming the colloidal crystal) in order to obtain accurate results. The Ti substrates used had the same area (2.4×2.4 cm^2) and the samples were deposited uniformly on them.

6.3.1 Synthesis of Bilayered ZnO/ZnO and TiO_2/ZnO Inverse Opals

Monolayer ZnO and TiO_2 inverse opals were synthesised as described previously in Chapter 5 (Section 5.3.2). The templating procedures to prepare the samples were performed on Ti substrates. For the synthesis of bilayered ZnO/ZnO inverse opal, the first layer was prepared according to the monolayer ZnO inverse opal procedure. Before calcination and removal of the PMMA

colloidal crystal, a second layer of PMMA colloidal crystal was then cast onto the first layer using the floating self-assembly approach. This was followed by adding the ZnO precursor solution by the same procedure performed on the first layer. The double infiltrated layers were then calcined as before. In such a way, the film thickness could be precisely controlled and the quality of the surface morphology was guaranteed. For the synthesis of bilayered TiO_2/ZnO inverse opal, the procedure was identical to that of bilayered ZnO/ZnO inverse opal described above, with a precursor variation on alternate layers. The first layer was prepared using the TiO_2 precursor and the top layer was prepared using the ZnO precursor, as described for the preparation of monolayer inverse opals.

6.3.2 Synthesis of ZnO Nanorods on Monolayer ZnO and Bilayered TiO_2/ZnO Inverse Opals

For the synthesis of ZnO nanorods on monolayer ZnO inverse opal, the as-prepared monolayer ZnO inverse opal was used as a layer of ZnO seeds to grow the ZnO nanorods on, using chemical bath deposition (CBD). The seeded Ti plate substrate was placed horizontally in a growth solution containing 10 mM zinc nitrate and 10 ml of hexamethylenetetramine (HMT) at the bottom of a beaker. The beaker was left in an oven at 85°C for 6 hours. The Ti plate was then removed and rinsed thoroughly with DI water and dried in air. For time dependent studies, different nanorod growth times in the above procedure were applied. For the synthesis of ZnO nanorods on bilayered TiO_2/ZnO inverse opal, the as-prepared TiO_2/ZnO sample on Ti plate was used as the seed substrate (the ZnO inverse opal was the top layer acting as the seeding layer), and the

identical CBD procedure described above was used for nanorod growth. Disordered aggregated ZnO nanorods were also prepared for comparison on a clean Ti plate without using the ZnO inverse opal. In this case the seed was prepared by dropping 4 drops of zinc acetate solution (0.05 M) in ethanol on the edges of the Ti plate substrate and allowing to cover the whole substrate. The nanorods were then grown on the substrate as before using CBD.

6.3.3 Synthesis of QD Sensitised ZnO Nanorods on Monolayer ZnO and Bilayered TiO_2/ZnO Inverse Opals

A 0.47 mM CdSe/ZnS quantum dot solution was prepared by diluting the commercial CdSe/ZnS core-shell quantum dots (Evident Technologies, core-shell Evidots, Cadsklll Green, absorption (AB):531 nm and emission (EM):548 nm) in toluene. The as-synthesised ZnO nanorods on monolayer ZnO inverse opal and ZnO nanorods on bilayered TiO_2/ZnO inverse opal samples on Ti substrates were placed face up at the bottom of 2 separate vials and the quantum dot solution was carefully added until it covered the whole of the substrates. The vials were covered with aluminium foil and placed in a dry dark place. After 12 hours, the samples were removed from the quantum dot dispersion and thoroughly rinsed with DI water.

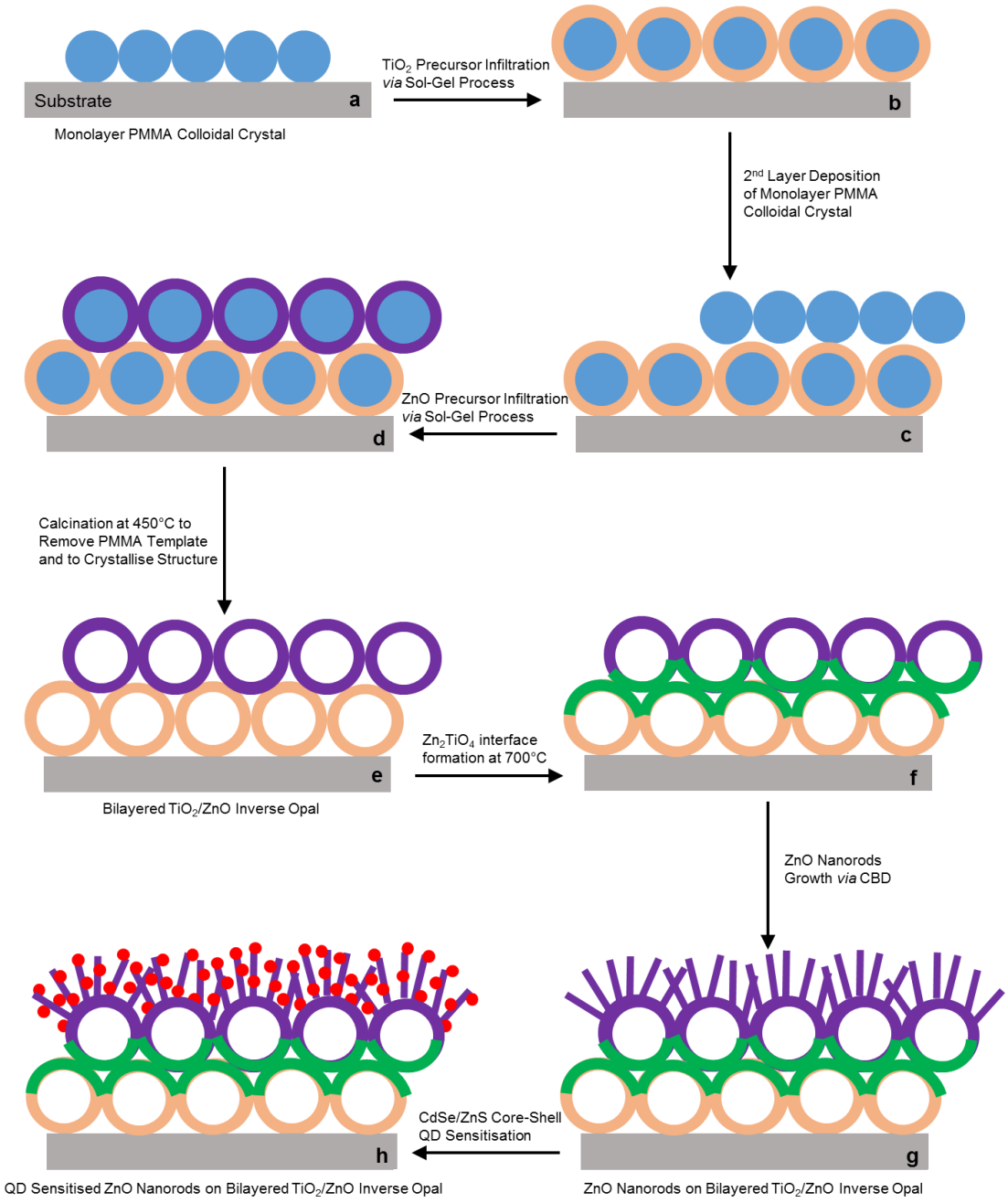

Figure. 6.1 Schematic illustration of different stages in the formation QD sensitised ZnO nanorods on bilayered TiO_2/ZnO inverse opal. Blue spheres = PMMA spheres, orange coating = TiO_2 coating, purple coating and rods = ZnO coating and rods, green parts = Zn_2TiO_4 interface and red dots = CdSe/ZnS QDs.

Figure 6.1 is a schematic showing the work flow in the formation of QD sensitised ZnO nanorods on bilayered TiO_2/ZnO inverse opal. In the first stage, a monolayer PMMA colloidal crystal was formed *via* the modified floating technique onto the substrate as described previously in Chapter 4 (a). Then by the horizontal sol-gel infiltration, the interstitial gaps of the colloidal crystal were infiltrated with a TiO_2 precursor solution (a TT^iP based solution) (b). The infiltrated precursor solution was allowed to solidify by hydrolysation and condensation reactions in air for 24 hours, before a second monolayer of PMMA colloidal crystal was deposited using the modified floating technique (c). The interstitial gaps of the top layer PMMA colloidal crystal was infiltrated in a similar fashion as the first layer, only this time using a ZnO precursor solution (a zinc acetate based solution) (d). After further ageing and drying in air for 24 hours, the bilayered coated film was calcined, first at a lower temperature of 450°C to remove the PMMA template and to form a crystalline bilayered TiO_2/ZnO inverse opal structure (e). The film was then annealed at a higher calcination temperature of 700°C, to form a Zn_2TiO_4 interface between the two inverse opal layers (Section 6.4.3) (f). In the next stage, the top ZnO inverse opal layer in the bilayered TiO_2/ZnO inverse opal was used as a seeding layer to grow ZnO nanorods on it *via* chemical bath deposition (CBD) (Section 6.4.1) (g). In the final stage, the sample was sensitised by narrow band gap CdSe/ZnS core-shell quantum dots (QDs) by soaking it in a toluene based solution containing such QDs for 12 hours (h). The final state of the art hierarchical nanostructure was formed and can be used as a photoanode in PEC water splitting experiments.

6.4 Results and Discussion

6.4.1 Growth Mechanism of ZnO Nanorods on Inverse Opals *via* Chemical Bath Deposition (CBD)

ZnO nanorods have been successfully grown on monolayer ZnO and bilayered TiO_2/ZnO inverse opals in this work. This consisted of first creating the seed templates by colloidal crystal templating, yielding inverse opals. The inverse opal seeds were then used as templates (secondary templating), on which to grow the nanorods *via* chemical bath deposition (CBD).

The growth of aligned nanorods and nanowires of ZnO from aqueous solutions without the seeding template was first developed by Vayssieres[222]. It involves the growth of zinc oxide nanorods from a growth solution of zinc nitrate and hexamethylenetetramine (HMT). Vayssieres' study used an equimolar solution of zinc nitrate and HMT ($(CH_2)_6N_4$); 10 mM for the growth of ZnO nanorods and 1 mM to grow ZnO nanowires. Their growth solution was heated to 85^0C and by varying the heating time, nanorods with different dimensions were produced.

This method was modified in this work with the use of a seeding template as well as the growth solution for managing the deposition of nanorods onto the Ti substrate for photovoltaic applications. Here, seeding is a sol-gel process in which zinc acetate solution is used as precursor. By using colloidal crystal templating, the sol-gel process takes place between the interstitial gaps of the PMMA colloidal crystal structure deposited previously onto the substrate which is subsequently removed in the calcination process. The result is a porous

crystalline ZnO inverse opal seed layer (achieved at a calcination temperature of 450°C). The crystallites in the inverse opal creates favourable sites for the growth of zinc oxide nanorods when the substrate is deposited in the growth solution. The mechanism for the growth process of ZnO nanorods is generally accepted to be as follows[227, 228]:

(1) $(CH_2)_6N_4 + 6H_2O \rightarrow 6H_2CO + 4NH_3$

(2) $NH_3 + H_2O \rightarrow NH_4^+ + OH^-$

(3) $Zn^{2+} + 4NH_3 \rightarrow Zn(NH_3)_4^{2+}$

(4) $Zn(NH_3)_4^{2+} + 4OH^- \rightarrow Zn(OH)_4^{2-} + 4NH_3$

(5) $Zn^{2+} + 4OH^- \rightarrow Zn(OH)_4^{2-}$

(6) $Zn(OH)_4^{2-} \rightarrow ZnO + H_2O + 2OH^-$

The role of the HMT is to release OH^- in a controlled manner and the formation of the ZnO nuclei largely follows these 6 reaction steps. The formation of the nuclei is slow and is the rate determining steps in the preparation of ZnO nanorods. Subsequently, crystalline ZnO hexagonal nanorods begin to grow on the seed surface (here ZnO inverse opal). The novel bilayered inverse opal process carried out in this work shows that ZnO nanorods are not limited to grow on single ZnO films and are able to grow on more complex heterostructures with different morphologies as long as the top layer of the structure consists of ZnO crystal seed. In this work, it was possible to grow ZnO nanorods on bilayered TiO_2/ZnO inverse opal with ZnO being the top inverse opal layer.

6.4.2 Morphology Characterization

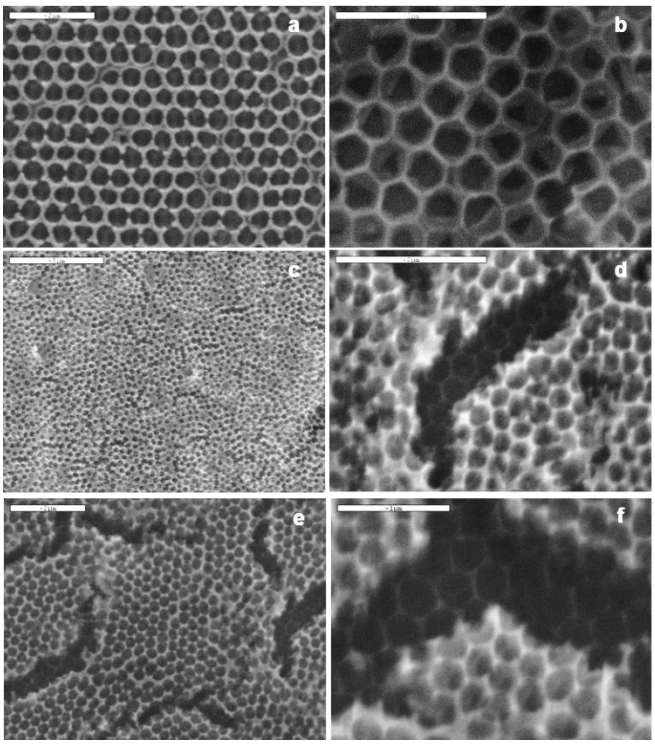

Figure. 6.2 SEM images showing the top surface of (a) monolayer ZnO and (b) monolayer TiO_2 inverse opals, (c, d) bilayered ZnO/ZnO and (e, f) bilayered TiO_2/ZnO inverse opals. Top layer (white) as ZnO inverse opal layer in (c-f). All the samples are deposited on Ti substrates. Scale bars: (a),(b),(d),(e) 2μm, (c) 5μm and (f) 1μm.

The SEM images in Figure 6.2(a) and (b) presents the monolayer ZnO and TiO_2 inverse opals respectively which are derived from PMMA colloidal crystals (with average sphere diameter 414 nm). The average air sphere (macropore) diameter is 410±6 nm. The wall thickness is 85±10 nm and 70±10 nm for ZnO and TiO_2 respectively (the SEM analysis of these monolayer inverse opals was previously explained in Section 5.4.3 in the previous chapter). The SEM images in Figure 6.2(c, d) and 6.2(e, f) show the bilayered

structures of ZnO/ZnO and TiO_2/ZnO inverse opals respectively. The apparent colour contrast in the images (top layer (white) as ZnO inverse opal layer in Figure 6.2(c-f)) indicates that the bilayer films are formed. The size and the orderliness of the top layer is the same as the first layer, although more cracks can be observed on the top layer. This may be due to the reduction in stability in the top layer during template removal in the lower layer.

Figure 6.3 shows the SEM images when ZnO nanorods are grown on the inverse opals of either the monolayer ZnO (6.3(a)) or bilayered TiO_2/ZnO (6.3(b)) inverse opals. Figure 6.3(c) is a high magnification SEM image of the same sample used in 6.3(b). Figure 6.3(d) shows the growth formation of ZnO nanorods on the monolayer ZnO inverse opal ring, 6.3(e) QD sensitised ZnO nanorods on bilayered TiO_2/ZnO inverse opal and 6.3(f) aggregated ZnO nanorods. The ZnO nanorod growth conditions are the same for all the samples using 10 mM growth solution for 6 h *via* CBD method. Samples are prepared on Ti substrates. The dimensions of the underlying inverse opals used to grow the nanorods on, are the same as described before for Figure 6.2. The length and diameter of the ZnO nanorods are 160±12 nm and 56±4 nm respectively identified from image 6.3(c). The dimensions of the ZnO nanorods for the rest of the images are similar. The SEM image in Figure 6.3(d) clearly demonstrates the importance of ZnO inverse opal as a seeding scaffold. The ZnO nanoparticles forming the inverse opal ring act as nucleation sites in the growth of the nanorod crystal structures. ZnO nanorod structures, as previously reported in literature are hexagonally shaped and have a preferred orientation in the c-axis normal to the substrate (i.e. in the direction of 002 plane)[221, 222] due to competition and optimisation rules by reaching the minimal surface energy[229].

The crystalline ZnO nanorods in this work are tilted more randomly. As the topology of the underlying inverse opal is periodically rippled, the ZnO nanorods which are perpendicular to the substrate, are tilted following the inverse opal surface structure. Due to the ring-like nature of the inverse opal seed, the nanorods may grow more freely with less obstruction from the neighbouring nanorods (Figure 6.3(a), (b), (c), (d) and (e)).

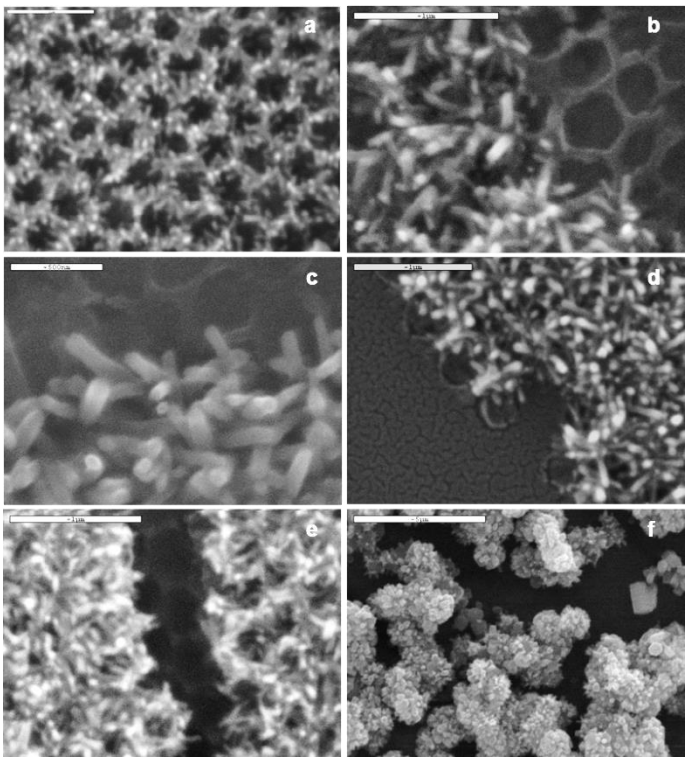

Figure. 6.3 SEM images showing the top surface of (a) ZnO nanorods on monolayer ZnO and (b, c) ZnO nanorods on bilayered TiO_2/ZnO inverse opals, (d) growth formation of nanorods on the ZnO inverse opal ring, (e) QD sensitised ZnO nanorods on bilayered TiO_2/ZnO inverse opal and (f) aggregated ZnO nanorods. The nanorods in all the samples are grown using 10 mM growth solution for 6 h. All the samples are deposited on Ti substrates. Scale bars: (a),(b),(d),(e) 1μm, (c) 500nm and (f) 5μm.

The SEM image in Figure 6.3(e) shows the quantum dot sensitised structure of the ZnO nanorods on bilayered TiO_2/ZnO inverse opal. The image clearly shows that the integrity of the structure remains intact even after leaving the sample in the QD solution for 12 h. The SEM image in Figure 6.3(f) shows the formation of nanorods without the presence of the inverse opal. It shows lack of interconnectivity and the nanorods are aggregated together forming agglomerates which may reduce the efficiency of the sample as an photoanode in water splitting experiments.

The SEM images in Figure 6.4 show the growth of ZnO nanorods on a monolayer ZnO inverse opal as a function of growth solution deposition time. In all images, the concentration of the growth solution is constant at 10 mM. The substrate used is a Ti plate for all the samples.

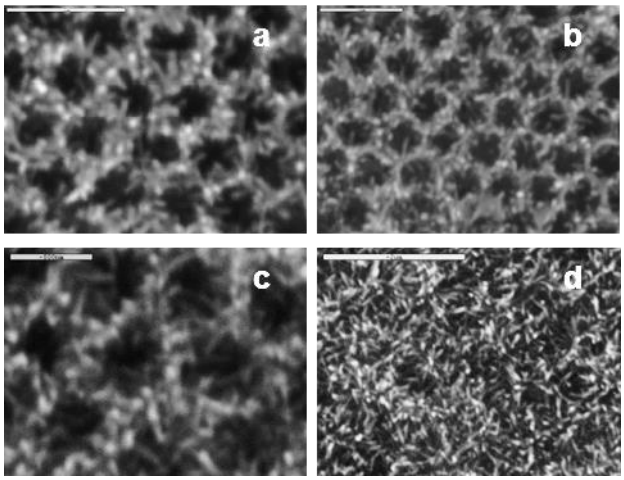

Figure. 6.4 SEM images of monolayer ZnO inverse opal left in a 10 mM ZnO nanorod growth solution for (a) 4 h, (b) 6 h, (c) 8 h and (d) 12 h. Scale bars: (a),(b) 1μm, (c) 500nm and (d) 2μm.

The SEM image in Figure 6.4(a) is the monolayer ZnO inverse opal sample that has been left in the ZnO nanorod growth solution for 4 h, increased

to 6 h in Figure 6.4(b), 8 h in 6.4(c) and 12 h in 6.4(d). As it can be seen from the images, the integrity of the underlying porous ZnO inverse opal structure is intact until the growth time is increased to 12 h. At this time, the air spheres (macropores) of the underlying inverse opal disappear and the structure becomes more disordered. This can be due to a sudden increase in the ZnO nanorods lengths from ~165 nm corresponding to the samples with growth deposition times of 4 h, 6 h and 8 h (Figure 6.4((a), (b) and (c))) respectively to ~220 nm corresponding to the sample with nanorod growth deposition time of 12 h (Figure 6.4(d)). The differences in nanorod lengths for the 4, 6 and 8 h samples are minimal and cannot be distinguished by SEM measurements.

Although the porosity of the structures are intact when the nanorod growth durations are 4 , 6 and 8 h, but due to the orientation and the position of the nanorods on the underlying monolayer ZnO inverse opal seeds, the porosity has shrunk compared to the original macropores of the inverse opals. For example, the air spheres (macropores) has an average diameter of 255 nm for the ZnO nanorods on monolayer ZnO inverse opal structure using a 6 h nanorod growth time (Figure 6.4(b)) compared to an average air sphere diameter of 410 nm for the pristine monolayer ZnO inverse opal sample. Such shrinkage in porosity may affect the optical (photonic) properties of the samples.

6.4.3 Crystal Property Characterisation

The orientation of the crystal planes and the size of the crystallites can be determined from XRD analysis. Figure 6.5 illustrates the XRD pattern of the as-

synthesised ZnO nanorods on monolayer ZnO inverse opal for different growth deposition times. All the diffraction peaks can be readily indexed to the hexagonal wurtzite phase of ZnO (JCPDS reference no. 01-075-1526). The peaks that are marked with stars (*) correspond to the underlying Ti substrate and are assigned to JCPDS reference number 44-1294.

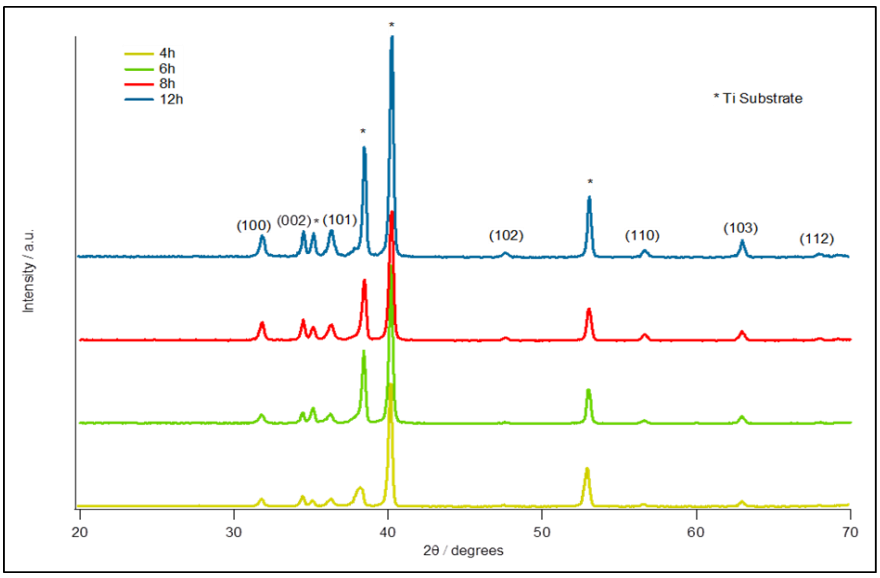

Figure. 6.5 XRD patterns of ZnO nanorods on ZnO inverse opals prepared using different growth solution deposition times (4 h, 6 h, 8 h and 12 h). (*) represents Ti substrate peaks.

The average ZnO crystallite size perpendicular to the main crystal planes can be calculated using the Debye-Scherrer equation[135]. The results show no alteration in size of the crystallites by changing the growth solution deposition time. However the intensity of the peaks in the 12 h nanorod growth solution sample increases compared to the other samples. This is expected as the nanorods length has increased for this sample compared to the other three samples (4 h, 6 h and 8 h), indicating more ZnO crystallites diffracting X-rays from the preferred planes. Table 6.1 shows the crystallite size calculated for

each diffraction peak from the XRD patterns in Figure 6.5 which remains constant for all the samples.

Diffraction Plane(s) (hkl)	(100)	(002)	(101)	(102)	(110)	(103)
2θ	31.74	34.39	36.24	47.47	56.61	62.95
ZnO Cristallite Size / nm	26.2	35.2	21.2	22	22.9	29.6

Table. 6.1 ZnO crystallite sizes for different diffraction planes.

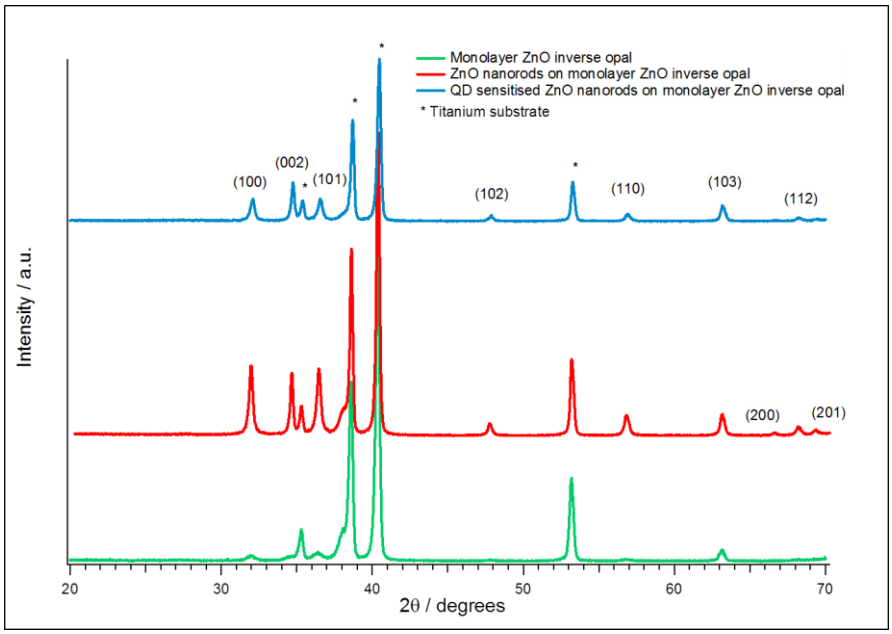

Figure. 6.6 XRD patterns for different stages of QD sensitised ZnO nanorods on monolayer ZnO inverse opal. The peaks indicated with (*) correspond to the underlying Ti substrates.

Figure 6.6 shows the XRD pattern in different stages of the creation of QD sensitised ZnO nanorods on monolayer ZnO inverse opal. All the ZnO peaks are indexed to the JCPDES reference number 01-075-1526. In this Figure, the green spectrum corresponds to the monolayer ZnO inverse opal

seed prior to ZnO nanorod growth deposition. As the film is monolayer and too thin (about 410 nm), the intensity of the ZnO peaks are weak, however the presence of (100), (002), (101) and (103) peaks corresponding to 2θ values of 31.92°, 34.74°, 36.58° and 63.12° is an indication of the growth of inverse opal seed dominating in these directions. After the growth of the ZnO nanorods (red pattern), the intensity of peaks corresponding to all the diffraction planes significantly increases. This suggests that the nanorods grow in these directions on inverse opal seeds following the inverse opal surface structure. In particular, there is a significant increase in the (002) plane from the original inverse opal, indicating the growth of ZnO nanorods have a preferred orientation in this direction. Other peaks with increased intensities after introducing the nanorods are present at 47.85° (102), 56.81° (110), 66.64° (200) and 68.29° (112). The blue spectrum corresponds to the QD sensitised structure. It appears similar to the spectrum prior to sensitisation (red pattern) except for the intensity reduction of the ZnO diffraction peaks. This is perhaps due to some ZnO nanorods being etched away during QD sensitisation in toluene solvent.

The XRD patterns in Figure 6.7 is a study for the formation of QD sensitised ZnO nanorods on bilayered TiO_2/ZnO inverse opal at different stages. The XRD spectra shows the diffraction patterns for the bilayered inverse opals starting from a bilayer of ZnO/ZnO inverse opal (light brown XRD pattern) formed at calcination temperature of 450°C, followed by bilayered TiO_2/ZnO inverse opal at calcination temperatures of 450°C (dark brown XRD pattern), 550°C (purple XRD pattern), 700°C (green XRD pattern), ZnO nanorods on bilayered TiO_2/ZnO inverse opal at 700°C (red XRD pattern) and QD sensitised ZnO nanorods on bilayered TiO_2/ZnO (blue XRD pattern). In all the XRD

patterns, the diffraction peaks are readily indexed to the hexagonal wurtzite phase of ZnO, anatse and rutile phases of TiO_2 crystal structures, from JCPDS references 01-075-1526, 00-001-0562 and 01-076-1941 respectively. The peaks which are marked as black dots correspond to the underlying titanium substrate.

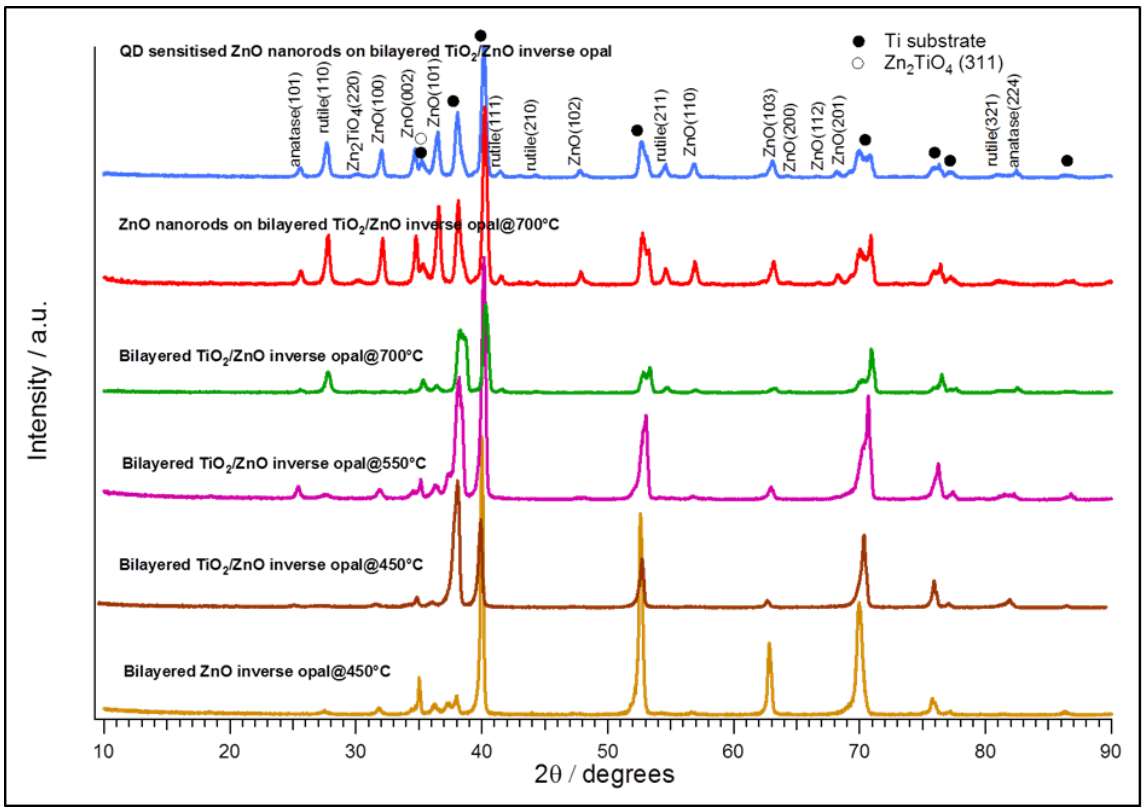

Figure. 6.7 XRD patterns for the study of the formation of QD sensitised ZnO nanorods on bilayered TiO_2/ZnO inverse opal at different stages.

As it can be seen from Figure 6.7, the formation of a bilayer of crystalline ZnO/ZnO (light brown pattern) shows typical inverse opal thin film XRD characteristics with strong (100), (200) and (101) peaks at corresponding 2θ of 32.02°, 34.07° and 36.52° respectively. By changing one of the layers to TiO_2 (forming a bilayer of TiO_2/ZnO inverse opal) anatase peaks begin to appear in

the XRD spectrum at 450°C with the dominant peak present at 25.66°(101) (dark brown pattern). At 550°C (purple pattern), the peaks corresponding to TiO_2 anatase become sharper and more intense due to crystal growth. When the temperature is increased to 700°C (green pattern), rutile peaks start to appear with the dominant peak at 27.74°(110), and the intensities of the anatase peaks decrease due to the phase transition in TiO_2 crystal structure. Furthermore, at this calcination temperature (700°C), new peaks belong to neither TiO_2 nor ZnO begin to appear. These peaks belong to zinc titanate (Zn_2TiO_4) according to JCPDS reference number 25-1164. The characteristic peaks for this crystal structure are present at 30.12°(220), 35.23°(311) and 43.01°(400). After the growth of nanorods (red pattern), the intensity of the ZnO peaks are intensified. The nanorods diffraction peaks follow the direction of the underlying ZnO inverse opal seeds. When this hierarchical structure is further sensitised by quantum dots (blue pattern) the position of the peaks remains unchanged. The characteristic peak of CdSe/ZnS core/shell quantum dots is the (111) diffraction peak[230] corresponding at 2θ value of 25.35°, which may be overlapped by the TiO_2 anatase 25.66°(101). The XRD spectrum in figure 6.8 gives a clearer presentation of the crystal properties for the QD sensitised bilayered TiO_2/ZnO inverse opal with the formation of zinc titanate (Zn_2TiO_4) interface. The XRD data of this nanostructure is summarised in Table 6.2.

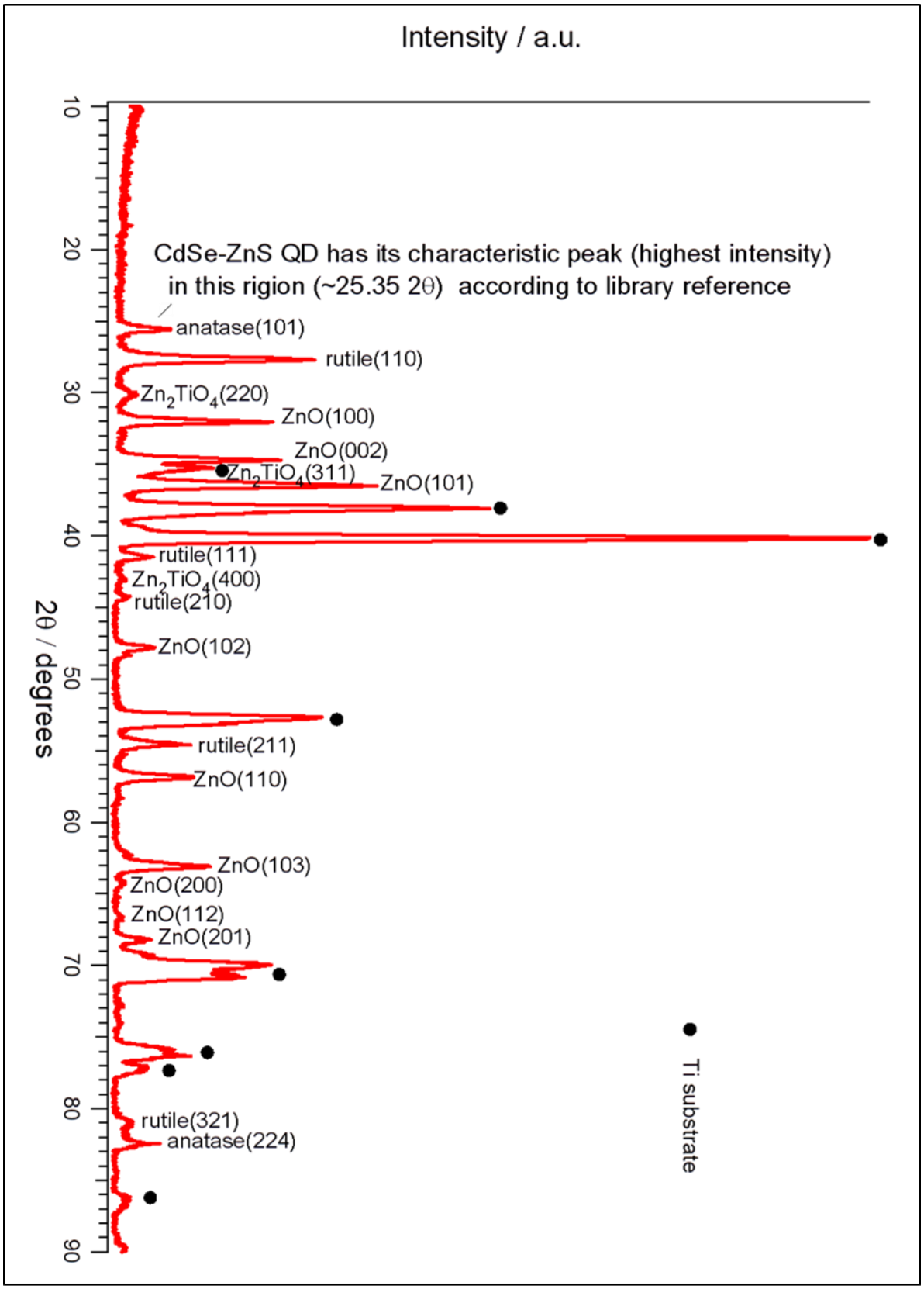

Figure 6.8 Clear presentation of XRD pattern for QD sensitised ZnO nanorods on bilayered TiO_2/ZnO inverse opal with zinc titanate interface

Material	**Diffraction Plane(s) (hkl)**	$2\theta(°)$
ZnO	(100)	32.02
	(002)	34.07
	(101)	36.52
	(102)	47.73
	(110)	56.98
	(103)	63.12
	(200)	64.24
	(112)	66.58
	(201)	68.18
TiO_2	(101) anatase	25.66
	(110) rutile	27.74
	(111) rutile	41.47
	(210) rutile	44.30
	(221) rutile	54.58
	(321) rutile	80.83
	(224) anatase	82.46
Zn_2TiO_4	(220)	30.12
	(311)	35.23
	(400)	43.01

Table 6.2 The XRD data of QD sensitised ZnO nanorods on bilayered TiO2/ZnO inverse opal with zinc titanate interface. The JCPDS reference numbers are: ZnO (01-075-1526), anatase TiO2 (00-001-0562) and rutile TiO2 (01-076-1941).

6.4.4 Comparing Optical Band Gaps of ZnO Inverse Opal and ZnO Nanorods on ZnO Inverse Opal

ZnO is a direct band gap semiconductor with bulk band gap of 3.37 eV[169]. In ZnO nanostructures, the band gap can be altered by many factors including change in morphology (shape and thickness)[167, 231] and crystal structure (size and orientation)[169, 232] by tailoring the synthetic conditions[168]. The engineering of the band gap is an important matter in solar light driven PEC water splitting experiments for enhancing visible light harvesting and forming suitable band edge positions for O_2/H_2 evolution. Figure 6.9 illustrates plots for measuring the optical band gaps of monolayer ZnO inverse opal and ZnO nanorods on monolayer ZnO inverse opal.

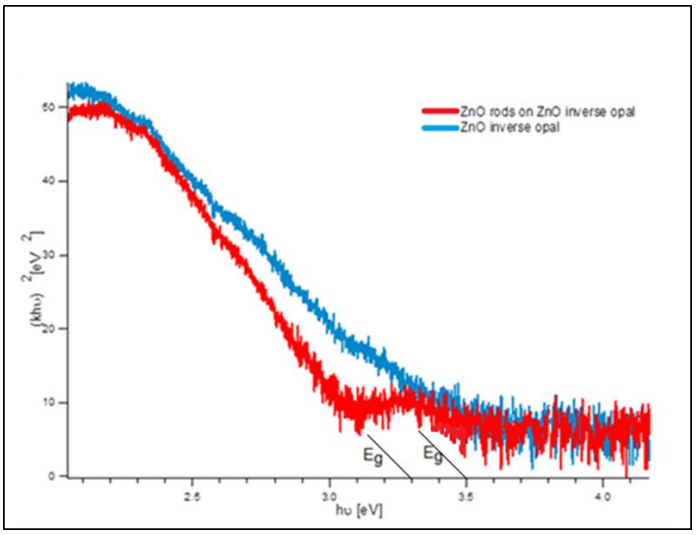

Figure. 6.9 Kubelka–Munk transformed reflectance spectra for band gap measurement of ZnO inverse opal (blue) and ZnO nanorods on monolayer ZnO inverse opal (red).

In order to determine the values for the optical band gaps using reflectance spectroscopy, the measured reflectance values were first converted to absorbance by using the Kubelka–Munk transformation function[167] and expressed using Tauc's relation[169] in terms of incidental photon energy (Chapter 2, Section 2.9) for these direct allowed band gap materials (as ZnO based). The band gap (E_g) values were determined by extrapolating the linear part of the graph in Figure 6.9 to the horizontal (x) axis. From the graph, it can be seen that the band gap for monolayer ZnO inverse opal is 3.5 eV (blue curve), which is larger than that of ZnO nanorods on ZnO inverse opal structure, having a band gap of 3.3 eV (blue curve).

The reduction in the value of the band gap from ZnO nanorods on monolayer ZnO inverse opal may be due to an increase in structural defects. Such defects may be formed at the interface between the ZnO nanorods and the monolayer ZnO inverse opal. The increase in defects can result in reduction of grain size and hence a reduction in band gap[169]. Sharma et al[233] reported that the presence of tensile stress in vertical ZnO nanorods can also reduce the band gap. In this work, the introduction of vertically orientated nanorods on top of the ZnO inverse opal seed may also induce some stress leading to the reduction in the band gap.

The lower energy band gap of ZnO rods on ZnO inverse opals compared to the pristine monolayer inverse opal may be advantageous in PEC water splitting as the absorption of light is red-shifted towards the visible spectrum for improved light harvesting. By further sensitising the nanorod-inverse opal structure with narrow band gap CdSe-ZnS quantum dots, a greater reduction in the band gap is expected[234].

6.4.5 Visible Spectrum of QD Sensitised ZnO Nanorods on Inverse Opals

Figure 6.10 shows the visible light absorption of ZnO nanorods on monolayer ZnO inverse opal before and after QD sensitisation. The spectra clearly show a significant increased visible light absorption with the QD sensitised sample. This indicates that the quantum dots were successfully loaded on the surface of ZnO nanorods on monolayer ZnO inverse opal, giving an absorbance maxima at approximately 530nm in the visible region of the spectrum. No absorption can be detected for the nanostructure in the visible region prior to quantum dot loading. Similar spectra are also obtained when the quantum dots are loaded onto the ZnO nanorods coupled to the bilayered TiO_2/ZnO inverse opal. Both ZnO and TiO_2 absorb light in the UV region between 375-385 nm, with no absorbance in the visible region.

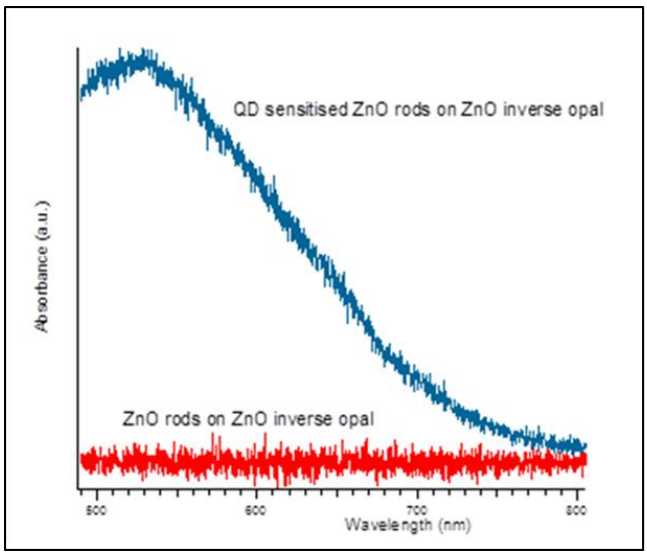

Figure 6.10 Visible spectra of ZnO rods on ZnO inverse opal with and without quantum dot coating.

6.4.6 Photoelectrochemical (PEC) Characterisation

I–V measurements were made in a three-electrode configuration; the as-prepared samples as working electrodes (photoanodes), a platinum plate as counter electrode (cathode) and Ag/AgCl as the reference electrode. All PEC studies were operated in a 1 M KOH solution (pH 13.6) as a supporting electrolyte medium. The working electrodes were illuminated with a 300 W xenon arc lamp equipped with a AM 1.5G filter. The power density of the lamp was adjusted to 300 mW/cm^2. The active illumination area on all the electrodes was kept constant at 0.5×0.5 cm^2. The *I–V* curves were obtained by using an eDAQ potentiostat. A set of linear sweep *I-V* scans were recorded under dark and illuminated conditions. The potential was swept linearly at a scan rate of 10 mV/s between 0.0 and 1.3 V_{RHE} (-1.0 and 0.3 $V_{Ag/AgCl}$). In dark conditions, all the photoanodes showed insignificant photocurrent of less than 0.2 mA/cm^2. This indicates there is insufficient electro-catalytic O_2/H_2 evolution when not illuminated. Under illumination, the photocurrents were measured at the bias potential of 1.23 V_{RHE} (corresponding to the potential required to split water). The current density–voltage *(I–V)* and photoefficiency characteristics of the photoanode samples under these conditions are presented in the next two sections (6.4.6.1 & 6.4.62).

6.4.6.1 PEC Performances at Different Stages in the Formation of QD Sensitised ZnO Nanorods on Monolayer ZnO Inverse Opal

The efficiency of the PEC may be enhanced if a monolayer ZnO inverse opal photoanode is coupled with ZnO nanorods and further sensitised with QDs,

which helps to harvest more visible light from the xenon lamp light source. Figure 6.11 shows the I-V characteristics (a) and photoconversion efficiency (b) curves at different stages in the creation of QD sensitised ZnO nanorods on monolayer ZnO inverse opal. The black curve in Figure 6.11(a) corresponds to PEC measurement under dark conditions. The brown curves in figure 6.11(a and b) correspond to the aggregated ZnO nanorods without templating. The green curves correspond to the monolayer ZnO inverse opal, the red curves to the ZnO nanorods on monolayer ZnO inverse opal and the blue curves to the QD sensitised ZnO nanorods on monolayer ZnO inverse opal photoanodes under illumination. The corresponding photovoltaic parameters of the four samples are summarised in Table 6.3.

Photoanodes	**(J_{max})/mAcm^{-2} at 1.23V$_{RHE}$**	**Onset potential/V_{RHE}**	**η%**
Aggregated nanorods	0.50	0.462	0.18
Monolayer ZnO inverse opal	0.88	0.449	0.32
ZnO nanorods on monolayer ZnO inverse opal	1.48	0.402	0.56
QD sensitized ZnO nanorods on monolayer ZnO inverse opal	2.91	0.381	0.99

Table. 6.3 PEC performance parameters at different stages in the formation of QD sensitised ZnO nanorods on monolayer ZnO inverse opal.

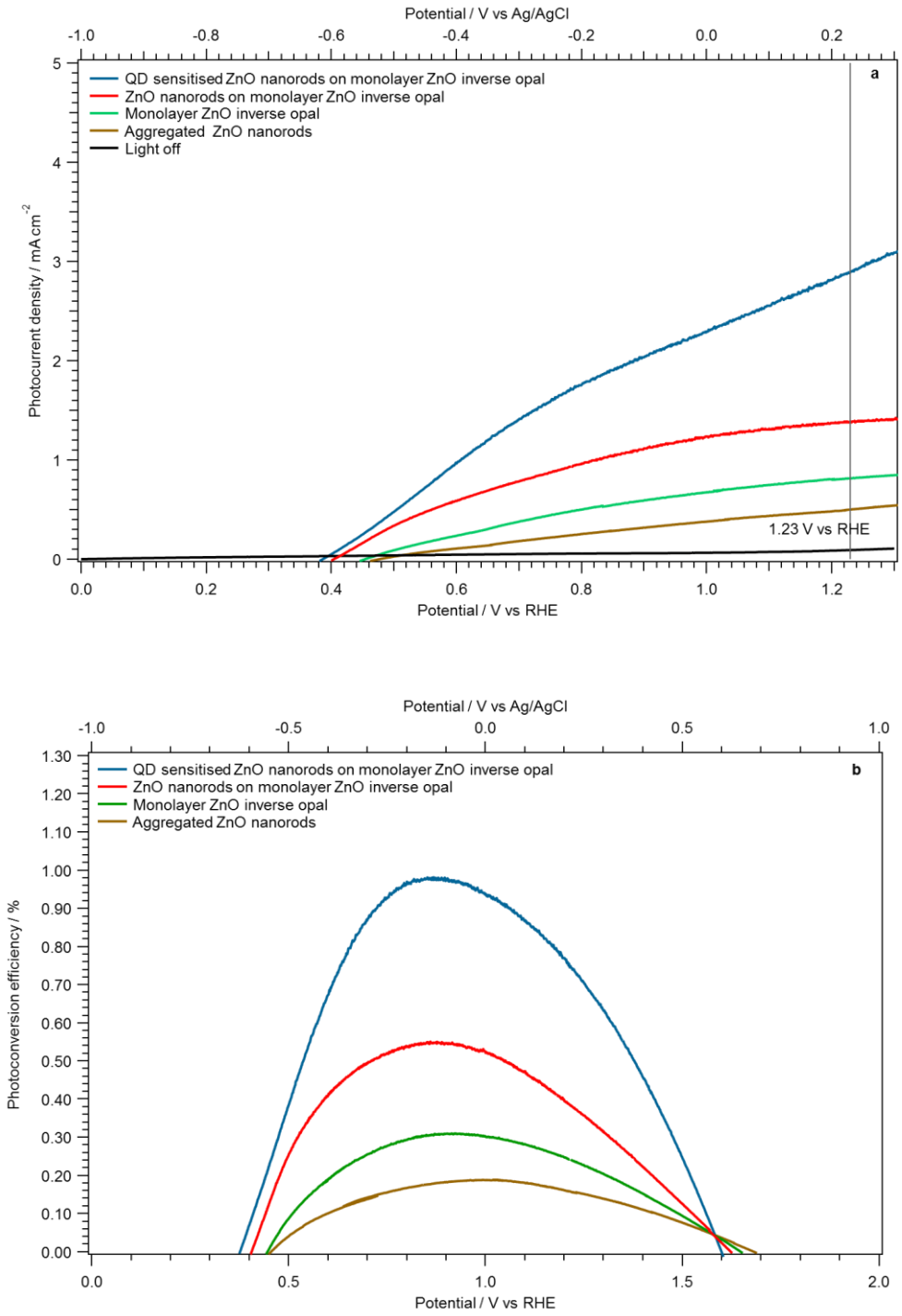

Figure. 6.11 (a) *I-V* characteristics and (b) Photoconversion efficiency curves at different stages in the formation of QD sensitised ZnO nanorods on monolayer ZnO inverse opal.

The increasing photocurrent, starting from ZnO nanorods aggregate to the final structure of hierarchical QD sensitised nanorods on inverse opal can

be clearly seen in Figure 6.11. In the first stage, the aggregated rods shows some photocurrent density which is attributed to the nature of the ZnO wide band gap harvesting light in the UV region. Additionally, the aggregates are made up of ZnO nanoparticulates containing porous ZnO crystallites (~26 nm), which can result in an increase of the internal surface area and facilitate the migration of electron–hole pairs to the surface while reducing the surface disorder due to crystallinity, leading to some useful photoconversion in the system (brown curves).

Comparing the inverse opal structure with the aggregated nanorods, the photocurrent density and photoefficiency are almost doubled from the aggregate form (green curves). This can be attributed to the considerable increase in the internal surface area caused by the porosity and interconnectivity of the inverse opal structure[4] as well as the enhanced internal light scattering through the photonic structure. The 410 nm pores can provide a channelled “highway”[2] for electrolyte diffusion. Such a quick diffusion of electrolyte can facilitate efficient ion mobility within the electrolyte. The crystallised interconnection within the inverse opal also helps for the charge carrier moving towards the counter electrode. In the aggregated nanorods, the charge transport is possibly limited to hopping between particles, but as the morphology improved in the inverse opal structure, higher charge collection may be achieved. Therefore, a thin monolayer inverse opal film can be sufficient to harvest light, resulting in a shortening of the distance for electron transport to the underlying titanium substrate in the PEC set up[2].

The main photonic property of the inverse opal without the presence of an interface (*i.e.* formation of a bilayer with another surface) is slow photon

phenomenon near the photonic stop band edges (Chapter 1)[102, 103, 139, 140]. This property can increase the effective optical path length of light, thereby resulting in an increased rate of photon/matter interaction[12]. The localisation of light at the photonic stop band edges of the ZnO inverse opal may contribute to a higher probability of white light absorption and a larger population of electron-hole pairs[103, 140].The periodic variation of the refractive index in the inverse opal (i.e ZnO and the electrolyte filled pores) produces photonic stop band, where photons cannot be propagated through and are consequently reflected back. The photonic stop band can be determined by the modified Bragg equation of diffraction for inverse opals[27]. For a first order Bragg diffraction, on the FCC (111) planes of the ZnO inverse opal at the normal incidence of light, the equation can be written as follows[6]:

$$\lambda_{max} = 1.633D[\emptyset n_{ZnO\ walls} + (1 - \emptyset)n_{electrolyte}] \qquad \text{(Equation 5.1)}$$

Where λ_{max} is the reflectance peak maximum in the UV/Vis spectrum corresponding to the photonic stop band, D is the interlayer spacing, which is 0.87[102] times the diameter of the cavity (pore spheres). Here, the pore diameter is 255 nm (due to the presence of ZnO nanorods grown on the macropores of monolayer ZnO inverse opal (Section 6.4.2), $\emptyset$ is the volume fraction occupied by ZnO solid wall (which is taken as 0.26 for the FCC structure) and n is the refractive index with $n_{ZnO\ walls} = 2.004$ and $n_{electrolyte} = 1.409$. By inserting these values to the above equation, the position of the photonic stop-band (λ_{max}) is determined to be about 651 nm, which lies in the visible region of the solar spectrum. In general, slow photons at the red-edge of the photonic stop-band have an associated electromagnetic field predominantly localised on the

high refractive index material (in this case ZnO walls) while that at the blue-edge is mainly localised on the low refractive index material (in this case electrolyte filled macropores)[12]. The degree of localisation of light, depends on the refractive index contrast with a higher contrast giving a higher degree of light confinement. In this inverse opal structure, the attenuation in group velocity of light in combination with enhanced light confinement at the photonic stop-band edges may be responsible in optical enhancement. However, it has been suggested that the photonic crystal properties of an inverse opal structure alone, cannot bring an overall increase in photoefficiency[12]. This may be due to the fact that, the strong reflectivity of the photonic stop-band outweighs the narrow wavelength window of slow photon enhancement (in this case at about 651 nm), so that the overall effect can be a decrease in the light harvesting properties instead. Therefore, the photoefficiency enhancement factor for the monolayer ZnO inverse opal can predominantly be due to the high surface area and crystallinity of the structure and not related to photonic effects.

By adding the ZnO nanorods onto the monolayer inverse opal, further enhancement is achieved (red curves). A fundamental property of nanorods is the high electron diffusion length[2, 4]. This phenomenon arises from the direct electron pathway nanorods offer, due to their structures being one dimensional, with minimum defects or grain boundaries. This can result in the reduction of charge traps and recombination centres[4]. ZnO nanorods have excellent charge collection properties. This was previously illustrated for ZnO nanowires[2] by explaining that in such a structure, the size of the individual nanowire was much larger than the Debye-Huckel length of ZnO (~4nm). The Debye-Huckel length is the scale over which mobile charge carriers screen out electric fields in a

conducting material. This length is proportional to the reciprocal of the ionic strength; the smaller the concentration of ions, the less shielding of the charge surface and the larger the Debye length will become, leading to the enhancement of charged surface properties[235, 236]. This would establish an internal electric field within the nanowires, which would be able to assist the carrier collection by separating injected electrons form the surrounding electrolyte and sweeping them toward the collecting electrode. From Table 6.3, it can be seen that the nanorod formation stage has the most negative onset potential shifting than any other stage (a negative shift of 0.047 V_{RHE} from the inverse opal to the nanorod formation stage can be detected). The smallest bias needed to completely separate the photogenerated electron-hole pairs at this particular stage, indicate that the ZnO nanorods have a low series resistance. This can be attributed to their properties stated above, making them more effective charge separators and thus, better light harvesters. The combination of ZnO nanorods onto the ZnO inverse opals may also promote a synergistic effect with respect to increasing internal surface area possessed by both the ZnO inverse opal and ZnO nanorods.

A further enhancement factor may be explained in terms of the reduction in the optical band gap. From Figure 6.9, it can be seen that the optical band gap is decreased by approximately 0.3 eV from the monolayer ZnO inverse opal to the ZnO nanorod-inverse opal stage. The decrease in band gap means light absorption properties of the nanorod-inverse opal structure is red-shifted toward the visible region of the solar-spectrum, resulting in enhanced light harvesting.

The photonic properties of the inverse opal when coupled to the nanorods may also contribute, further improving light harvesting properties. This

is due to back-reflections[4] and formation of resonant modes[102] at the nanorod-inverse opal interface, caused by the inverse opal photonic crystal. It was previously predicted that coupling photonic crystals, such as inverse opals, to another nanocrystalline layer would create localised states in the surface of the non-opal layer (in this case the ZnO nanorods). The monolayer ZnO inverse opal layer may therefore act as a reflective mirror in this bilayer architecture enhancing photoefficiency, with the enhancement in the photocurrent over a broad range of wavelength[12], with its photonic stop band centred at 651 nm, as stated earlier. Another photoefficiency enhancement factor related to the photonic crystal properties of the monolayer ZnO inverse opal when coupled to the ZnO nanorods, may arise from the creation of standing waves (resonant modes) at the interface, giving rise to photon localisation within the ZnO nanorods and result in a greatly increased probability of photon absorption over a range of frequencies[140]. These light-matter interaction phenomena in opal/non-opal bilayer structures were later confirmed by using Incident Photon to Current Efficiency (IPCE) measurements[139, 140].

The improved PEC properties from the inverse opal to the nanorod-inverse opal stage (~2.6× increase in the photocurrent and ~75% increase in the photoefficiency values) in this work is probably due to the presence of an intimate physical contact between the two crystalline phases of the nanorods-inverse opal structure, which leads to the strong opto-electrical coupling effects stated above.

In the final stage, the photoanode was sensitised by CdSe/ZnS quantum dots, leading to highest photocurrent density and efficiency values of 2.91 mA/cm^2 and 0.99% respectively. The main factor for this is the narrow

band gap nature of the CdSe/ZnS core-shell quantum dots (1.74 eV[224] for the CdSe active phase) allowing light harvesting in the visible region. Therefore, by coupling the quantum dots with the nanorods-inverse opal structure, light can be harvested in both UV and visible regions of sunlight spectrum.

By looking at Table 6.3, it can be seen that the onset potential is reduced further in this final stage, owing to better charge separation and faster kinetics (photon injection properties[188]) attributed to the quantum dots. Quantum dots have large intrinsic dipole-moments which may lead to rapid charge separation in the band alignment configuration. When photons excite the electrons from the valence band to the conduction band of the quantum dot, the injection of the photogenerated electrons are made energetically possible into the conduction band of the ZnO nanorods-inverse opal structure. This is attributed to the more negative (higher) conduction band of the quantum dots than that of the ZnO producing an electric field with electrons and holes moving in opposite directions producing a junction. An n-n type(II) energy band alignment between the two semiconductors is formed, which favours interfacial charge transfer and separation, due the high dipole moments of the quantum dots. A further potential factor contributing to the PEC enhancement from the addition of quantum dots can be attributed to their unique property of generating multiple excitons (multiple electron-hole pairs per photon)[223, 237] under illumination. This phenomenon can significantly increase the light harvesting properties of the photoanode. Quantum dots act as “light antennas”[188] in this hierarchical system.

A synergistic effect from quantum dots-inverse opal coupling may also arise due to the slow photon phenomena at the band edges of the inverse opal photonic crystal, resulting in enhanced efficiency. The monolayer ZnO inverse

opal has a photonic band gap of 651 nm as mentioned earlier. CdSe-ZnS quantum dots show an optical absorption peak at ~530 nm in the visible region arising from its narrow electronic band gap. Therefore the photonic band edge of the inverse opal and the quantum dot absorption edge may have a synergistic effect on visible light absorption. At photonic stop-band edges, the group velocity of light is decreased due to the bending of the photon dispersion curve[103]. This leads to light trapping (heavy photon phenomenon) at the absorption edges of the quantum dot. This light trapping phenomenon is useful to enhance light absorption properties of CdSe based quantum dot sensitisers due to its low extinction coefficient[4]. The slow photon phenomenon can manifest itself by an increase in the absorbed light intensity when using IPCE measurements at the quantum dot absorption edges as reported in other works[4, 188].

The use of CdSe-ZnS quantum dots in the form of core-shells instead of using the neat CdSe quantum dots alone is advantageous. A drawback of using quantum dots in photovoltaic experiments is the significant carrier loss caused by non-radiative recombination processes at the interface of quantum dots with the photoanode and electrolyte, and the adjacent quantum dots. Photo-degradation and reduction in fluorescence quantum yields[238] are other limiting factors. These shortcomings are significantly reduced by using ZnS inorganic semiconductor as a shelling material onto the optically active CdSe phase. The role of a ZnS shell is to passivate the surface of the CdSe core from its surrounding media[148]. The ZnS shell has a higher valance and conduction band edge, forming a type-*I* band alignment heterostructure[239]. The heterostructure band alignment may also increase the rate of charge transport to the nanorod-

inverse opal system due to the formation of an internal electric field at the core-shell interface of the quantum dot and also reduce back-recombination due to the ZnS barrier shell[131]. Figure 6.12 shows a representation of charge transport processes in a type-*II* quantum dot sensitised ZnO nanorod-inverse opal heterostructure as a photoanode in a PEC water splitting device. The conduction band edges of ZnO nanorod and inverse opal are assumed to be equal with the latter having a larger band gap as discussed earlier in Section 6.4.5. In this diagram the visible light harvesting mechanism due to the presence of QDs are shown. The ZnO nanorod- inverse opal system can also harvest the UV part of solar spectrum. The synergistic effect facilitates enhanced photocurrent and improved photoconversion efficiencies.

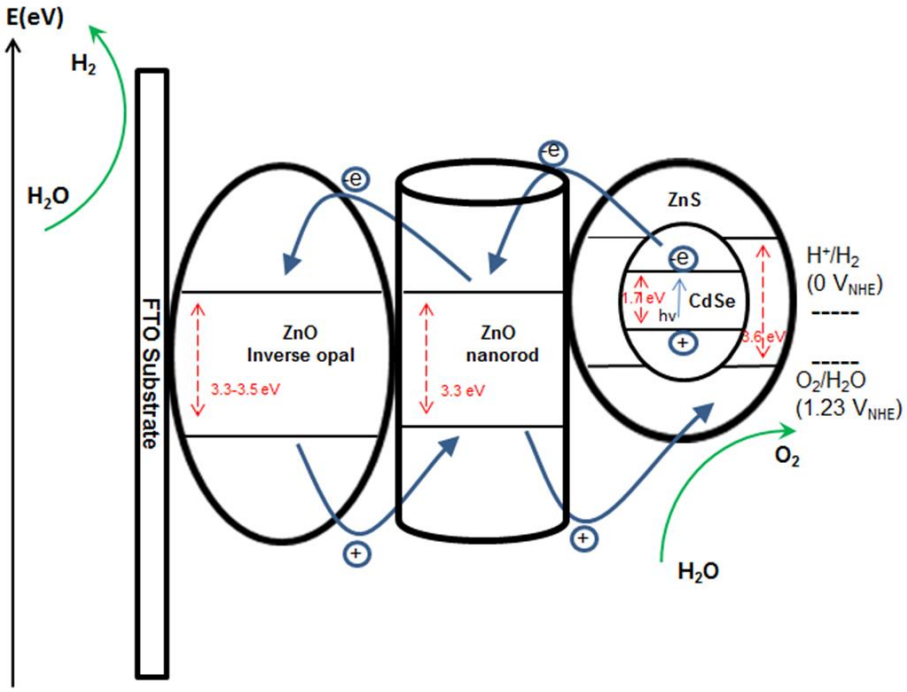

Figure. 6.12 Schematic representation of charge transfer processes in QD sensitised ZnO nanorod-ZnO monolayer inverse opal photoanode in PEC water splitting (visible light harvesting) under bias potential.

6.4.6.2 PEC Performances at Different Stages in the Formation of QD Sensitised ZnO Nanorods on Bilayerd TiO_2/ZnO Inverse Opal

The efficiency of the PEC can be further improved if a layer of TiO_2 inverse opal is introduced to the QD sensitised ZnO nanorods on monolayer ZnO inverse opal system explained before in Section 6.4.6.1. This is due to the formation of Zn_2TiO_4 interface between the monolayer TiO_2 (bottom layer) and monolayer ZnO (top layer) inverse opals, which may enhance charge separation and transport properties of this hierarchical system. Figure 6.13 show the I-V characteristics (a) and photoconversion efficiency (b) curves at different stages in the formation of QD sensitised ZnO nanorods on bilayered TiO_2/ZnO inverse opal. The black curve in Figure 6.13(a) corresponds to PEC measurement under dark conditions. The brown curves in Figure 6.13(a and b) correspond to the bilayered ZnO inverse opal, the green curves to the bilayered TiO_2/ZnO inverse opal with zinc titanate interface (formed at 700°C), the red curves to the ZnO nanorods on bilayered TiO_2/ZnO inverse opal with zinc titanate interface, the purple curves to the QD sensitised ZnO nanorods on bilayered TiO_2/ZnO inverse opal with zinc titanate interface photoanodes under illumination. The QD sensitised photoanode was also exposed to the electrolyte media of the water splitting setup for one hour before PEC measurements (the blue curves). The spikes (photocurrent noises) observed at the beginning of the I-V and photoefficiency curves corresponding to the QD sensitised samples (blue and purple), likely come from the underlying titanium substrates holding these nanostructures; some areas of the substrates may not be fully covered by the samples and currents are produced by conducting titanium substrates interacting with the electrolyte medium. The other possible source of the small

photocurrent peaks may be due to the contamination of electrolyte media by some of the ZnS shells of CdSe/ZnS core-shell quantum dots getting detached from the sample in the electrolyte solution. These species may be oxidised by the photogenerated holes form the photoanode sample, leading to higher photocurrent peak. The spikes diminish as the soon as the contamination is settled and fully oxidised. The corresponding photovoltaic parameters of the five samples are summarised in Table 6.4.

Photoanodes	**(J_{max})/mAcm^{-2} at 1.23V_{RHE}**	**Onset potential/V_{RHE}**	***η%***
Bilayered ZnO/ZnO inverse opal	2.41	0.576	0.49
Bilayered TiO_2/ZnO inverse opal (with zinc titanate interface)	3.84	0.465	0.69
ZnO nanorods on bilayered TiO_2/ZnO inverse opal (with zinc titanate interface)	4.50	0.411	0.78
Quantum dot sensitized ZnO nanorods on bilayered TiO_2/ZnO inverse opal (with zinc titanate interface)	10.02	0.200	2.35
Quantum dot sensitized ZnO nanorods on bilayered TiO_2/ZnO inverse opal (with zinc titanate interface) after 1 h electrolyte exposure	6.32	0.292	1.13

Table. 6.4 PEC performance parameters at different stages in the formation of QD sensitised ZnO nanorods on bilayered TiO_2/ZnO inverse opal.

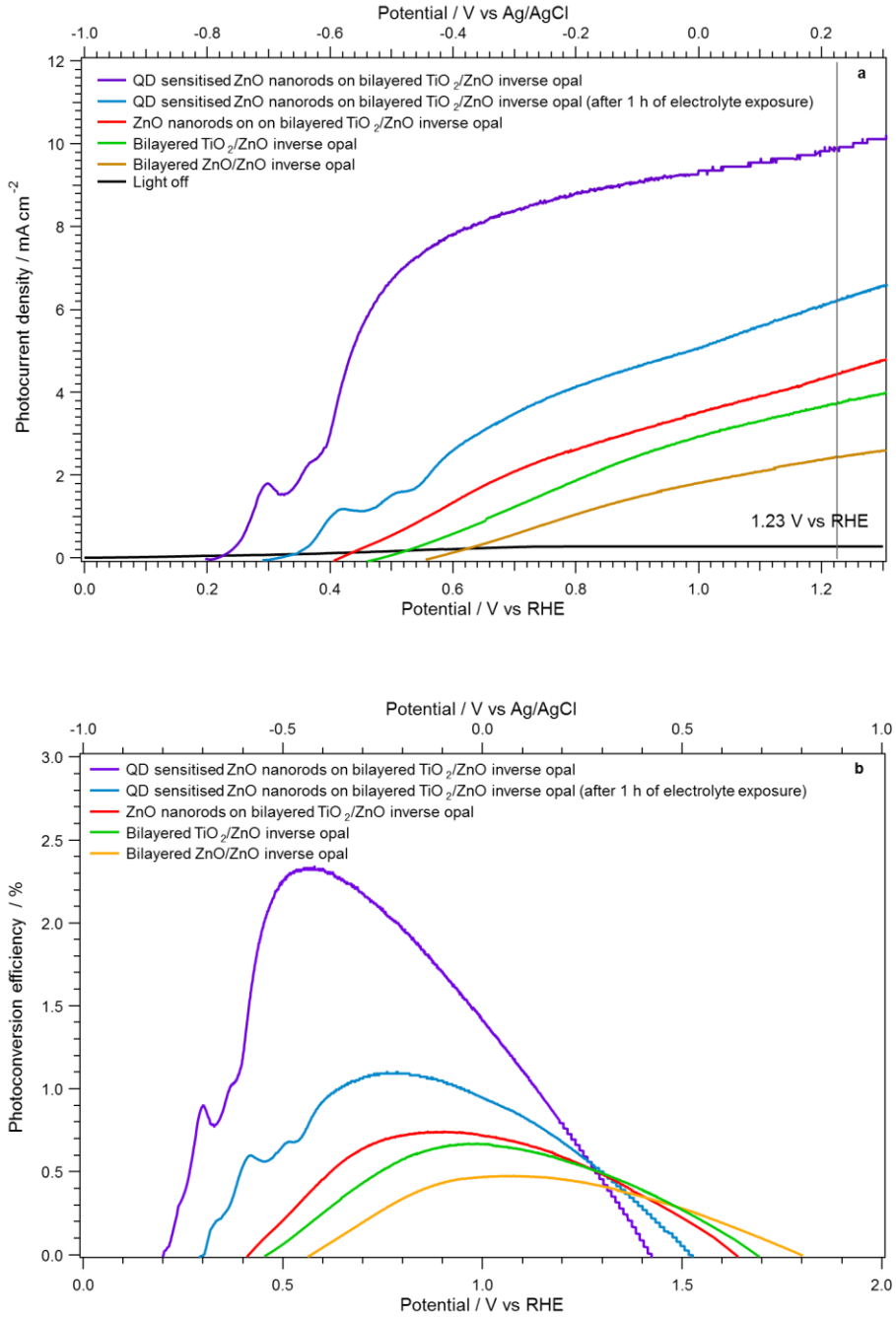

Figure. 6.13 (a) *I-V* characteristics and (b) Photoconversion efficiency curves at different stages in the formation of QD sensitised ZnO nanorods on bilayered TiO_2/ZnO inverse opal.

The ascending pattern of PEC enhancement from the starting bilayered ZnO/ZnO inverse opal to the final product of QD sensitised ZnO nanorods on bilayered TiO_2/ZnO inverse opal is clearly demonstrated in Figure 6.13. It

confirms the contribution of each step in enhancing photoefficiency. The bilayered ZnO/ZnO inverse opal (brown curves (Figure 6.13)) produce some photocurrent density owing it to the ZnO semiconductor properties as a wide band-gap light harvester and also to the inverse opal morphology it possesses. The bilayered inverse opal with its high surface area and three-dimensional interconnected macroporous skeleton can enhance charge transport kinetics. The photonic properties of the inverse opal include the ability to trap, reflect and slow the light, and thus act as an infrastructure to enhance the light-matter interaction through optical coupling, which contributes to photoefficiency enhancement.

By changing one of the ZnO layers into TiO_2 inverse opal layer (the bottom layer), further efficiency enhancement occurs (green curves (Figure 6.13)). This is due to the junction that is formed between the two metal oxides forming a type-II band alignment[240] and formation of a zinc titanate charge barrier interface (formed at 700°C calcination temperature). At lower temperature of 550°C, the TiO_2/ZnO heterojunction produces an internal electric field that is caused by electron movement from the higher positioned conduction band edge[133] of ZnO (-0.35 V_{RHE}) to the lower TiO_2 (-0.17 V_{RHE}) layer and simultaneous movement of holes in the opposite direction. This may result in faster charge transport and less recombination. Moreover, it has been reported that ZnO in ZnO treated TiO_2 semiconducting nanomaterials can act as a charge barrier[241] and/or provide a surface dipole across the TiO_2 layer due to its higher isoelectric point (IEP)[242]. The latter phenomenon can shift the conduction band edge of TiO_2 in a negative direction reducing charge recombination and resulting in accumulation of a larger number of electrons in

the TiO_2/ZnO heterojunction. This elevates the Fermi level of the system, leading to an increase in the internal energy[240], and thus better water splitting properties. The charge barrier phenomenon can suppress back-charge recombination. Both factors can decrease the onset potential and increase the photocurrent density, leading to higher photoefficiency. The TiO_2/ZnO heterojunction can be further optimised to increase PEC enhancement by calcining the bilayered inverse opal to 700°C, forming a thin zinc titanate layer at the interface, acting as a charge barrier. The formation of the barrier is confirmed by the introduction of three peaks in the XRD spectrum of the hierarchical structure which are assigned to the (220), (311) and (400) planes at the corresponding 2θ values of 30.12°, 35.23° and 43.01°; a zinc titanate cubic phase[243] (Figure 6.8).

Compared with the bilayered homostructure of ZnO/ZnO inverse opal (brown curves (Figure 6.13)), the onset potential for the heterostructured bilayer of TiO_2/ZnO inverse opal (green curve (Figure 6.13)) is shifted more negatively from 0.576 to 0.465 V_{RHE} (Table 6.4). This behaviour may be attributed to the formation of zinc titanate at the interface of the TiO_2/ZnO system, acting as a charge barrier contributing to significant reduction in charge recombination losses at the interface of the bilayered inverse opal. Although the conduction band edge of ZnO (-0.35 V_{RHE}) [133] is lower than that of the Zn_2TiO_4 (-0.95 V_{RHE}) [133] and charge injection is energetically not favoured in that direction (*i.e.* movement of electron from ZnO to zinc titanate), the photogenerated electrons may overcome this by quantum tunnelling through this thin barrier. The photogenerated electrons are then transported to the lower positioned conduction band edge of TiO_2 (-0.17 V_{RHE})[133] and thus, charge injection is

energetically favoured. The relatively high energy barrier between the zinc titanante and TiO_2 layers (0.78 V_{RHE}) forbids the classical back-flow of electrons, suppressing recombination. Simultaneously, the holes are moved in the opposite direction, leading to a strong internal electric filed produced at two separate junctions. Therefore the TiO_2/ZnO heterojunction coupled with the zinc titanate interface barrier can simultaneously reduce back-recombination and increase charge transport kinetics leading to higher photocurrent density and photoefficiency, as represented by the results obtained in this work. Figure 6.14 shows the band gap energy diagram for the bilayered TiO_2/ZnO inverse opal with a zinc titanate interface.

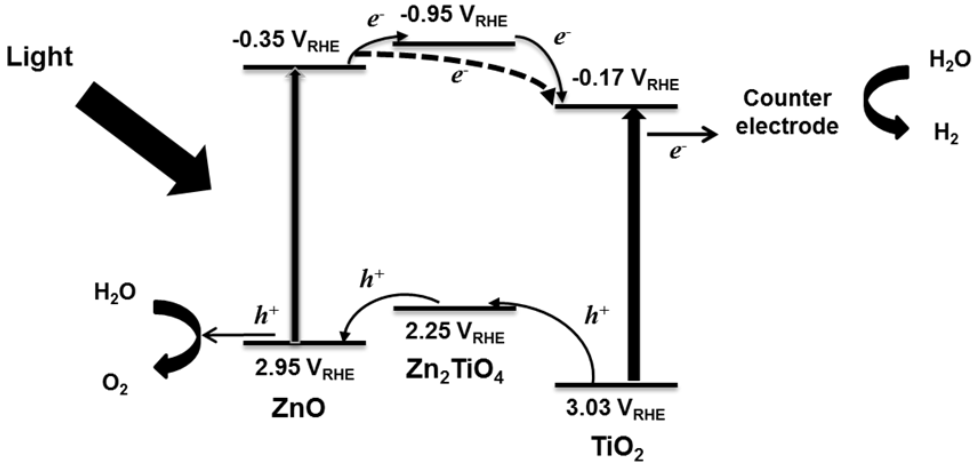

Figure. 6.14 Band gap energy diagram for the heterostructure of bilayered TiO_2/ZnO inverse opal with a Zn_2TiO_4 interface used as a photoanode in PEC water splitting.

The higher valence and conduction band edges of Zn_2TiO_4 than those of TiO_2 and ZnO have been confirmed by computational methods using dynamic functional theory (DFT) approaches in two separate studies carried out by Conesa[244] and Ali et al[245]. Both studies argued that these higher band edges

could be due to the Ti and Zn orbitals which could mutually dilute one another at specific sites of the titanante crystal structure. In terms of the electronic band structure, they argued that the split of the 3d orbitals of the Ti (due to t_{2g} and e_g-type components) in the bottom of the conduction band which was narrower than in the TiO_2. This is possibly due to the lower overall overlap between these 3d orbitals resulting from the smaller overall density of Ti atoms in the titanante structure. The Zn-4s contributions in the conduction band seems to lie at higher energies than that of ZnO, as such orbitals mix to some extent with the e_g branch of the Ti conduction band, but less with the t_{2g} branch, possibly due to the nonbonding character of t_{2g}, giving rise to higher conduction band edge in Zn_2TiO_4. The higher valence band edge of Zn_2TiO_4 could again be due to the overlap of the orbitals, namely Zn-3d and O-2p, leading to hybridisation at energies closer to the Fermi level of the titanante structure. A wide band gap of 3.1 eV exists between the maximum of valence band and the minimum of conduction band of Zn_2TiO_4[246].

By adding the ZnO nanorods to the heterojunction system further enhancement is achieved (red curves (Figure 6.13)). This is attributed to several properties of nanorods, including, direct electron-transport pathway, reduced carrier diffusion length and diminished charge recombination, due to the result of their one-dimensional morphology which prevents defects or grain boundaries[2, 4]. This can lead to fast charge transport at the photoanode /electrolyte interface by reducing the number of interparticle hops[220, 247]. The nanorod-inverse opal synergistic effects raised from increase in the internal surface area, coupled with photonic induced properties from the inverse opal (as discussed previously in Section 6.4.6.1), may further improve efficiency. The

realisation of such electrical and optical coupling results in significant efficiency enhancement, which may be attributed to the intimate physical contact that is formed between the bilayered TiO_2/ZnO inverse opal and the ZnO nanorods. This indicates the successful synthetic methods used in this work.

By sensitising the hierarchical structure with narrow band gap CdSe/ZnS core-shell quantum dots, the photocurrent density and the photoefficiency are significantly improved (purple curves in Figure 6.13). The reasons and the mechanism for such enhancements were discussed before in Section 6.4.6.1. The drastic photocurrent increase from the onset potential in the *I-V* curve for this sample (purple curve in Figure 6.13 (a)) may demonstrate the much improved charge separation and transport properties of this hierarchical structure compared to other samples which show less onset photocurrent increase (other *I-V* curves in Figure 6.13(a)). The structure shows photodegradation after being exposed to the electrolyte medium for 1 hour (blue curves in Figure 6.13) possibly owing to photocorrosion of the quantum dots and the reduction of photostability in the hierarchical ZnO nanorods on bilayered ZnO/TiO_2 inverse opal nanostructure by losing some structural integrity in the electrolyte medium.

The on/off *I-V* curve in Figure 6.15 clearly shows the behaviour of charge separation & transport under illumination and charge relaxation & recombination under dark conditions. The curve also shows spikes of photocurrent initially. These photocurrent spikes are possibly due to the accumulated photoexcited holes at the photoanode/electrolyte interface. They are a result of carrier oxidised trap states of the semiconducting photoanode sample, or slow oxygen evolution reaction kinetics[248]. This actually tell us that the charge mobility is

restricted, which is understandable as the structural complexity of the sample increases and the presence of Zn_2TiO_4 charge transport barrier between the ZnO and TiO_2 layers is expected. Initially there is high current, since there is no charge accumulated in the oxide layers. However, once the charge begins to accumulate, the current will drop, then recover as the potential increases. Such spikes can be suppressed when photoexited holes experience less or no barrier to oxidising the electrolyte under better interface charge transfer kinetics.

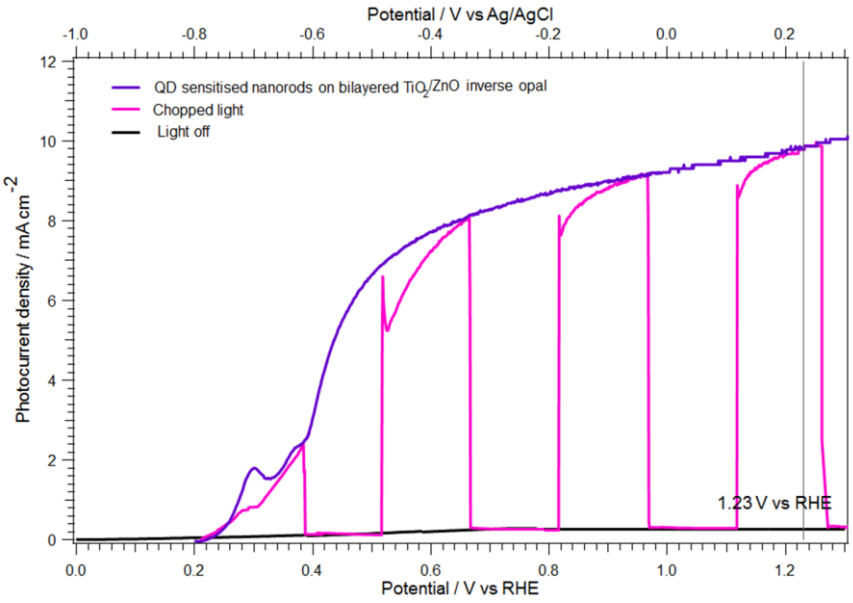

Figure. 6.15 *I-V* curve for QD sensitised ZnO nanorods on bilayered TiO_2/ZnO inverse opal with 15 s light on/off cycles.

Figure 6.16 provides a schematic representation of possible electron-hole transport processes among junctions in the QD sensitised ZnO nanorods on bilayered TiO_2/ZnO inverse opal photoanode in a PEC water splitting device. The hierarchical structure is synthesised at 700°C, where a zinc titanate interface at the TiO_2/ZnO junction is formed acting as a charge barrier. For better illustration of the heterojunctions, the ZnO nanorod and the ZnO inverse

opal top layer are assumed as one species. In this diagram the visible light harvesting mechanism due to the presence of QDs are shown. The TiO_2/ZnO system can also harvest the UV part of solar spectrum. The synergistic effect facilitates enhanced photocurrent and improved photoconversion efficiencies.

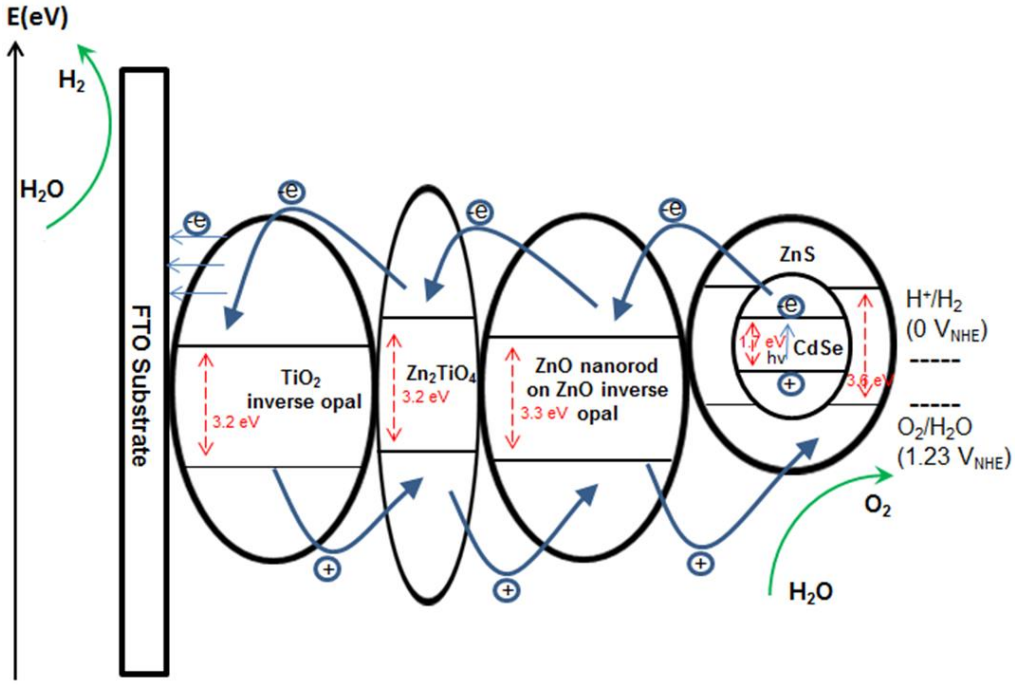

Figure. 6.16 Schematic representation of the electron-hole transport processes in QD sensitised ZnO nanorods on bilayered TiO_2/ZnO inverse opal with a Zn_2TiO_4 interface used as a photoanode in PEC water splitting (visible light harvesting) under bias potential.

By comparing the results of the QD sensitised ZnO nanorods on monolayer ZnO inverse opal (Figure 6.11) with the QD sensitised ZnO nanorods on bilayered TiO_2/ZnO inverse opal (Figure 6.13) with respect to their PEC results, it is obvious that the improvements are much more pronounced in the latter photoanode. A photocurrent density increase to 10.02 mA/cm^{-2} compare to 2.91 mA/cm^{-2} and conversion photoefficiency increased to 2.35%

compare to 0.99% from QD sensitised ZnO nanorods on bilayered TiO_2/ZnO inverse opal system to the QD sensitised ZnO nanorods on monolayer ZnO inverse opal can be detected. These improved results are potentially due to the formation of the titanate barrier, coupled with the TiO_2/ZnO heterojunction possessed in the latter photoanode as opposed to the monolayer ZnO system. Such junctions can increase charge transport and significantly suppress recombination. The fundamental property of quantum dots as "light antennas"[188] can be significantly realised in this heterojunction system. A significant amount of the photogenerated electrons produced by such quantum dots can contribute to water splitting with the presence of the junctions.

6.5 Conclusion

A novel and facile synthetic approach was used to synthesise ZnO nanorod-monolayer ZnO inverse opals and ZnO nanorod–bilayered TiO_2-ZnO inverse opal hierarchical structures for applications in PEC water splitting devices. SEM, XRD and *I-V* characterisations confirm that the hierarchical systems possess intimate physical contact, high crystallinity and well-defined morphologies with large coverage areas and minimal cracks and boundaries.

The PEC performance of photoanodes with different hierarchical structures show ascending enhancement contributions from each stage. The enhancement factors are attributed to the positive effects arising from the high internal surface area and the photonic properties of the macroporous inverse opals, the good charge separating properties of the nanorods. Such synergistic effects of ZnO nanorods-inverse opal system can realise the dual benefits of

light trapping and surface area enhancement. In the bilayered heterostructure system of TiO_2/ZnO system further improvement is achieved through the formation of titanante interface acting as a charge barrier to reduce charge recombination.

The photoefficiency of the hierarchical structures are improved further by sensitising them with narrow band gap CdSe/ZnS core-shell quantum dots acting as “light antennas”, and thus, light harvesting in the visible region of the spectrum. The QD sensitised hierarchical structure of TiO_2/ZnO shows a very pronounced enhancement in the PEC parameters compared to the single system. Such a large improvement can give rise to the realisation of heterojunction nanostructures coupled with highly photon absorbing quantum dots as promising light harvesters in PEC devices.

Throughout the work, it was clear that the predominant factors in determining the performance of the photoanodes in PEC water splitting experiments are based on the balance between the photogenerated electron transport and charge recombination. The present synthetic method in this work can be readily extended to the creation of many other bilayered or layer-by-layer heterojunction inverse opals coupled with nanorods, that can be tailored to achieve specific qualities, and be utilised for various PEC applications.

Chapter 7: Bilayered Inverse Opal Photoanodes in Dye Sensitised Solar Cells (DSSCs)

7.1 Abstract

Bilayered TiO_2-ZnO (as ZnO on top), ZnO-TiO_2 (as TiO_2 on top) , and TiO_2-TiO_2 inverse opal heterostructures were used as photoanodes in DSSCs. Potassium titanate ($K_2Ti_4O_9$) nanobelts were also synthesised *via* the solid state reaction between K_2CO_3 and TiO_2 and then subsequently coupled with a ZnO inverse opal. Photocurrent-voltage (*I*-*V*) characteristics were measured in a two electrode DSSC set-up with a I_3^-/I^- electrolyte placed between the two electrodes, under illumination by a 300 W xenon arc lamp with an AM 1.5G filter. The intensity of the lamp was adjusted to 100 mW/cm^2. The effects of cation identity and concentration in the electrolyte media of a DSSC were investigated. The highest photoefficiency in the first set of experiments was recorded for bilayered TiO_2-ZnO inverse opal with ZnO as the top layer (0.43%), followed by the bilayered TiO_2-TiO_2 inverse opal (0.30%) and finally the bilayered ZnO-TiO_2 inverse opal with TiO_2 as the top layer (0.19%). In the second set of experiments the highest efficiency was recorded for ZnO inverse opal coupled with $K_2Ti_4O_9$ (1.19%) with respect to the single system of $K_2Ti_4O_9$ (1.04%) indicating that the ZnO inverse opal acted as a photonic crystal under-layer material.

7.2 Introduction

In the quest to enhancing DSSC efficiency, the use of bilayered heterostructures consisting of two different nanostructures[2, 131, 220] as photoanodes shows promise. The high surface area possessed by the macroporous inverse opal nanostructures can enhance dye absorption and electrolyte infiltration[106, 249]. The formation of hierarchical porosity introduced by two inverse opal layers may combine the benefit of increased surface area with enhanced mass transport with better charge separation and therefore act as another photoenhancement factor. ZnO and TiO_2, as two wide band gap semiconductors with similar band gaps, are appropriate candidates to produce such heterostructures[240]. ZnO treated TiO_2 nanostructures may also lead to a reduction in back charge recombination and therefore increase the photoefficiency of the DSSC devices[149, 220]. The movement of the conduction band edge of TiO_2 in a more negative direction[149] and the introduction of an energy barrier[241] after ZnO treatment are proposed as the two main causes for the reduction of recombination centres. The photonic crystal properties of ZnO and TiO_2 inverse opals may also contribute to enhanced light harvesting as suggested previously for single inverse opal systems when combined with a conventional TiO_2 (P25) thin film based DSSCs[140]. By coupling the inverse opal to another nanostructured material, the unique photonic properties of the inverse opal used as a light localising and scattering material may enhance the efficiency of the DSSC.

In this chapter, the novel creation of bilayered TiO_2-ZnO inverse opal as an effective photoanode for dye sensitised solar cells (DSSCs) will be

discussed. The coupling effects and the order of deposition of TiO_2 and ZnO inverse opals together as well as coupling between a monolayer ZnO inverse opal with another nanostructure, namely potassium titanate ($K_2Ti_4O_9$) nanobelts have also been investigated. The reasons for choosing potassium titanate nanobelts as another nanostructured material to couple with ZnO inverse opal are as following: 1) as a wide band gap (3.53 eV[250]) semiconductor, potassium titanate may contribute to enhance charge separation and transfer properties of the photoanode, 2) composites of titanates with other metal oxide nanostructures have shown better light harvesting properties due to the formation of interfaces[251], 3) the average length of titanate nanobelts used in this work is in the scale of several tens of micrometres, therefore they could cover the top of the underlying ZnO inverse opal film and may introduce more surface area for better electrolyte infiltration, effective dye sensitisation and charge collection. More importantly, this semiconductor nanostructured material has been used in this work to investigate the effects of the underlying macroporous monolayer ZnO inverse opal in enhancing light harvesting for better energy conversion.

7.3 Experimental Procedures

The substrate of the electrodes used in the experiments were made of transparent conductive FTO glasses. They were cleaned prior to deposition by first being immersed in isopropanol (IPA) (15 minutes) followed by immersion in ethanol (15 minutes) and finally washing thoroughly with DI water before being dried in air.

The electrodes were coated with a thin film of 0.01 M $TT^{i}P$ solution (4 drops at the edges of each electrode) and allowed to dry for 1h prior to deposition metal oxide thin films. This was performed to achieve better adhesion to the samples on the FTO electrodes and also to construct a blocking layer[149] to prevent back recombination between the FTO electrode and the electrolyte. This was especially important in the case of monolayer thin inverse opal samples with high porosity.

The monolayer ZnO, bilayered TiO_2-TiO_2 and TiO_2-ZnO (with alternating the order of deposition) inverse opals were prepared *via* the same procedure as described previously in Chapters 6 (Section 6.3.1) and 5 (Section 5.3.2), with the exception of using an FTO glass substrate instead of a Ti plate for deposition. For the set-up of DSSCs, the thickness of the electrodes was defined by the layers of colloidal crystal templating. Each layer was approximately 410 nm (double layers 820 nm) and, with inclusion of the TiO_2 blocking layer, each photoanode electrode was about 900 nm thick. The calcination temperature for template removal was kept constant for all the samples (550°C) with a ramping rate of 2°C/min for 2 h.

$K_2Ti_4O_9$ nanobelts were synthesised according to the solid-state method described by Allen et al[252]. K_2CO_3 and TiO_2 (P25) were mixed and ground together in a 1:3 molar ratio using a mortar and a pestle followed by annealing at 960°C for 10 h with a ramping rate of 15°C/min. In order to prepare the photoanode sample of monolayer ZnO inverse opal-$K_2Ti_4O_9$ nanobelts composite onto the FTO glass substrate, first a paste of $K_2Ti_4O_9$ nanobelts was made as following: Polyvinyl alcohol (PVA) water solution (30%, 3g) was dissolved in a mixed solvent of water (9.0ml) and ethanol (12.5 ml). A sample of

$K_2Ti_4O_9$ nanobelts (2.2 g) was then added to create the nanobelts suspension. Then, after the suspension was dispersed, two samples were made; first, a layer of $K_2Ti_4O_9$ nanobelts paste was deposited onto the previously made monolayer ZnO inverse opal on the FTO substrate *via* the doctor blade technique. As a reference, a second photoanode sample was made, this time, a layer of $K_2Ti_4O_9$ nanobelts paste was directly deposited onto the FTO glass substrate again using the doctor blade technique. The thickness was controlled by use of a layer of double sided cellophane. The thickness of both films above the FTO surface was approximately 25 microns. The samples were dried for 2 h before calcining them at 550°C with a ramping rate of 3°C/min for 2 h to remove the organic residues from the pastes.

For the purpose of investigating the effects of cation identity and concentration in the electrolyte media of a DSSC, TiO_2 (P25) was used as the photoanode nanomaterial. To prepare the P25 sample on the FTO glass, a P25 paste was made in a similar fashion used to make the $K_2Ti_4O_9$ nanobelts paste, replacing $K_2Ti_4O_9$ with P25 (1.62g). Doctor blade was again applied to deposit the P25 paste onto the FTO substrate (Film thickness above the FTO surface was about 25 microns) before drying and calcining as before. The calcination process (2 h at 550°C) was used not only to remove the organic residues from the P25 paste but also to improve the crystallinity of the P25 sample. Figure 7.1 illustrates a successful deposited layer of P25 paste on a FTO substrate using the doctor blade technique prior to dye sensitisation.

Figure 7.1 P25 film prepared by paste and deposited by doctor blade technique on FTO.

All the as-sensitised films deposited on the FTO glass substrates were heated at 85°C for 30 minutes immediately prior to dye sensitisation to enhance dye adhesion. These photoanode samples were then immersed in a dye solution, N719 dye (0.3 mM) in ethanol for 24 hours. The counter electrodes (photocathodes) were then prepared. For creating a counter electrode, a clean FTO glass substrate was coated with a drop of 0.5 mM chloroplatinic acid (H_2PtCl_6) in ethanol before calcining it at 400°C for 20 minutes. The result was a very thin layer of Pt (about 100 nm thick) deposited on the FTO substrate. Each photoanode was then paired with a counter electrode and assembled into a sandwich type cell. When the two electrodes were put together, the active sides of the photoanode and counter electrode faced each other. The gap between the two electrodes was controlled using a spacer (2 layers of double sided tape (50 microns)). The assembled electrodes were then sealed using UV-sensitive glue (Loctite 358) leaving the top side of the cells unsealed for electrolyte infiltration. The cells were placed under a UV light source for 45 min to dry the seals. An active area of 1 cm^2 was kept constant for all the cells. A few drops of

I^-_3 / I^- electrolyte solution consisting of 0.6M 1-methyl-3-n-propylimidazolium iodide (PMII), 0.5 M 4-tert-butylpyridine (TBP), 0.05 M iodine (I_2) and 0.1M lithium iodide (LiI) in dry acetonitrile was introduced from the unsealed sides of the cells into the gap between the working and counter electrodes. Infiltration took place *via* capillary forces, wetting the entire active areas of the cells. This yielded the finished DSSCs.

7.4 Results and Discussion

7.4.1 Morphology Characterisation

The effects of bilayered inverse opal systems consisting of monolayer TiO_2 and ZnO inverse opals together with investigating the order of deposition in such systems in DSSCs will be one of the objectives in this chapter.

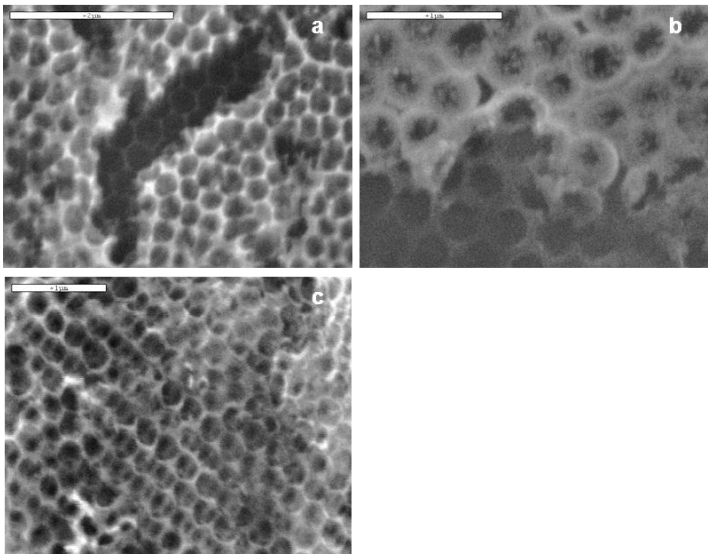

Figure. 7.2 SEM images of bilayered (a) TiO_2-ZnO (as ZnO on top), (b) ZnO-TiO_2 (as TiO_2 on top) and (c) TiO_2-TiO_2 inverse opals deposited on FTO glass substrates. Scale bars: (a) 2μm and (b),(c) 1μm.

Moreover, the photoefficiencies of such bilayered photoanode materials will be compared with a single species bilayer of TiO_2-TiO_2 inverse opal. For this purpose, three samples were made with their corresponding SEM images shown in Figure 7.2. Image 7.2(a) shows the ZnO inverse opal layer is on top of the TiO_2 layer, 7.2(b) when the TiO_2 layer is on top of the ZnO layer and 7.2(c) is with both inverse opal layers as TiO_2.

The diameter of the air spheres (macropores) and the thickness of the walls in the bilayered inverse opal structures in the SEM images of Figure 7.2 were measured and discussed previously in Chapters 5 and 6 (air sphere diameter is 410nm and wall thicknesses are 70nm and 85nm for TiO_2 and ZnO inverse opals respectively). By examining the SEM images above, when the ZnO layer is deposited on top of the TiO_2 layer (Figure 7.2(a)) and when both layers consist of TiO_2 (Figure 7.2(c)), the signature characteristics of the inverse opal structures are preserved (orderliness, periodicity and porosity). However when the TiO_2 is deposited on top of the ZnO inverse opal (Figure 7.2(b)), the top layer loses its inverse opal integrity with the filling of the macropores. The clear morphological differences among the three images indicate that the type of precursor used and the order of deposition is important to maintain the integrity of the bilayered structure.

The reason for these morphological differences can be assigned to the differences in viscosity, the rate of hydrolysation and the physisorption between the precursors fabricating the two layers. When both layers are TiO_2 (Figure 7.2(c)), they naturally can stack on each other without problem. When using different precursors however, there is a mismatch between them. In this work, after the first layer is made by colloidal crystal templating, the second templating

is carried out before template removal. In the case of ZnO as the top layer (Figure 7.2(a)), the integrity of the bilayered inverse opal is better preserved than when the TiO_2 layer is above (Figure 7.2(b)). The main precursors used to synthesise the ZnO and TiO_2 inverse opals are zinc acetate and TT^iP respectively. Zinc acetate is much more stable than TT^iP in air. Therefore, it will be kept mobile in the liquid phase and will possibly to follow the morphology of the PMMA spheres in colloidal crystal in the templating stage and form shells. The PMMA scaffold with its interstitial gaps already filled with the first set of precursors seems impenetrable and therefore, the slower rate of hydrolysation and condensation possessed by the zinc acetate sol-gel precursor for the formation of solid network of ZnO in the top layer may be beneficial. On the other hand, the faster hydrolysation and condensation reactions possessed by the sol-gel TT^iP precursor to form the solid network of TiO_2 may cause premature precipitation, and thus lead to the formation of overlayer as seen in the SEM image in Figure 7.2(b).

Moreover, In the template removal stage by calcination, the mismatch between the two precursors for the formation of solid ZnO and TiO_2 (Figure 7.2(a) and (b)) may also lead to some structural damage as there are fewer Van der Waals interactions compared to when both layers consist of same species of TiO_2 (Figure 7.2(c)). The reduction in porosity can have consequences in DSSC devices due to the loss of internal surface area and decrease in dye adsorption, with light harvesting limited to the top surface.

P25 has been used as a photoanode material to investigate the effects of cation identity and concentration in the electrolyte media of a DSSC. The SEM image in Figure 7.3 (a) shows a layer of P25 deposited onto a FTO glass using

the doctor blade technique (film thickness above the substrate ~25 microns). $K_2Ti_4O_9$ nanobelts have been used to couple with a monolayer ZnO inverse opal and used as photoanode in a DSSC to see the effects of the underlying inverse opal in terms of enhancing the photoefficiency of the cell. Figure 7.3(b) shows a layer of $K_2Ti_4O_9$ nanobelts deposited on a FTO glass using the doctor blade technique (film thickness above the substrate ~25 microns). Figure 7.3(c) shows a monolayer ZnO inverse opal synthesised by colloidal crystal templating on a FTO glass substrate (film thickness ~410 nm) and 7.3(d) shows a monolayer ZnO inverse opal-$K_2Ti_4O_9$ nanobelt composite deposited on a FTO glass. The $K_2Ti_4O_9$ nanobelts have been deposited directly onto the underlying inverse opal thin film *via* doctor blade technique.

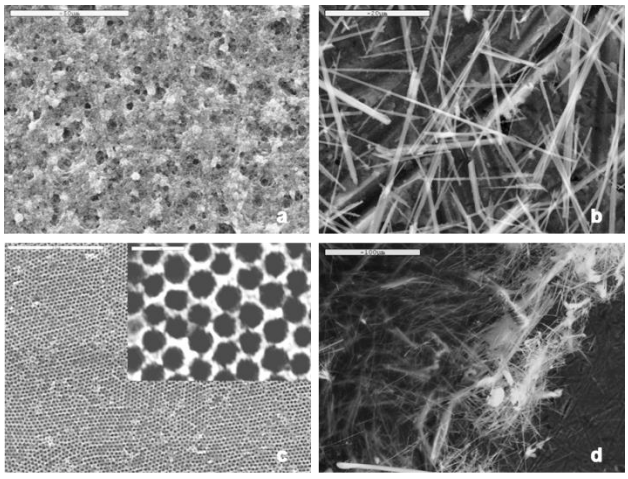

Figure. 7.3 Thin film SEM images of (a) P25, (b) $K_2Ti_4O_9$ nanobelts, (c) monolayer ZnO inverse opal and (d) monolayer ZnO inverse opal-$K_2Ti_4O_9$ nanobelts composite. FTO glass substrates are used for all the samples. Scale bars: (a) 50μm, (b) 20μm, (c) 10μm, (c inset) 1μm and (d) 100μm.

The P25 sample (Figure 7.3(a)) is composed of aggregated crystalline TiO_2 nanoparticles. The average crystallite size is 20 nm, which was determined

via the Scherrer equation. The $K_2Ti_4O_9$ nanobelt structure in Figure 7.3(b) is highly crystalline; this is confirmed *via* XRD in the next section. The nanobelts have various thicknesses (60 nm to 170 nm) and lengths (1.5 to 6 microns) respectively. The SEM image in Figure 7.3(c) shows clearly the highly ordered and crack-free monolayer ZnO inverse opal, which is used as a photonic crystal under-layer when combined with $K_2Ti_4O_9$ nanobelts (Figure 7.3(d)).

7.4.2 Crystal Property Characterisation

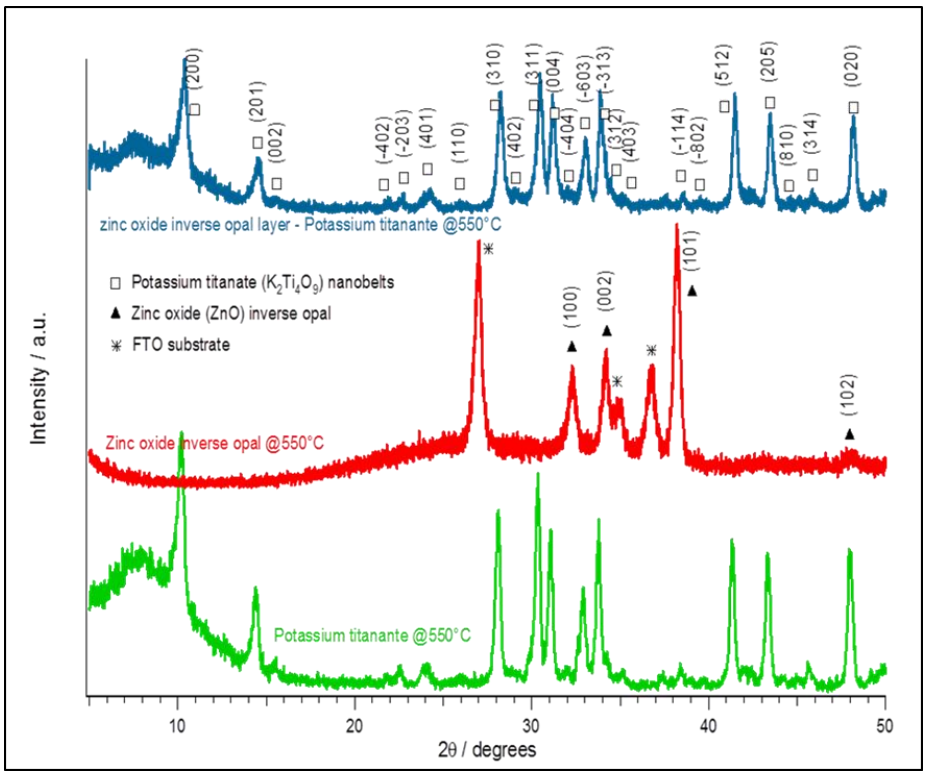

Figure. 7.4 XRD patterns for $K_2Ti_4O_9$ nanobelts (green spectrum), ZnO inverse opal (red spectrum) and monolayer ZnO inverse opal-$K_2Ti_4O_9$ nanobelts composite (blue spectrum) all produced at 550°C.

The crystal structures of the bilayered nanostructures have been discussed previously in Chapter 6. The sequence in the formation of the crystal structure

of the other nanomaterial used as photoanode in DSSC experiments in this chapter, namely monolayer ZnO inverse opal-$K_2Ti_4O_9$ nanobelt composite can be seen in Figure 7.4; first, the XRD pattern for $K_2Ti_4O_9$ nanobelts (green spectrum), followed by the monolayer ZnO inverse opal (red spectrum) and finally the monolayer ZnO inverse opal-$K_2Ti_4O_9$ nanobelts composite (blue spectrum).

The diffraction peaks of the ZnO inverse opal sample (red) can be readily indexed to a hexagonal wurtzite phase of ZnO (JCPDS reference no. 01-075-1526). The peaks that are labelled with stars correspond to the underlying FTO glass substrate. The diffraction peaks of the titanate sample (green) are in good accordance with that reported in the literature[252], indicating the crystalline phase of $K_2Ti_4O_9$. The peaks can be readily indexed to the JCPDS reference card number (00-032-0861). The peaks are sharp and intense, which indicates the high crystallinity of the sample. The $K_2Ti_4O_9$ crystallite size perpendicular to the (200) plane was calculated by using the Debye-Scherrer equation (25 nm).

Xiong et al[250] exposed the crystal phase of $K_2Ti_4O_9$ as a member of $M_2O_{.n}TiO_2$ (M= Na, K, Rb, Cs) with n = 0.5, 1.0, 2.0, $K_2Ti_4O_9$ (when n=4) possesses a layered structure consisting of ribbons of edge and corner shared TiO_6 octahedral units separated by K ions.

After introducing the monolayer ZnO under-layer (blue), the composite only shows the resolved diffraction peaks for the $K_2Ti_4O_9$ nanobelts with no characteristic changes from its original spectrum (green). The very thin nature of the underlying monolayer ZnO inverse (about 410 nm thick) may result in the intensities of its diffraction peaks to be very low in comparison to the thick layer

of $K_2Ti_4O_9$ nanobelts on top (about 25 microns thick) which produces high intensity diffraction peaks. This may explain why the XRD patterns for the underlying inverse opal thin film cannot be detected.

7.4.3 Photovoltaic Characterisation

In a two electrode system, the photocurrent-voltage (*I*–*V*) characteristics of the DSSCs were measured by an eDAQ potentiostat, scanning from a negative bias of -1200 mV to a positive bias of 200 mV. The measurements were made under artificial solar light, produced by a 300 W xenon lamp and AM 1.5G filter (simulated solar spectrum 350-750 nm). The intensity of the lamp was adjusted to a power density of 100 mW/cm^2, corresponding to 1 sun.

7.4.3.1 Sodium Iodide (NaI) and Lithium Iodide (LiI) Based Electrolytes

The effects of cation identity in the electrolyte media of a TiO_2 (P25) based DSSC was investigated in this work. Figure 7.5 shows the plot of output power density as a function of voltage for a cell with two different cation based electrolyte solutions (NaI and LiI). As described in Chapter 2, the open circuit voltage (V_{oc}) can be affected when photogenerated electrons in the conduction band of the semiconductor (here TiO_2) recombine with the oxidised species in the electrolyte (I_3^-) or dye (D^+). The short circuit current can also suffer from recombination according to Equation (7.1) [253] as well as poor charge transport properties.

$$I_3^- + 2e_{cb}^- \rightarrow 3I^- \qquad \text{(Equation 7.1)}$$

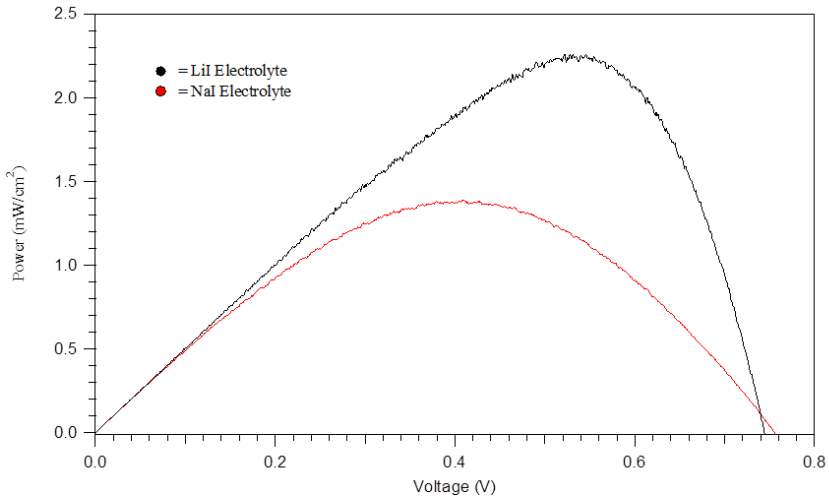

Figure. 7.5 Plot of output power against voltage for LiI based (black) and NaI based (red) electrolyte solutions in a P25 DSSC.

In a TiO_2 based DSSC, there is a strong electrostatic coupling of the motions of ions in the electrolyte and of electrons in the TiO_2 network[254]. A balanced ambipolar diffusion is essential for reducing and accumulation of ions on either electrodes (cathode and anode). This ensures that the electron transport is effective through the electrolyte, whereby the amount of negative charge is roughly equal to the amount of positive charge over the cell area[255]. Li^+ has a smaller ionic radius (76 pm)[256] than Na^+ (102 pm) [256]. Therefore it can penetrate the mesoporous TiO_2 network more effectively. This leads to a faster transport rate (higher effective electron diffusion coefficient) due to an ambipolar diffusion mechanism[254] leading to an increase in the short circuit current (J_{SC}) and hence higher efficiency[257]. However, Li^+ can also react more readily with the triiodide in the electrolyte than Na^+ (due to its greater ionic strength), which leads to a higher recombination rate, which reduces the open circuit voltage (V_{OC}). The reduction in V_{OC}, although minimal, can be observed in Figure 7.5, in

which it decreases from 0.756 V to 0.745 V. By using LiI as the cation species instead of NaI, the overall efficiency is significantly improved as can be seen in Figure 7.5. This is because cation charge transport speed is the dominant factor, which leads to a higher J_{sc}, which significantly outweighs the recombination with triiodide. The overall effect is a small reduction in *Voc*.

Another factor contributing to the rise in efficiency when using LiI instead of NaI in the electrolyte media can be attributed to cation adsorption on the band-edges and surface charges of TiO_2. The Li^+ cation is a stronger Lewis acid than Na^+ and may coordinate more effectively to oxygen rows in the TiO_2 crystal structure (anatase) and therefore increase the electron density acceptor ability of the neighbouring Ti atoms[258]. This may explain the resulting higher rate of electron injection from dye species into the TiO_2[259] and subsequently lead to enhanced efficiency.

7.4.3.2 Optimising Lithium Iodide (LiI) Concentration in Electrolyte Solution

The effects of concentration in the electrolyte media of a TiO_2 (P25) based DSSC was investigated. Figure 7.6 shows the plot of photoconversion efficiency as a function of LiI concentration for the cell. The optimum concentration of LiI in the electrolyte solution is 0.1M. The factors determining the optimum LiI concentration may be explained by the following two factors: ambipolar diffusion mechanism (the role of cation in terms of dictating the speed of electron transport in TiO_2) and secondly, the effects of adsorbed cations on the TiO_2 surface, by changing the band edges of TiO_2 relative to the dye and hence

influencing the rate of electron injection from dye to TiO_2. Too high a concentration of LiI can also result in back recombination between the photogenerated electrons in the conduction band of TiO_2 and the oxidised triiodie in the electrolyte media and lead to a reduction in efficiency according to Equation (7.1) mentioned previously.

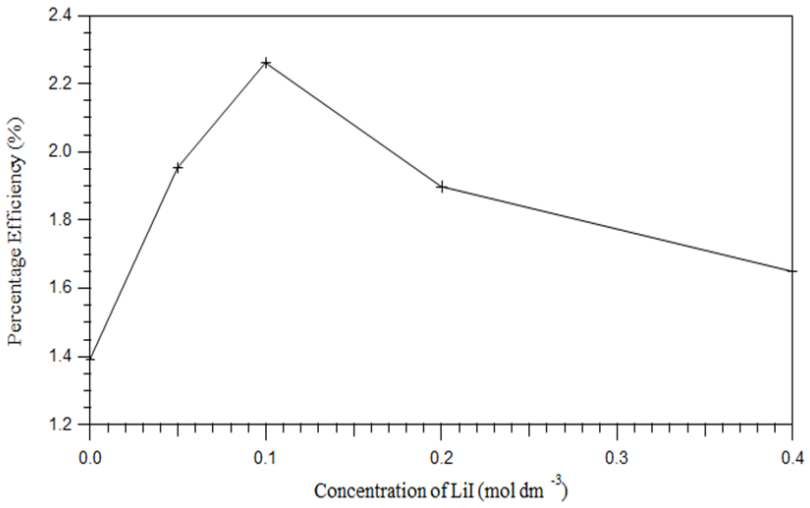

Figure. 7.6 Plot of efficiency against concentration of LiI for a P25 DSSC.

7.4.3.3 DSSC Performances of Different Bilayered Inverse Opals

The effects of bilayered inverse opal systems consisting of monolayer TiO_2 and ZnO inverse opals as photoanodes together with the effects of the order of deposition in such systems with respect to enhancing the performance of DSSCs were investigated. Moreover, the photoefficiencies of such bilayered photoanode materials were compared with a single species bilayer of TiO_2-TiO_2 inverse opal.

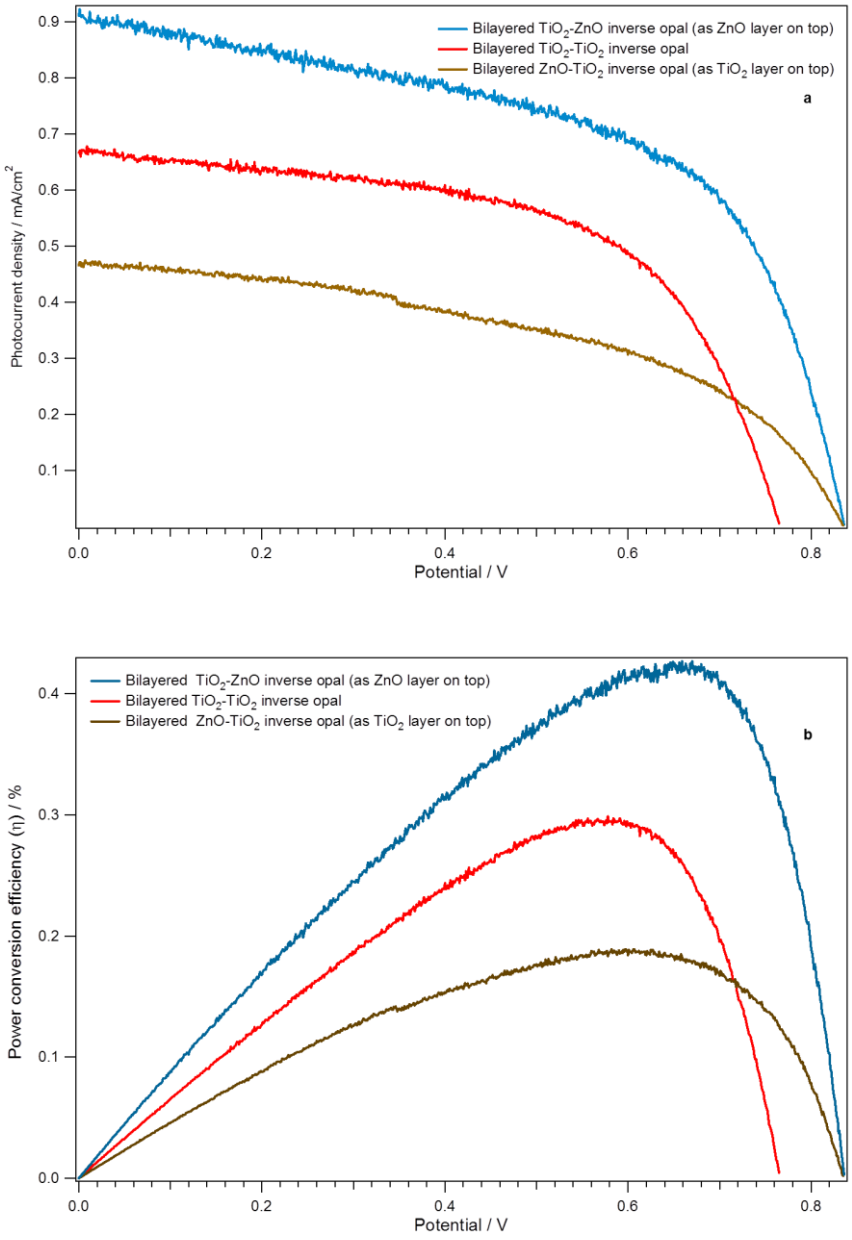

Figure. 7.7 (a) *I-V* characteristics and (b) photoefficiencies of the DSSCs assembled with bilayered TiO_2-ZnO (as ZnO on top (blue)), TiO_2-TiO_2 (red) and ZnO-TiO_2 (as TiO_2 on top (brown)) inverse opals as photoanodes.

Figure 7.7 shows the *I-V* characteristics (Figure 7.7(a)) and photoconversion efficiency (Figure 7.7(b)) curves for the as-assembled cells with different bilayered inverse opals acting as photoanodes under 100 mW cm^{-2} irradiation. The blue curves correspond to the bilayered TiO_2-ZnO (as

ZnO on top), the red curves to TiO_2-TiO_2 and the brown curves to the ZnO-TiO_2 (as TiO_2 on top) inverse opals. The corresponding photovoltaic parameters of these three cells are summarised in Table 7.1.

Photoanodes (Bilayered inverse opals)	$\mathbf{J_{SC}/mAcm^{-2}}$	$\mathbf{V_{OC}/V}$	**η%**	**FF**
TiO_2–ZnO (as ZnO on top)	0.911	0.836	0.43	0.560
TiO_2–TiO_2	0.667	0.765	0.30	0.583
ZnO–TiO_2 (as TiO_2 on top)	0.466	0.835	0.19	0.486

Table. 7.1 Photovoltaic Parameters of the DSSCs assembled with bilayered TiO_2-ZnO (as ZnO on top), TiO_2-TiO_2 and ZnO-TiO_2 (as TiO_2 on top) inverse opal photoanodes.

From Table 7.1, the highest efficiency (η%), short circuit current (J_{SC}) and open circuit voltage (V_{OC}) is that of bilayered TiO_2-ZnO inverse opal based DSSC with a ZnO layer on the top of TiO_2 layer. Its efficiency is almost 2.5 times as high than that of the hybrid structure with the TiO_2 layer on top and 43% higher than the single system bilayered TiO_2-TiO_2 inverse opal. The higher efficiency in this cell arises directly from the larger values of J_{SC} and V_{OC} as can be seen from the above table. This means the cell possesses better light harvesting ability and more effectively suppresses charge recombination. Coupling of ZnO with TiO_2 metal oxide semiconductors tends to form a

heterojunction with a staggered type-*II* band alignment[240]. Kim et al.[149] and Kanmani et al.[241] both suggested that by introducing ZnO nanostructures to a TiO_2 (P25) based DSSC, the efficiency would be enhanced due to the increase in the V_{OC}. Kim's argument suggested the increase in V_{OC} could be assigned to the introduction of the ZnO layer, which acted as charge barrier between the TiO_2/electrolyte interface. This in turn was suggested to lead to a reduction in recombination losses. They argued that although TiO_2 and ZnO both have similar band gaps, due to a slightly higher conduction band in ZnO (-0.35V vs V_{RHE}) compared to TiO_2 (-0.17 vs V_{RHE}) [133], it energetically favours the injection of photogenerated electrons to TiO_2. The TiO_2 structure is shielded from back electron transport and interfacial recombination, which results in larger V_{OC}. On the other hand, Kanmani argued that the increase in V_{OC} was due to the movement of the conduction band edge of TiO_2 to a more negative direction after the ZnO treatment, due to the formation of a dipole layer across the TiO_2 surface. This is as opposed to the formation of barrier layer. ZnO has a higher isoelectric point (~8.5) than of TiO_2 (~5)[2] that may induce a surface dipole directed towards the TiO_2, leading to a negative shift of the conduction band of the TiO_2 by increasing the work function of its Fermi level higher and hence increasing the V_{OC} of the cell.

From the above, it is clear that the arguments are valid only when the system acts in a core-shell manner, with ZnO as the shell and TiO_2 as the core. By examining the findings of this work, one factor for the superior performance of bilayered TiO_2-ZnO inverse opal (with ZnO as the top layer) compared to when TiO_2 is the top layer can be explained by either or both of these mechanisms.

The greater J_{SC} of the heterojunction system (with ZnO as the top layer) can also be explained in terms of the ZnO behaving as a charge barrier. The shifting of the TiO_2 conduction band edge may also energetically improve electron injection from the dye (by improved band alignment) and also enhance transport leading to a higher J_{SC} value. Suppression of back electron transport by the ZnO layer shielding effect may in addition improve J_{SC}. Compared to the single system bilayer of TiO_2-TiO_2 inverse opal, the low photovoltaic efficiency for the ZnO-TiO_2 inverse opal with TiO_2 on top can be assigned to poor electron injection from the less negative (lower positioned) conduction band edge of TiO_2 to the more negative (higher positioned) ZnO conduction band; TiO_2 can act as the blocking layer for forward electron transport and hence hinder light harvesting. The other possible reason for this particular photoanode's poor performance may be attributed to its morphology. By referring back to Figure 7.3, the SEM images for the other two electrodes, the bilayered TiO_2-ZnO (as ZnO on top) (Figure 7.3(a)) and TiO_2-TiO_2 (Figure 7.3(c)) inverse opals show high degrees of porosity and orderliness. In stark contrast, in this sample, the bilayered ZnO-TiO_2 (as TiO_2 on top), the porosity is not well preserved. This can lead to loss of internal surface area and therefore a significant reduction in dye absorption, leading to lower photoefficiency. The reduction of porosity and orderliness in such bilayered inverse opal can hinder light localisation and scattering[140], which are two important characteristics of inverse opals acting as photonic crystals. This may further contribute to reduce the light harvesting properties.

From Table 7.1, it can be seen that the single system cell of bilayered TiO_2-TiO_2 inverse opal has a slightly higher fill factor than that of the two

heterjunction systems. It is suggested that this is due to less internal transport resistance[126] in the single system compared to higher charge resistivity in TiO_2-ZnO systems, due to the formation of the heterojunction. However this slight improvement in the fill factor is not enough to make the single system superior in terms of overall efficiency and is indeed significantly outweighed by the increase in J_{SC} and V_{OC} in the heterojunction system of bilayered TiO_2-ZnO with the ZnO layer on top of the TiO_2 layer.

Some researchers have suggested[2, 149] that leaving ZnO nanostructures in the dye environment for too long might reduce the efficiency of the cell. They reported that the protons released from the dye molecules could dissolve the ZnO and destroy the ZnO nanostructure. The formation of dye-Zn^{2+} agglomerates would also deactivate the dye molecules and result in poor light harvesting. However, this problem could not be detected in this work as the highest photovoltaic results were obtained for the bilayered TiO_2-ZnO inverse opals with the ZnO layer being on top. This may be due to the use of relatively low concentration of dye (0.3 mM) compared to the literature experiment (0.5 mM)[241] and additionally not leaving the electrode in the dye solution for more than 24 hours.

7.4.3.4 DSSC Performance of $K_2Ti_4O_9$ Nanobelts Coupled with Monolayer ZnO Inverse Opal

$K_2Ti_4O_9$ nanobelts were coupled with a monolayer ZnO inverse opal and used as a photoanode in a DSSC to see the effects of the underlying inverse opal on the performance of the cell. A pristine sample of $K_2Ti_4O_9$ nanobelts was also

used as a reference without the presence of the underlying monolayer inverse opal.

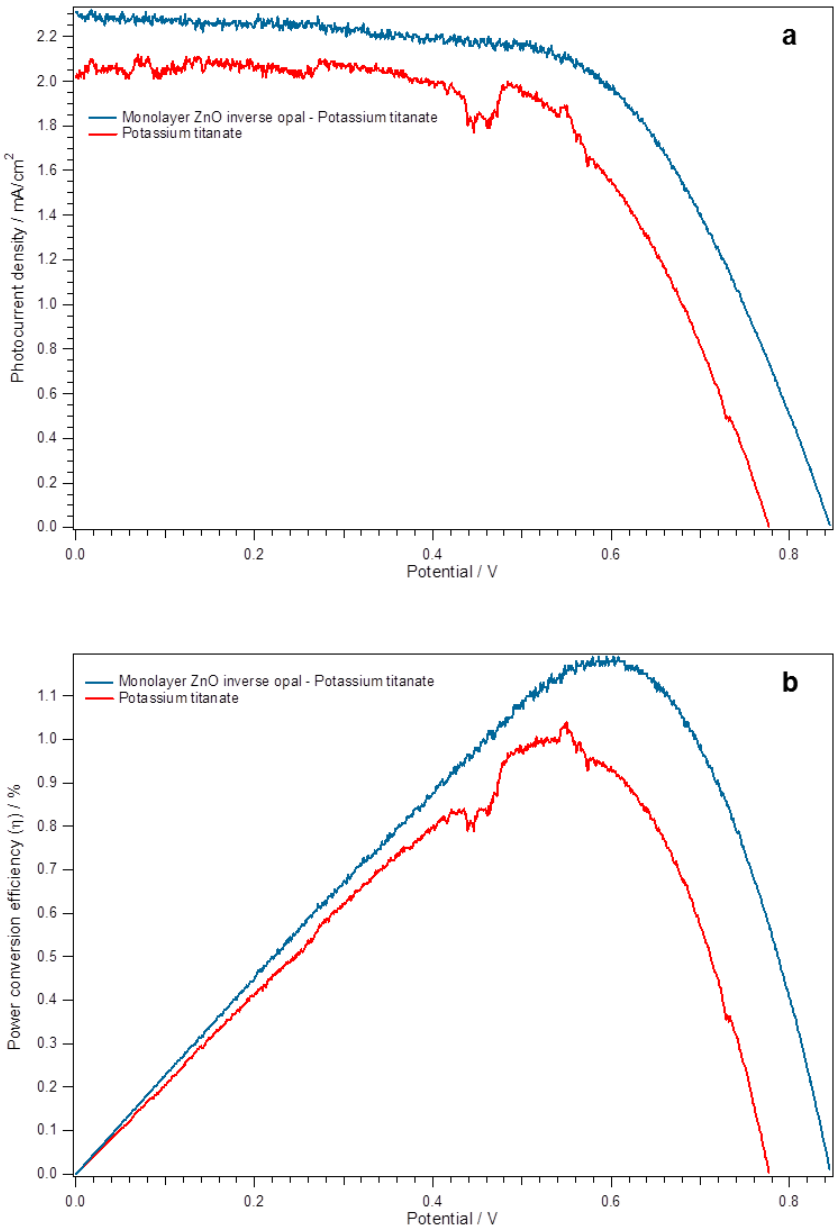

Figure. 7.8 (a) *I-V* characteristics and (b) photoefficiencies of the DSSCs assembled with monolayer ZnO inverse opal-$K_2Ti_4O_9$ nanobelts composite (blue) and $K_2Ti_4O_9$ nanobelts only (red) as photoanodes.

Figure 7.8 shows the *I-V* characteristics (Figure 7.8(a)) and photoconversion efficiency (Figure 7.8(b)) curves for the as-assembled cells

with monolayer ZnO inverse opal-$K_2Ti_4O_9$ nanobelt composite (blue curves) and $K_2Ti_4O_9$ nanobelts only (red curves) acting as photoanodes under 100 mW cm^{-2} irradiation. The corresponding photovoltaic parameters of the two cells are summarised in Table 7.2.

Photoanodes	$\mathbf{J_{SC}/mAcm^{-2}}$	$\mathbf{V_{OC}/V}$	**η%**	**FF**
Monolayer ZnO inverse opal-$K_2Ti_4O_9$ nanobelt	2.31	0.845	1.19	0.611
$K_2Ti_4O_9$ nanobelts only	2.02	0.777	1.04	0.660

Table. 7.2 Photovoltaic Parameters of the DSSCs assembled with monolayer ZnO inverse opal-$K_2Ti_4O_9$ nanobelts composite and $K_2Ti_4O_9$ nanobelts only as photoanodes.

From Table 7.2, it is clear the main parameters, J_{SC}, V_{OC} and photo-conversion efficiency (η%), are improved when the $K_2Ti_4O_9$ nanobelt structure is coupled with a thin underlying monolayer ZnO inverse opal in comparison to, when there is no underlying monolayer inverse opal. These results may suggest the role of the underlying inverse opal layer in enhancing light harvesting. From the XRD patterns in Figure 7.4, no new peaks nor any change in the characteristics of the $K_2Ti_4O_9$ nanobelts can be detected. This may lead to the conclusion that there are no any new structures formed at the interface between the two layers. Mallouk and his colleagues[102, 103] demonstrated the importance of coupling an inverse opal layer of TiO_2 as a photonic crystal layer to a non-structured layer of TiO_2 thin film in a DSSC. Their efficiency was enhanced by using the inverse opal as a top layer on a TiO_2 based DSSC and irradiating from the anode side (the back side). They proposed that the TiO_2 inverse opal

layer acted as photonic crystal mirror in this bilayer architecture created localised states in the non-structured surface layer of TiO_2 thin film and led to enhanced efficiency. ZnO inverse opal may act as a reflective mirror. The creation of partially localised resonant modes in the $K_2Ti_4O_9$ top layer via the underlying inverse opal may also be another photonic enhancement effect arising in this bilayer architecture as suggested previously[12]. The underlying ordered structure of monolayer ZnO inverse opal may therefore act as a photonic crystal material in the inverse opal-$K_2Ti_4O_9$ nanobelts composite for better light harvesting over a broad wavelength.

In addition to the photonic properties, the ZnO inverse opal, also has a high surface area with interconnected macroporous skeleton, which may be beneficial with respect to higher dye sensitizer loading and faster electron transport. The highly porous structure may also behave as a “highway” for better electrolyte diffusion in this inverse opal-$K_2Ti_4O_9$ nanobelt composite system. The shorter diffusion distance between the photoanode/electrolyte may reduce charge recombination at this interface.

The higher fill factor in the single system of $K_2Ti_4O_9$ nanobelts can be assigned to its lesser internal transport resistance in comparison to the monolayer ZnO inverse opal-$K_2Ti_4O_9$ nanobelts composite. However, as can be seen from Table 7.2, J_{SC} and V_{OC} are the dominant factors in determining efficiency enhancement.

7.5 Conclusion

In this work, the importance of the cation in the electrolyte media was investigated. It was demonstrated that LiI with a concentration of 0.1M is the best candidate in P25 based DSSC devices. Coupling of TiO_2 and ZnO inverse opals (with ZnO the top layer) shows the highest photoefficiency. This is largely due to the formation of a heterojunction with the ZnO layer acting as an energy barrier and also providing a dipole layer across the TiO_2 surface. The photonic properties of both layers can also contribute to efficiency enhancement. The ZnO inverse opal acting as a photonic crystal material increases the efficiency of a $K_2Ti_4O_9$ nanobelt based cell possibly by enhancing light localisation and scattering due to the photonic crystal mirror effect and by the creation of resonant modes in this bilayer architecture[12]. The enhanced internal surface area arising from the highly interconnected porous inverse opal can also contribute to enhancing light harvesting due to a shorter diffusion length and better dye adsorption.

By engineering a suitable multilayer heterojunction of layer-by-layer inverse opal nanostructure with alternative p-n layers, the efficiencies of DSSCs may be improved much further. A challenge in the future will be establishing suitable semiconductors, which can align their band edges together forming junctions. The order of deposition in the layer-by-layer formation of such systems should not be ignored, as its importance was demonstrated in this work for bilayered structures consisting of TiO_2 and ZnO inverse opals.

7.6 Thesis Key Findings, Challenges and Future Work

The work conducted herein has demonstrated the synthesis of monodisperesed colloidal PMMA spheres by using both single step and seeded SFEP methods. The Stokes' law measurements was used to quantify the diameter of the colloidal spheres which was compared with SEM measurements. At the time of carrying out the SFEP experiments, dynamic light scattering (DLS) was unavailable to determine the size distribution profile. As size distribution and monodispersity of colloidal spheres in templating processes are of utmost importance, the use of DLS is highly recommended in future similar experiments.

By using bottom-up colloidal crystal self-assembly techniques including vertical deposition and a modified floating approach, ordered close packed PMMA colloidal crystals have been successfully fabricated in this work. The modified floating approach can be considered as a powerful and facile technique to produce monolayer and multilayer colloidal crystals with the possibility of controlling the thickness (the number of colloidal crystal layers). This technique with its multiple deposition abilities can be used in colloidal crystal templating to produce various inverse opal systems with controlled chemical composition. At the time of carrying out these experiments, X-ray scattering techniques, in particular, ultrasmall-angel synchrotron X-ray scattering (USAXS) was unavailable for the analysis of PMMA colloidal crystals formed. This characterisation technique can be beneficial to be used alongside SEM and TEM in future colloidal crystal self-assembly experiments, in order to

evaluate the quality of the colloidal crystals in terms of ordering, pore size determination and identifying defects.

The use of template directed synthesis *via* sol-gel coating and infiltration to produce various metal oxide hollow spheres and inverse opals has been successfully demonstrated in this work. Simple sol-gel chemistry of different metal salts in the presence of water can be easily used in templating approaches to produce such porous nanostructures with enhanced opto-electronic properties. The successful synthesis of sphere-in-sphere hollow spheres in this work may be beneficial in the future photovoltaic experiments. For the first time, bilayered 3D metal oxide inverse opal structure with different chemical composition in each layer namely TiO_2 and ZnO has been produced using the combination of floating technique with horizontal colloidal crystal templating approach in this work. So far, the production of hollow spheres and inverse opal systems contained one of TiO_2, ZnO, SiO_2, Fe_2O_3 and CuO metal oxides. The facile templating routes explained in this thesis may be extended to other metal oxide systems or even titanates such as $BaTiO_3$ and $SrTiO_3$ with their desirable band gap energies, with applications in PEC water splitting experiments[260]. For example, titanium butoxide may be combined with barium acetate or strontium acetate in a presence of water to produce the sol-gel precursors necessary for coating or infiltrating the PMMA templates. The metal oxide or titanante precursors obtained, can then be used in one of the two new templating techniques developed in this work to produce sphere-in-sphere hollow spheres or bilayered and multilayered inverse opals with controlled chemical composition.

For the first time, a novel nanoarchitectured electrode design through the formation of CdSe/ZnS quantum dot sensitised ZnO nanorods on monolayer ZnO and bilayered TiO_2/ZnO inverse opals for PEC hydrogen production have been demonstrated in this thesis. A promising photoconversion efficiency of 2.35% for the ultimate QD sensitised ZnO nanorods on a bilayered system of TiO_2/ZnO inverse opal with a zinc titanante interface at 0.23 V versus *Ag/AgCl* (1.23 V *vs RHE*) bias under simulated solar-light illumination has been achieved. In this hierarchical heterostructured system, the synergistic effects originating from each individual layer have contributed to the opto-electronic enhancement for better energy conversion. The photoefficiency obtained in this work is compatible with other TiO_2 or ZnO based photoanodes sensitised with various quantum dots under similar conditions (~1.83 and 2.62% photoefficiencies as reported in the literature)[188, 223]. To the best of the author's knowledge, the highest solar-to-hydrogen efficiency (under unbiased) conditions has been reported at 4.9% in a bismuth vanadate-silicon tandem photoelectrode[143]. In this system, cobalt phosphate on tungsten-doped bismuth vanadate with improved carrier-separation combined with a Si solar cell in a tandem configuration. The photoefficiency of the state of the art photoanode used in this work may also be improved by combining the photoanode to a Si , dye (DSSC) or even QD sensitised solar cell (QDSSC) forming a tandem configuration. By proper band gap engineering in this system, it may be possible to absorb more of the sun light energy and also produce a solar water-splitting device to determine the overall solar to hydrogen conversion efficiency (STH)[131] without the need of external applied bias. This approach may offer new pathways towards low cost and efficient devices for solar hydrogen generation.

By examining other quantum dots as narrow band gap sensitisers such as CdTe or CdS, the efficiency of the system may further be improved. For example, CdTe quantum dots have shown better photocatalytic enhancements when combined with ZnO nanocrystals due to a better contact between the two nanocrystals forming a more effective nanojunction for charge movement[261]. CdTe has also a more favourable conduction band energy (E_{CB} = -1.0 V *vs. NHE*) for faster injection of electrons into ZnO than CdSe (E_{CB} = -0.6 V *vs. NHE*)[223].

In this work, the importance of an under-layer metal oxide inverse opal namely monolayer ZnO inverse opal when combined with another semiconducting nanomaterial (here $K_2Ti_4O_9$ nanobelts) for increasing the efficiency of a DSCC has been demonstrated. The macroporous interconnected structure with its high surface area and photonic crystal properties may have contributed to efficiency enhancement. A photoconversion efficiency of 1.19% under the simulated AM 1.5G, one sun illumination was achieved which was higher than the single system of titanante photoanode (1.04%). The optimised bilayered TiO_2-ZnO inverse opal (with ZnO as the top layer) had a photoefficiency of 0.43%. The aim of this part of the project was to design the construction of such multilayer structures, to compare different bilayered inverse opals, to investigate the photonic properties and to see the effect of order of deposition in efficiency enhancement. The photoefficiencies reported in literature for a monolayer and multilayered TiO_2 inverse opal based DSSCs were 1.1 and 1.27% respectively[106], which is comparable to our data. For ZnO treated TiO_2 inverse opal[242] much higher photoconversion efficiency was achieved at 5.3%. Our results may be enhanced further by optimising the DSSC

device mainly by minimising the overpotentials associated with the two electrode set up and possibly by optimising the electrolyte with more systematic examination. The thickness of the films should also not be ignored, as in this work the bilayered systems might have been too thin which could have induced more recombination centres between the FTO glass and the electrolyte, and also reduced the light absorption.

By using the novel colloidal crystal templating approach developed here, other bilayered or even multilayered inverse opal based photoanodes with different chemical compositions may be synthesised for better light harvesting in DSSC devices. The state of the art QD sensitised bilayered photoanodes used in PEC water splitting in this work may also be used directly as photoanodes in QDSSCs. These hierarchical structures can then be tested and compared with the dye sensitised versions in terms of photoefficiency enhancement. In the literature, the use of QDs as sensitisers in QDSSCs are few compared to the use of dyes in DSSCs. The use of QDs as sensitisers may open new possibilities owing to their large absorption coefficient, quantum size confinement effect (tunability of their absorption spectrum) and possibility of multiexciton generation[237, 262]. The challenge in producing high performance QDSSCs lie in the materials and interfaces in the cell set up, including; the choice of QDs (for better visible light absorption), the inherent triple junction of nanostructure semiconductor/QDs/electrolyte at the photoanode (for better energy band alignment and reducing charge recombination), the choice of redox electrolyte (increasing the V_{OC} of the system) and counter electrode (to be able to catalyse the regeneration of the oxidised charge carrier ions, and hence increase the photocurrent and reduces recombination losses)[262].

By using the novel synthetic approach in this work, the development of layer-by-layer p-n junction inverse opals of different metal oxides may also be realised to be used in PEC water splitting and DSSC (or QDSSC) devices. Further doping of the inverse opals with electron donors (n-doping) or acceptors (p-doping) may further enhance the efficiency of such systems by improving the charge transfer processes by altering the band gap energies of the semiconductors understudy. As it has been demonstrated here, the order of deposition in the construction of layer-by-layer metal oxide inverse opals should also be taken care with great deal. An optimised morphology (including high integrity of porosity and interconnectivity of each individual inverse opal layer) and intrinsic chemistry of the metal oxides at interfaces (including the favourable positioning of band gap edges and the formation of effective junctions) depend on the order in which the inverse opal layers stack up on each other, starting from the underlying substrate. An optimised layer-by-layer inverse opal photoanode will improve the charge transport and separation properties of a PEC or DSSC device and lead to better energy conversion.

At the end, it is also important to mention that the resistance of the photoanode materials to corrosion in the aqueous environment of the electrolyte in both the PEC water splitting and DSSC experiments has to be taken into account seriously which will affect the overall lifetime of the system, if any of the state of the art photoanodes developed here (or any other novel nanomaterials developed) are going to be commercialised in the future.

Chapter 8: References

1. Y. N. Xia, P. D. Yang, Y. G. Sun, Y. Y. Wu, B. Mayers, B. Gates, Y. D. Yin, F. Kim and Y. Q. Yan, *Adv Mater*, 2003, **15**, 353.

2. Q. Zhang and G. Cao, *Nano Today*, 2011, **6**, 91.

3. J. H. Zhang, Z. Q. Sun and B. Yang, *Curr. Opin. Colloid Interface Sci.*, 2009, **14**, 103.

4. S. K. Karuturi, C. W. Cheng, L. J. Liu, L. T. Su, H. J. Fan and A. I. Y. Tok, *Nano Energy*, 2012, **1**, 322.

5. A. Stein, B. E. Wilson and S. G. Rudisill, *Chem Soc Rev*, 2013, **42**, 2763.

6. C. I. Aguirre, E. Reguera and A. Stein, *Adv Funct Mater*, 2010, **20**, 2565.

7. H. L. Shen, H. H. Hu, D. Y. Liang, H. L. Meng, P. G. Li, W. H. Tang and C. Cui, *J Alloy Compd*, 2012, **542**, 32.

8. Z. Z. Gu, Y. H. Yu, H. Zhang, H. Chen, Z. Lu, A. Fujishima and O. Sato, *Appl Phys a-Mater*, 2005, **81**, 47.

9. Z. Y. Cai, J. H. Teng, Z. G. Xiong, Y. Q. Li, Q. Li, X. M. Lu and X. S. Zhao, *Langmuir*, 2011, **27**, 5157.

10. V. L. Colvin, *Mrs Bulletin*, 2001, **26**, 637.

11. C. Paquet and E. Kumacheva, *Mater. Today*, 2008, **11**, 48.

12. J. I. L. Chen, G. von Freymann, S. Y. Choi, V. Kitaev and G. A. Ozin, *J Mater Chem*, 2008, **18**, 369.

13. S. W. Choi, Y. Zhang, M. R. MacEwan and Y. N. Xia, *Adv Healthc Mater*, 2013, **2**, 145.

14. F. Bai, J. K. Zhang, Z. Wang, J. X. Lu, J. A. Chang, J. A. Liu, G. L. Meng and X. Dong, *Biomed Mater*, 2011, **6**.

15. Y. N. Xia, B. Gates, Y. D. Yin and Y. Lu, *Adv Mater*, 2000, **12**, 693.

16. Y. L. Cao, Y. P. Wang, Y. Z. Zhu, H. B. Chen, Z. H. Li, J. Ding and Y. B. Chi, *Superlattices Microst.*, 2006, **40**, 155.

17. A. J. Wang, S. L. Chen and P. Dong, *Mater Lett*, 2009, **63**, 1586.

18. S. L. Kuai, V. V. Truong, A. Hache and X. F. Hu, *J Appl Phys*, 2004, **96**, 5982.

19. C. Lopez, *Adv Mater*, 2003, **15**, 1679.

20. M. Muller, R. Zentel, T. Maka, S. G. Romanov and C. M. S. Torres, *Chem Mater*, 2000, **12**, 2508.

21. W. Stober, A. Fink and E. Bohn, *J Colloid Interf Sci*, 1968, **26**, 62.

22. F. G. Santamaría, PhD, Universidad Autónoma de Madrid, 2003.

23. J. Ballato and A. James, *J. Am. Ceram. Soc.*, 1999, **82**, 2273.

24. M. J. A. de Dood, B. Berkhout, C. M. van Kats, A. Polman and A. van Blaaderen, *Chem Mater*, 2002, **14**, 2849.

25. S. Kalele, S. W. Gosavi, J. Urban and S. K. Kulkarni, *Curr Sci India*, 2006, **91**, 1038.

26. M. Egen and R. Zentel, *Macromol Chem Physic*, 2004, **205**, 1479.

27. R. C. Schroden, M. Al-Daous, C. F. Blanford and A. Stein, *Chem Mater*, 2002, **14**, 3305.

28. J. W. Goodwin, J. Hearn, C. C. Ho and R. H. Ottewill, *Colloid Polym. Sci.*, 1974, **252**, 464.

29. G. Odian, *Principles of Polymerization*, 4th edn., Wiley, 2004.

30. T. Tanrisever, O. Okay and I. C. Sonmezoglu, *J Appl Polym Sci*, 1996, **61**, 485.

31. A. M. Telford, B. T. T. Pham, C. Neto and B. S. Hawkett, *J Polym Sci Pol Chem*, 2013, **51**, 3997.

32. J. Ramos and J. Forcada, *Eur. Polym. J.*, 2007, **43**, 4647.

33. M. Bardosova and R. H. Tredgold, *J Mater Chem*, 2002, **12**, 2835.

34. C. G. Dobie and K. V. K. Boodhoo, *Chem Eng Process*, 2010, **49**, 901.

35. Z. D. Duke M., Semiat R., *Functional Nanostrucutred Materials and Membranes for Water Treatment* Wiley-VCH, Germany, 2013.

36. P. J. Feeney, D. H. Napper and R. G. Gilbert, *Macromolecules*, 1987, **20**, 2922.

37. F. Sordello, V. Maurino and C. Minero, *Molecular Photochemistry*, InTech, Italy, 2012.

38. A. Blanco, P. D. Garcia, D. Golmayo, B. H. Juarez and C. Lopez, *IEEE J. Sel. Top. Quant. Electron.*, 2006, **12**, 1143.

39. O. D. Velev and E. W. Kaler, *Adv Mater*, 2000, **12**, 531.

40. X. Y. Zhang, T. W. Wang, W. Q. Jiang, D. Wu, L. Liu and A. H. Duan, *Chinese Chem Lett*, 2005, **16**, 1109.

41. H. Fudouzi, *Adv Powder Technol*, 2009, **20**, 502.

42. C. I. Aguirre, E. Reguera and A. Stein, *Adv Funct Mater*, 2011, **21**, 210.

43. G. I. N. Waterhouse and M. R. Waterland, *Polyhedron*, 2007, **26**, 356.

44. S. M. Yang, S. G. Jang, D. G. Choi, S. Kim and H. K. Yu, *Small*, 2006, **2**, 458.

45. J. F. Galisteo-López, M. Ibisate, R. Sapienza, L. S. Froufe-Pérez, Á. Blanco and C. López, *Adv Mater*, 2011, **23**, 30.

46. S. Kedia, R. Vijaya, A. K. Ray, S. Sinha and K. Dasgupta, *Pramana*, 2010, **75**, 975.

47. M. Fu, L. Deng, A. Zhao, Y. Wang and D. He, *Opt. Mater.*, 2010, **32**, 1210.

48. J. W. Galusha, C.-K. Tsung, G. D. Stucky and M. H. Bartl, *Chem Mater*, 2008, **20**, 4925.

49. Y. Yang, H. Yan, Z. Fu, B. Yang, J. Zuo and S. Fu, *Solid State Commun*, 2006, **139**, 218.

50. H. Li, Y. Zhou, C. Lv and M. Dang, *Mater Lett*, 2011, **65**, 1808.

51. Y. Cao, Y. Wang, Y. Zhu, H. Chen, Z. Li, J. Ding and Y. Chi, *Superlattices Microst.*, 2006, **40**, 155.

52. V. Jovic, J. B. Metson, T. Soehnel and G. I. N. Waterhouse, Wagga, Australia, 2011.

53. Y. N. Fu, Z. G. Jin, Z. F. Liu and W. Li, *J Eur Ceram Soc*, 2007, **27**, 2223.

54. Y. W. G. Cao, *Nanostructures and Nanomaterials: Synthesis, Properties & Applications*, Imperial College Press, London, 2004.

55. Atkins P.W and D. P. J., *Atkins' Physical Chemistry* Oxford University Press, Oxford, UK, 2006.

56. F. Meseguer, *Colloid Surface A*, 2005, **270**, 1.

57. C. M. Doherty, R. A. Caruso, B. M. Smarsly and C. J. Drummond, *Chem Mater*, 2009, **21**, 2895.

58. J. Fang, Y. Xuan and Q. Li, *Sci. China Tech. Sci.*, 2010, **53**, 3088.

59. B. T. Holland, C. F. Blanford and A. Stein, *Science*, 1998, **281**, 538.

60. R. D'Amato, I. Venditti, M. V. Russo and M. Falconieri, *J Appl Polym Sci*, 2006, **102**, 4493.

61. B. Mandlmeier, J. M. Szeifert, D. Fattakhova-Rohlfing, H. Amenitsch and T. Bein, *J Am Chem Soc*, 2011, **133**, 17274.

62. J. Wijnhoven, S. J. M. Zevenhuizen, M. A. Hendriks, D. Vanmaekelbergh, J. J. Kelly and W. L. Vos, *Adv Mater*, 2000, **12**, 888.

63. P. Ferrand, M. Egen, B. Griesebock, J. Ahopelto, M. Muller, R. Zentel, S. G. Romanov and C. M. S. Torres, *Appl Phys Lett*, 2002, **81**, 2689.

64. Y. Fu, Z. Jin, Z. Liu, Y. Liu and W. Li, *Mater. Lett.*, 2008, **62**, 4286.

65. J. Fang, Y. Xuan and Q. Li, *Chinese Sci. Bull.*, 2011, **56**, 2156.

66. J. Li, S. Zhang, H. Chen, Z.-Z. Gu and Z. Lu, *Colloid Surface A*, 2007, **299**, 54.

67. F. Jonsson, C. M. S. Torres, J. Seekamp, M. Schniedergers, A. Tiedemann, J. H. Ye and R. Zentel, *Microelectron Eng*, 2005, **78-79**, 429.

68. Z. Liu, J. Ya, Y. Xin, J. Ma and C. Zhou, *J. Cryst. Growth*, 2006, **297**, 223.

69. P. Ferrand, M. Egen, R. Zentel, J. Seekamp, S. G. Romanov and C. M. S. Torres, *Appl Phys Lett*, 2003, **83**, 5289.

70. J. Fang, Y. Xuan and Q. Li, *Chinese Science Bulletin*, 2011, **56**, 2156.

71. Z. Li, J. Wang and Y. Song, *Particuology*, 2011, **9**, 559.

72. Y.-Q. Zhang, J.-X. Wang, Z.-Y. Ji, W.-P. Hu, L. Jiang, Y.-L. Song and D.-B. Zhu, *J Mater Chem*, 2007, **17**, 90.

73. P. Jiang, J. Cizeron, J. F. Bertone and V. L. Colvin, *J Am Chem Soc*, 1999, **121**, 7957.

74. A. Chiappini, C. Armellini, A. Chiasera, M. Ferrari, L. Fortes, M. C. Goncalves, R. Guider, Y. Jestin, R. Retoux, G. N. Conti, S. Pelli, R. M. Almeida and G. C. Righini, *J Non-Cryst Solids*, 2009, **355**, 1167.

75. P. Jiang and M. J. McFarland, *J Am Chem Soc*, 2004, **126**, 13778.

76. J. P. Hoogenboom, A. K. van Langen-Suurling, J. Romijn and A. van Blaaderen, *Phy. Rev. E*, 2004, **69**.

77. P. Tessier, O. D. Velev, A. T. Kalambur, A. M. Lenhoff, J. F. Rabolt and E. W. Kaler, *Adv Mater*, 2001, **13**, 396.

78. C. H. Chan, C. C. Chen, C. K. Huang, W. H. Weng, H. S. Wei, H. Chen, H. T. Lin, H. S. Chang, W. Y. Chen, W. H. Chang and T. M. Hsu, *Nanotechnology*, 2005, **16**, 1440.

79. Y. Imura, H. Nakazawa, E. Matsushita, C. Morita, T. Kondo and T. Kawai, *J. Coll. Inter. Sci.*, 2009, **336**, 607.

80. N. P. Johnson, D. W. McComb, A. Richel, B. M. Treble and R. M. De la Rue, *Synth. Met.*, 2001, **116**, 469.

81. Z. R. Li, J. X. Wang and Y. L. Song, *Particuology*, 2011, **9**, 559.

82. S. H. Park and Y. N. Xia, *Adv Mater*, 1998, **10**, 1045.

83. S. R. Yeh, M. Seul and B. I. Shraiman, *Nature*, 1997, **386**, 57.

84. F. L. Calderon, T. Stora, O. M. Monval, P. Poulin and J. Bibette, *Phys Rev Lett*, 1994, **72**, 2959.

85. J. P. Ge, Y. X. Hu, M. Biasini, W. P. Beyermann and Y. D. Yin, *Angew Chem Int Edit*, 2007, **46**, 4342.

86. N. D. Denkov, O. D. Velev, P. A. Kralchevsky, I. B. Ivanov, H. Yoshimura and K. Nagayama, *Langmuir*, 1992, **8**, 3183.

87. N. V. Dziomkina and G. J. Vancso, *Soft Matter*, 2005, **1**, 265.

88. P. Jiang, J. F. Bertone, K. S. Hwang and V. L. Colvin, *Chem Mater*, 1999, **11**, 2132.

89. A. J. Wang, S. L. Chen, P. Dong, Q. Zhou, G. M. Yuan and G. C. Su, *Chin. Phys. Lett.*, 2009, **26**.

90. I. Huuva, MSc, Umea University, 2012.

91. J. C. Loudet and B. Pouligny, *Eur Phys J E*, 2011, **34**.

92. X. Z. Ye and L. M. Qi, *Sci China Chem*, 2014, **57**, 58.

93. X. Ma, B. Li and B. S. Chaudhari, *Appl Surf Sci*, 2007, **253**, 3933.

94. H. Yan, M. Wang, Y. Ge and P. Yu, *Opt. Fiber Technol.*, 2009, **15**, 324.

95. E. Yablonovitch, *Phys Rev Lett*, 1987, **58**, 2059.

96. S. John, *Phys Rev Lett*, 1987, **58**, 2486.

97. Y. N. Xia, B. Gates and Z. Y. Li, *Adv Mater*, 2001, **13**, 409.

98. D. M. Kuncicky, B. G. Prevo and O. D. Velev, *J Mater Chem*, 2006, **16**, 1207.

99. C. J. Wu, Y. C. Hsieh and H. T. Hsu, *Prog. Electromagn.*, 2011, **114**, 271.

100. R. H. Lipson and C. Lu, *Eur. Phys. J.*, 2009, **30**, S33.

101. J. Zhang, Z. Sun and B. Yang, *Curr. Opin. Colloid Interface Sci.*, 2009, **14**, 103.

102. S. H. A. Lee, N. M. Abrams, P. G. Hoertz, G. D. Barber, L. I. Halaoui and T. E. Mallouk, *J Phys Chem B*, 2008, **112**, 14415.

103. L. I. Halaoui, N. M. Abrams and T. E. Mallouk, *J Phys Chem B*, 2005, **109**, 6334.

104. P. G. O'Brien, N. P. Kherani, S. Zukotynski, G. A. Ozin, E. Vekris, N. Tetreault, A. Chutinan, S. John, A. Mihi and H. Miguez, *Adv Mater*, 2007, **19**, 4177.

105. J. F. Galisteo-Lopez, M. Ibisate, R. Sapienza, L. S. Froufe-Perez, A. Blanco and C. Lopez, *Adv Mater*, 2011, **23**, 30.

106. H. Li, Y. Zhou, C. X. Lv and M. M. Dang, *Mater Lett*, 2011, **65**, 1808.

107. V. Abramova and A. Sinitskii, *Superlattice Microst*, 2009, **45**, 624.

108. W. Dong, H. J. Bongard and F. Marlow, *Chem Mater*, 2003, **15**, 568.

109. B. Hatton, L. Mishchenko, S. Davis, K. H. Sandhage and J. Aizenberg, *Proc. Natl. Acad. Sci. U.S.A.*, 2010, **107**, 10354.

110. Y. K. Koh, L. K. Teh and C. C. Wong, in *Advanced Materials for Micro and Nano Systems, Singapore-MIT Alliance*, School of Material Engineering, Nanyang Technological University, 2005.

111. A. A. Chabanov, Y. Jun and D. J. Norris, *Appl Phys Lett*, 2004, **84**, 3573.

112. J.-H. Lee, *Sensor Actuat B-Chem*, 2009, **140**, 319.

113. M. Yoshimura and H. Suda, *Hydroxyapatite and Related Materials*, 1994, 45.

114. N. D. Hoa and S. A. El-Safty, *Nanotechnology*, 2011, **22**.

115. H. X. Yang, J. F. Qian, Z. X. Chen, X. P. Ai and Y. L. Cao, *J Phys Chem C*, 2007, **111**, 14067.

116. S. Kalele, R. Dey, N. Hebalkar, J. Urban, S. W. Gosavi and S. K. Kulkarni, *Pramana*, 2005, **65**, 787.

117. J. Hu, M. Chen, X. S. Fang and L. W. Wu, *Chem. Soc. Rev.*, 2011, **40**, 5472.

118. R. A. Caruso, A. Susha and F. Caruso, *Chem. Mat.*, 2001, **13**, 400.

119. Z. Y. Zhong, Y. D. Yin, B. Gates and Y. N. Xia, *Adv. Mater.*, 2000, **12**, 206.

120. F. Kleitz, PhD, Max-Plank-Institut fur Kohlenforschung, 2002.

121. T. Hyodo, K. Sasahara, Y. Shimizu and M. Egashira, *Sensor Actuat B-Chem*, 2005, **106**, 580.

122. I. B. Jang, J. H. Sung, H. J. Choi and I. Chin, *Synth. Met.*, 2005, **152**, 9.

123. A. Imhof, *Langmuir*, 2001, **17**, 3579.

124. D. B. Wang, C. X. Song, Y. S. Lin and Z. S. Hu, *Mater. Lett.*, 2006, **60**, 77.

125. J. G. Wang, J. M. Yu, X. L. Zhu and X. Z. Kong, *Nanoscale Res. Lett.*, 2012, **7**, 1.

126. H. E. Wang, L. X. Zheng, C. P. Liu, Y. K. Liu, C. Y. Luan, H. Cheng, Y. Y. Li, L. Martinu, J. A. Zapien and I. Bello, *J Phys Chem C*, 2011, **115**, 10419.

127. S. Lou, X. M. Guo, T. X. Fan and D. Zhang, *Energ Environ Sci*, 2012, **5**, 9195.

128. M. I. Baraton, *The Open Nanoscience Journal*, 2011, **5**, 64.

129. A. Wolcott, W. A. Smith, T. R. Kuykendall, Y. P. Zhao and J. Z. Zhang, *Adv Funct Mater*, 2009, **19**, 1849.

130. R. van de Krol, Y. Q. Liang and J. Schoonman, *J Mater Chem*, 2008, **18**, 2311.

131. S. Choudhary, S. Upadhyay, P. Kumar, N. Singh, V. R. Satsangi, R. Shrivastav and S. Dass, *Int J Hydrogen Energ*, 2012, **37**, 18713.

132. L. Li, PhD, Carnegie Mellon University.

133. Y. Matsumoto, *J Solid State Chem*, 1996, **126**, 227.

134. A. Janotti and C. G. Van de Walle, *Rep Prog Phys*, 2009, **72**.

135. Z. H. Zhang, M. F. Hossain and T. Takahashi, *Int J Hydrogen Energ*, 2010, **35**, 8528.

136. Y. Sun, G. X. Wang and K. P. Yan, *Int J Hydrogen Energ*, 2011, **36**, 15502.

137. Q. Kang, J. Y. Cao, Y. J. Zhang, L. Q. Liu, H. Xu and J. H. Ye, *J Mater Chem A*, 2013, **1**, 5766.

138. A. Fujishima and K. Honda, *Nature*, 1972, **238**, 37.

139. A. Mihi, C. J. Zhang and P. V. Braun, *Angew Chem Int Edit*, 2011, **50**, 5711.

140. S. Guldin, S. Huttner, M. Kolle, M. E. Welland, P. Muller-Buschbaum, R. H. Friend, U. Steiner and N. Tetreault, *Nano Lett*, 2010, **10**, 2303.

141. L. Etgar, *Materials*, 2013, **6**, 445.

142. B. Oregan and M. Gratzel, *Nature*, 1991, **353**, 737.

143. F. F. Abdi, L. H. Han, A. H. M. Smets, M. Zeman, B. Dam and R. van de Krol, *Nat Commun*, 2013, **4**.

144. J. H. Wu, Z. Lan, S. C. Hao, P. J. Li, J. M. Lin, M. L. Huang, L. Q. Fang and Y. F. Huang, *Pure Appl Chem*, 2008, **80**, 2241.

145. A. Usami, S. Seki, Y. Mita, H. Kobayashi, H. Miyashiro and N. Terada, *Sol Energ Mat Sol C*, 2009, **93**, 840.

146. K. E. Lee, M. A. Gomez, S. Elouatik and G. P. Demopoulos, *Langmuir*, 2010, **26**, 9575.

147. F. De Angelis, S. Fantacci, E. Mosconi, M. K. Nazeeruddin and M. Gratzel, *J Phys Chem C*, 2011, **115**, 8825.

148. E. H. Kong, Y. J. Chang, Y. C. Park, Y. H. Yoon, H. J. Park and H. M. Jang, *Phys Chem Chem Phys*, 2012, **14**, 4620.

149. H. N. Kim and J. H. Moon, *Curr Appl Phys*, 2013, **13**, 1545.

150. Q. Y. Jia, W. X. Que, X. K. Qiu, P. Zhong and J. Chen, *Sci China Phys Mech*, 2012, **55**, 1158.

151. Q. F. Zhang and G. Z. Cao, *Nano Today*, 2011, **6**, 91.

152. H. Moosmuller, R. K. Chakrabarty and W. P. Arnott, *J Quant Spectrosc Ra*, 2009, **110**, 844.

153. Z. G. Zhang, PhD, Ecole Polytechnique Federale de Lausanne (EPFL), 2008.

154. K. M. and R. E., *Zeitschrift fur physik*, 1932, **78**, 318.

155. C. Scheu and W. D. Kaplan, *In-Situ Electron Microscopy: Applications in Physics, Chemistry and Materials Science*, Wiley-VCH, Germany, 2012.

156. C. Herring and M. H. Nichols, *Rev Mod Phys*, 1949, **21**, 185.

157. R. Pecora, *Dynamic Light Scattering : Applications of Photon Correlation Spectroscopy*, Plenum Press, New York an London, 1985.

158. R. J. Hunter, *Foundations of Colloid Science*, Clarendon Press, Oxford, UK, 1987.

159. B. J. Berne and R. Pecora, *Dynamic light Scattering : With Applications to Chemistry, Biology, and Physics*, General Publishing Company, Toronto, Canada, 2000.

160. J. W. Goodman, *J Opt Soc Am*, 1976, **66**, 1145.

161. A. Pich, S. Bhattacharya, A. Ghosh and H. J. P. Adler, *Polymer*, 2005, **46**, 4596.

162. Atkins P.W and C. M.J., *Principles of Physical Chemistry*, Pitman Publishing, London, 1982.

163. W. H. Bragg, *P R Soc Lond a-Conta*, 1914, **89**, 575.

164. J. I. Langford and A. J. C. Wilson, *J. Appl. Cryst.*, 1978, **11**, 102.

165. R. Guinebretiere, *X-Ray Diffraction by Polycrystalline Materials*, Wiley, New York, 2007.

166. A. B. Murphy, *Sol Energ Mat Sol C*, 2007, **91**, 1326.

167. S. Valencia, J. M. Marín and G. Restrepo, *The Open Materials Science Journal*, 2010, **4**, 9.

168. F. Yakuphanoglu, *J Alloy Compd*, 2010, **507**, 184.

169. K. Siraj, K. Javaid, J. D. Pedarnig, M. A. Bodea and S. Naseem, *J Alloy Compd*, 2013, **563**, 280.

170. A. Sinitskii, V. Abramova, N. Grigorieva, S. Grigoriev, A. Snigirev, D. V. Byelov and A. V. Petukhov, *Epl-Europhys Lett*, 2010, **89**.

171. D. N. Wang, V. L. Dimonie, E. D. Sudol and M. S. El-Aasser, *J. Appl. Polym. Sci.*, 2002, **84**, 2721.

172. J. Hu, M. Chen and L. M. Wu, *Polym Chem-Uk*, 2011, **2**, 760.

173. C. H. M. Caris, L. P. M. Vanelven, A. M. Vanherk and A. L. German, *Brit Polym J*, 1989, **21**, 133.

174. E. Schreiber, U. Ziener, A. Manzke, A. Plettl, P. Ziemann and K. Landfester, *Chem Mater*, 2009, **21**, 1750.

175. H. Lamb, *Hydrodynamics*, 4th Edition edn., University of Cambridge Press, Cambridge, 1916.

176. S. Armini, C. M. Whelan, M. Smet, S. Eslava and K. Maex, *Polym J*, 2006, **38**, 786.

177. L. C. Zheng, B. T. Li, P. Lin, X. X. Zhang, C. L. Zhang, B. Zhao and T. T. Wang, *Microfluid Nanofluid*, 2013, **15**, 11.

178. J. W. Goodwin, J. Hearn, C. C. Ho and R. H. Ottewill, *Colloid Polym Sci*, 1974, **252**, 464.

179. M. Müller, R. Zentel, T. Maka, S. G. Romanov and C. M. Sotomayor Torres, *Chem Mater*, 2000, **12**, 2508.

180. L. Group, Max Planck Institute for Polymer Research, Mainz, Germany, 2012.

181. D. J. Norris, E. G. Arlinghaus, L. L. Meng, R. Heiny and L. E. Scriven, *Adv Mater*, 2004, **16**, 1393.

182. Y. W. Cong, MSc, National University of Singapore, 2007.

183. J. E. G. J. Wijnhoven, L. Bechger and W. L. Vos, *Chem Mater*, 2001, **13**, 4486.

184. T. A. Scott, *J Phys Chem-Us*, 1946, **50**, 406.

185. N. Kolesnikov and E. Borisenko, *Modern Aspects of Bulk Crystal and Thin Film Preparation*, InTech, Singapore, 2012.

186. K. Liu, T. A. Schmedake and R. Tsu, *Phys. Lett. A*, 2008, **372**, 4517.

187. K. Liu, T. A. Schmedake and R. Tsu, *Phys. Lett. A*, 2009, **373**, 1885.

188. C. W. Cheng, S. K. Karuturi, L. J. Liu, J. P. Liu, H. X. Li, L. T. Su, A. I. Y. Tok and H. J. Fan, *Small*, 2012, **8**, 37.

189. J. Chattopadhyay, R. Srivastava and P. K. Srivastava, *J Appl Electrochem*, 2013, **43**, 279.

190. Z. H. Dong, X. Y. Lai, J. E. Halpert, N. L. Yang, L. X. Yi, J. Zhai, D. Wang, Z. Y. Tang and L. Jiang, *Adv Mater*, 2012, **24**, 1046.

191. C. Cheng, S. K. Karuturi, L. Liu, J. Liu, H. Li, L. T. Su, A. I. Y. Tok and H. J. Fan, *Small*, 2012, **8**, 37.

192. Y. Fu, Z. Jin, Z. Liu and W. Li, *J Eur Ceram Soc*, 2007, **27**, 2223.

193. J. W. Galusha, C.-K. Tsung, G. D. Stucky and M. H. Bartl, *Chem Mater*, 2008, **20**, 4925.

194. Y. Zeng, X. Wang, H. Wang, Y. Dong, Y. Ma and J. N. Yao, *Chem Commun*, 2010, **46**, 4312.

195. X. Y. Lai, J. Li, B. A. Korgel, Z. H. Dong, Z. M. Li, F. B. Su, J. A. Du and D. Wang, *Angew Chem Int Edit*, 2011, **50**, 2738.

196. L. L. Wang, Z. Lou, T. Fei and T. Zhang, *J Mater Chem*, 2011, **21**, 19331.

197. S. Kalele, R. Dey, N. Hebalkar, J. Urban, S. W. Gosavi and S. K. Kulkarni, *Pramana-J. Phys.*, 2005, **65**, 787.

198. G. H. Wang, L. Xu, J. Zhang, T. T. Yin and D. Y. Han, *Int J Photoenergy*, 2012.

199. A. Stein, F. Li and N. R. Denny, *Chem Mater*, 2007, **20**, 649.

200. M. Sadakane, C. Takahashi, N. Kato, T. Asanuma, H. Ihara and W. Ueda, *Chem Lett*, 2006, **35**, 480.

201. S. Gupta and M. Tripathi, *Chinese Sci Bull*, 2011, **56**, 1639.

202. H. Morkoc and U. Ozgur, *Zinc Oxide : Fundamentals, Materials and Device Technology* Wiley-VCH, Weinheim, Germany, 2009.

203. U. Diebold, *Surf Sci Rep*, 2003, **48**, 53.

204. H. Rath, S. Anand, M. Mohapatra, P. Dash, T. Som, U. P. Singh and N. C. Mishra, *Indian J Phys*, 2009, **83**, 559.

205. J. A. Bearden, *Rev. Mod. Phys.*, 1967, 78.

206. J. R. Song, L. X. Wen, J. F. Chen and H. M. Ding, *Adv Mat Res*, 2006, **11-12**, 551.

207. J. J. Yuan, T. A. Zhou and H. T. Pu, *J Phys Chem Solids*, 2010, **71**, 1013.

208. B. Ding, H. Kim, C. Kim, M. Khil and S. Park, *Nanotechnology*, 2003, **14**, 532.

209. E. Garcia, Z. B. Zhang and T. W. Coyle, *Liquid Precursors Plasma Spraying of TiO2 and Ce-Doped Ba(Zr0.2Ti0.8)O3 Coatings*, ASM International, Ohia, USA, 2007.

210. D. L. Vezie, E. L. Thomas and W. W. Adams, *Polymer*, 1995, **36**, 1761.

211. J. Jiang, F. Gu, W. Shao and C. Z. Li, *Ind Eng Chem Res*, 2012, **51**, 2838.

212. A. Esmanski and G. A. Ozin, *Adv Funct Mater*, 2009, **19**, 1999.

213. L. Y. Yang and W. B. Liau, *Synthetic Met*, 2010, **160**, 609.

214. H. B. Ni, M. Wang and W. Chen, *Opt Express*, 2011, **19**, 25900.

215. J. H. Lee, *Sensor Actuat B-Chem*, 2009, **140**, 319.

216. J. Zhang, S. R. Wang, Y. Wang, M. J. Xu, H. J. Xia, S. M. Zhang, W. P. Huang, X. Z. Guo and S. H. Wu, *Sensor Actuat B-Chem*, 2009, **139**, 411.

217. O. Shchepelina, V. Kozlovskaya, S. Singamaneni, E. Kharlampieva and V. V. Tsukruk, *J Mater Chem*, 2010, **20**, 6587.

218. G. M. Wang, H. Y. Wang, Y. C. Ling, Y. C. Tang, X. Y. Yang, R. C. Fitzmorris, C. C. Wang, J. Z. Zhang and Y. Li, *Nano Lett*, 2011, **11**, 3026.

219. M. A. Henderson, *Fundamental Investigations of Water Splitting on Model TiO2 Photocatalysts Doped for Visible Light Absorption*, Chemical

and Material Sciences Division Pacific Northwest National Laboratory, 2008.

220. K. Pan, Y. Z. Dong, W. Zhou, Q. J. Pan, Y. Xie, T. F. Xie, G. H. Tian and G. F. Wang, *Acs Appl Mater Inter*, 2013, **5**, 8314.

221. L. L. Yang, Q. X. Zhao, M. Willander and J. H. Yang, *J Cryst Growth*, 2009, **311**, 1046.

222. L. Vayssieres, *Adv Mater*, 2003, **15**, 464.

223. H. M. Chen, C. K. Chen, Y. C. Chang, C. W. Tsai, R. S. Liu, S. F. Hu, W. S. Chang and K. H. Chen, *Angew Chem Int Edit*, 2010, **49**, 5966.

224. C. Levy-Clement, J. Elias and R. Tena-Zaera, *Phys Status Solidi C*, 2009, **6**, 1596.

225. T. S. Kang, A. P. Smith, B. E. Taylor and M. F. Durstock, *Nano Lett*, 2009, **9**, 601.

226. J. Elias, C. Lévy-Clément, M. Bechelany, J. Michler, G.-Y. Wang, Z. Wang and L. Philippe, *Adv Mater*, 2010, **22**, 1607.

227. H. Wang, J. A. Xie, K. P. Yan and M. Duan, *J Mater Sci Technol*, 2011, **27**, 153.

228. R. Wahab, Y. S. Kim, K. Lee and H. S. Shin, *J Mater Sci*, 2010, **45**, 2967.

229. H. Oh, J. Krantz, I. Litzov, T. Stubhan, L. Pinna and C. J. Brabec, *Sol Energ Mat Sol C*, 2011, **95**, 2194.

230. B. H. Dong, L. X. Cao, G. Su and W. Liu, *Chem Commun*, 2010, **46**, 7331.

231. Y. Lee and M. Kang, *Mater Chem Phys*, 2010, **122**, 284.

232. N. Ghobadi, *Int. Nano Lett.*, 2013, 2.

233. B. K. Sharma, N. Khare and M. Kumar, *J. Nanosci. Nanotechnol.*, 2010, **10**, 8424.

234. W. Lee, S. K. Min, V. Dhas, S. B. Ogale and S. H. Han, *Electrochem Commun*, 2009, **11**, 103.

235. M. S. Johal, *Understanding Nanomaterials*, CRC Press : Taylor & Francis Group, Florida, USA, 2011.

236. E. Stern, R. Wagner, F. J. Sigworth, R. Breaker, T. M. Fahmy and M. A. Reed, *Nano Lett*, 2007, **7**, 3405.

237. Z. J. Ning, H. N. Tian, C. Z. Yuan, Y. Fu, H. Y. Qin, L. C. Sun and H. Agren, *Chem Commun*, 2011, **47**, 1536.

238. J. Huang, K. L. Mulfort, P. W. Du and L. X. Chen, *J Am Chem Soc*, 2012, **134**, 16472.

239. P. Reiss, M. Protiere and L. Li, *Small*, 2009, **5**, 154.

240. I. A. Ji, M. J. Park, J. Y. Jung, M. J. Choi, Y. W. Lee, J. H. Lee and J. H. Bang, *B Korean Chem Soc*, 2012, **33**, 2200.

241. S. S. Kanmani and K. Ramachandran, *Renew Energ*, 2012, **43**, 149.

242. H. N. Kim and J. H. Moon, *Curr Appl Phys*, 2013, **13**, 841.

243. H. J. Fan, Y. Yang and M. Zacharias, *J Mater Chem*, 2009, **19**, 885.

244. J. C. Conesa, *Catal Today*, 2013, **208**, 11.

245. Z. Ali, S. Ali, I. Ahmad, I. Khan and H. A. R. Aliabad, *Physica B*, 2013, **420**, 54.

246. J. S. Jang, P. H. Borse, J. S. Lee, K. T. Lim, O. S. Jung, E. D. Jeong, J. S. Bae, M. S. Won and H. G. Kim, *B Korean Chem Soc*, 2009, **30**, 3021.

247. P. Charoensirithavorn and S. Yoshikawa, in *Sustainable Energy and Environment*, Kyoto University, Bangkok, 2006, pp. 1.

248. Z. D. Li, C. H. Yao, Y. H. Yu, Z. Y. Cai and X. D. Wang, *Adv Mater*, 2014, **26**, 2262.

249. Y. Chen, Z. F. Tang and Z. G. Chen, *J Inorg Organomet P*, 2013, **23**, 839.

250. Z. G. Xiong and X. S. Zhao, *J Am Chem Soc*, 2012, **134**, 5754.

251. T. K. Townsend, N. D. Browning and F. E. Osterloh, *Acs Nano*, 2012, **6**, 7420.

252. M. R. Allen, A. Thibert, E. M. Sabio, N. D. Browning, D. S. Larsen and F. E. Osterloh, *Chem Mater*, 2010, **22**, 1220.

253. S. Y. Ku and S. Y. Lu, *Int J Electrochem Sc*, 2011, **6**, 5219.

254. N. Kopidakis, E. A. Schiff, N. G. Park, J. van de Lagemaat and A. J. Frank, *J Phys Chem B*, 2000, **104**, 3930.

255. K. D. Benkstein, N. Kopidakis, J. van de Lagemaat and A. J. Frank, *J Phys Chem B*, 2003, **107**, 7759.

256. T. O. P. Atkins, J. Rourke, M. Weller and F. Armstrong, *Inorganic Chemistry*, 4th edn edn., Oxford University Press, Oxford, England, 2006.

257. H. W. a. L. M. Peter, *J. Phys. Chem.*, 2012, **116**, 10468.

258. T. A. H. Onishi, C. Egawa and Y. Iwasawa, *Surf. Sci.*, 1987, **199**, 54.

259. F. F. C. A. Kelly, D. W. Thompson, J. M. Stipkala and G. J. Meyer, *Langmuir*, 1999, **15**, 7047.

260. L. Li, G. S. Rohrer and P. A. Salvador, *J Am Ceram Soc*, 2012, **95**, 1414.

261. C. Eley, T. Li, F. L. Liao, S. M. Fairclough, J. M. Smith, G. Smith and S. C. E. Tsang, *Angew Chem Int Edit*, 2014, **53**, 7838.

262. I. Hod and A. Zaban, *Langmuir*, 2014, **30**, 7264.